

**SURFACE MODIFICATION OF PAPER AND CELLULOSE USING
PLASMA ENHANCED CHEMICAL VAPOR DEPOSITION
EMPLOYING FLUOROCARBON PRECURSORS**

A Dissertation

Presented to

The Academic Faculty

By

Sudeep Vaswani

In Partial Fulfillment

Of the Requirements for the Degree

Doctor of Philosophy in Chemical Engineering

Georgia Institute of Technology

January 2005

**SURFACE MODIFICATION OF PAPER AND CELLULOSE USING
PLASMA ENHANCED CHEMICAL VAPOR DEPOSITION
EMPLOYING FLUOROCARBON PRECURSORS**

Approved by:

Dr. Dennis W. Hess, Advisor
School of Chemical & Biomolecular
Engineering
Georgia Institute of Technology

Dr. Peter J. Ludovice
School of Chemical & Biomolecular
Engineering
Georgia Institute of Technology

Dr. Timothy Patterson
School of Mechanical Engineering
Georgia Institute of Technology

Dr. Sue A. Bidstrup Allen
School of Chemical & Biomolecular
Engineering
Georgia Institute of Technology

Dr. Clifford L. Henderson
School of Chemical & Biomolecular
Engineering
Georgia Institute of Technology

Date Approved: January 13, 2005

Dedicated

to my best friend and wife, Akanksha, for her never ending love and support

ACKNOWLEDGEMENTS

First and foremost, I would like to express my sincere appreciation and gratitude to my advisor, Dr. Dennis Hess, for his invaluable guidance, patience and continuous support on all the facets of my academic life. His technical expertise, his boundless excitement for research and creativity, and his attention to detail were constant sources of inspiration and motivation. One of the things that I admire about Dr. Hess is his always being available to his students for research discussions and advice. He always encouraged me to come up with creative and independent ideas.

I also want to thank my committee members, Dr. Sue Ann Bidstrup Allen, Dr. Pete Ludovice, Dr. Cliff Henderson, Dr. Jere Koskinen and Dr. Tim Patterson, for providing valuable suggestions during this work and for serving on my committee.

During my stay at Georgia Tech, I have received support and assistance from several faculty and research groups. I am thankful to Dr. Cliff Henderson and Dr. Paul Kohl for allowing me to use the equipment in their labs. I would also like to thank Dr. Ron Sabo (IPST) and Dr. Ravindra Tanikella for their help and assistance. I am indebted to Dr. Johannes Leisen (PTFE), who was of immense help in conducting MRI studies. His valuable suggestions and MATLAB codes were very useful in my research work. I am very thankful to him for his patience and support.

I am grateful to my research group (Plasma Processing and Surface Cleaning) members who made my stay here a great learning experience. In particular, many thanks to Galit Levitin for helping me with SEM and for discussing ideas with me, to Jie Diao for help with cleanroom processing, to Satya Myneni for helping me with SEM studies and XPS analysis, and to Prabhakar Tamirisa for assisting me in quickly setting up our lab in ES&T after the move from Bunker Henry and for helping me with various lab activities requiring ‘muscle power’ (especially lifting the heavy top plate of our behemoth plasma system). I would also like to thank Enrique Sanchez for helping me with paper making.

I am thankful to Microelectronics Staff, especially Bob Rose and Scott Fowler, for help with equipment related issues. Scott Fowler was of great help to me with his expertise in plasma and RF related issues. He helped me great number of times with identifying RF leakage and grounding issues. I am also thankful to Linda Perry, Imogene Baker and Gloria Beale for rapidly processing my purchase orders.

Finally, I would like to thank my family and parents for their constant love and support. My father and mother have always given me the best and loved me beyond any bounds. My brother Rakesh and sister Neelam have always encouraged and supported me in my endeavors. My father-in-law and mother-in-law have always had great faith in me and have supported me during trying times. My brother-in-law Gaurav and sister-in-law Naina have motivated and encouraged me on all fronts [Chota Nikku – has delighted me with her cute activities]. Last but not the least, my loving wife Akanksha has been my best friend and has always stood by my side. I am the luckiest to have her as my wife.

TABLE OF CONTENTS

Acknowledgements.....	iv
List of Tables.....	xi
List of Figures.....	xiii
Summary.....	xxii
1. Introduction.....	1
2. Background.....	8
2.1 Surface Modification	8
2.2 Barrier Coatings on Paper and Cellulose	11
2.3 Plasma Deposition of Fluorocarbon Materials	14
2.3.1 Plasma Background and Fundamentals	14
2.3.2 Background on Fluorocarbon Plasmas	17
2.3.3 Plasma Pulsing	22
2.4 Overview of Paper Making Process (Fiber and Paper Surface Formation)....	25
2.5 Surface Modification of Paper and Cellulose using Plasmas	29
2.6 Thesis Organization	35
3. Experimental Procedures and Analytical Techniques.....	38

3.1 Plasma Reactor Configuration and Operating Details	39
3.2 Contact Angle	45
3.3 Film Thickness and Optical Properties	47
3.4 Chemical Structure and Properties.....	51
3.4.1 X-ray Photoelectron Spectroscopy	51
3.4.2 Infrared Spectroscopy	56
3.5 Physical Properties.....	59
3.5.1 Moisture Uptake of Fluorocarbon Films.....	59
3.6 Surface Morphology	62
3.7 Magnetic Resonance Imaging Studies	64
3.7.1 Principles of Magnetic Resonance Imaging	65
3.7.2 MRI Experimental Conditions	72
3.8 Thick Handsheet Preparation.....	73
3.9 Fluorocarbon Coating Depth in Paper	77
3.10 Organic Vapor Quartz Crystal Microbalance Studies	80
3.10.1 Vacuum QCM Design.....	81
3.10.2 QCM System Operation.....	84

4. Fluorocarbon Film Deposition On Paper and Cellulose Using Pentafluoroethane and Octafluorocyclobutane Precursors.....	86
4.1 Results.....	87
4.1.1 Fluorocarbon Film Deposition Rates on a 4-cm Parallel Plate System	87
4.1.2 XPS studies on Fluorocarbon Films	97
4.1.3 Fourier Transform Infrared Spectroscopy of Fluorocarbon Films	106
4.1.4 Scanning Electron Microscopy	107
5. Hydrophobic Properties Of Fluorocarbon Films On Paper/Cellulose and Moisture Absorption Studies Using a Quartz Crystal Microbalance.....	115
5.1 Hydrophobic Properties of Fluorocarbon Films	115
5.1.1 Hydrophobic Properties with Varying Fluorocarbon Film Thickness.	116
5.1.2 Hydrophobic Properties with Varying Fluorocarbon Film Composition	121
5.2 Moisture Absorption Studies using QCM Measurements	128
5.2.1 Steady State Moisture Uptake.....	130
5.2.2 Transient Moisture Absorption Studies	134
6. Lipophobic Properties Of Fluorocarbon Films On Paper and Quantification Of Grease Barrier Properties.....	139
6.1 Grease Barrier Materials and Properties	139

6.2 Grease Barrier Properties of PFE Coated Copy Paper.....	145
6.2.1 Oleic Acid Penetration Studies	145
6.2.2 TAPPI T559 Grease Barrier Test.....	146
6.3 Hexadecane Vapor Studies Using a Quartz Crystal Microbalance	148
6.3.1 Hexadecane Uptake by Fluorocarbon Films.....	149
6.3.2 Hexadecane Sorption and Desorption Kinetics	152
6.3.3 Hexadecane Diffusion Mechanism in Fluorocarbon Films	167
6.4 Magnetic Resonance Imaging of Hexadecane Permeation.....	172
6.4.1 MRI Sample Preparation.....	172
6.4.2 MRI Experiment Methodology.....	174
6.4.3 MRI Calibration Curve for Quantifying MRI SE Signal Data	175
6.4.4 MRI Image and Data Processing	177
6.5 Flow Through Porous Media	187
6.6 Fluorocarbon Penetration Depth in PFE Coated Paper.....	207
6.7 Conclusions of Grease Barrier Experiments.....	214
7. Dual Layer Films Of Fluorocarbon and Hydrogel	216
7.1 Multilayer Structures for Packaging.....	216

7.2 Dual layer films (Fluorocarbon film and hydrogel film)	219
7.3 Dual Layer Film Deposition Using Plasma Enhanced CVD	220
7.3.1 Experimental Conditions	220
7.3.2 Dual Layer Film Characterization	221
7.3.3 Results and Discussion	222
7.3.4 Conclusions.....	235
8. Summary and Future Directions	237
8.1 Summary	237
8.2 Recommendations for Future Work.....	242
References.....	247
Vita.....	266

LIST OF TABLES

Table 3.1 Regions of Infrared Spectrum.....	57
Table 4.1 Published literature values of absolute binding energies [19, 110-115].....	102
Table 4.2 Relative Concentrations of chemical moieties in fluorocarbon films deposited from PFE and C ₄ F ₈ precursors.....	103
Table 4.3 Relative Concentrations of chemical moieties in fluorocarbon films deposited from PFE with varying plasma duty cycle (varying t _{off} time in pulsing). ...	105
Table 5.1 Effect of varying plasma duty cycle on composition of fluorocarbon films deposited on paper.	123
Table 5.2 Thickness and Refractive Index of Fluorocarbon Films Deposited on Silicon	130
Table 5.3 Diffusivity data for PFE and C ₄ F ₈ films at 85% relative humidity [Deposition Conditions: 30W, 120°C, and 1 Torr].....	137
Table 6.1 Test Kit Reagents (TAPPI T559 Test) [153].....	147
Table 6.2 Grease Resistance Testing Results for PFE coated copy paper (TAPPI T559).	147
Table 6.3 Hexadecane Diffusivity in Fluorocarbon Films of Different Thicknesses (Error values represent 95% confidence interval over the mean).	170
Table 6.4 Parameters of handsheets fabricated from SWBK with varying refining time.	173
Table 7.1 XPS sampling depths at various take-off angles for an element with $\lambda = 2\text{nm}$	229

Table 7.2 Elemental Composition of thin p-NIPAAM film (4.5 nm) on top of PFE film at various take-off angles with respect to the detector	229
Table 7.3. High Resolution C1s spectra peak deconvolution of dual layer film (4.5 nm p-NIPAAM on top of PFE film).	230
Table 7.4 Elemental Composition of thin PFE film (10 nm) on top of p-NIPAAM film at various take-off angles with respect to the detector	233
Table 7.5 High Resolution C1s spectra peak deconvolution of dual layer film (10 nm of PFE on top of p-NIPAAM film).	234

LIST OF FIGURES

Figure 1.1. Sales of barrier packaging used in various applications [3].	2
Figure 1.2 Percentage share of various packaging substrates in the US market in the year 2003 [2].	4
Figure 2.1 Schematic diagram of incident and outgoing particle fluxes at a surface in contact with a low-pressure plasma [11].	17
Figure 2.2. Boundary between etching and polymerization processes of fluorocarbons as a function of fluorine to carbon ratio of the feed monomer [13].	19
Figure 3.1 Parallel Plate Plasma Reactor Set up	40
Figure 3.2 Setup of 6” Parallel Plate Plasma Deposition System	44
Figure 3.3 Set-up for contact angle measurements.	46
Figure 3.4 Contact angle showing a wetting (a) and a non-wetting surface (b).	46
Figure 3.5 A schematic of the geometry of an ellipsometry measurement	49
Figure 3.6 Simple Schematic of X-ray Photoelectron Spectroscopy System [82].	52
Figure 3.7 Schematic representing the basic principle of XPS [82].	54
Figure 3.8 Schematic showing various characterization modes with an SEM [88].	63
Figure 3.9 The precession of a non-parallel atomic magnetic moment μ around an external magnetic field B_0 at an angular frequency ω_L	67

Figure 3.10 Experimental timing diagrams for the following: (a) the basic SE sequence. A magnetization echo is created using two RF pulses spaced by an adjustable $TE/2$. Recording of magnetic resonance images requires repetition of the basic sequence (as shown) separated by a repetition time, TR , using different settings of magnetic field gradients for subsequent sequences. (b) Variation of the basic sequence used for the calibration of image intensities with gravimetrically determined moisture contents. By subsequently recording the magnetization for a single-pulse excitation (no field gradients) and SE (field gradients set for an imaging experiment), the direct comparison of intensities may be used for construction of a calibration curve [96].	70
Figure 3.11 One-dimensional signal generation schematic showing the decay length, L , for thermal-waves and the optical decay lengths for lower (α_1) and higher (α_2) values of absorption coefficient. As α increases, more of the absorption occurs in the region near the sample's surface that is active in signal generation [101].	79
Figure 3.12 Experimental setup for organic vapor (Hexadecane) QCM system	83
Figure 4.1 Deposition Rate of PFE (nm/min) with varying RF Power [$P = 1$ Torr; $T_{\text{BottomElectrode}} = 120$ °C; PFE flowrate = 20 sccm; Ar flowrate = 75 sccm; 4-cm electrode area].	89
Figure 4.2 Deposition rate of PFE (nm/min) with varying substrate temperature (°C) [Other deposition conditions constant: $P = 1$ Torr; RF = 30 W; Ar flowrate = 75 sccm; PFE flowrate = 20 sccm].	90
Figure 4.3 Arrhenius plot for PFE film deposition [$P = 1$ Torr; RF = 30 W; Ar flowrate = 75 sccm; PFE flowrate = 20 sccm].	91
Figure 4.4 Deposition Rate of OFCB (nm/min) with varying RF Power [$P = 1$ Torr; $T_{\text{BottomElectrode}} = 120$ °C; OFCB flowrate = 15 sccm; Ar flowrate = 75 sccm; 4-cm electrode area].	92
Figure 4.5 Deposition rate of OFCB (nm/min) with varying substrate temperature (°C) [Other deposition conditions constant: $P = 1$ Torr; RF = 30 W; Ar flowrate = 75 sccm; OFCB flowrate = 15 sccm].	93
Figure 4.6 Arrhenius plot for OFCB film deposition [$P = 1$ Torr; RF = 30 W; Ar flowrate = 75 sccm; OFCB flowrate = 15 sccm].	94

Figure 4.7 Deposition Rate of PFE (nm/min) with varying RF Power [P = 1 Torr; $T_{\text{BottomElectrode}} = 120\text{ }^{\circ}\text{C}$; PFE flowrate = 20 sccm; Ar flowrate = 75 sccm; 6-inch electrode area].	95
Figure 4.8 Deposition rate of PFE (nm/min) with varying substrate temperature ($^{\circ}\text{C}$) [Other deposition conditions constant: P = 1 Torr; RF = 100 W; Ar flowrate = 75 sccm; PFE flowrate = 20 sccm].	96
Figure 4.9 Arrhenius plot for PFE film deposition [P = 1 Torr; RF = 30 W; Ar flowrate = 75 sccm; PFE flowrate = 20 sccm; 6-inch electrode size].	97
Figure 4.10 XPS survey scan of cellulose showing carbon and oxygen peaks	98
Figure 4.11 Structure of cellulose consists of long polymer chains of glucose units connected by a <i>beta-acetal</i> linkage [106].	99
Figure 4.12 Cellulose C1s peak deconvoluted into four Gaussian peaks corresponding to C-C or C-H, C-O, C=O, O-C=O.	100
Figure 4.13 Survey scan of fluorocarbon film deposited from PFE showing C1s, F1s, and O1s peaks.	101
Figure 4.14 High resolution C1s spectrum of fluorocarbon film deposited on cellulose surface [Deposition conditions: RF = 30 W; P = 1 Torr, T = 120 $^{\circ}\text{C}$; PFE flowrate = 20 sccm, Ar flowrate = 75 sccm]	103
Figure 4.15 FTIR absorption spectra of fluorocarbon film deposited from PFE [P = 1 Torr, RF = 30 W, T = 120 $^{\circ}\text{C}$; Ar flowrate = 75 sccm; PFE flowrate = 20 sccm]	107
Figure 4.16 SEM micrograph of PFE film deposited on silicon wafer [P = 1 Torr, T = 120 $^{\circ}\text{C}$; RF = 100 W on 6" platen; Film thickness = 1 μm]	108
Figure 4.17 SEM micrograph of the surface of: (a) an uncoated paper sample, and (b) a PFE coated paper sample. Solid aggregates between the fibers are inorganic filler material in the paper.	110
Figure 4.18 SEM micrograph of the cross-section of: (a) an uncoated paper sample, and (b) a PFE coated paper sample.	111

Figure 4.19 SEM micrograph of a copy paper coated with 5 μm PFE film [P = 120 $^{\circ}\text{C}$, T = 120 $^{\circ}\text{C}$; RF = 100 W on 6" platen]	112
Figure 4.20 High magnification SEM micrographs of copy paper coated with 5 μm PFE film. Globule-like morphology of plasma polymerized PFE is evident.	114
Figure 5.1 Video contact angle of water droplet on surface of 90 nm fluorocarbon coated cellulose. High contact angle indicates hydrophobic behavior. [1, t, 2, L, and R points on the water droplet above indicate curve fitting points].....	117
Figure 5.2 Variation of water contact angle with time for PFE films of different thicknesses deposited on cellulose. Films with > 70 nm of PFE thickness provide stable contact angles over an extended period of time.	119
Figure 5.3 Contact angle data with time for ~100 nm fluorocarbon films deposited on paper with varying pulse "off" times [RF power = 100 W; t_{on} = 10 ms; P = 1 Torr; T = 120 $^{\circ}\text{C}$ for all the samples].....	123
Figure 5.4 Sessile drop initial water contact angle (t = 0 min) measured on coated paper substrate as a function of (%CF ₃ + %CF ₂) incorporation in fluorocarbon film.	124
Figure 5.5 Percentage (CF ₃ + CF ₂) incorporation in fluorocarbon film with varying "off" times in plasma pulsing.	125
Figure 5.6 Effect of varying pulse "off" times on F:C ratio of fluorocarbon films.	126
Figure 5.7 Comparison of initial water contact angle (t = 0 ms) on fluorocarbon coated copy paper and on a Si wafer with varying pulse "off" times. Higher surface roughness of paper contributes to its higher contact angle. Both surfaces follow essentially the same trend with varying pulse "off" times.	127
Figure 5.8 Steady-state moisture uptake (ng) as a function of relative humidity (%) for films of two different thicknesses (t_1 = 0.68 μm and t_2 = 1.88 μm) deposited from PFE. Deposition conditions: 30W, 120 $^{\circ}\text{C}$, 1 Torr. The data points were reproducible with less than 3% variation.....	131
Figure 5.9 Steady-state moisture uptake (ng) as a function of relative humidity (%) for films of two different thicknesses (t_3 = 0.77 μm and t_4 = 2.32 μm) deposited	

from C ₄ F ₈ . Deposition conditions: 30W, 120 °C, 1 Torr. The data points were reproducible with less than 3% variation.....	132
Figure 5.10 Steady-state moisture uptake (wt %) as a function of relative humidity (%) for films deposited from PFE and C ₄ F ₈ (PFE = 0.68 μm; C ₄ F ₈ = 0.77 μm).Deposition conditions: 30W, 120 °C, 1 Torr. The data points were reproducible with less than 3% variation.....	133
Figure 5.11 Normalized water vapor mass uptake by PFE film (at RH = 85%) as a function of square root of time (\sqrt{t}) divided by film thickness (L) [Deposition conditions: 30W, 120 °C, 1 Torr]. Theoretical plot refers to purely Fickian Type I Diffusion.	135
Figure 5.12 Normalized water vapor mass uptake by OFCB film (at RH = 85%) as a function of square root of time (\sqrt{t}) divided by film thickness (L) [Deposition conditions: 30W, 120 °C, 1 Torr]. Theoretical plot refers to purely Fickian Type I Diffusion.	136
Figure 6.1 Hexadecane uptakes with varying hexadecane vapor concentration by fluorocarbon films of different thicknesses. The errors in measurements were less than 3%.	150
Figure 6.2 Wt% hexadecane uptakes with varying hexadecane vapor concentration by fluorocarbon films of different thicknesses. The errors in measurements were less than 3%.	152
Figure 6.3 Typical frequency versus time data for hexadecane absorption and desorption on PFE film thickness of 500 nm and a hexadecane concentration of 6.5 mg/L.....	153
Figure 6.4 Normalized mass uptake of hexadecane vapor by a 500 nm fluorocarbon film at a hexadecane concentration of 6.5 mg/L as a function of square root of time.	154
Figure 6.5 Normalized mass loss (desorption) of hexadecane by 500 nm fluorocarbon film at a hexadecane concentration of 6.5 mg/L as a function of square root of time.	155

Figure 6.6 Normalized mass uptake of hexadecane vapor by 750 nm fluorocarbon film at a hexadecane concentration of 6.5 mg/L as a function of square root of time.	157
Figure 6.7 Normalized mass loss (desorption) of hexadecane by 750 nm fluorocarbon film at a hexadecane concentration of 6.5 mg/L as a function of square root of time.	158
Figure 6.8 Normalized mass uptake of hexadecane vapor by 1 μ m fluorocarbon film at a hexadecane concentration of 6.5 mg/L as a function of square root of time.	159
Figure 6.9 Normalized mass loss (desorption) of hexadecane by 1 μ m fluorocarbon film at a hexadecane concentration of 6.5 mg/L as a function of square root of time.	160
Figure 6.10 Normalized mass uptake of hexadecane vapor by 500 nm fluorocarbon film at a hexadecane concentration of 19.5 mg/L as a function of square root of time.	162
Figure 6.11 Normalized mass loss (desorption) of hexadecane by 500 nm fluorocarbon film at a hexadecane concentration of 19.5 mg/L as a function of square root of time.	163
Figure 6.12 Normalized mass uptake of hexadecane vapor by 750 nm fluorocarbon film at a hexadecane concentration of 19.5 mg/L as a function of square root of time.	164
Figure 6.13 Normalized mass loss (desorption) of hexadecane by 750 nm fluorocarbon film at a hexadecane concentration of 19.5 mg/L as a function of square root of time.	165
Figure 6.14 Normalized mass uptake of hexadecane vapor by 1 μ m fluorocarbon film at a hexadecane concentration of 19.5 mg/L as a function of square root of time.	166
Figure 6.15 Normalized mass loss (desorption) of hexadecane by 1 μ m fluorocarbon film at a hexadecane concentration of 19.5 mg/L as a function of square root of time.	167

Figure 6.16 MRI Calibration Curve for relating MRI Signal Intensity to Wt% of Hexadecane in Paper Sample.....	177
Figure 6.17 MRI images of paper samples with 10 μ l of hexadecane dispensed as a function of time. The red box represents the paper sample and white contrast represents the hexadecane distribution (Higher the concentration of hexadecane, higher the image contrast).....	179
Figure 6.18 MRI signal intensity as a function of time and position for an uncoated paper sample that had undergone 5 minutes of refining.....	180
Figure 6.19 Wt% hexadecane as a function of time and position for an uncoated paper sample that had undergone 5 minutes of refining.....	181
Figure 6.20 Figure 6.13 MRI images of PFE coated paper sample with 10 μ l of hexadecane dispensed as a function of time. Red box represents the paper sample.....	183
Figure 6.21 MRI signal intensity as a function of time and position on PFE coated paper sample that had undergone 5 minutes of refining [PFE film thickness = 5.5 μ m].....	184
Figure 6.22 Wt% hexadecane as a function of time and position on PFE coated paper sample that had undergone 5 minutes of refining [PFE film thickness = 5.5 μ m].....	185
Figure 6.23 Schematic showing liquid penetration through a pore.	192
Figure 6.24 Influence of pore size (r_c) on the penetration time of fluid in porous media [171].....	195
Figure 6.25 Influence of contact angle (θ) on the penetration time of fluid in porous media [171].....	196
Figure 6.26 Influence of surface tension (γ) on the penetration time of fluid in porous media [171].....	196

Figure 6.27 Influence of coefficient of viscosity (μ) on the penetration time of fluid in porous media [171].	197
Figure 6.28 Cross-section of a capillary suddenly expanding from narrow neck to a wider neck.	198
Figure 6.29 SEM micrograph of 5 minute refined (a) an uncoated paper sample, (b) a 5.5 μ m PFE coated paper sample.	202
Figure 6.30 SEM micrograph of 25 minute refined (a) an uncoated paper sample, (b) a 5.5 μ m PFE coated paper sample.	203
Figure 6.31 SEM micrograph of 45 minute refined (a) an uncoated paper sample, (b) a 5.5 μ m PFE coated paper sample.	205
Figure 6.32 High resolution SEM micrograph of (a) 25 minute refined (b) a 45 refined paper sample both coated with a 5.5 μ m PFE film.	206
Figure 6.33 Photoacoustic Spectra of Uncoated Paper Sample at a Modulation Frequency of 209 Hz.	209
Figure 6.34 Photoacoustic Spectra of PFE coated Paper Sample at a Modulation Frequency of 209 Hz [PFE film thickness measured on Si wafer = 5.5 μ m].	210
Figure 6.35 Characteristic Peak Identification in Photoacoustic Spectra.	211
Figure 6.36 Ratio of Integrated Fluorocarbon Peak to that of Paper Peak with Varying Penetration Depth of Thermal Signal for different Paper Samples.	213
Figure 7.1 Schematic arrangement of dual layer films on Si substrate (PFE film at top)	222
Figure 7.2 Contact angle data for dual layer films where 10 nm and 286 nm PFE films are the top layers (p-NIPAAM layer below). Contact angle data for PFE films deposited on Si under similar conditions are also shown for comparison...	223

Figure 7.3 Schematic arrangement of dual layer films on Si substrate (p-NIPAAM film at top).....	224
Figure 7.4 Contact angle data for dual layer films where 4.5 nm and 275 nm p-NIPAAM films are the top layers (PFE layer below). Contact angle data for p-NIPAAM films deposited on Si under similar conditions are also shown for comparison.....	225
Figure 7.5 XPS survey scan of 275 nm p-NIPAAM film on top of PFE film. This scan is characteristic of p-NIPAAM film on Si wafer [188].....	226
Figure 7.6 XPS survey scan of 280 nm PFE film on top of p-NIPAAM film.....	227
Figure 7.7 Schematic for determining the XPS sampling depth for a given take-off angle.	228
Figure 7.8 C1s Peak Deconvolution of thin p-NIPAAM (4.5 nm) film on top of PFE film (at 45° takeoff angle)	232
Figure 7.9 C1s Peak Deconvolution of a thin PFE (10 nm) film on top of a p-NIPAAM film (at 45° takeoff angle).....	235

SUMMARY

With increasing demand for flexible barrier packaging, the industry has no choice but to continue to innovate and develop new materials and packaging solutions to meet the needs of a growing market. Paper and cellulosic materials hold a good promise of being candidates for flexible packaging materials provided suitable barrier properties such as water repellence and grease resistance are imparted to them. One of the methods to achieve these objectives is to surface modify paper/cellulose by applying thin fluorocarbon coatings on the surface. Fluorocarbon thin films produced by plasma enhanced chemical vapor deposition (PECVD) offer several advantages over the films produced by conventional polymerization means. Plasma deposited films are pinhole-free, chemically inert, insoluble, mechanically tough, thermally stable and highly coherent and adherent to variety of substrates. In this work, we investigate the use of PECVD technique to produce barrier films on paper and cellulosic materials. These films, with composition and properties not much different from PTFE, repel water and act as a good barrier to lipophilic materials.

A 6-inch parallel plate RF plasma reactor was designed and used for deposition of the fluorocarbon films on surface of paper and cellulose. Two different monomers, pentafluoroethane (PFE; CF_3CHF_2) and octafluorocyclobutane (OFCB; C_4F_8), were investigated and compared in terms of deposition rates and final film properties. Various analytical techniques (XPS, FT-IR, SEM, Ellipsometry, Contact Angle Goniometry, etc.)

were used to characterize the fluorocarbon films. The fluorocarbon coated paper exhibited hydrophobic character as evidenced by high water contact angles. Although the films allow water vapor diffusion, the films are hydrophobic and are not “wetted” when liquid water contacts these layers. Based on various thickness of these films deposited on surface of cellulose, there was a minimum PFE film thickness required to achieve a stable hydrophobic behavior.

The fluorocarbon films investigated in this work also exhibited good resistance to lipophilic materials (e.g. oils, fatty acids, etc.). While techniques such oleic acid penetration and TAPPI “oil-kit” test are commonly used in paper industry to qualitatively test the grease barrier properties of paper/cellulose, this work attempts to quantify the grease barrier properties of fluorocarbon coated paper using techniques such as magnetic resonance imaging (MRI) and quartz crystal microbalance (QCM). Finally, the feasibility of deposition of dual layer films by PECVD was investigated using PFE and n-isopropylacrylamide (NIPAAM) as precursors for applications in barrier packaging and printing.

1. INTRODUCTION

Packaging is an \$800 billion global industry [1]. In the packaging industry, flexible packaging has gained considerable attention recently. Flexible packaging types range from bags and bubble wrap to tubes, stand-up pouches and foam cushioning materials. Rigid packaging items include blisters, bottles, cartridges, clam shells, pallets, and trays. Polymers are used in caps and closures, sacks, bags, labels, adhesives, rigid containers, films and other flexibles. With improving technologies in materials and processing, flexible packaging plays an increasingly important role in many markets such as food and beverage, semiconductors, pharmaceuticals, automotives, and others. The flexible packaging industry is a highly competitive industry, and a new innovation, such as a thinner yet stronger packaging structure or a better barrier, can change packaging (and consumer) choices.

US demand for converted flexible packaging is projected to grow 2.4 percent yearly to 6.8 billion pounds in 2008, with a value of \$14 billion [2]. Advances will be spurred by recent developments such as breathable films for fresh cut produce and meats and reclosable stand-up pouches. Although demand for paper packaging will expand only marginally, paper will remain an important player in packaging markets due to its low cost, environmental compatibility and use in laminations. Food packaging will remain the leading flexible packaging market based on cost considerations and needs for improved barrier structures. Converted flexible packaging advances over the next decade will encompass better sealing and barrier properties, improved mechanical strength and

printing surfaces, and lower cost. Flexible barrier packaging is used for variety of purposes such as packaging snack foods, meats, and pharmaceuticals. Figure 1.1 presents the sales of barrier packaging classified by its use in various applications [3].

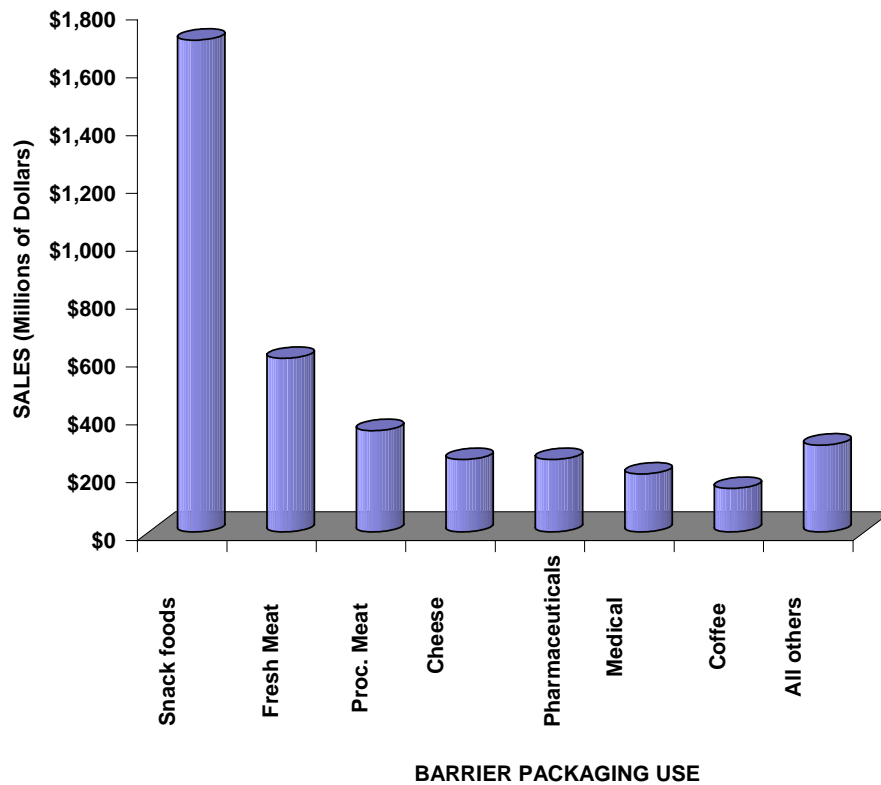


Figure 1.1. Sales of barrier packaging used in various applications [3].

In all packaging applications, the package must contain and protect its products or contents. Depending on the product, these two major functions can take on a wide range of meanings. For example, paper and paperboard can be of greater value in their ability to contribute strength and stiffness or rigidity to a container. Plastics, glass and metals may also offer strength and stiffness, but paper is more resilient than glass and can be more

resilient than plastic over a wider temperature range. Paper and paperboard can also be lighter and far more easily printed on than the other materials. The only difficulty in packaging with paper and paperboard is their low barrier properties. In most cases, paper and paperboard must be coated with waxes or plastics, or laminated to plastic films or foils to establish barrier capabilities to water, grease, vapor, gases or odors. Figure 1.2 presents the percentage share of various substrates used in packaging in the US for the year 2003 [2].

Key developments in flexible packaging include recent equipment advances that have enabled co-extrusion of films with more than seven layers. New package structures such as multilayer standup pouches and metallized films have also allowed plastic films to aggressively compete against rigid packaging in areas such as pet foods and specialty chemicals, and against other flexible materials such as laminated foils in medical and snack food packaging.

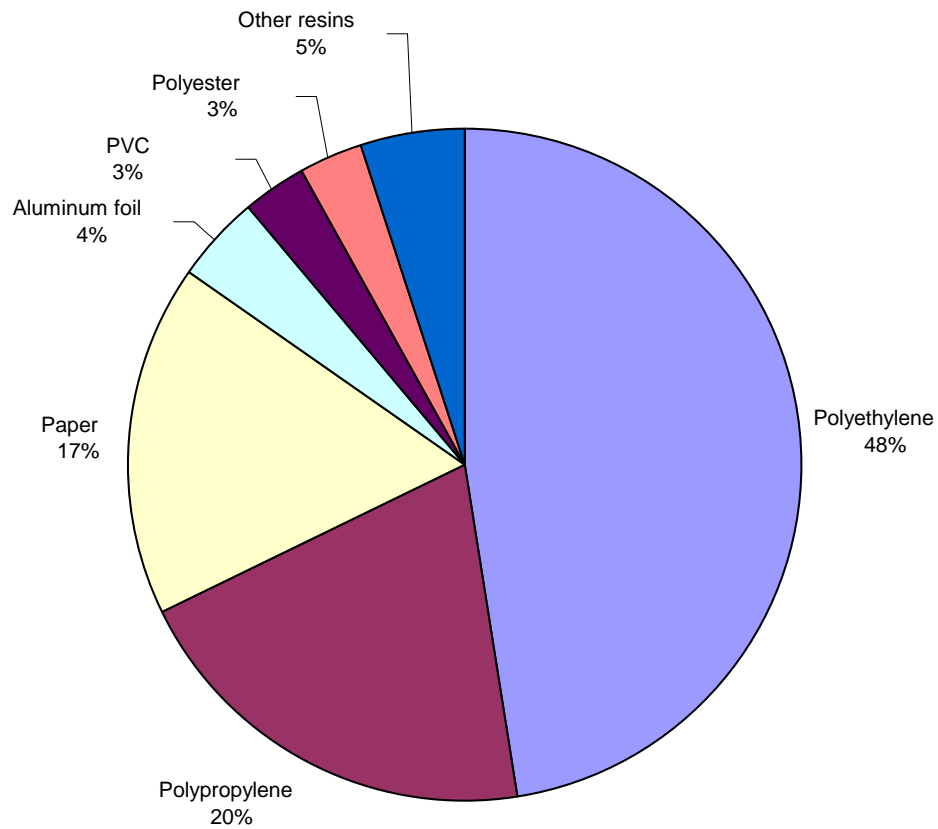


Figure 1.2 Percentage share of various packaging substrates in the US market in the year 2003 [2].

High-barrier packaging can comprise several different layers and various types of resins, which provide advanced features for such characteristics as extended shelf life and the ability to allow permeation of certain gases to change product coloring. The average consumer probably has no idea that the packaging of a typical product he or she might purchase weekly may have as many as six layers of plastic (even more are quite likely) and can sit on the shelf and remain fresh for several months, possibly up to a year. For a number of years many companies, both plastics suppliers and converters, have been

involved in the development of high-barrier packaging with various substrates, including plastic film, paper, and foil.

In the early 1990s, four basic coatings were used as barrier materials: nylon, PVDC [polyvinylidene chloride], EVOH [ethylene vinyl alcohol], and metallized films. But consumer demands to have fresher, more flavorful, higher quality foods has driven the need for more sophisticated packaging solutions. Today, there are multilayer film constructions that use 15 layers [4]. Environmental concern over the extent of packaging consumption and disposal is a major factor considered by packaging professionals seeking to conserve materials and reduce solid waste. Recycling is another major environmental concern associated with packaging materials.

To date, packaging materials have been to a large extent based on nonrenewable materials. The only widely-used renewable packaging materials are paper and board which are based on cellulose, the most abundant renewable polymer worldwide. The materials used for packaging today consist of a variety of petroleum-derived plastic polymers, metals, glass, paper and board or combinations thereof. These materials and polymers are used in various combinations to prepare materials with unique properties which efficiently ensure safety and quality of food products from processing and manufacturing through handling and storage and, finally, to consumer use. Notably, these materials fulfill a very important task as the absence of packaging or insufficient packaging can result in rapid deterioration of quality and safety giving way to massive commercial losses of valuable foodstuffs. Individual food products have specific

optimum requirements for storage that the packaging materials must provide. When contemplating the concept of food packaging, the entire dynamic interaction between food, packaging material and ambient atmosphere has to be considered.

There is a need to consider alternative ways of achieving barrier packaging properties in materials and substrates to satisfy the growing demand in flexible barrier packaging. As discussed above, paper and cellulose-based materials are renewable resources and are important packaging substrates. One of the important aspects of barrier films in a package is to prevent the contents of the package from coming into contact with liquids such as water and oil (also referred to as lipophilic materials or grease). While normal paper or cellulosic substrates cannot prevent water or oil permeation, lamination with an extrusion coating or wax applied to paper surfaces can provide barrier properties to the paper. Another important requirement is that the paper substrate retain its physical properties after a coating has been applied. This requirement can be achieved if the applied coating is breathable or allows water vapor diffusion. With multiple layers applied to the paper surface, it is difficult to achieve a breathable coating. Use of metallic coatings (e.g. aluminum) further complicates the breathability and recycling.

Paper and cellulose materials treated with fluorochemicals offer some advantages over polymer coated paper or laminates. For example, paper treated with fluorochemicals provides the flexibility of varying the amount of fluorochemical to control the degree of water or oil repellency required for a particular application. Also, paper treated with fluorochemicals can be easily recycled whereas polymer extrusion coatings and waxes

must be separated from the paper during the recycling process [5]. Plasma enhanced chemical vapor deposition can be used to apply a thin fluorocarbon coating on the surface of paper or cellulose to achieve barrier properties such as hydrophobicity and oleophobicity. A thin fluorocarbon film applied using plasma-assisted deposition can be breathable and it does not provide significant challenges in the recycling of coated paper. A single thin fluorocarbon film deposited onto the surface of paper or cellulose will eliminate the need to apply multiple layers of films to achieve barrier properties. This will not only reduce the processing cost to produce certain types of barrier packaging (due to the many processing steps involved) but will also reduce the costs incurred to recycle coated paper while simultaneously reducing the environmental burden.

As a result of the above needs and driving forces, the investigation of fluorocarbon film coatings on paper and cellulose for use as barrier materials in packaging along with the associated methods of deposition are most appropriate. This work focuses on the development and characterization of plasma-deposited fluorocarbon films to serve as barrier films in paper packaging and investigates the extent of barrier properties provided by thin fluorocarbon layers.

2. BACKGROUND

2.1 Surface Modification

Solid surfaces and phenomena which occur at solid surfaces are of tremendous importance in various fields of science and engineering. Every material, whether polymers, metals, or ceramics, has a surface at the boundary with air or has an interface where it contacts another material. The chemical and physical properties at the surface are different from those of the bulk material and special functions (e.g. hydrophobicity and hydrophilicity) may operate at the surface or the interface. These special functions at the surface have given birth to challenging area of surface and interfacial science.

The surface modification of polymer materials is a useful way to obtain functional polymers by controlling their surface properties. Surface modification techniques, as the name suggests, is restricted to a shallow depth of the material undergoing surface modification. Ideally, the modified layer should be a few monolayers of the polymer surface and the deeper layers (bulk material) should not be modified. This translates into the top few monolayers having different (generally desired) properties than the bulk material, which retains original properties. Major polymer surface modification techniques include plasma polymerization, plasma spray coating, ion implantation and ion-beam-assisted deposition. Surface modification process can be classified into four categories [6]:

- 1) Contamination removal: Surface contamination removal involves physical ablation and/or chemical reactions to remove contaminants. Plasma ablation can dislodge contamination from the surface but may roughen the surface on an atomic scale. Reaction of gas phase species (e.g., free radicals, neutrals, excited state species, ions) in the plasma with contaminants can generate volatile species and thereby remove contaminants from the surface.
- 2) Surface activation: Plasma surface activation employs gases, such as oxygen, nitrogen, hydrogen, and ammonia, which, when exposed to the plasma, will dissociate and react with the surface, creating new chemical functional groups on the surface. The functional groups thus created modify the chemical activity of the surface. For example, surface activation can cause modification of the hydrophilicity and the biochemical reactivity of a polymer surface.
- 3) Deposition or etching: Some gases (e.g. CH_4 , C_4F_8) can be plasma polymerized, and thus coat the polymer surface with a thin layer of a different polymer. This is referred to as plasma deposition of a polymer film on a given surface. Plasma etching, on the other hand, is characterized by creation of highly reactive chemical species that cause the reaction at solid interface producing volatile by-products, which are pumped in the vacuum system. Etching chemistry can be tailored such that one material is selectively etched in the presence of other materials.

- 4) Crosslinking: Plasma-induced crosslinking employs inert gases such as argon or helium which remove certain atomic species (e.g., H) from the polymer structure, thereby generating reactive radicals which react with other species in the surface to form chemical bonds and create a crosslinked surface.

Generally, chemical reactions that involve the implantation of elements (oxygen, nitrogen, fluorine atoms, etc.) or moieties (hydroxyl, carbonyl, carboxylate, etc.) and the grafting of monomers are applied for the modification process [6].

Non-equilibrium plasma chemistry (often known as cold-plasma chemistry) has led to the synthesis of new macromolecular surfaces and structures through polymer deposition, grafting and surface functionalization mechanisms. The synthesis of thin film polymers and surface modification of a variety of inorganic and organic polymeric substrates is an area of on-going research. The excited state and kinetic energies of the active species in plasmas are sufficiently high to dissociate even the strongest bonds. Various ions, monofunctional and multifunctional free radicals, excited state species, and fast neutrals are available as a result of glow discharges. Consequently, a number of simultaneous recombination mechanisms are possible even for simple chemical compounds [7]. Plasma species can also become attached to polymer substrate surfaces creating new functionalities and characteristics. The possibility of modifying even the most inert inorganic and organic material creates endless opportunities in the field of plasma surface chemistry. Applications of surface modification and/or functionalization can be

envisioned in the fields of microelectronics (e.g., low dielectric constant films), optics (e.g., graded refractive index layers), barrier coating technologies (e.g., controlled gas and liquid permeability, corrosion protection), mechanics (e.g., controlled tribological characteristics), and biotechnology (e.g., enzyme and oligonucleotide immobilization).

Surface modification or functionalization has also been achieved by coating the surface of the material with polymer by means of spin coating. The idea is to coat the surface of material with a very thin layer of polymer with the desired properties thereby achieving surface functionalization of material without changing the material bulk properties. Spin-on techniques offer advantages such as good gap fill ability, planarization, etc, but the resulting films may have pinholes, poor gap fill ability on small features, require baking and curing, undergo shrinkage leading to stress, require solvents in processing and may create significant hazardous waste. Plasma polymerization has several advantages over conventional spin-on processes such as the ability to produce thin, uniform, pinhole free films with a wide range of desired properties, good gap fill ability in small features, and does not require the use of solvents.

2.2 Barrier Coatings on Paper and Cellulose

The paper industry manufactures a large variety of packaging materials for applications in food display and storage. A stain or leak-proof barrier is required for paper that comes into contact with oily, greasy or watery foods. Polymeric barriers such as polyethylene

are costly to apply to paper and interfere with its repulpability or recyclability after its intended use, and are being increasingly restricted by regulations [8]. Fluorine-containing chemicals and copolymers, collectively referred to as fluorochemicals, have been used for a number of years to impart water, oil and grease resistance to substrates such as paper because of their effectiveness at low concentrations and their adaptability to conventional methods of manufacturing paper.

Fluorochemicals are generally applied to such materials either by surface coating on the paper or by addition to the paper pulp before the paper is formed. Surface application may be carried out by means such as spraying, dipping, roller-coating or padding to apply the fluorochemical to one or both sides of the essentially finished product. This type of treatment has the advantage that the overall amount of fluorochemical on the paper is directly controllable since there is limited opportunity for loss at this stage of the process. It has the disadvantage that the fluorochemical is applied primarily to the surface of the paper and may offer only limited protection to deeper liquid penetration. As noted earlier, it may be easier to recycle the fluorochemical treated paper as opposed to the one with a wax coating on the surface [5].

Alternatively, the fluorochemical can be added to the paper pulp under appropriate conditions that all or the majority of the fluorochemical is retained by the paper after it is dewatered. In this type of treatment the fluorochemical exists throughout the thickness of the paper, not primarily on the surface. This more uniform treatment is particularly important in providing resistance to penetrating liquids if the paper is creased or abraded

in some areas. However, since the fluorochemical is applied throughout the mass of the paper, the overall fluorine content of the package may be higher than regulations specify, and thus not safe for contact with food items. For instance, the Food and Drug Administration (FDA) has established a limit for fluorine content in paper and paperboard that comes in contact with aqueous and fatty foods; the limit is within the range of 0.09% to 0.26% depending on the weight basis of the paper [9].

In many food packaging applications, the fluorochemical treated paper is provided with one or more additional layers to improve package properties such as ink receptivity, gloss and strength. These layers are typically on the outside of the package while the fluorochemical treated paper layer or layers are on the inside of the package, thereby providing a barrier against oil and grease contained in the packaged food. Such paper laminates are generally fabricated by using an adhesive to fix the fluorochemical treated paper layer to a substrate, e.g., another paper layer free of fluorochemical. For example, a paper board used in the packaging of pet food, which is typically food with high grease content, is a paper laminate of at least three layers in the order given: a top layer of a clay coating, a fluorochemical treated paper layer and an untreated paper layer. The fluorochemical treated paper layer and untreated paper layer may be bonded to each other with an adhesive layer. Similarly, coffee bean packaging may consist of a paper laminate containing a fluorochemical treated and untreated paper layer bonded to each other by an adhesive. Many papers are also treated with wax to provide a moisture barrier and allow the paper to be heat sealed. However, a simple wax coating is easily damaged by folding or by abrasive foods. This is overcome by laminating the wax between layers of paper

and/or polyethylene. Waxed papers are used for bread wrappers and inner liners for cereal cartons.

In addition to conventional methods of coating paper (spraying, dipping, roller-coating or padding to apply the fluorochemicals), plasma polymerization is another manner in which thin fluoropolymer coatings can be applied to surfaces of paper and cellulose to create barrier properties such as hydrophobicity and oleophobicity.

2.3 Plasma Deposition of Fluorocarbon Materials

2.3.1 Plasma Background and Fundamentals

A plasma, also referred to as a glow discharge, is a partially ionized gas composed of electrons, ions, and a variety of neutral species. Typically, plasmas are excited by applying radio frequency (RF) or microwave energy to a volume of gas. These plasmas are characterized by pressures in the range of 0.01 to 10 torr, electron densities between 10^8 and 10^{12} cm^{-3} , and electron energies between 1 and 10 eV (such energies correspond to 10^4 - 10^5 K). Glow discharges are termed non-equilibrium plasmas since the electron temperatures are much greater than the temperatures of ions and neutral species (300-600 K) [10]. Furthermore, these plasmas are weakly ionized; the ratio of the concentration of electrons to the neutral species concentration is of the order of 10^{-3} - 10^{-6} . As a result, atoms, radicals, and molecules are primarily responsible for deposition and etching

reactions. The only exceptions are low pressure, high-density discharges such as electron cyclotron resonance (ECR), helicon, and inductively coupled plasmas where the charged species densities can be as large as 10 % that of the neutral density. However, the main body of the plasma is quasineutral, with an approximately equal number of positive and negative charge carriers.

Due to greater mobility of electrons (higher velocities) compared to ions, all surfaces in contact with plasma assume a time-average potential that is more negative than the bulk plasma. Thus, a potential difference (ranging from few volts to more than 500 V) arises between the plasma and the substrate, which leads to positive ion bombardment on all surfaces. This energetic ion bombardment can lead to the formation of adsorption sites, and to enhancement of chemical reactions on the surface. These characteristics impart plasmas with unique and useful properties.

It is important to note that the energy range of most electrons in the plasma (0.1 – 20 eV) is sufficiently high to dissociate all chemical bonds involved in organic structures. Because of electron collisions with neutral gas phase molecules, bond breaking occurs, and highly reactive chemical species are produced for deposition and etching even at low temperatures. The nonequilibrium nature of the plasmas and electron impact dissociation of molecules allows kinetic limitations of chemical reactions to be overcome, and thus chemical reactions that would require high (>500 °C) temperatures under thermal excitation, can occur at much lower (<100 °C) temperatures. The combination of physical (ion bombardment, radiation) and chemical processes (due to free radicals) results in the

formation of highly crosslinked films that possess unique properties. Figure 2.1 presents a schematic indicating the types of species bombarding a surface during plasma treatment of substrates [11]. Since plasma-generated macromolecular networks generally do not retain the structural characteristics of the starting materials, they are not based on repeating units, as are traditional solution-polymerized polymers. Consequently, the term ‘plasma-polymer’ is a misnomer because conventional polymers have a single repeat unit. However, the term is still commonly used in the literature.

The nature of plasmas, the modalities of transferring energy via electric or electromagnetic field intensities to the reaction system, the geometry of the reactor or system (shape and volumes of the chamber, geometrical location of electrodes and substrates, etc.) and the selected experimental conditions (pressure, substrate temperature, power, and gas flowrates, etc.) are all critical in determining the gas-phase and surface plasma chemistry. Therefore, it is important to understand the effect of individual parameters on the plasma chemistry in order to be able to predict or at least control the surface properties of plasma modified substrates.

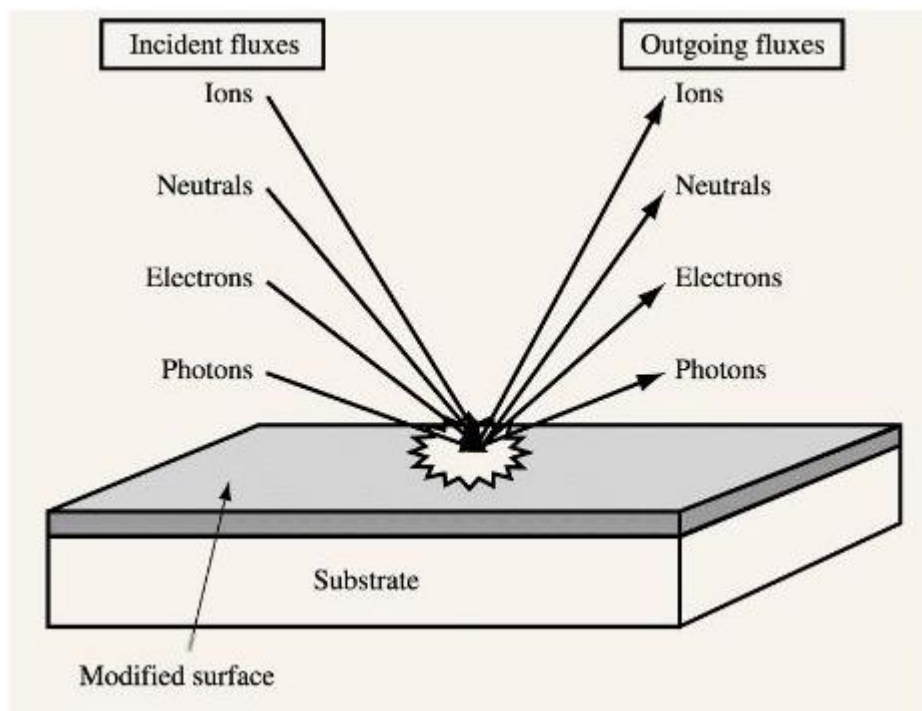


Figure 2.1 Schematic diagram of incident and outgoing particle fluxes at a surface in contact with a low-pressure plasma [11].

2.3.2 Background on Fluorocarbon Plasmas

Plasmas interact with polymers to modify their chemical and physical properties. Surface modification is mainly due to the formation of new functional groups on surfaces (Process I) and the etching of surfaces (Process II) [6]. For example, in process I, radicals in the plasma can remove hydrogen atoms (when available) from the polymer surface to form carbon radicals on the surface. The carbon radicals combine with radicals or other species in the plasma to form new functional groups on the polymer surface. On the other hand, in process II, electrons and ions bombard the polymer surface to cause C – C (or other) bond scission in the polymer chains and form carbon radicals in the polymer

chains. As a result, degradation reactions of the polymer chain initiate from the carbon radical to yield degradation products with low-molecular weight on the polymer surface. Some of the degradation products volatilize from the surface, and weight-loss of the polymer material occurs. This is an essential reaction for the etching of the polymer surface. The etching process may not be desirable for surface modification, because the surface is contaminated by degradation products. However, since the plasma creates reactive species for modification of polymer surfaces, the etching process is generally not avoided during modification reactions. To avoid etching processes, charged species (electrons or ions) should be minimized in the plasma, and radicals should be predominantly used as active species for surface modification [12].

Plasma polymerization of fluorocarbons also involves two opposing processes: polymer formation, which leads to the deposition of material and etching or ablation, which leads to the removal of material. As shown in Figure 2.2, a fluorocarbon plasma can result in net etching or net deposition based on the operating conditions and the fluorine to carbon ratio of the precursor [13]. It has been shown that CF_x radicals (CF_3 , CF_2 , CF) in the plasma are responsible for polymerization or deposition, while fluorine free radicals are responsible for etching of the surface. Addition of oxygen to the monomer flow enhances the etching rate by increasing the fluorine atom concentration, while addition of hydrogen improves polymerization by scavenging the fluorine free radicals in the plasma. Film growth on a substrate occurs as a result of reaction of radicals with activated surface sites created by bombardment with charged species or high energy neutrals in the plasma. To achieve surface functionalization of a polymer in a controllable way, plasma

parameters such as type of precursor or monomer, gas flowrates, deposition temperature, deposition pressure, RF power applied and time of deposition can be varied. Over the years, researchers have used these plasma parameters to achieve desired polymer structures, thereby controlling the deposited polymer properties.

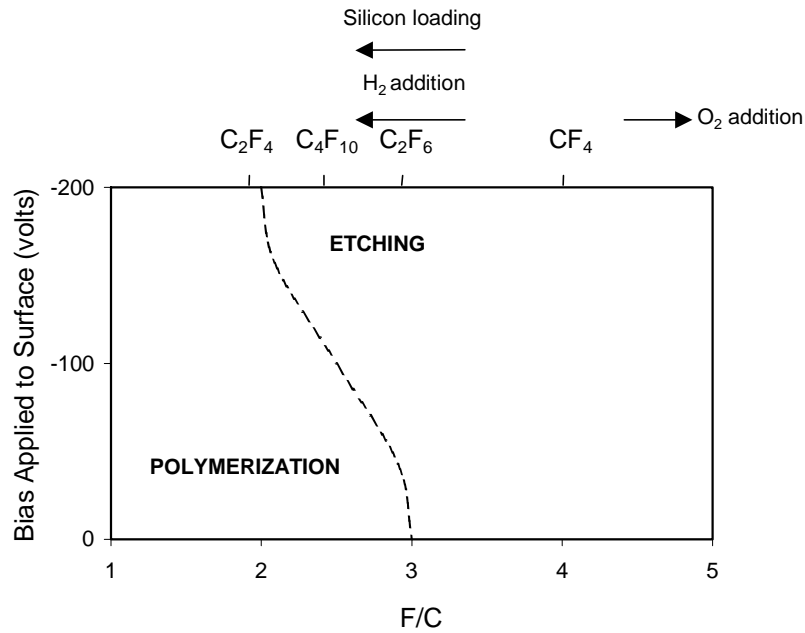
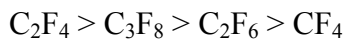


Figure 2.2. Boundary between etching and polymerization processes of fluorocarbons as a function of fluorine to carbon ratio of the feed monomer [13].

Fluorocarbon plasmas have been widely used in a number of industries for variety of purposes. The semiconductor industry has utilized fluorocarbon plasmas primarily for etching and cleaning applications for the past twenty-five years [11, 14]. More recently,

fluorocarbon plasmas have been considered for depositing thin fluoropolymer films for use as interlevel dielectric materials for future generations of integrated circuits [15-17].

Fluorocarbon films have many desirable qualities including low dielectric constant [18-20], hydrophobicity [21-26]; oleophobicity (oil-repellency)[27-30], low coefficient of friction [21, 31-33], low surface energy [23, 25, 34, 35], high electrical resistivity [33], biocompatibility [28, 36, 37], inhibition of biofouling [38], and resistance to chemical and oxidative degradation [21, 39, 40]. The unique characteristics of the fluorine atom give fluoropolymers outstanding properties. The bond energy of the C-F bond is remarkably high (488 kJ/mol), as compared to the C-C bond (348 kJ/mol) [28, 40]. The uniqueness of the C-F bond is apparent not only by its bond strength, but also by the distribution of electrons. The F atom is the most electronegative atom, imparting a dispersive intermolecular force to the C-F bond. When fluorine free radicals react with polymerizing fragments such as CF_3 they form gaseous species e.g., CF_4 , which do not participate in polymer formation. Also, the highly reactive fluorine free radicals consume most of the active sites on the growing polymer surface without promoting polymerization. Hence, for monomers with higher fluorine to carbon ratios, the fluorine concentration in the plasma phase is much higher than the CF_x concentration and thus surface etching predominates over polymerization. Plasma precursors such as C_2F_4 , C_4F_8 [18], C_3F_8 , C_6F_6 [20], and C_2F_6 have been used to deposit fluorocarbon films on various substrates mainly to achieve low-dielectric constant films. Based on the fluorine to carbon ratio, the expected polymerizing capacity of the precursor gas follows the order below [28]:



Applications for fluorocarbon polymers are diverse and widespread due to their unique properties, as outlined above. Since many of these properties are surface phenomena (coefficient of friction, biocompatibility, surface energy), a fluoropolymer coating could impart these surface qualities to other polymers, while retaining bulk properties [6, 41]. Fluoropolymers, in general, are more expensive to synthesize in a bulk form than other polymers [35]. Therefore, a less expensive polymer with a fluorocarbon coating is a cost-effective alternative for many applications. As mentioned previously, fluorocarbon films also have one of the lowest dielectric constants of a dense material (1.8 – 2.5), which makes them useful as dielectrics in microprocessors [18, 28]. Fluorocarbon films have shown promise for low coefficient of friction coatings on various biomaterials, such as the lead wires for pacemakers [36] and artificial heart valves [37]. Furthermore, fluorocarbon films have been shown to greatly decrease platelet adhesion to polyethylene terephthalate (PET) [42]. Clearly, many of these coatings show promise for important applications, but have not yet been commercialized due to processing challenges.

There are many obstacles to producing fluoropolymer coatings. Since the melt viscosity is very high, polytetrafluoroethylene (PTFE) coatings cannot be produced by conventional melt processing techniques [27]. Films are usually produced from pressing and sintering PTFE powder or solvent spin coating [43]. However, the sintering powder technique is complicated, may leave pinholes, and is difficult to process in a reproducible manner [44]. Solvent spin coating may result in films with reduced thickness control, and

environmentally, it is desirable to limit solvent use, if possible. Surface fluorination of polymeric surfaces may be achieved using fluorine gas, but this method is undesirable due to the toxicity of fluorine gas [27]. Therefore, production of films using plasma deposition is a viable alternative to conventional fluorination techniques. It should be noted that continuous wave plasmas are typically used in fluorocarbon deposition. However, pulsed plasmas have also been commonly used for fluorocarbon film deposition. The following section described pulsed plasma deposition and its advantages relative to continuous wave plasmas.

2.3.3 Plasma Pulsing

Pulsing a plasma essentially implies applying time modulation to the applied power. In a pulsed plasma deposition process, which is a modification of traditional PECVD, RF power is applied only for a specified “on” time, followed by an “off” period during which no excitation is used. A pulsed plasma is also referred to as a modulated-power discharge. Since the RF power is “off” for a specified period of time, the effective power supplied to the gaseous electrons and ions is less than that supplied by a continuous wave plasma. The average power (also known as equivalent wattage), $P_{AVG.}$, for a pulsed plasma is defined as (Equation 2.1):

$$P_{AVG.} = \left(\frac{t_{ON}}{t_{ON} + t_{OFF}} \right) P_{PEAK} \quad (2.1)$$

where t_{ON} and t_{OFF} are the plasma “on” and “off” times and P_{PEAK} is the power input during the plasma “on” portion of the duty cycle. Modulation of power or pulsing of power yields more control over the plasma properties because two additional parameters, the period (t_{OFF}) and the duty ratio ($t_{\text{ON}}/t_{\text{ON}} + t_{\text{OFF}}$), can be independently controlled. During the “on” time, both ions and reactive neutrals are produced. However, since ions generally have shorter lifetimes than neutrals, during the “off” time the ratio of neutrals to ions will increase, and thus, the competition between growth and etching reactions at the surface will be altered to favor film deposition from reactive neutrals. Also, by pulsing the plasma in this manner, some degree of control over the extent and energy of ion bombardment to which a substrate is exposed can be invoked.

Pulsed plasmas have been used in a wide variety of applications ranging from the creation of low-k interlayer dielectric materials to the synthesis of biocompatible membranes. For instance, fluorocarbons films for use as low dielectric constant materials in integrated circuit (IC) fabrication have been deposited by pulsed plasma enhanced chemical vapor deposition from 1,1,2,2- $\text{C}_2\text{H}_2\text{F}_4$, CH_2F_2 , and CHClF_2 [19]. Super-hydrophobic fluorocarbon coatings with ribbon-like morphology have been deposited from pulsed RF discharges using tetrafluoroethylene (C_2F_4) for applications such as textiles, packaging, and ICs [26]. An aromatic perfluorocarbon monomer (perfluoroallyl benzene) has also been invoked in a pulsed plasma environment to form low dielectric constant and high thermal stability fluoropolymer films, again for IC applications [45]. In addition, low surface energy polymer films have been formed from fluorinated alkenes in a pulsed plasma environment to produce water and oil repellent coatings [25, 34, 46].

Pulsed plasma excitation has been reported to: (a) alter the plasma discharge chemistry [47]; (b) alter the properties of deposited films (e.g. fluorocarbon films) [48]; (c) minimize dust particle formation [49]; and (d) maintain etch/deposition rates despite lower (equivalent) power [50]. For polymer modification, pulsed plasmas provide additional ‘control knobs’ for tailoring the structure of polymer films. Over the past 20 years, pulsed RF plasmas have been successfully employed in plasma polymerization of a variety of monomers [51-53]. With pulsed plasma polymerization, high retention of the monomer functional group in the resulting films can be achieved [54]. In addition, pulsed plasmas provide access to lower continuous wave (CW) equivalent powers because RF power is on for only a portion of the cycle time. Use of pulsed power sources reduces trapped radicals in the film, lowers deposition surface temperatures, decreases high-energy ion bombardment and UV flux to the surface, and provides greater control over the resulting film chemistry [55]. In contrast, films deposited from continuous wave (CW) plasmas may be amorphous polymeric materials with little resemblance to the original monomer [56], depending upon the specific plasma parameters used.

Plasma polymerized fluorocarbon films can be deposited on paper and cellulose surfaces to modify their surface properties for barrier applications. However, it is important to understand the surface of paper and how it is formed from pulp fibers in order to gain insight into plasma modification. The following section presents an overview of the paper formation process.

2.4 Overview of Paper Making Process (Fiber and Paper Surface Formation)

The process of making paper is based on the fact that wet cellulose fibers bind together when dried under restraint. The processing of paper usually involves the initial separation of the cellulose fibers to form a wet pulp, some form of treatment such as beating and refining while in the pulped state to enhance the quality of the final product, forming of the sheet paper by hand molding or by a paper making machine, and drying [57]. Further processing is often carried out before or during drying to acquire the desired surface finish. Raw materials typically used for paper making include wood, straw (e.g. from wheat, barley or rice), bagasse (from sugar cane after sugar has been extracted), maize stalks, bamboo, cotton, jute, and others [58]. After the raw materials have been selected, the following steps are usually employed:

1) Preparation of Raw Material: Straw preparation, for example, requires that the straw be cleaned to remove dust and then cut into short lengths. Bagasse, on the other hand, is reduced to a suitable size at the sugar mill, but the pith still needs to be removed. Wood, both hard and soft, is chipped to an appropriate size. Specialized equipment is required for this kind of preparation. The material is then usually transported to the pulping area on a conveyor belt [57].

2) Pulping process: Pulping refers to different processes by which wood or other fibrous feedstocks are converted into a product mass with liberated fibers. Digestion, the first stage of the pulping process, is the process of removing lignin and other components of the wood from the cellulose fibers which will be used to make paper [59]. Lignin is the

"glue" which holds the wood together; it rapidly decomposes and discolors paper if it is left in the pulp (as in newsprint, which is usually made from groundwood pulp with little or no chemical treatment). There are two types of pulping processes: (a) mechanical pulping; and (b) chemical pulping.

(a) Mechanical pulping: Mechanical pulping uses a mechanical process whereby the raw material is broken down by attrition into its individual fibers by grinding. This process is not wholly satisfactory, as the fibers are broken into smaller pieces and relatively little lignin is released, resulting in a poor quality, 'woody' paper [57, 59, 60]. The mechanical process is also energy intensive. Mechanical pulp is used for newsprint as the paper is highly absorbent and therefore soaks up ink and dries quickly.

(b) Chemical pulping: Chemical pulping uses a variety chemicals as part of a high temperature cooking, or digestion, process which breaks down the lignin, freeing the cellulose fibers. This process produces a high quality product, although the type of chemical used determines the properties of the final product: Caustic soda or sodium sulfate produce a pulp with coarse, strong fibers (known as Kraft) suitable for strong boxes [61]. Ammonia or calcium sulfate produce a finer fiber suitable for high quality printing and writing paper. The prepared stock is fed into the top of a digester and mixed with the cooking chemicals, which are called "white liquor" at this point. Digestion may be carried out on a batch or a continuous basis [59]. Batch digesters are able to cope with a variety of stock feeds, for example straw, baggase, cotton and wood, in the same mill. As the stock and liquor move through the digester, lignin and other components are

dissolved, and the cellulose fibers are released as pulp. After leaving the digester, the pulp is rinsed, and the spent chemicals (now known as "black liquor") are separated and recycled [57, 61].

3) Bleaching and Refining of Pulp: After chemical pulping, the stock is lignin free but brownish in color and therefore, too dark for most grades of paper. As a result, it is important to bleach the pulp by treating it with chlorine, chlorine dioxide, ozone, hydrogen peroxide, or any of several other treatments. Multiple stages of bleaching, often with different treatments in each step, may be used to produce a bright white pulp [62]. Chlorine bleaching generally provides the best performance with the least damage to the fibers, but concerns about dioxins and other by-products have led the paper industry to move towards more environmentally friendly alternatives [63-65]. After bleaching, the individual cellulose fibers are still somewhat hollow and stiff, so they must be broken down to help them stick to one another in the paper web. This is accomplished by "beating" the pulp in refiners, which are vessels with a series of rotating serrated metal disks. The pulp is beaten for various lengths of time depending on its origin and on the type of paper product that will be manufactured. At the end of the process, the fibers are flattened and frayed, and are now ready to bond together to form a sheet of paper [66].

4) Paper Sheet Formation: After the pulp has been bleached and refined, it is rinsed and diluted with water, and fillers such as clay or chalk may be added. The stock thus prepared, containing at least 99% water, is pumped into the flow box of the paper machine [66]. From the head box, the stock is dispensed through a long, narrow slice

onto the wire, a moving continuous belt of wire (not used since early 1960s) or plastic mesh. As the stock travels down the wire, much of the water drains away or is pulled away by suction from underneath the belt. The cellulose fibers, trapped on the wire as the water drains away, adhere to one another to form the paper web. From the wire, the newly formed sheet of paper is transferred onto a cloth belt (or "felt") in the press section, where rollers squeeze out much of the remaining water [57, 59].

5) Paper Coating, Drying and Calendering: After leaving the press section, the sheet encounters the drying cylinders. These are large hollow metal cylinders, heated internally with steam, which dry the paper as it passes over them. The sheet is wound up and down over many cylinders in the drying process. Between dryer sections, the paper may be coated with starch (also called "sizing") to improve the printing and strength characteristics [57, 62]. After another round of drying, the paper sheet is passed through a series of polished, close-stacked metal rollers known as a "calender" where it is pressed smooth. Calendering is often done "off" machine. Finally, the sheet is collected on a take-up roll and removed from the paper machine. The paper roll formed may be rewound on a new core, inspected, and shipped directly to the customer. Other paper grades, however, may be further smoothed by passing them through a "supercalender" where the sheet is polished by passing between steel and hard cotton rollers (analogous to ironing a fabric), or they may be embossed with a decorative pattern [59].

It is important to note that surface finish and the physical and mechanical properties of paper, are highly dependent on variations that could occur in any of the steps described

above. In this thesis, however, a commercial copy paper of known thickness and brightness was used as received. For experiments involving the use of magnetic resonance imaging (MRI) to evaluate grease barrier properties, thick handsheets (1.5 – 1.7 mm) were prepared from Soft Wood Bleached Kraft (SWBK) and Hard Wood Bleached Kraft (HWBK) pulps using a modified TAPPI method T205-sp2 [67].

2.5 Surface Modification of Paper and Cellulose using Plasmas

Wettability and repellency are important properties of solid surfaces from both fundamental and practical aspects. When the effects of surface stains or adsorption of molecular substances can be ignored, the wettability of the solid surface is a characteristic property of materials and strongly depends on both the surface energy and the surface roughness. Since the surface energy is an intrinsic property of a specific material, it is generally difficult to control the wettability of a solid surface for a long exposure period [68]. Various industrial products require hydrophilicity or hydrophobicity depending on the application. Surface modification of polymers is a potentially useful method for reducing moisture absorption in polymers, since modification will enhance the surface and barrier properties of polymers. A variety of techniques have been proposed to improve the surface properties of polymers. Almost all surface modification processes reported involve chemical reactions [69]. Fluorination of a polymer surface by ion implantation is an attractive method, as the process can give rise to a highly hydrophobic

surface. It has been reported that direct fluorination with fluorine gas can result in a marked decrease in the total surface tension of high-density polyethylene [70].

Hydrophobicity and hydrophilicity are the polymer characteristics that are critical from the point of view of surface polymer properties. These characteristics are particularly important when one of the applications of the polymer is to serve as a membrane or as a barrier. Membranes in an aqueous environments have an attractive or repulsive response to water. The material composition of the membrane and its corresponding surface chemistry determine the interaction with water. Hydrophilic literally means "water-loving" and such material surfaces readily adsorb water. The surface chemistry allows these materials to be wetted forming a water film or coating on their surface. Hydrophilic materials also possess a high surface tension value and have the ability to form "hydrogen-bonds" with water. On the other hand, hydrophobic materials ("water hating") have little or no tendency to adsorb water and water tends to "bead" on their surfaces (i.e., discrete droplets). Hydrophobic materials possess low surface tension values and lack active groups in their surface chemistry for formation of "hydrogen-bonds" with water.

Magalhaes and de Souza have coated solid softwood with plasma polymers for water repellence [71]. Since solid wood is hygroscopic, moist wood is vulnerable to attack by fungi and termites, and loses its dimensional stability. In particular, solid softwood has been coated with plasma polymers for water repellence. The focus of this study was the modification of water absorption characteristics and repellence of solid wood surfaces through the deposition of plasma-polymers from vinyl acetate, ethylene, acetylene, and 1-

butene. A static sessile drop method was used to measure contact angles. Water contact angles as high as 140° were reported but the treated wood was permeable to water vapor because of the inability of the plasma technique to coat small capillaries. The authors acknowledged that substrate roughness or the porosity altered the contact angle in accordance with Wenzel's law [71]. Thus, the apparent contact angle was higher than the true contact angle.

Hydrophobic coatings have been deposited on porous cellulose-based filter papers by using a five-layer stack of filter paper as a model porous medium [72]. Perfluoromethylcyclohexane was used as the monomer for plasma deposition of hydrophobic films at a frequency of 40 kHz. The influence of operating parameters such as deposition pressure and deposition time on the permeation of plasma species into the model porous media was studied by water absorption. Higher deposition times led to deeper penetration of plasma coatings in the stacked filter paper. High fluorine content appeared responsible for the hydrophobic behavior of the deposited films.

The influence of RF plasmas on the surface properties of paper has also been studied [73]. In these experiments, unprinted, unsized, and sized security papers (SP) were treated with plasmas of SiCl_4 , O_2 , and CF_4 . At short treatment times and low RF power levels, the highest wettability was produced with SiCl_4 and O_2 plasmas regardless of sizing. The Si-Cl bonds present on the surface (after plasma treatment) were converted to Si-OH functionalities upon exposure to atmospheric moisture. This enhanced concentration of Si-OH groups on the surface led to hydrophilic character. The printing

and durability characteristics of the plasma-treated substrates were equivalent or superior to those of the untreated samples. The main objective of the study, however, was to modify the surfaces and improve ink adhesion to both unsized and sized security paper. The effect of oxygen and hydrogen plasmas on the chemical composition and wettability of cellulose has also been reported [74]. Observations indicated that the water wettability of greaseproof paper improved after the O₂ plasma treatment. Finally, surface fluorination of paper using CF₄ plasmas generated fluorine contents as high as 51% in the coating [23]. Depending upon the specific application, such values may represent a particularly large fluorine content. As noted earlier, the Food and Drug Administration (FDA) regulates the limit of fluorine content in paper and paperboard that comes in contact with aqueous and fatty foods [9].

Deposition of low surface energy 1H,1H,2H,2H-heptafluorodecyl acrylate plasma polymer layers onto micro-roughened PTFE substrates was shown to have high repellency toward polar and nonpolar probe liquids (hydrophobicity and oleophobicity) [25, 46]. More recently, the oleophobicity of plasma polymerized fluorocarbon films was investigated. Plasma polymerized fluorocarbon films rich in CF₂ species have been deposited onto polyethylene (PE) using 1H,1H,2H-perfluoro-1-dodecene as the monomer [30]. The high concentration of CF₂ species in the resulting fluorocarbon films led to oil-repellent films with surface energies as low as 2.7 mJ/m². One possible reason for the oleophobicity cited in the work was that the films might have CF₂ chain orientation normal to the substrate terminated by CF₃ groups. However, no information on the permeation of oleophobic molecules through these fluorocarbon films was presented.

Lipophilic materials are long-chain aliphatic acids, usually with a chain length of ten or more carbon atoms, which occur naturally in fats, oils, and related compounds (lipids) including acids of closely related structure [75]. Improvement in hydrophobicity and oleophobicity has been attributed to an increased content of the non-polar groups, including CF_2 , CF_3 , and $\text{CH}_2\text{-CF}_2$ [76]. To evaluate the water and grease barrier properties of paper, it is important to consider microscopic characteristics such as surface morphology, porosity, and relative surface energies of the lipophilic material, coating material and paper. On the macroscopic level, it is important to consider the effect of surface tension and viscosity of the droplets of the lipophilic material, and the temperature dependence of these properties, as well as how changes in relative humidity alter the interaction between the lipophilic material and the surface.

The use of fluorocarbon materials to lower the surface energy, improve biocompatibility, tailor hydrophobicity or hydrophilicity of the surface, and enhance membrane properties of cellulose have received significant attention recently. Researchers are exploring modification of cellulose derivatives using fluorocarbons plasmas for use as biomaterials by masking or substituting the hydroxyl groups on cellulose with fluorine moieties. An ideal biopolymer should not adsorb proteins. Ikada *et al.* have shown that a lower protein adsorption rate is obtained either with a biomaterial that is “superhydrophilic” (such as polyethylene grafted with acrylamide, cellulose grafted with poly vinyl alcohol) or a biomaterial that is “superhydrophobic” such as perfluoro polymers [77]. The fluorine moieties mentioned above make the surface of cellulose highly hydrophobic thereby

reducing the protein adsorption rate significantly. Cellulose membranes have also been surface modified for application in membrane distillation of aqueous solutions, where hydrophobicity of membranes is very important to prevent the wetting of membrane surfaces [78]. Also, fluorocarbon coatings on cellulose, which produce hydrophobic films, are important for making ultra water repellent coatings for various applications.

Plasma surface modification has also been studied from the perspective of its use in the textile industry. Plasma treatments have been shown to enhance dyeing rates of polymers, to improve colorfastness and wash resistance of fabrics, to increase adhesion of coatings, and to modify the wettability of fibers and fabrics [79]. Improvements in toughness, tenacity, and shrink resistance can be achieved by subjecting various thermoplastic fibers to a plasma atmosphere. Recently, plasma treatments have produced increased moisture absorption in fibers, altered degradation rates of biomedical materials (such as sutures), and deposition of low friction coatings.

Carlsson and Strom have studied reduction and oxidation of cellulose surfaces by plasma [74]. Their main intent was to study the effect of oxygen and hydrogen plasmas on the chemical composition and wettability of two cellulose materials: filter paper made from a very pure cotton cellulose and greaseproof paper containing fairly high amounts of wood resins. It was found that treatment with a hydrogen plasma reduced the hydroxyl groups on the cellulose and low molecular weight materials were formed. The water wettability of pure cellulose was reduced due to the lower polarity of the surface. Oxygen plasma treatment was found to both oxidize (through oxygen incorporation due to hydroperoxide

formation) and reduce (through double bond creation in cellulose) the surface. Hydroperoxides were formed along with other oxygen containing groups. The water wettability of greaseproof paper improved after the O₂ plasma treatment.

Clearly, the above studies demonstrate that tailoring the hydrophobicity and hydrophilicity of polymer surfaces such as cellulose and cellulose derivatives (paper and paper board materials) can open up a number of avenues for the use of cellulose in novel ways.

2.6 Thesis Organization

The main objective of this study is to deposit fluorocarbon films on paper and cellulose for improvement of their barrier properties. A second objective of this study is to demonstrate the hydrophobic behavior of the fluorocarbon films on paper and to show that although the films allow water vapor diffusion, the films are not “wetted” when liquid water contacts these layers. A final objective of this study is to demonstrate the grease barrier properties of fluorocarbon films and to develop methods to quantify the grease resistance.

To achieve the objectives listed above, a six-inch parallel plate plasma system was designed, assembled and optimized for fluorocarbon depositions and was used to conduct the experiments described in this work. Various thin film characterization techniques were used to analyze the deposited fluorocarbon films. The experimental procedures and

analytical techniques used along with the details of the plasma reactor are presented in Chapter 3.

Fluorocarbon film depositions were conducted in both 6-inch parallel plate and 4-cm parallel plate systems using Pentafluoroethane (C_2F_5H ; PFE) and Octafluorocyclobutane (C_4F_8 ; OFCB) as precursors. Chapter 4 describes film deposition rates, resulting film structure, composition, and properties of the fluorocarbon films deposited from these precursors.

Chapter 5 presents the hydrophobic properties of fluorocarbon films on paper and cellulose. Moisture absorption studies conducted on films deposited from PFE and OFCB using a quartz crystal microbalance are also presented in Chapter 5.

Chapter 6 presents the oleophobic properties of fluorocarbon films deposited on paper. This chapter also presents the methods used to quantify the grease barrier properties of fluorocarbon films and describes evaluations of the fluorocarbon coating depth into paper.

Chapter 7 describes the deposition of dual layer films of PFE and p-NIPAAM on silicon. This chapter also presents information on the applications of dual layer films, their deposition, and their characterization using various analytical techniques.

Finally, Chapter 8 presents conclusions of this work and offers recommendations for future work in this area.

3. EXPERIMENTAL PROCEDUES AND ANALYTICAL TECHNIQUES

This chapter presents a detailed description of the plasma reactor and its configuration along with experimental procedures used to deposit fluorocarbon films on various substrates. Substrates with deposited films were characterized and analyzed using a variety of analytical techniques whose descriptions will also be presented in this chapter. The techniques used involved both determination of the physical properties as well as the chemical structure and composition of deposited thin films. Spectroscopic techniques such as Fourier transform infrared spectroscopy (FTIR) was used to determine chemical structures while the surface sensitive of x-ray photoelectron spectroscopy (XPS) was used to evaluate the chemical composition and bonding information of the deposited films. The techniques used to characterize film properties such as thickness, refractive index, hydrophobicity, oleophobicity, and physical properties such as water vapor or organic vapor absorption are described in detail. Since fluorocarbon film deposition on porous substrates such as paper may change the surface morphology and penetrate the porous network, surface morphological studies using scanning electron microscopy (SEM) and photoacoustic FTIR have been used to evaluate the fluorocarbon coating depth. Magnetic resonance imaging (MRI), used to characterize the grease barrier properties of coated paper, has also been presented.

3.1 Plasma Reactor Configuration and Operating Details

A parallel plate plasma reactor operating at radio frequency (RF) was used to deposit fluorocarbon films; Figure 3.1 shows the experimental reactor configuration. The reactor (or chamber) was a 6-way stainless steel cross sealed top and bottom by high vacuum conflat flanges. The other four ports of the reactor were: (i) gas inlet, (ii) reaction products outlet, (iii) pressure transducer port, and (iv) viewport. The top and bottom electrodes were circular steel discs of 4 cm diameter and were electrically isolated from the rest of the system. The top electrode was supplied with RF power while the bottom electrode was electrically grounded. The distance (also known as interelectrode spacing) between top and bottom electrode was fixed at 3 cm for all experiments. A 13.56 MHz RF power generator (300W max), HF-300 by ENI Power Systems, was used to supply RF energy to the top electrode. To maximize RF power transfer to the plasma system (i.e. minimize the reflected power), a Heathkit SA-2060A matching network was between the power supply and top electrode. The bottom electrode was heated with Omegalux CIR 2015 cartridge heaters. A type K thermocouple was used to monitor the temperature of the bottom electrode. The temperature of the bottom electrode was regulated by a Syskon RKC temperature controller employing an electromagnetic relay.

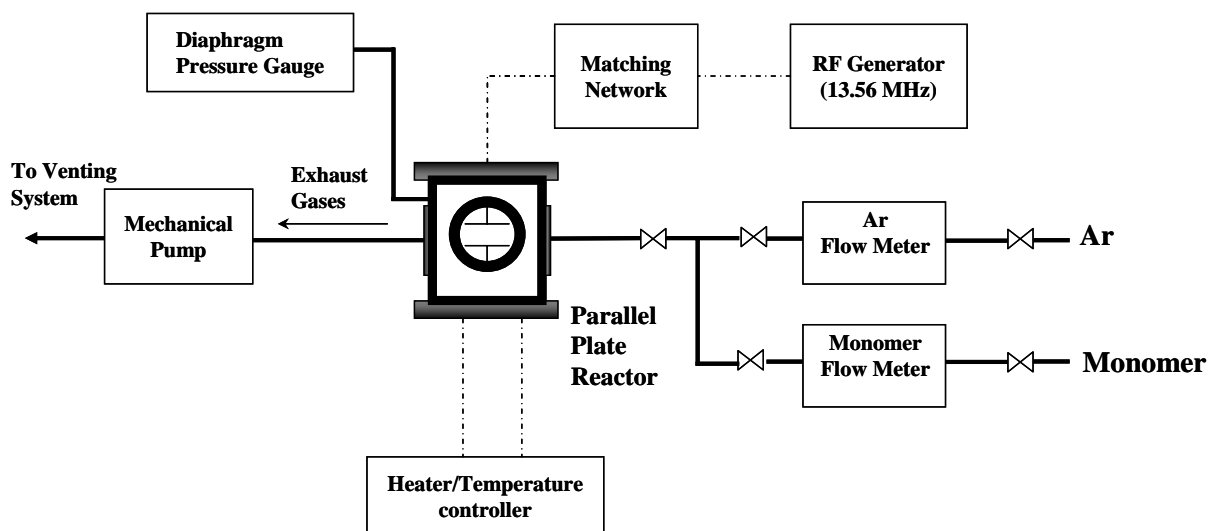


Figure 3.1 Parallel Plate Plasma Reactor Set up.

Substrates were placed on the bottom (grounded) electrode, which was maintained at a constant temperature between 60 °C and 200 °C depending on the specific experiment to be performed. The pressure inside the reactor was monitored with a Kurt J. Lesker vacuum gauge with a range of 1500 torr to 1 mtorr. The typical base pressure in the chamber was less than 9 mtorr, while the operating pressure was varied between 0.7 torr and 1 torr for deposition experiments. The gaseous precursors investigated in this study were pentafluoroethane (C_2F_5H) and octafluorocyclobutane (C_4F_8). Argon (Air products, 99.99 % purity) was used as the carrier gas for each monomer. Flowrates were regulated by teflon flowmeters (rotameters). In the case of the solid precursor, n-isopropylacrylamide (NIPAAM), the precursor was heated to 110 °C and vaporized. The vapors were then transported by an argon flow through the heated tube assembly. The reactor was evacuated with an Alcatel 2063C chemical series vacuum pump through the

left side port while reactants were introduced from the opposite side. The operating pressure, power and substrate temperature were held constant during a deposition run.

The reactor system was periodically checked for leaks and rise in reactor base pressure (upto 5 mTorr rise in base pressure was acceptable). Periodic tightening of Swagelok valves and oil changes (Fomblin) after every 100 runs ensured trouble free operation of the system.

The detailed system operating procedure for deposition of fluorocarbon films is as follows:

- 1) Vent the chamber to atmosphere by filling it with nitrogen gas (throttle valve on the pump closed).
- 2) Open the view port (also the sample loading port) and place the substrate (paper, cellulose membrane, or a piece of silicon wafer) on the bottom electrode.
- 3) Close the view port and carefully pump down the chamber by slowly opening the throttle valve between the chamber and the mechanical pump. The slow pump down prevents lighter samples such as paper from blowing toward the vacuum pump.
- 4) Wait until the reactor reaches the base pressure. The typical base pressure achieved during the pump down is between 8 – 10 mtorr.
- 5) Turn on the heater for the grounded bottom electrode. Heat the bottom electrode to a desired set point using the temperature controller. Wait for about 35 – 40 minutes until bottom electrode temperature stabilizes at desired the set point.

- 6) Open the argon and precursor flow valves. Adjust the inlet gas flowrates of argon and precursor to the desired set points using teflon flowmeters. Wait for about 15 minutes for the gas flowrates to stabilize.
- 7) Adjust the throttle value between the reactor and the mechanical pump to maintain the reactor at a desired pressure (also known as deposition pressure), typically between 0.7 – 1.0 Torr.
- 8) When the reactor pressure stabilizes to the set point value, turn on the RF power to the top electrode; plasma should be visible through the viewport. If no plasma appears, turn off the RF power to the reactor immediately.
- 9) If plasma is observed through the viewport, adjust the variable capacitors and inductors on the matching network to achieve minimum reflected RF power. This also corresponds to the maximum RF power coupled to the reactant gas system.
- 10) Note the reactor pressure and bottom electrode temperature during the deposition run to ensure controlled deposition conditions.
- 11) After running the system for a desired period of time, turn off the RF power to the top electrode. Check the viewport; the plasma should have extinguished.
- 12) Turn off the argon and monomer gas flows.
- 13) Turn off the heater to the bottom electrode.
- 14) At this point, slowly open the throttle value to a complete open position to begin system evacuation to the base pressure.
- 15) Wait for about 25 minutes to ensure that all the reactants and plasma products have been pumped out of the chamber.

- 16) Close the throttle valve and open the nitrogen value to fill the reactor with nitrogen until atmospheric pressure is reached.
- 17) When the system is at atmospheric pressure, open the viewport and carefully remove the processed sample from the bottom electrode.
- 18) Close the viewport and pump down the chamber to base pressure. To prevent the system from developing leaks and to prevent moisture adsorption by the walls of the chamber over time, it is important that the system be kept under vacuum except for the purpose of sample introduction.
- 19) During the deposition process, fluorocarbon film not only deposits on the substrate, but also on the electrodes and the reactor walls. These deposits, if not removed, can flake off the walls and deposit on the samples during subsequent runs. Thus they need to be removed or ashed from the surfaces. This can be accomplished by striking an oxygen plasma in the reactor for a time sufficient to completely etch the film deposited on both top and bottom electrodes.

While initial experiments (almost half of the work during this thesis) was conducted using the parallel plate plasma system described above, a significant amount of time was devoted to designing, assembling, and optimizing a 6" parallel plate plasma system.

Figure 3.2 shows a schematic of the 6" parallel plate system.

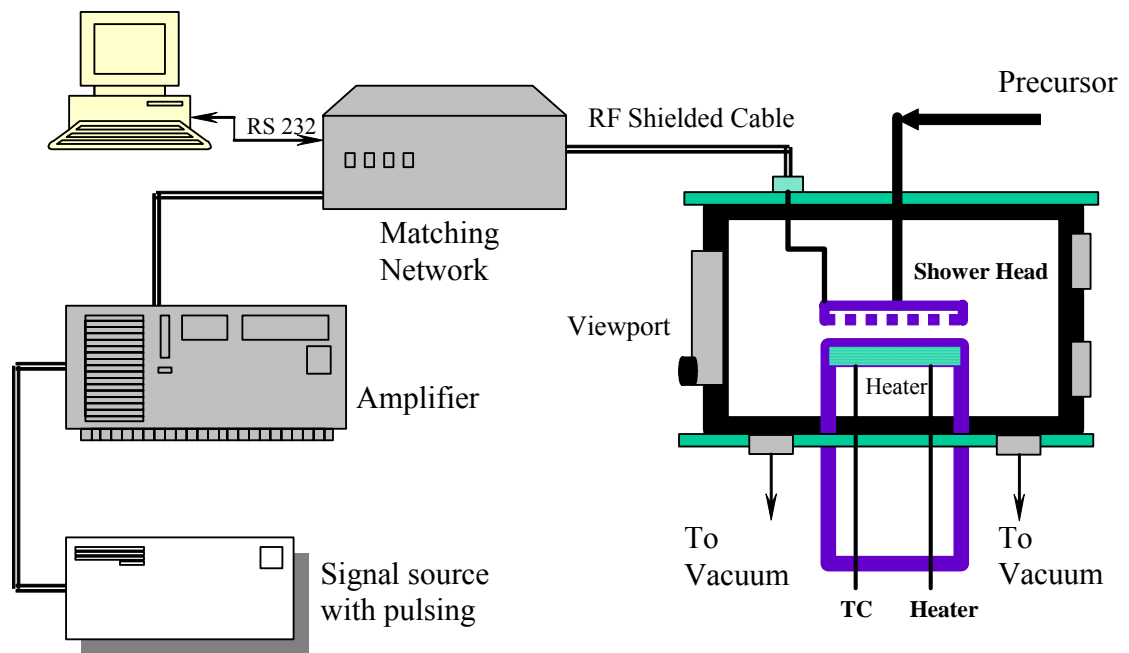


Figure 3.2 Setup of 6" Parallel Plate Plasma Deposition System

The salient features of this system are:

- 1) 6" wafer processing capability.
- 2) Top electrode (also the powered electrode) is a shower head for uniform gas distribution.
- 3) Heatable and electrically isolated bottom electrode.
- 4) Large (8") hinged door with quartz viewport for loading samples.
- 5) Variable frequency signal source (9 kHz to 1.1 GHz) with built-in pulsing unit for pulsing the plasma on millisecond timescales.

- 6) Variable frequency RF Power Amplifier (2 – 30 MHz) capable of amplifying the input signal up to 600 W.
- 7) Automatic/Manual Matching Network (Optimized for 13.56 MHz RF frequency)
- 8) Computer for impedance monitoring and matching (using RS232 serial cable).

3.2 Contact Angle

Hydrophobic properties (water repellence) or hydrophobicity was determined using contact angle goniometry. Contact angle measurements were performed on fluorocarbon coated cellulose substrates; a VCA 2500 XE system (AST Products, Inc.) was used for these measurements. The sample was placed in a controlled humidity chamber to prevent evaporation of the water droplet, enabling measurements over extended periods of time. The humidity chamber, made from Plexiglass, was transparent to light to allow pictures to be obtained of the dispensed drop at various times. The humidity inside the humidity chamber was controlled in the range of 95% – 99% using a combination of dry and wet N₂ streams. A drop size of 2 μ l was dispensed for each measurement and the temperature was held constant at room temperature (25 °C). Contact angles were measured over a period of one hour to observe the change in contact angle with time. Figure 3.3 shows a schematic of a contact angle goniometer system.

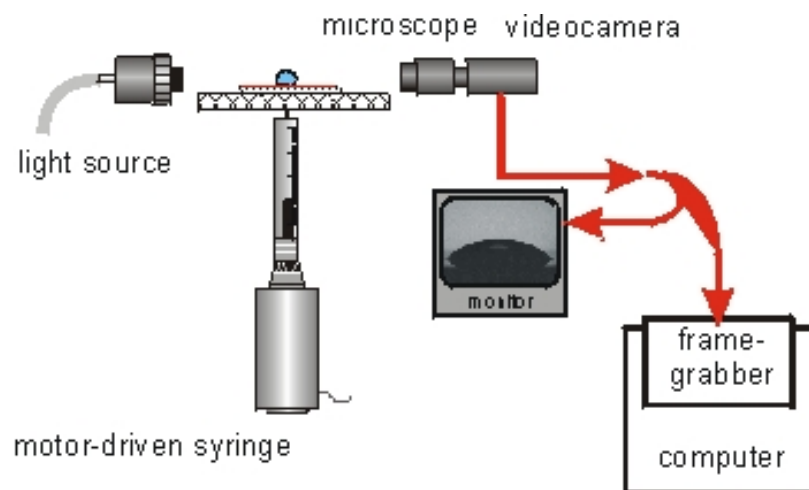


Figure 3.3 Set-up for contact angle measurements.

Contact angle, θ , is a quantitative measure of the wetting of a solid by a liquid. It is defined geometrically as the angle formed by a liquid at the three phase boundary where a liquid, gas and solid intersect (Figure 3.4):

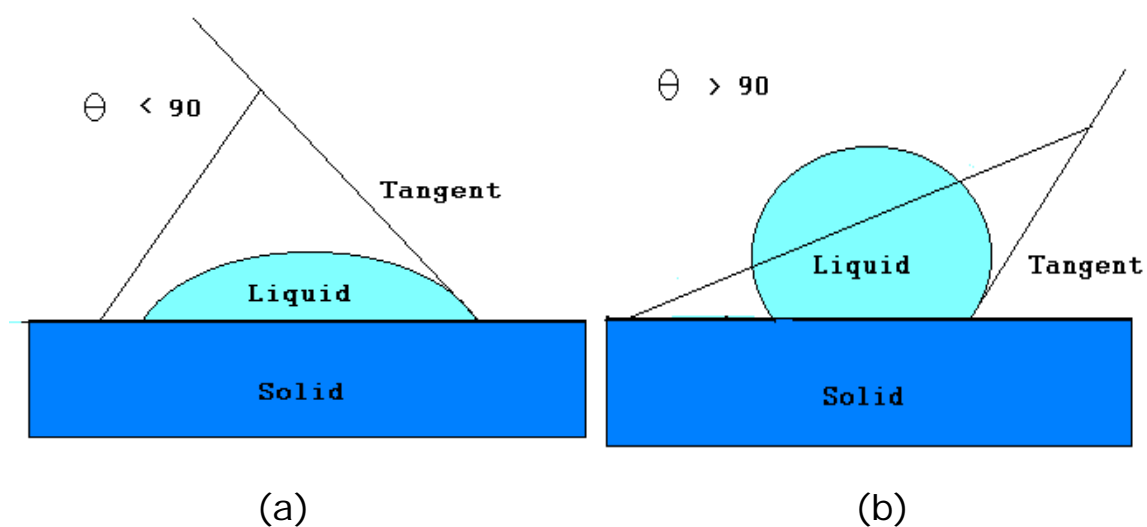


Figure 3.4 Contact angle showing a wetting (a) and a non-wetting surface (b).

Clearly, low values of θ indicate that the liquid spreads, or wets the surface well, while high values indicate poor wetting. If $\theta < 90^\circ$, the liquid is said to wet the solid. If the contact angle is greater than 90° , the surface is said to be non-wetting. A zero contact angle represents complete wetting.

A detailed description of this method and its theoretical background may be found in Adamson and references cited therein [80]. Briefly, according to Young's equation, the contact angle, θ , is a function of the interfacial tensions between the solvent, sample and vapor (Equation 3.1):

$$\cos \theta = \frac{\gamma_{SV} - \gamma_{SL}}{\gamma_{LV}} \quad (3.1)$$

with γ_{SL} , γ_{SV} , γ_{LV} denoting the interfacial tension between solid and liquid phase, solid and vapor phase, and liquid and vapor phase, respectively. Hydrophobic, i.e. non-wetting surfaces exhibit large contact angles whereas hydrophilic, i.e. wettable surfaces show small contact angles when a water droplet is placed in contact with the surface.

3.3 Film Thickness and Optical Properties

It is important to have accurate values for the fluorocarbon film thickness and optical constants. Since it is difficult to measure film thicknesses on paper or cellulose, a piece of

a Si wafer was placed by the side of another sample (paper or cellulose) to ensure that the sample was exposed to same environment and essentially experiences the same deposition conditions (temperature, plasma, grounding) as those for the Si wafer. The primary purpose of introducing a silicon substrate was to enable to measurement of the film thickness on a , flat, smooth surface under the assumption that the film deposited on silicon is of similar thickness and has same properties as the film deposited on paper.

Spectroscopic ellipsometry was used to measure the fluorocarbon film thickness and optical constants (primarily refractive index) on a silicon substrate. Ellipsometry measures the change in polarization state of light reflected from the surface of a sample. This change in polarization of incident light can be correlated to the properties of the material being analyzed such as thickness, refractive index, surface roughness, and anisotropy. The intensity and polarization state of the reflected light is measured by the detector in the form of two parameters, ψ and Δ . These values are related to the ratio of Fresnel reflection coefficients, R_p and R_s for *p-polarized* (parallel to the plane of incidence) and *s-polarized* (perpendicular to the plane of incidence) light, respectively.

$$\tan(\Psi) e^{i\Delta} = \frac{R_p}{R_s} \quad (3.2)$$

Figure 3.5 illustrates how a linearly polarized input beam is converted to an elliptically polarized reflected beam. For any angle of incidence greater than 0° and less than 90° , p-polarized light and s-polarized will be reflected differently.

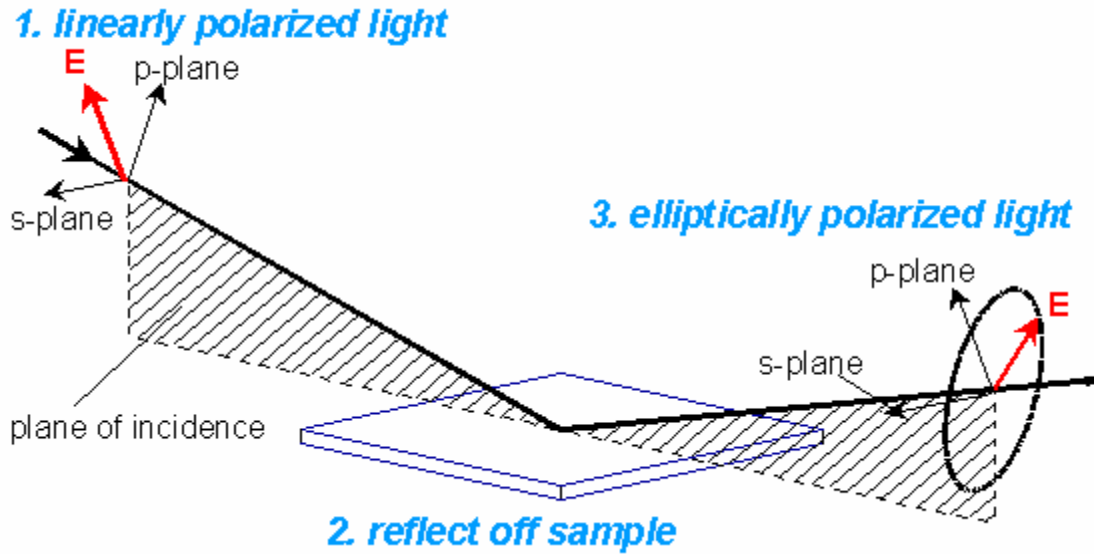


Figure 3.5 A schematic of the geometry of an ellipsometry measurement

Typically, Ψ and Δ data are acquired as a function of wavelength and angle of incidence. An optical model that describes the sample structure is entered using as much information about the sample as possible. It is important to account for all layers in the sample structure. Theoretical data is generated from the optical model that corresponds to the experimental data. Generated data is compared to the experimental data. Unknown parameters in the optical model, such as film thickness or optical constants or both, are varied to produce a "best fit" (i.e. minimizing mean square error) to the experimental data. Regression algorithms are used to vary unknown parameters and minimize the difference between the generated and experimental data. Physical parameters of the sample such as film thickness, optical constants, composition, surface roughness, etc. are obtained when a good "fit" (based on error minimization) to the experimental data is achieved. A fitted model consists of a known number (and order) of layers with

appropriate dispersion relations for each layer. For fluorocarbon films and p-NIPAAAM films analyzed in this study, Cauchy relationships were used to model the dependence of optical constant on wavelength (Equation 3.3).

$$n(\lambda) = A + \frac{B}{\lambda^2} + \frac{C}{\lambda^4} \quad (3.3)$$

where, A, B, and C are Cauchy parameters. Using the above equation, ‘n’ can be calculated at various wavelengths.

The optical constants define how light interacts with a material. The complex refractive index is a representation of the optical constants of a material, and is represented by equation 3.4 as:

$$\tilde{n} = n + ik \quad (3.4)$$

The real part or index of refraction, n , defines the phase velocity of light in a material while the imaginary part or extinction coefficient, k , determines how fast the amplitude of the wave decreases as it penetrates the material. Thus, the extinction coefficient is directly related to the light absorption of a material.

Film thickness and refractive index measurements in this thesis were performed on two different ellipsometers – Variable Angle Spectroscopic Ellipsometer (VASE[®]) manufactured by J.A. Woollam Co. and Model M-2000 (J. A. Woollam Co.). The

VASE instrument has high accuracy since it consists of a rotating analyzer and is insensitive to source polarization. Most measurements are performed over the wavelength range 100 nm-1100 nm with a step size of 2 nm at three different angles 65°, 70°, and 75°. These angles are chosen because the maximum sensitivity of this technique to material properties occurs at the Brewster angle of the film. For solid films, the Brewster angle lies between 56° and 80°. Data collection and analysis are performed using WVASE32™ software in both ellipsometers.

3.4 Chemical Structure and Properties

X-ray photoelectron spectroscopy (XPS) and Fourier transform Infrared spectroscopy (FT-IR) were used to characterize the chemical properties and structure of thin fluorocarbon films.

3.4.1 X-ray Photoelectron Spectroscopy

X-ray photoelectron spectroscopy is a surface sensitive technique used to measure the surface atomic composition and bonding structure of materials [81]. A surface sensitive technique preferentially provides more sensitivity to atoms near the surface than in the bulk away from the surface i.e. the majority of the signal originates from the surface region. . XPS gives information limited to essentially the top 5 -10 nm of the film, and is based on the photoelectric effect. This technique is commonly used in a variety of applications to identify elements and bonding structures in the outermost atomic layers,

to determine depth profile, to detect contamination present at surfaces and interfaces, to determine chemical interactions at interfaces, to study oxidation and surface modification, to understand the causes of adhesion failure, and to study bonding structures of dielectric and barrier films. Figure 3.6 shows a schematic of the XPS system [82].

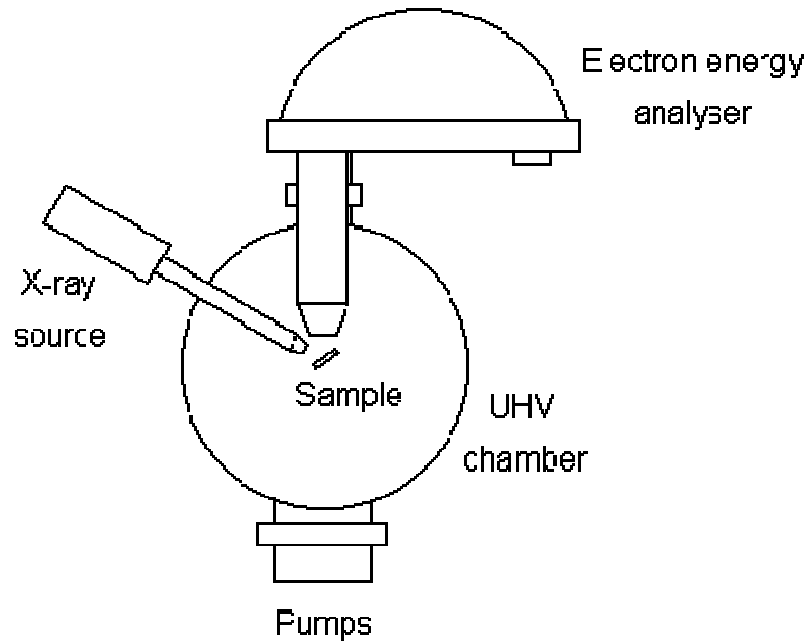


Figure 3.6 Simple Schematic of X-ray Photoelectron Spectroscopy System [82].

In XPS, a monochromatic x-ray beam irradiates the sample surface and is absorbed by an atom in a solid, leading to ionization and the emission of a core (inner shell) electron. The kinetic energy distribution of the emitted photoelectrons (i.e. the number of emitted photoelectrons as a function of their kinetic energy) can be measured using any appropriate electron energy analyzer and a photoelectron spectrum can thus be recorded.

From knowledge of the kinetic energies of these photoelectrons, the electron binding energy can be calculated based on the expression given below (Equation 3.5):

$$BE = h\nu - KE - \phi \quad (3.5)$$

where $h\nu$ corresponds to the incident energy of the x-rays (1486.6 eV for aluminum, Al- $K\alpha$), KE is the kinetic energy of the ejected photoelectrons (as measured by detector), BE is the binding energy of the ejected photoelectrons, and ϕ is the work function, which is a constant for a given spectrometer. Figure 3.7 illustrates the photoelectron emission which is the basis of XPS [82].

The amount of energy required for the electron to overcome the attractive (Coulombic) force of the nucleus is called the binding energy. Thus, binding energy is the attractive force between the electron and the nucleus. Since the attractive force on the electron depends on the charge of the nucleus, every atom has characteristic binding energies for electron in different orbitals. This principle is exploited by XPS to identify different atoms in a specific sample. When evaluating the concentration of atoms from photoelectron signals, the geometry of the system, atomic mass, photoemission cross-section, electron attenuation length, and spectrometer transmission and detection efficiency are taken into account. The XPS chamber is maintained at ultra-low pressure ($<5 \times 10^{-9}$ torr) to avoid collisions between emitted photoelectrons and other electrons or residual gas molecules, thereby minimizing alteration of the kinetic energy of the emitted photoelectrons.

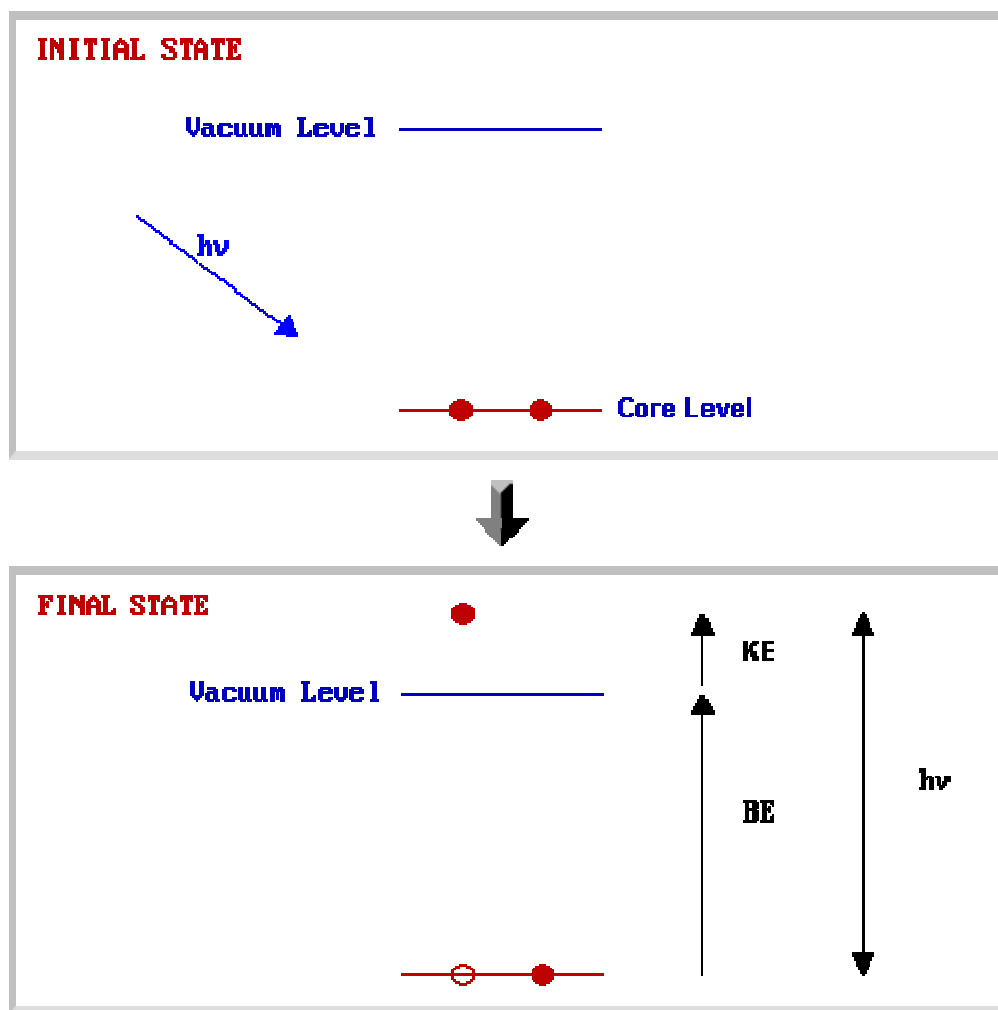


Figure 3.7 Schematic representing the basic principle of XPS [82].

In addition to the surface atom composition of materials, XPS can also provide useful information on the bonding structure in thin film. The presence of chemical bonding (and hence, neighboring atoms) causes binding energy shifts that can be used to extract information about the chemical nature of atomic species (such as atomic oxidation state)

in the sample surface. For this reason, XPS is also known as Electron Spectroscopy for Chemical Analysis (ESCA). XPS can also be used to determine composition variation in shallow regions of the film. Because the energy of the photoelectrons is strongly attenuated by passage through the sample material, the information obtained comes originates in the sample surface, mostly the top layers (1 – 10 nm).

The XPS spectra in this thesis were collected using a Perkin Elmer PHI model 1600 spectrometer with a work function ϕ of 3.7 eV. Monochromatic x-rays were generated using a water-cooled Al K_{α} anode operated at a power of 350 W. Ejected photoelectrons were detected and collected in a 180° hemispherical analyzer and a multichannel detector. Photoelectron energies were measured in the analyzer with high sensitivity and energy resolution. XPS chamber pressure was typically held below 5×10^{-9} torr during analysis. The C1s peak (284.8 eV) was used as a reference to maximize the photoelectron count by adjusting the position (z-position) of the sample relative to the source and the detector. Low resolution spectra (called survey mode) were collected first (0.5 eV, 50 ms/step) to identify all chemical elements on the thin film surface. Subsequently, high resolution spectra were collected with a different set of conditions (0.05 eV and 300 ms/step) for each of the elements detected. Data were collected at a 45° angle with respect to the detector. An electron pass energy of 11.75 eV was used to analyze various elements present in the thin film sample, which were typically C_{1s}, F_{1s}, O_{1s}, N_{1s}, and Si_{2p}. Since fluorocarbon films are insulating, surface charging occurs which leads to the shift in binding energies. Some of the surface charge build up was overcome by using a low energy electron flood gun to neutralize the charge buildup. However, in most cases

binding energy shifts were still not eliminated completely with the neutralizer. Therefore, in most cases the shift was corrected by assigning the highest binding energy CF_3 component of the C-1s peak to 293 eV.

To study the change in film composition with film depth and to obtain interfacial (between film and substrate) bonding information, data were collected at different take off angles on the same sample. This manner of data collection is also referred to as angle resolved XPS (AR-XPS) and is commonly used for sample depth profiling. For AR-XPS studies, the spectra were collected at photoemission angles ranging from 10° to 80° at 10° intervals. To obtain the relative compositions of the various species in the deposited films, C1s peak was deconvoluted into different contributing peaks which were determined by curve fitting each spectral region. In peak fitting, Gaussian-Lorentzian peaks were used while minimizing the error between the actual data and the sum of the deconvoluted peaks.

3.4.2 Infrared Spectroscopy

The term "infrared" covers the range of the electromagnetic spectrum between 0.78 and 1000 μm . The infrared region is usually divided into three sections; *near*, *mid* and *far* infra red as indicated in Table 3.1. In the context of infrared spectroscopy, wavelength is measured in "wavenumbers". A wavenumber is defined as the reciprocal of wavelength ($= 1/\text{wavelength}$) and has the units of cm^{-1} .

Table 3.1 Regions of Infrared Spectrum

Region	Wavelength range (μm)	Wavenumber range (cm^{-1})
Near	0.78 - 2.5	12800 - 4000
Middle	2.5 - 50	4000 - 200
Far	50 - 1000	200 - 10

IR radiation does not have sufficient energy to induce electronic transitions as seen with ultraviolet radiation. Absorption of IR is restricted to compounds with small energy differences in allowed vibrational and rotational states. For a molecule to absorb IR, the vibrations or rotations within a molecule must cause a net change in the dipole moment of the molecule. The alternating electrical field of the radiation (electromagnetic radiation consists of an oscillating electrical field and an oscillating magnetic field, perpendicular to each other) interacts with fluctuations in the dipole moment of the molecule. If the frequency of the radiation matches the vibrational frequency of the molecule then radiation will be absorbed, causing a change in the amplitude of molecular vibration [83]. The wavenumbers (sometimes referred to as *frequencies*) at which an organic molecule absorbs radiation give information on functional groups present in the molecule (i.e. the types of chemical bonds present). Certain groups of atoms absorb energy and therefore, give rise to bands at approximately the same frequencies. IR spectra can be analyzed with

the help of functional group tables which correlate frequencies with chemical functional groups [84].

A typical IR spectrum consists of the wavenumber, plotted on the X-axis, which is proportional to energy; therefore, the highest energy vibrations are on the left. The percent transmittance (%T) is plotted on the Y-axis. Absorption of radiant energy is therefore represented by a “trough” in the curve: zero transmittance corresponds to 100% absorption of light at that wavelength. Band intensities can also be expressed as absorbance (A). Relationship between absorbance and transmittance is given by (Equation 3.6):

$$A = \text{Log}_{10} \left(\frac{1}{T} \right) \quad (3.6)$$

Fourier Transform Infrared Spectroscopy (FTIR) is a powerful tool to identify chemical bond types in a molecule by producing an infrared absorption spectrum that serves as a molecular "fingerprint". The term Fourier Transform Infrared Spectroscopy (FTIR) refers to the manner in which the data is collected and converted from an interference pattern to a spectrum.

Infrared spectroscopy was used to evaluate the chemical bonding structure of the deposited fluorocarbon films. Infrared spectra were collected in reflection mode at a grazing angle of 70° using a Nicolet Magna-IR 560 FTIR spectrometer. All spectra were recorded at a resolution of 4 cm⁻¹ and averaged over 512 scans. Typical thicknesses for

films deposited from pentafluoroethane were 1 μm while thicknesses of films deposited from C_4F_8 were 2 μm .

3.5 Physical Properties

3.5.1 Moisture uptake of fluorocarbon films

A quartz crystal nanobalance (QCN) was used to measure the moisture uptake of the deposited fluorocarbon films. The QCN is basically a mass sensing device with the ability to measure in real-time a very small mass changes on a quartz crystal resonator. The sensitivity of the QCN is approximately 100 times higher than an electronic balance with a sensitivity of 0.1 μg . This means that QCNs are capable of measuring mass changes as small as a fraction of a monolayer or a single layer of atoms. The high sensitivity and the real time monitoring of mass changes on the sensor crystal make QCM a very attractive technique for a large range of applications such as thin film thickness monitoring in sputtering and deposition, electrochemistry of interfacial processes at electrode surfaces, detection of biomolecules, and absorption of species or vapors into various polymers.

The heart of the QCN is the piezoelectric AT-cut quartz crystal sandwiched between a pair of electrodes. When the electrodes are connected to an oscillator and an AC voltage applied to the electrodes, the quartz crystal oscillates at its resonance frequency due to the piezoelectric effect. This oscillation is generally very stable due to the high quality of the oscillation (high Q factor). The QCN is based on the principle that the frequency shift of

a quartz crystal resonator is directly proportional to added mass. This change in frequency is given by Sauerbrey equation [85, 86] as (Equation 3.7):

$$\Delta f = - \frac{2 f_0^2 \Delta m}{\sqrt{\rho_q \mu_q}} \quad (3.7)$$

where: Δf = measured frequency shift,

f_0 = resonant frequency of the fundamental mode of the crystal,

Δm = mass change per unit area (g/cm^2),

ρ_q = density of quartz, $2.648 \text{ g}/\text{cm}^3$,

μ_q = shear modulus of quartz, $2.947 \times 10^{11} \text{ g}/\text{cm}/\text{s}^2$

Frequency shift (Δf) is the difference between f_L (resonant frequency of the loaded crystal in Hz.) and f_q (resonant frequency of unloaded crystal in Hz). The Sauerbrey equation assumes that the additional mass or film deposited on the crystal has the same acousto-elastic properties as quartz. Under this assumption, the change in frequency is a function of mass per unit area. Therefore, in theory, the QCM mass sensor does not require calibration. It should be noted, however, that the Sauerbrey equation is only strictly applicable to uniform, rigid, thin-film deposits. Since plasma deposited fluorocarbon films are highly crosslinked and uniform, the Sauerbrey equation can be used with little error incurred.

Moisture absorption studies were performed with a quartz crystal nanobalance (Model EQCN-701 from ElchemaTM Inc., NY). Fluorocarbon films were deposited on 10 MHz quartz crystals with an active area (gold electrode area) of 0.2 cm². In each deposition, films were also deposited on a silicon wafer to enable subsequent film characterization studies. After film deposition, the difference in the resonant frequencies of the loaded (after deposition) and unloaded quartz crystals were used to determine the mass of the deposited film. Subsequently, the quartz crystal was placed in a specially designed leak-proof glass cell to provide a controlled environment for relative humidities between 0% and 98% in air or other gas (e.g. nitrogen). The relative humidity inside the cell was varied between 5% and 90%, by controlling the dew point on the incoming stream. The glass cell purged with pure/dry nitrogen (referred to as “dry environment”) was at 0% relative humidity. The change in steady-state resonant frequency of the quartz crystal was recorded as a function of humidity. All moisture absorption measurements were performed at room temperature (25 °C). Transient moisture absorption studies to determine the rate of moisture uptake and diffusivity were also conducted using this apparatus. Humidity cycling (switching from dry environment (0% humidity) to wet environment (90% humidity)) was also conducted to determine if water was chemisorbed in the fluorocarbon film. The fluorocarbon film density was calculated by following equation (Equation 3.8):

$$\rho_{FC} = \frac{\Delta m_{Film}}{L_{Film}} = \frac{M_{Film}}{A_q L_{Film}} \quad (3.8)$$

where Δm_{Film} refers to change in quartz crystal mass per unit active area due to film deposition (g/cm^2); L_{Film} refers to the film thickness as measured ellipsometrically; M_{Film} refers to the total mass of film on the crystal (g); and A_q refers to the active area on the quartz crystal (cm^2). The weight percentage moisture uptake by fluorocarbon films was calculated by following equation (Equation 3.9):

$$\text{Wt\% Uptake} = \frac{\Delta f_{\text{Humidity}}}{\Delta f_{\text{Film}}} \times 100 = \frac{\Delta m_{\text{Humidity}}}{\Delta m_{\text{Film}}} \times 100 \quad (3.9)$$

where $\Delta f_{\text{Humidity}}$ and $\Delta m_{\text{Humidity}}$ refer to change in frequency and change in mass due to exposure to water vapor, respectively.

3.6 Surface Morphology

Scanning Electron Microscopy (SEM) was used to image the surface of fluorocarbon coated paper samples. The scanning electron microscope generates a beam of electrons in a vacuum; the beam is collimated by electromagnetic condenser lenses, focused by an objective lens, and scanned across the surface of the sample by electromagnetic deflection coils. The primary imaging method is collection of secondary electrons released by the sample [87]. The secondary electrons are detected by a scintillation material that produces flashes of light from the electrons. The light flashes are then detected and amplified by a photomultiplier tube. SEM has the ability to produce highly magnified images (up to 300,000X) through rastering of focused electrons onto the

surface of a material. SEM is versatile in the sense that it can provide additional information besides the surface topography. For example, compositional analysis of a material may also be obtained by monitoring secondary X-rays produced by the electron-specimen interaction. Thus, detailed maps of elemental distribution can be produced from multi-phase materials or other complex materials. Figure 3.8 shows various characterization modes possible with SEM that can be obtained from the beam of incident electrons.

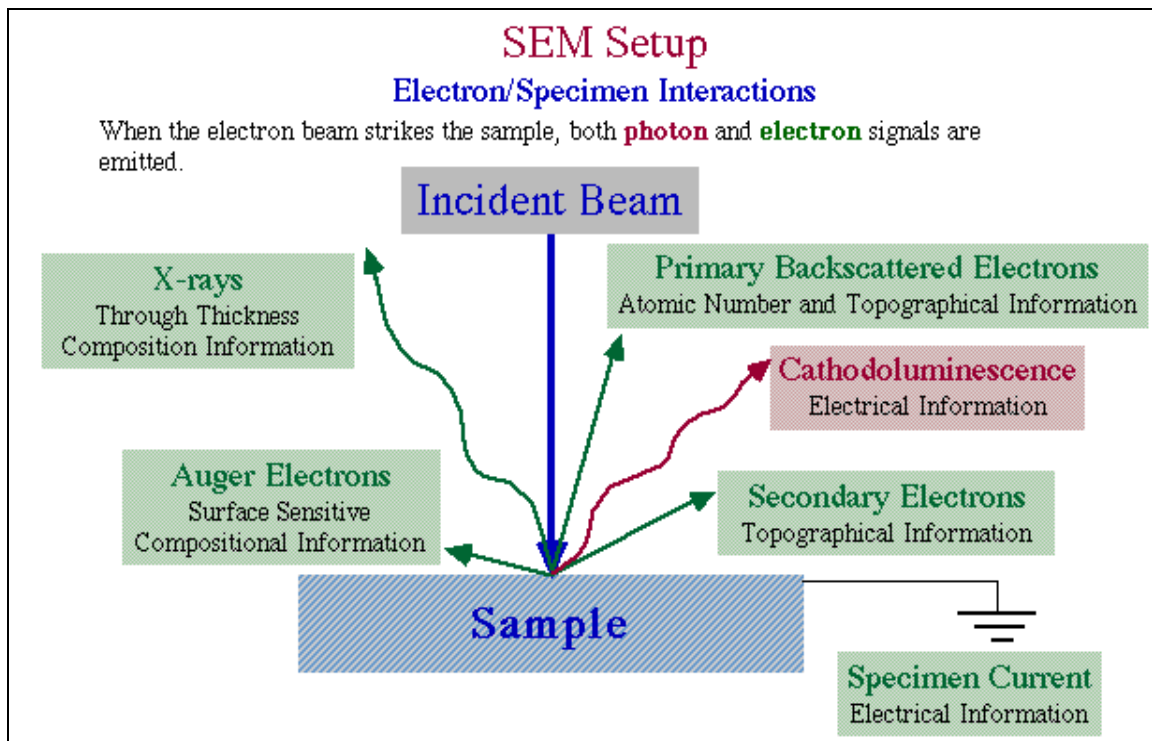


Figure 3.8 Schematic showing various characterization modes with an SEM [88].

A Hitachi S-800 Field Emission-SEM (FE-SEM) was used to study the surface morphology of uncoated and fluorocarbon coated paper in addition to fluorocarbon coated Si wafers. The accelerating voltage used was usually set at 10 kV. Since paper samples and fluorocarbon coated samples are non-conductive, a desktop sputter coater was used to coat the samples with a thin (conductive) gold layer. The sputter coater consisted of a gold target with argon used as an inert gas in the plasma environment. Coating thickness varied but was usually in the 3 to 5 nm range.

3.7 Magnetic Resonance Imaging Studies

Magnetic Resonance Imaging (MRI) is an imaging technique that is used to obtain an image of internal structure or details of a material. MRI has been used primarily in medical settings (tomography) to scan the human body and can show bones, muscles, joints, blood vessels, nerves and other structures in great detail [89]. MRI scans can provide information about almost all tissue types and can be used to differentiate between tissues of similar density. The information obtained can then be analyzed to determine specific health maladies and detect diseases [90]. MRI is based on the principles of nuclear magnetic resonance (NMR), a spectroscopic technique used by scientists to obtain microscopic chemical and physical information on molecules [91]. In addition to vast applications in medical science, MRI has been used in various fields such as textiles, wood science, paper science, material science, and the study of macromolecules. With MRI, it is possible to study molecular structure and dynamics of systems such as zeolites,

catalysts, semiconductors, nanocrystals, nanotubes, liquid crystals, polymers and proteins [92, 93]. The terms MRI and NMR are used interchangeably in the literature.

3.7.1 Principles of Magnetic Resonance Imaging

The center of an atom, the nucleus, has a property called “spin.” When an atom is placed in a magnetic field, the axis of spin moves around the magnetic field lines with a frequency that depends on the strength of the magnetic field. This motion is called “precession,” and is similar to the motion of a spinning top in a gravitational field. Because nucleons have spin, as do electrons, their spins can pair up when the orbitals are being filled and cancel out resulting in a net zero spin. MRI is meaningful only when performed on isotopes with a non-zero nuclear spin. Some the nuclei which have been studied in MRI are ^1H , ^2H , ^{31}P , ^{23}Na , ^{14}N , ^{13}C , and ^{19}F . The hydrogen atom is the most common example of an atom with a non-zero nuclear spin and is widely used in MRI. The spin in the nucleus (i.e. a proton in case of ^1H) causes the proton to behave like a tiny magnet with a north and south pole. Thus, the proton has a magnetic moment vector (μ). When a sample containing ^1H nuclei (e.g. water or hexadecane) is placed in an external magnetic field, the spin vector of the particle aligns with the external field such that the magnetic moment vectors of each nucleus in the sample add to yield a net magnetization (M). The net magnetization (M) can be expressed as (Equation 3.10):

$$M = \chi_o B_o \quad (3.10)$$

where χ_o is a proportionality constant, called magnetic susceptibility (between applied and induced magnetic field), and B_o is the strength of the applied external magnetic field. The applied magnetic field creates a torque on the induced magnetization, causing it to precess parallel to the magnetic field direction. The direction of the precession is perpendicular to the magnetic field B_o and to the proton's magnetic moment μ (which is in the same direction as the proton spin axis). Therefore, the proton precesses in the $\mu \times \mathbf{B}$ direction. The field strength B is linearly proportional to the precession frequency ω_L , and is expressed by the Larmor equation (Equation 3.11)

$$\omega_L = \gamma B_o \quad (3.11)$$

where γ is called the gyromagnetic ratio and is 42.57 MHz/T for hydrogen nuclei. The frequency ω_L is also called the Larmor frequency. Figure 3.9 shows the response of a nuclear spin (magnetic moment) to an external magnetic field. The most common magnetic field strengths are in the range of 0.5 to 14 Tesla, which yields precessional frequencies of 20 to 600 MHz for hydrogen nuclei. These frequencies correspond to electromagnetic radiation in the radio frequency (RF) range. If the sample under consideration is irradiated with RF which has same frequency as the MRI precessional frequency of the nuclei, a resonance effect is achieved. Under resonance conditions, energy is absorbed from the RF field resulting in distortion from the equilibrium magnetization, also referred to as excitation.

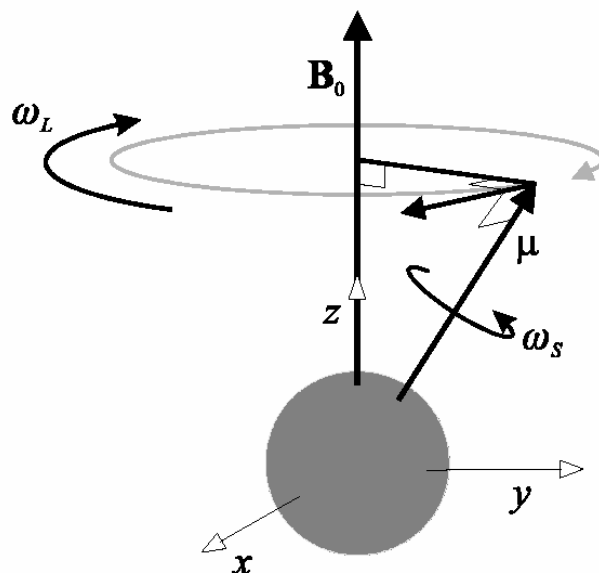


Figure 3.9 The precession of a non-parallel atomic magnetic moment μ around an external magnetic field B_0 at an angular frequency ω_L .

The detected signal in NMR spectroscopy results from the difference between the energy absorbed by the spins which excite a transition from the lower energy state to the higher energy state, and the energy emitted by the spins which simultaneously cause a transition from the higher energy state to the lower energy state. The signal is thus proportional to the population difference between the energy states. NMR is a sensitive spectroscopy since it is capable of detecting these very small population differences. It is the resonance, or exchange of energy at a specific frequency between the spins and the spectrometer, which gives NMR its sensitivity.

In order to perform an MRI experiment, radiation must be supplied to the protons in a specific sample at the frequency at which they will absorb the radiation. This frequency is

identical to the energy difference between the two possible alignment states, and in the case of a 1.5 T applied magnetic field, the frequency is 63.87 MHz (2×10^{-6} eV). Radiation is only applied for a short time and is referred to as a radiofrequency radiation (RF) pulse. After the sample is excited, it emits an RF signal that must be received and quantified in order to produce the MRI image. Transmission of the excitation pulse and the detection of the resulting RF signal are performed by the RF coil, which acts as both a transmitter and receiver. In each MRI study, a number of individual steps are required. A pulse sequence is selected, an image location is chosen, and image data is acquired in order to address specific questions relating to each individual case. Each pulse sequence is defined in order to determine how the magnetic field gradients are applied during image acquisition.

A magnetic field gradient can be superimposed on the static field by additional coils, causing a linear spatial variation of the magnetic field. These gradients, $G_r = \partial B / \partial r$, along with a static field introduce a spatial dependence (r) to the magnetic resonance frequency:

$$\omega(r) = -\gamma [B + r G_r] \quad (3.12)$$

In practice, various magnetic field gradients with different orientations may be applied along with RF excitation to obtain frequency data sets that can be processed into magnetic resonance images [94, 95]. Spin-echo (SE) sequence is one of the most common techniques used in MRI and is the one used in this study. Spin-echo uses two RF pulses and is thus primarily characterized by two time delays, the echo time (TE) and

the recovery time (TR). The signal intensity for each pixel of the MRI image is greatly influenced by the lengths of these time delays, which can be employed as variable experimental parameters. Figure 3.10 depicts the SE sequence in MRI [96].

Contrast in SE images is governed by the relative intensity of the pixels, represented as $I(r)$, and is expressed as (Equation 3.13):

$$I(r) \propto \rho(r) F_1[TR, T_1(r)] F_2[TE, T_2(r)] F_3[TE, G, D(r)] \quad (3.13)$$

where F_1 , F_2 , F_3 are termed contrast functions because they describe the signal attenuation for each pixel resulting from variations in local physical characteristics across the sample and $\rho(r)$ is the spin density of nuclei which assists in the characterization of solute (e.g. hexadecane in our experiments) distribution and diffusion. Thus F_1 , F_2 , F_3 attenuate the spin density depending on the local physical characteristics of the sample. Contrast function F_1 is due to T_1 relaxation caused by interactions between the nuclei and the overall sample [95, 97]:

$$F_1[TR, T_1(r)] = 1 - \exp[-TR/T_1(r)] \quad (3.14)$$

For values of $TR \gg T_1$, signal attenuation due to F_1 will be almost non-existent. Thus, by judicious choice of parameters, it is always possible to completely eliminate the effect of F_1 as long as sufficient time exists to perform a single MRI experiment.

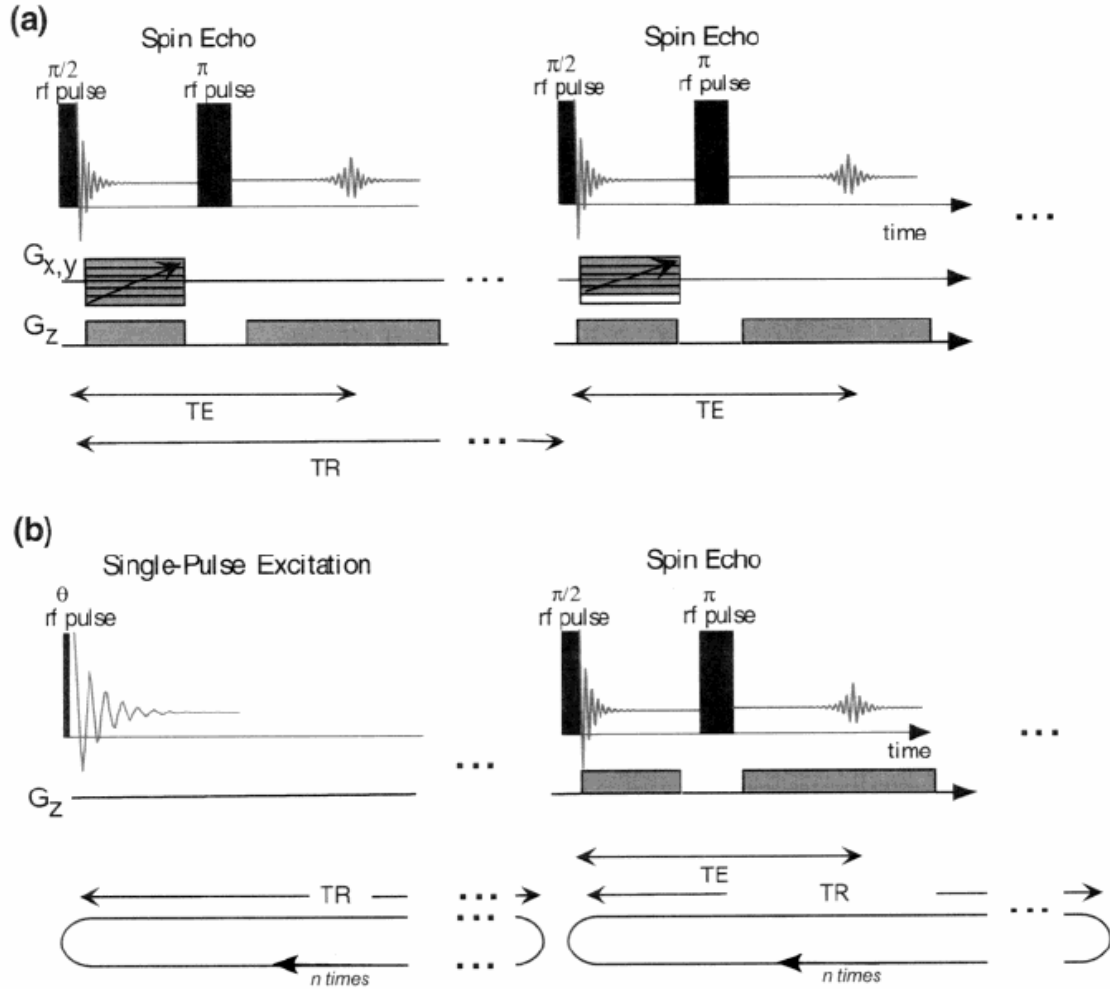


Figure 3.10 Experimental timing diagrams for the following: (a) the basic SE sequence. A magnetization echo is created using two RF pulses spaced by an adjustable $TE/2$. Recording of magnetic resonance images requires repetition of the basic sequence (as shown) separated by a repetition time, TR , using different settings of magnetic field gradients for subsequent sequences. (b) Variation of the basic sequence used for the calibration of image intensities with gravimetrically determined moisture contents. By subsequently recording the magnetization for a single-pulse excitation (no field gradients) and SE (field gradients set for an imaging experiment), the direct comparison of intensities may be used for construction of a calibration curve [96].

Contrast function F_2 is due to T_2 relaxation, caused by internuclear interactions [95, 97]:

$$F_2[TE, T_2(r)] = \exp[-TE/T_2(r)] \quad (3.15)$$

To minimize the effect of the F_2 contrast function, TE can be set as small as experimentally possible. Because of scanner hardware limitations, TE can not be set too short or the signal attenuation due to F_2 will be eliminated. Contrast function F_3 is due to molecular diffusion, displacement of molecules due to Brownian motion, or other type of random mass transport. While it is not possible to eliminate the contribution of F_3 , the signal attenuation due to F_3 is low for samples with a low concentration of bound fluid. This can be the case for hexadecane diffusion if there is no bound hexadecane in the paper. Equations for F_1 and F_3 are appropriate for a simple case where the solute (hexadecane) may exist in paper in a single well-defined environment.

To obtain quantitative information from the MRI images recorded using the SE sequence, the contrast functions (F_1, F_2, F_3) must be reduced to unity so that the measured signal intensity is directly proportional to spin density and therefore to hexadecane concentration, i.e. $I(r) \propto \rho(r) \propto \text{Hexadecane Conc.}$ Unfortunately, it is difficult to reduce contrast functions to unity because imaging sequences that can do so return weak signal intensities. An acceptable way to address this issue is to use the standard SE sequence but to obtain a relationship between measured signal intensity and the gravimetrically determined hexadecane concentration [96, 98]. The calibration curve thereby obtained can be used to establish the hexadecane concentration by measuring the signal intensity at a particular point. Thus, quantification of the MRI image can be achieved via a calibration curve under the assumption that the paper matrix volume does

not change significantly with hexadecane absorption, which in this case is a reasonable assumption. The equation obtained from polynomial fitting of the calibration curve was used to convert experimental image intensities to actual hexadecane concentrations.

3.7.2 MRI Experimental Conditions

All experiments were performed in a magnetic field of 9.4 T using a Bruker DSX-400 NMR spectrometer with a microimaging accessory (Bruker Biospin GmbH, Rheinstetten, Germany). Standard SE imaging sequences were employed. Using a 10 mm RF coil, 90° pulse lengths of 200 μs and 180° pulse lengths of 1000 μs were achieved. Experiments were performed using 90° “hard” RF pulses and 180° Gaussian-shaped pulses with gradients switched off; thus, two dimensional (2D) images correspond to 2D projections of the hexadecane concentration across the entire sample width. A matrix of 32×32 complex data points was recorded using 32 gradient steps and a spectral width of 50 kHz. Because the through-plane hexadecane distribution is of interest, the magnetic field gradients were set to provide higher resolution in this direction. The field of view in the direction parallel to the paper surface (in-plane, x-direction) was 20 mm, while the field of view in the direction perpendicular to the paper surface (through-plane, z-direction) was 3 mm. MRI data were analyzed using the XWIN NMR and ParaVision software packages supplied with the spectrometer. Additional data processing was completed using a personal computer with IGOR Pro (Wave Metrics, Inc., Lake Oswego, OR). The acquired data was also processed using MATLAB.

3.8 Thick Handsheet Preparation

For most of this thesis, normal copy paper was used as the substrate (thickness $\sim 100\ \mu\text{m}$). After coating the sample with a fluorocarbon film, the thickness of the coated paper sample was still $100\ \mu\text{m}$. Magnetic Resonance Imaging systems used to image material has a resolution of about $25\ \mu\text{m}$, i.e., one pixel of the image is generated for a film depth of $25\ \mu\text{m}$. Using a coated copy paper sample for grease barrier studies in an MRI system would result in very few data points for the accurate tracking of grease transport. Therefore, thick paper sheets (known as hand sheets) were prepared for use as samples for grease barrier studies conducted in an MRI system.

A modified TAPPI standard method T 205 – sp02 was used to prepare the samples of paper for use in MRI studies [67]. Before making a handsheet, it was important to set a basis weight of the sheet desired. *Basis weight* is defined as the weight in grams of one sheet of paper that is one square meter in area and, therefore, has units of g/m^2 . It was determined through preliminary studies that a basis weight of $900\ \text{g/m}^2$ would yield a handsheet thickness of 1.5-1.7 mm (after drying) when using a standard 159-mm-diameter sheet machine. Thus, the basis weight of the handsheets was fixed at $900\ \text{g/m}^2$. A British Handsheet mold was used. It consisted of a nominal 12 liter, 159-mm diameter cylindrical container set above a wire mesh grid plate fitted with an 80-mesh screen supporting a 120-mesh stainless steel gauze. Drainage occurs via a hand-operated valve into a vacuum leg 800 mm long ending in a siphon chamber. Forming wire (80-mesh

screen) is the surface on which the wet sheet is deposited during drainage. The weight of pulp required to form a 159-mm diameter sheet was calculated as follows:

Screen size (D) = 0.159 m

Screen Area (A) = $\pi D^2/4 = 0.0198 \text{ m}^2$

Wt. of pulp required = Basis Weight x Screen Area

For a basis weight of 900 g/m², wt. of pulp required = $0.0198 \times 900 = \underline{17.82 \text{ g}}$

If 17.82 g of pulp is mixed with 4.45 L of nanopure water, the consistency of the resulting pulp-water mixture can be calculated as follows (Equation 3.16):

$$\text{Consistency} = \frac{f}{f + w} \quad (3.16)$$

where ‘f’ is the weight of the fiber (pulp) and ‘w’ is the weight of water in the mixture. Thus, if fiber weight is 17.82g and water weight is 4450 g (assuming water density = 1000 g/L), then the consistency of resulting pulp mixture would be 0.4 % [=17.82/(17.82 + 4450)].

The following procedure was used to form the handsheets [67]:

- 1) Previously weighed pulp sheet was torn into small pieces (< 1 inch pieces) and soaked in nanopure water overnight.

- 2) Pulp mixture is disintegrated in a standard disintegrator at 3000 rpm until all fiber bundles are dispersed. After disintegration, the stock should be well stirred to ensure good dispersion.
- 3) After cleaning the forming screen of the paper machine, the machine should be half filled with water. The entire stock prepared (4.45 L of 0.4% consistency) is poured into the sheet machine. Additional water should be added until the depth is about 350 mm above the surface of the forming wire.
- 4) After mixing the pulp with a perforated stirrer, fully open the drain of the machine with a rapid movement and let the water drain through the sheet under suction from the water leg. The result is a wet thick sheet of paper formed on the forming screen.
- 5) With two sheets of blotting paper placed on the top of formed handsheet, place a couch plate on top of the blotting papers. Set the couching roll in the middle, and rotate back and forth to remove excess water (water gets absorbed by blotting paper).
- 6) With a blotting paper on the top, press the handsheet between weights in a press. The sheet should be first pressed at a pressure of 50 psi for 5 minutes. With the old blotting paper replaced with a dry one, press again at a pressure of 50 psi for 2 minutes.
- 7) The semi-dry sheet obtained after pressing is then restraint dried in air (50% RH, 23°C atmosphere) by placing the sheet into a drying ring, assembled so that each test sheet is uppermost and in contact with the rubber seat of the next ring above

it. With a heavy weight on top of the stack of rings, the sheet is left to dry for 24 – 48 hrs.

8) The dried sheet is then left in a 50% RH environment until use.

While tests were conducted on the pulp to obtain its freeness, steps were taken to generate pulps of different freeness using the valley beater method [99]. Freeness of pulp is a measure of the rate at which a dilute suspension of pulp may be dewatered. The drainage rate, or freeness, has been shown to be related to the surface conditions and swelling of the fibers, and is a useful index of the amount of mechanical treatment given to the pulp [100]. It should be noted that the higher the beating action (i.e. more the refining of the fibers), the lower the freeness of the pulp because dewatering takes a longer time. A sheet made from a high freeness pulp will have a higher porosity than a sheet made from low freeness pulp.

In a valley beater method, a measured amount of pulp of specified stock concentration is beaten between the roll bars and the bedplate of a laboratory beater. Samples are withdrawn at regular intervals during treatment to determine their beating degree (freeness) and to be made into laboratory handsheets for evaluation [99]. Both hard and soft wood pulp were refined in a valley beater using TAPPI standard T 200 sp-01 method. Freeness of all the samples was measured using TAPPI standard T 227 om-99 method. After different sheets were formed using TAPPI standard T 205 sp-02 method, sheet porosity, thickness and roughness were measured in a paper testing laboratory (IPST, Georgia Institute of Technology).

3.9 Fluorocarbon Coating Depth in Paper

In order to understand the effect of fluorocarbon coatings on paper surfaces and to determine the extent of the barrier properties provided by the coating, it is important to have an estimate of how deep the fluorocarbon coating penetrates the porous structure of paper during plasma thin film deposition. To obtain the information on coating depth and to probe the coating and paper interface, photoacoustic spectroscopy was used.

As discussed previously, Fourier transform infrared (FT-IR) spectroscopy is used to obtain absorbance spectra of samples. In many cases, however, direct analysis of “as received” samples by transmission or reflection methods is not practical because the sample either transmits inadequate light for accurate measurements or it lacks suitable surface or particle size conditions for reflectance spectroscopies. In other cases, reflectance spectroscopies may not probe deeply enough into the sample to yield the desired information. Photoacoustic spectroscopy (PAS) is unique as a sampling technique because it does not require that the sample be transmitting. PAS has low sensitivity to surface conditions, and can probe over a range of selectable sampling depths from several micrometers to more than 100 μm [101-103]. PAS directly measures infrared (IR) absorption by sensing absorption-induced heating of the sample within an experimentally controllable sampling depth below the sample surface. Heat deposited within this depth transfers to the surrounding gas at the sample surface, producing a thermal-expansion driven pressurization in the gas, known as the PAS signal, which is detected by a

microphone. The magnitude of the PAS signal varies linearly with increasing absorptivity, concentration or sampling depth until at high values of their product a gradual roll off in sensitivity (saturation) occurs. The phase of the PAS signal corresponds to the time delay associated with heat transfer within the sample.

PAS signal generation is initiated when the FT-IR beam, which oscillates in intensity, is absorbed by the sample resulting in the absorption-induced heating in the sample and oscillation of the sample temperature. The temperature oscillations occurring in each light-absorbing layer within the sample launch propagating temperature waves called thermal-waves, which decay strongly as they propagate through the sample. It is this thermal-wave decay process that defines the layer thickness, or sampling depth, from which spectral information is obtained in FT-IR PAS analysis. The sampling depth can be increased by decreasing, via FT-IR computer control, the IR beam modulation frequency imposed by the interferometer. The lower modulation frequency allows a longer time for thermal-waves to propagate from deeper within the sample into the gas. As the sampling depth increases, the saturation of strong bands in PAS spectra increases analogous to those in absorption spectra measured by IR transmission as sample thickness increases. The photoacoustic signal contains information on the sample absorption spectrum and on the depth below the sample surface from which the signal evolves, thus allowing materials with layered or gradient compositions to be studied. Photoacoustic signal generation can be modeled assuming an optically and thermally homogeneous slab sample geometry which is thick on the scale of the thermal-wave decay length with the

rear sample face thermally grounded and optically nonreflective [101]. Figure 3.11 shows a schematic of signal generation in PAS.

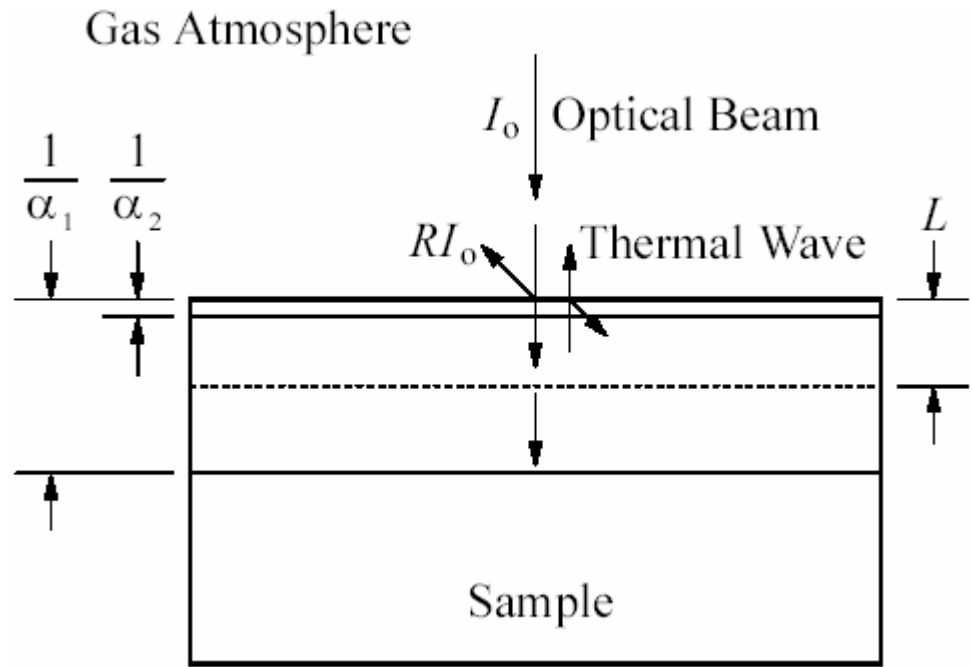


Figure 3.11 One-dimensional signal generation schematic showing the decay length, L , for thermal-waves and the optical decay lengths for lower (α_1) and higher (α_2) values of absorption coefficient. As α increases, more of the absorption occurs in the region near the sample's surface that is active in signal generation [101].

The depth (L) over which the thermal signal is generated is directly related to the modulation frequency (f) as (Equation 3.17):

$$L = \frac{\alpha}{\pi f} \quad (3.17)$$

where α is the thermal diffusivity of the material. Thus, depth dependent information can be obtained easily by varying the modulation frequency [101, 104].

Spectra were collected on both uncoated and fluorocarbon coated paper samples. The photoacoustic spectroscopy experiments were carried out on an IFS-55 FTIR spectrometer (Bruker) with an MTEC 300 photoacoustic detection module. Helium gas (>99.99 %) was used as the photoacoustic transfer gas. The spectra were collected over the range $4000 - 400 \text{ cm}^{-1}$ with a resolution of 5 cm^{-1} . Modulation frequencies were chosen in the range of 101 – 732 Hz and with an amplitude of $4\lambda_{\text{HeNe}}$.

3.10 Organic Vapor Quartz Crystal Microbalance Studies

A quartz crystal microbalance was used to study the absorption of hexadecane vapor by fluorocarbon films to assess the grease barrier properties of the fluorocarbon films. Hexadecane is a non polar lipophilic material with low surface tension and has been used previously as a grease (or oil) surrogate [30, 34]. To quantify the grease absorption of fluorocarbon films, hexadecane vapor sorption and desorption was studied on fluorocarbon films deposited on quartz crystals. Since hexadecane has a boiling point of 287°C at atmospheric pressure, it would be difficult to conduct the QCM experiments at 1 atm. To carry out hexadecane sorption and desorption experiments, a vacuum system, described below, was designed and built.

3.10.1 Vacuum QCM Design

A vacuum QCM system for hexadecane vapor experiments consisted of a 6-way stainless steel cross with quick flange (QF50) connectors at all six arms. These six connectors provided ports for attaching various instruments. Figure 3.12 shows the experimental configuration of the QCM system with all the relevant details. The six ports were fitted with the following attachments:

- 1) A pressure Transducer (Model: ConvecTorr, Varian, Inc.) was attached to measure the pressure inside the vacuum chamber (6-way cross). The transducer was connected to a Multi-Gauge™ Controller (Varian, Inc.) to obtain the chamber pressure at any time.
- 2) A nitrogen port to purge the system and to allow venting to atmospheric pressure.
- 3) A microsyringe (Valco, Inc.) to inject hexadecane (or other grease surrogate) into the vacuum system. The microsyringe (Series A-2, Valco) was a high precision syringe (1 µl least count) equipped with a push button valve to isolate the syringe from the vacuum chamber, thereby restricting hexadecane injection due to atmospheric pressure. The syringe was fitted in a female luer adapter attached to a tapped hole in a blank quick flange (QF50) through a valco fitting. This design ensured a vacuum tight fit.
- 4) A quartz window or view port was attached to the quick flange directly opposite the microsyringe port to monitor hexadecane injection.
- 5) A custom QCM sensorhead (ASF-241; Maxtek, Inc.) to hold the quartz crystal was fitted onto a 2 ¾" conflat flange for vacuum operation. The sensorhead

consisted of a crystal holder (vacuum side) which attached to sensor pinheads used to conduct the quartz crystal signal to the frequency counter (air side). The QCM sensorhead consisted of cooling water tubes (to cool the crystal holder if required) although they were not used in any of the experiments described in this thesis. Signals from the sensor head were sent to a frequency counter (XTM-2 Deposition Rate Monitor, Inficon, Inc.) which read the crystal frequency. The measured frequency was conveyed to a desktop computer through a RS-232 cable for data acquisition and calculations.

- 6) Finally, the bottom port was connected to a mechanical pump (2-stage rotary pump, Edwards) to evacuate the vacuum system. A throttle was connected between the system and the pump to isolate the system from the vacuum pump during experiments.

The above system was maintained under vacuum when not used for experiments to maintain a low base pressure. The following section describes the operation of the system.

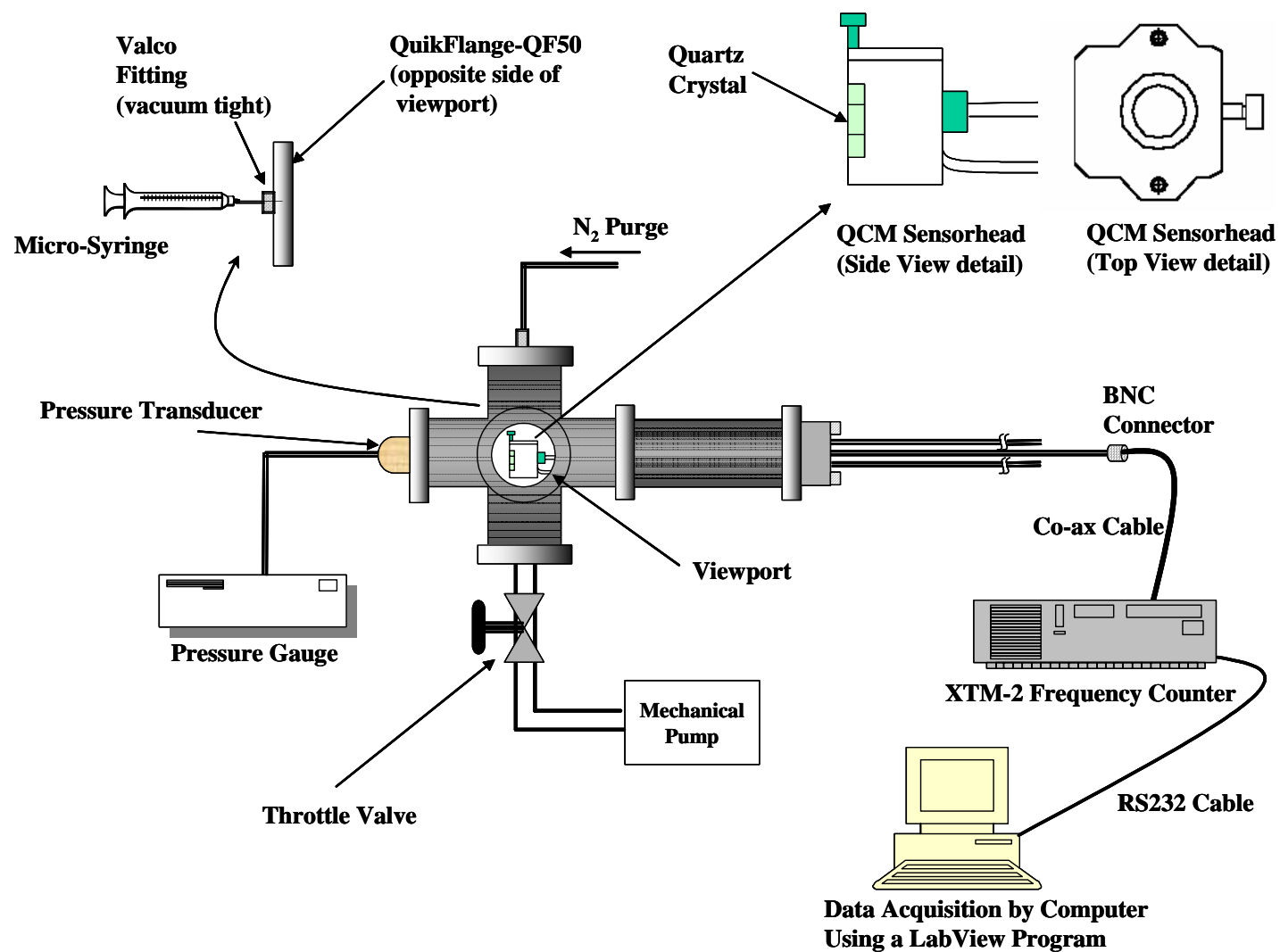


Figure 3.12 Experimental setup for organic vapor (Hexadecane) QCM system

3.10.2 QCM System Operation

The frequency of the blank quartz crystal was noted before depositing the fluorocarbon film onto the crystal (f_0 , Hz). The frequency of the crystal was noted again (f_1 , Hz) after the film was deposited. The difference between the frequencies corresponds to the mass of the film deposited as per the Sauerbrey equation described in section 1.5. After measuring the loaded crystal frequency, the crystal was placed in a crystal holder which was then inserted in the sensorhead. The sensorhead was inserted into the 6-way cross (also referred to as chamber) through its designated port. The chamber was then pumped down to the base pressure (between 4 -5 mTorr). A LabView program for QCM data acquisition developed by Rentian Xiong (ChBE, Georgia Institute of Technology) was used to acquire the real time frequency data. The program started collecting frequency data after the base pressure was achieved. Data was displayed in the form of a frequency versus time plot. When the program showed attainment of a stable frequency (invariant with time), the system was assumed to be in equilibrium with zero hexadecane concentration in the chamber.

While at base pressure and stable initial frequency, the throttle valve between the pump and the chamber was closed completely, isolating the chamber from the pump. At this point (referred to as $t = 0$), a known volume of hexadecane (as measured by graduation marks on the syringe) was injected into the system while observing the injection port through the view port. The program recorded the real time change in frequency (decrease in frequency) as hexadecane was absorbed into the fluorocarbon film. The point at which

there was no further change in frequency was referred to as establishment of equilibrium with the known concentration of hexadecane vapor. The data was continuously acquired for a longer period of time to ensure equilibrium. The pressure inside the chamber increased due to vapor pressure of hexadecane and was directly proportional to the mass of hexadecane injected (from the ideal gas law). This was the sorption phase of the experiment. During the desorption phase, the throttle valve between the pump and chamber was completely opened while purging the chamber with nitrogen. The program again recorded the real time change in frequency (increase in frequency) as hexadecane was desorbed from the fluorocarbon film. The data was acquired until no further change in frequency was observed (usually at complete desorption). The frequency versus time data for both sorption and desorption phases was imported into an EXCEL file and further analyzed.

4. FLUOROCARBON FILM DEPOSITION ON PAPER AND CELLULOSE USING PENTAFLUROETHANE AND OCTAFLUOROCYCLEBUTANE PRECURSORS

This chapter presents the results of fluorocarbon film deposition using pentafluoroethane (PFE) and octafluorocyclobutane (OFCB) as precursors with argon (Ar) as a carrier in each case. Some of the initial experiments in this work were conducted in a 4-cm electrode parallel plate system. Deposition rates and properties of the films obtained using PFE and OFCB as a precursor are presented in this chapter. For the majority of experiments described, a 6-inch electrode parallel plate plasma system was used. The deposition rates and properties of the fluorocarbon films obtained in the 6-inch system are presented in this chapter as well. For fluorocarbon film characterization, x-ray photoelectron spectroscopy and infrared spectroscopy were used to gain insight into the film composition and chemical bonding information of the deposited films. Film thickness was measured using spectroscopic ellipsometry. Scanning electron microscopy was used to assess evaluate the surface morphology before and after fluorocarbon film deposition on paper. It should be noted here that due to recent environmental concerns regarding the long atmospheric lifetimes of fluorocarbon monomers, a hydrofluorocarbon such a PFE (CF_3CHF_2) was used as the deposition precursor most of the times because it has relatively shorter atmospheric lifetime and does not produce environmentally detrimental degradation products [105].

4.1 Results

4.1.1 Fluorocarbon Film Deposition Rates on a 4-cm Parallel Plate System

Paper and cellulose are strongly polar due to hydroxyl groups, acetal and ether linkages (C-O-C) in their structures. The surface of paper consists of hydroxyl (-OH) groups thus rendering it hydrophobic in nature. Silicon substrates, upon exposure to oxygen or air, oxidize to form silicon dioxide (SiO_2). In the presence of moisture, the native oxide formed in the presence of water vapor has hydroxyl functionalities on the surface, making the surface of silicon hydrophilic. Thus, while the silicon and paper substrates are materially different, their surfaces are essentially similar in functionality. Therefore, plasma deposition on silicon wafers is comparable to that on paper or cellulose. Fluorocarbon films were deposited on paper and cellulose. Since it is difficult to measure film thicknesses on paper, a piece of Si was included along with the paper samples to enable film thickness measurement using ellipsometry.

Initially, on the 4-cm system, four different RF power levels of 20 W, 30 W, 40 W, and 50 W were used which correspond to power densities of 1.58 W/cm^2 , 2.38 W/cm^2 , 3.17 W/cm^2 and 3.96 W/cm^2 , respectively, based on the flat electrode area. Other deposition conditions were fixed (Pressure = 1 Torr; $T_{\text{BottomElectrode}} = 120 \text{ }^\circ\text{C}$; PFE flowrate = 20 sccm; Argon flowrate = 75 sccm). After fluorocarbon film deposition, film thicknesses were measured on the silicon wafer. Deposition rate was defined as the ratio of the film

thickness to the deposition time. Initially, all the films were deposited for a period of 5 minutes.

Figure 4.1 presents the fluorocarbon deposition rate as a function of RF power where PFE was used as the precursor. It is clear that as the RF power (all other conditions constant) increases, the deposition rate of the fluorocarbon film also increases. It can be seen from the figure that the deposition rate increases more slowly as the RF power is increased. This trend can be attributed to simultaneous deposition and etching reactions taking place on the surface. At higher powers increased etching appears to occur because of the increased concentration of fluorine radicals, leading to slower increases in the deposition rates with power. It is possible that at very high power (above the limits of our equipment), the etching and deposition rates may equal each other leading to no further increase in deposition rate with power. An RF power of 30 W was used in most of the experiments in the 4-cm parallel plate system.

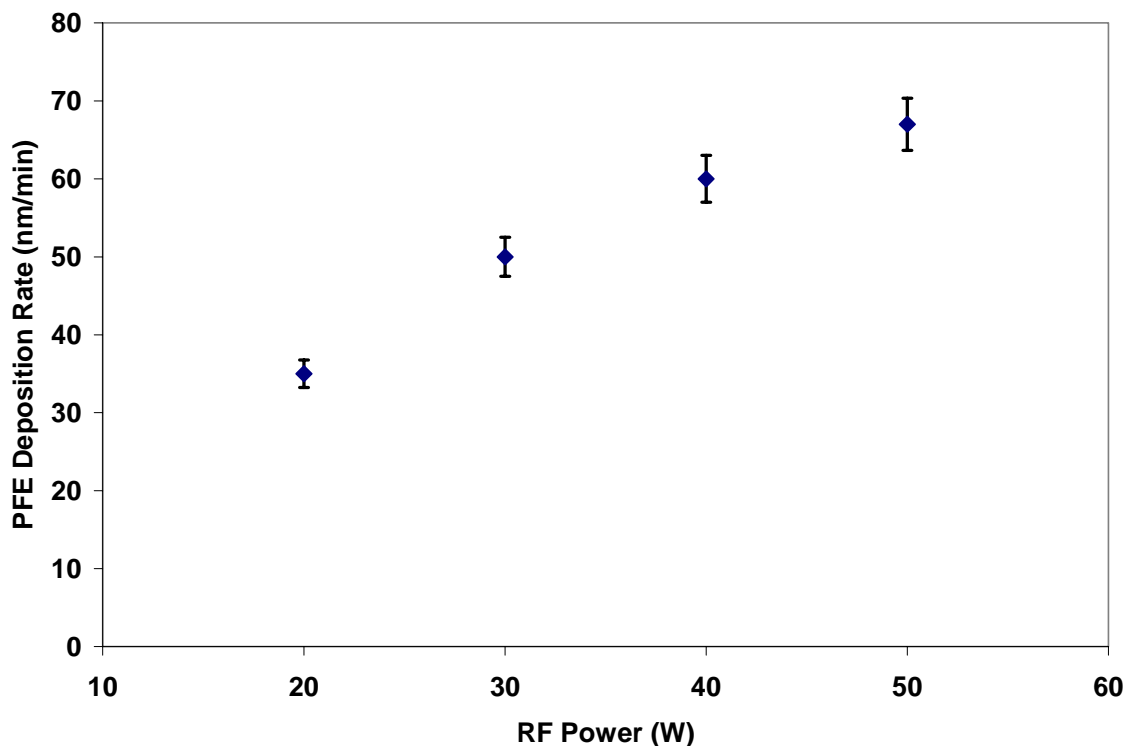


Figure 4.1 Deposition Rate of PFE (nm/min) with varying RF Power [$P = 1$ Torr; $T_{\text{BottomElectrode}} = 120$ °C; PFE flowrate = 20 sccm; Ar flowrate = 75 sccm; 4-cm electrode area].

The deposition rate with PFE was also studied as a function of substrate temperature during deposition. While 120 °C was used as the substrate temperature in most of the experiments, some of the samples were deposited at a temperature lower than 120 °C (e.g 90 °C) to inhibit sample degradation at higher temperatures. The fluorocarbon film was deposited at four different temperatures: 90, 120, 150, and 180 °C. Figure 4.2 presents the PFE deposition rate as a function of temperature. Other deposition conditions were held constant ($P = 1$ Torr, RF = 30 W; PFE flowrate = 20 sccm; Ar flowrate = 75 sccm). It can be seen from the figure that as substrate temperature increases, the deposition rate decreases. This suggests that film deposition is controlled by reactant adsorption on the

surface (rate determining step). The deposition rate versus substrate temperature data is replotted in Figure 4.3 in the form of the natural log of deposition rate versus inverse of temperature on an absolute scale. A least square line is fitted to the data using linear regression. The positive slope ($-E_a/R$) of the line indicates a negative activation energy; thus, reactant adsorption is the rate limiting step in fluorocarbon deposition. The apparent activation energy (slope times the universal gas constant, R) for the fluorocarbon deposition is calculated to be -12.17 kJ/mol.

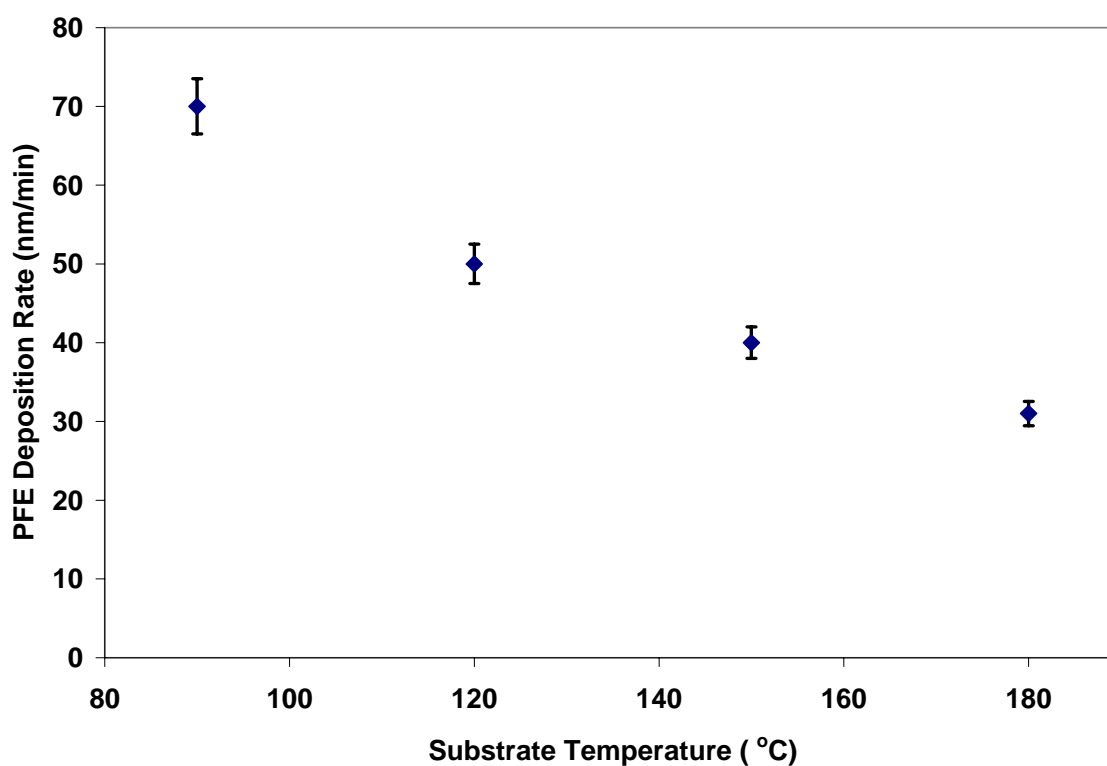


Figure 4.2 Deposition rate of PFE (nm/min) with varying substrate temperature (°C) [Other deposition conditions constant: $P = 1$ Torr; $RF = 30$ W; Ar flowrate = 75 sccm; PFE flowrate = 20 sccm]

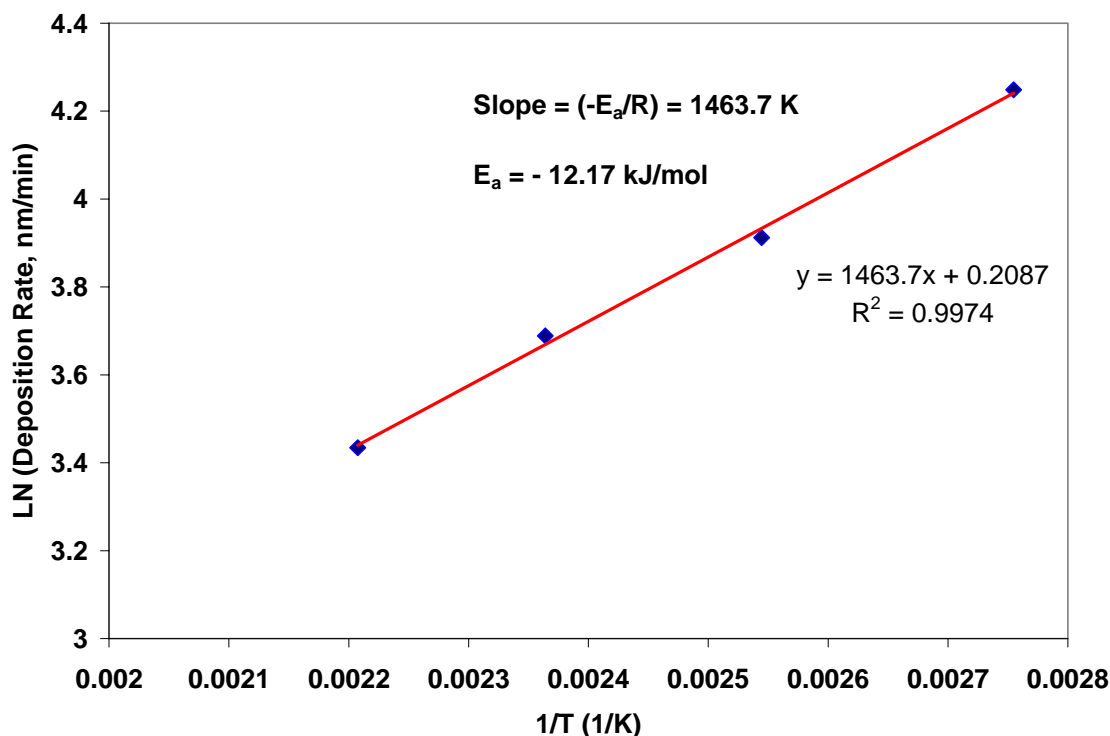


Figure 4.3 Arrhenius plot for PFE film deposition [P = 1 Torr; RF = 30 W; Ar flowrate = 75 sccm; PFE flowrate = 20 sccm]

Like PFE, deposition rates using octafluorocyclobutane (OFCB, C_4F_8) as the precursor were also studied at RF power levels of 20 W, 30 W, 40 W, and 50 W. Other deposition conditions were fixed (Pressure = 1 Torr; $T_{\text{BottomElectrode}} = 120 \text{ }^\circ\text{C}$; OFCB flowrate = 15 sccm; Argon flowrate = 75 sccm). After fluorocarbon film deposition, the film thickness was measured on a silicon wafer. Again, all films were deposited for a period of 5 minutes initially. Figure 4.4 presents the fluorocarbon deposition rate as a function of RF power where OFCB was used as the precursor. It is clear that as the RF power (all other conditions constant) increases; the deposition rate of the fluorocarbon film also increases.

Again, it can be seen from the figure that the relative increase in deposition rate is lower at higher power levels for the reasons explained previously.

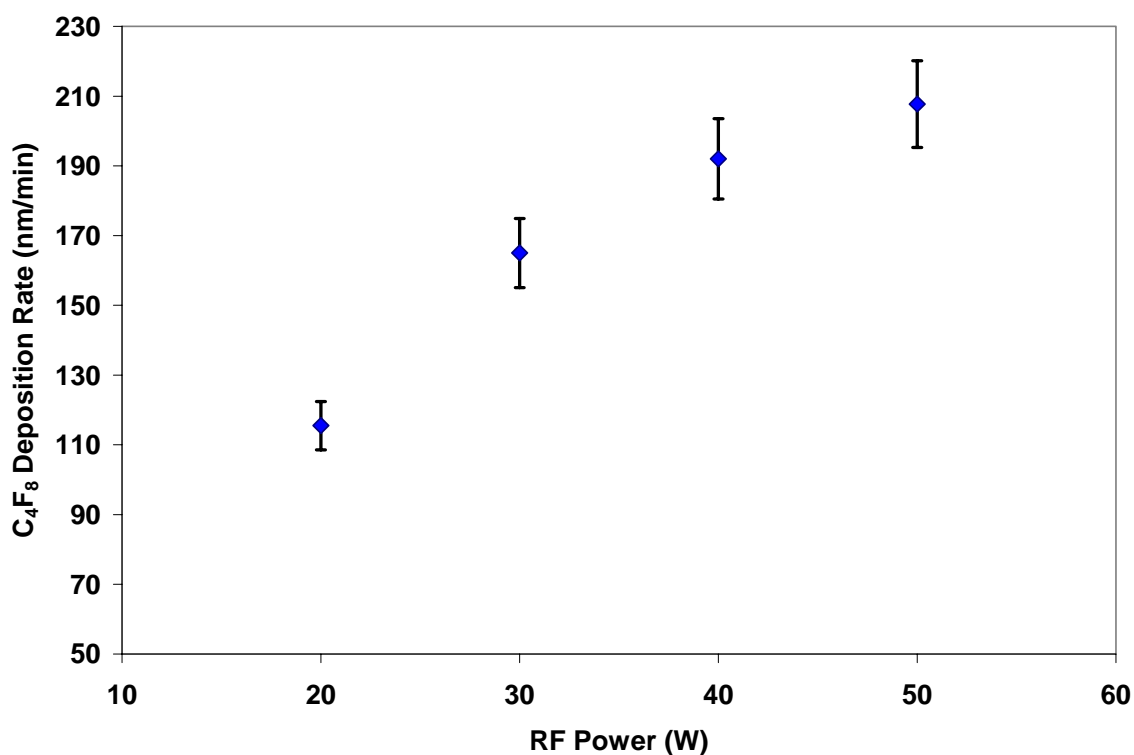


Figure 4.4 Deposition Rate of OFCB (nm/min) with varying RF Power [P = 1 Torr; $T_{\text{BottomElectrode}} = 120\text{ }^{\circ}\text{C}$; OFCB flowrate = 15 sccm; Ar flowrate = 75 sccm; 4-cm electrode area].

The deposition rate with OFCB also decreases with increasing substrate temperature indicating that reactant adsorption is the rate limiting step. Figure 4.5 presents the OFCB deposition rate as a function of temperature. Other deposition conditions were held constant (P = 1Torr, RF = 30 W; OFCB flowrate = 15 sccm; Ar flowrate = 75 sccm).

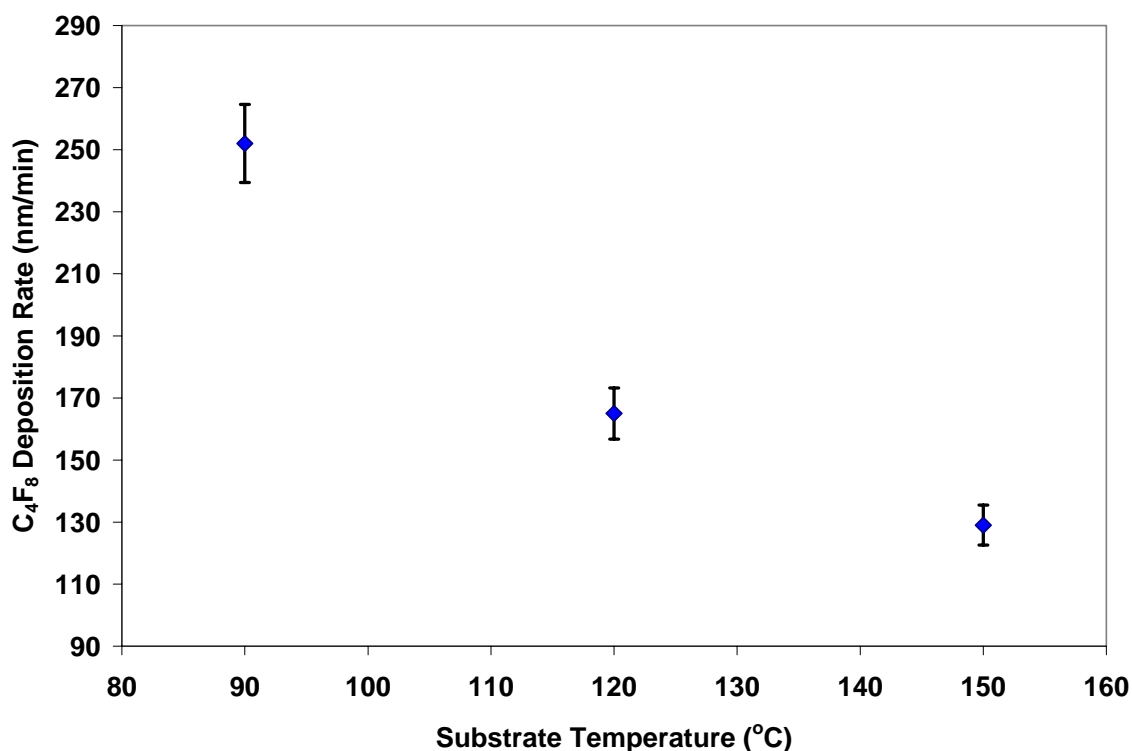


Figure 4.5 Deposition rate of OFCB (nm/min) with varying substrate temperature (°C) [Other deposition conditions constant: P = 1 Torr; RF = 30 W; Ar flowrate = 75 sccm; OFCB flowrate = 15 sccm].

The deposition rate versus substrate temperature data is replotted in Figure 4.6 in the form of natural log of deposition rate versus inverse of temperature. The slope of the line ($-E_a/R$) is shown in the figure. The apparent activation energy for fluorocarbon deposition from the OFCB precursor is calculated to be -14.32 kJ/mol. The difference between the activation energies of PFE and OFCB film deposition rate is possibly due to different dissociation chemistry of the two precursors which leads to generation of different dissociation fragments that adsorb differently on the substrate. It was difficult to accurately calculate the power density in the 4-cm electrode diameter parallel plate system because the plasma extended along the metal column above the top electrode,

thereby increasing the effective electrode area. In the 6-inch parallel plate system, the glow region was confined between the two electrodes, therefore, the power density in the system could be more accurately determined.

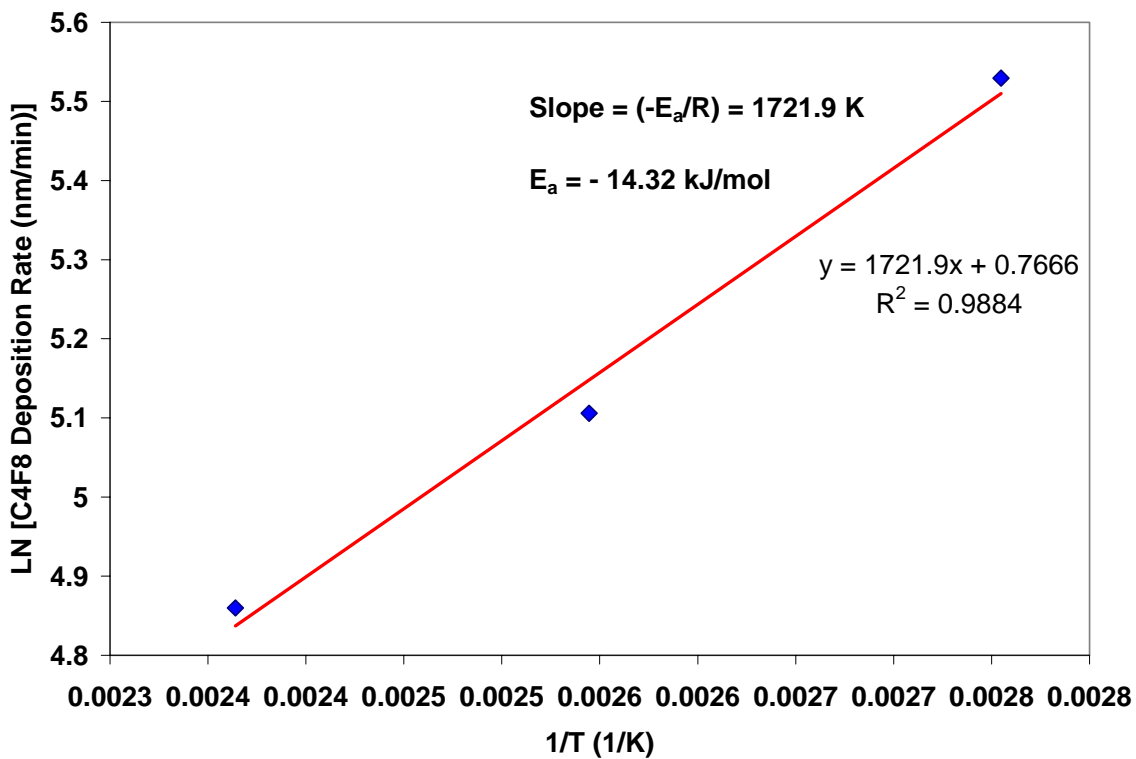


Figure 4.6 Arrhenius plot for OFCB film deposition [P = 1 Torr; RF = 30 W; Ar flowrate = 75 sccm; OFCB flowrate = 15 sccm]

All the experiments performed in the 6-inch parallel plate system used PFE as a precursor and Ar as the carrier gas. The deposition rates in a 6-inch system were approximately three times those in a 4-cm system when compared at varying temperature and RF power;

overall, the rates followed similar trends. The difference in deposition rates can be attributed to difference in reactor sizes and difference in RF power densities.

With increasing RF power, PFE deposition rate also increased in the 6-inch system. Four different RF power levels (75 W, 100 W, 125 W, and 150 W) were used which correspond to power densities of 0.41 W/cm^2 , 0.55 W/cm^2 , 0.69 W/cm^2 and 0.82 W/cm^2 , respectively (6" electrode diameter). Figure 4.7 presents the PFE deposition rate as a function of applied RF power.

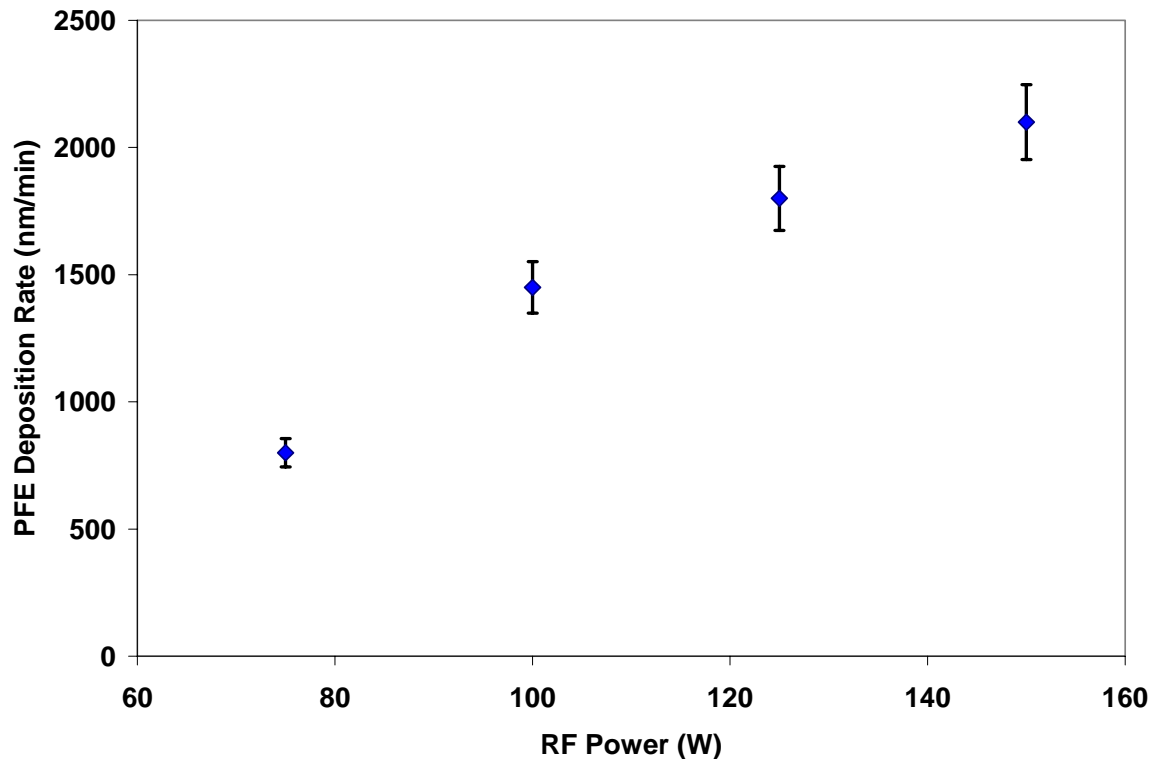


Figure 4.7 Deposition Rate of PFE (nm/min) with varying RF Power [P = 1 Torr; $T_{\text{BottomElectrode}} = 120 \text{ }^{\circ}\text{C}$; PFE flowrate = 20 sccm; Ar flowrate = 75 sccm; 6-inch electrode area].

As the substrate temperature increases (keeping other conditions constant), PFE deposition rates decreased. This trend is similar to the one obtained for PFE in the 4-cm parallel plate system. Figure 4.8 presents the PFE deposition rate as a function of substrate temperature. After replotting the deposition rate versus temperature data as an Arrhenius plot, the apparent activation energy was calculated to be -14.20 kJ/mol (see Figure 4.9). The calculated activation energy in a 6-inch parallel plate is different when compared to activation energy in a 4-cm parallel plate system. This is possibly due to difference in RF power densities in the two systems.

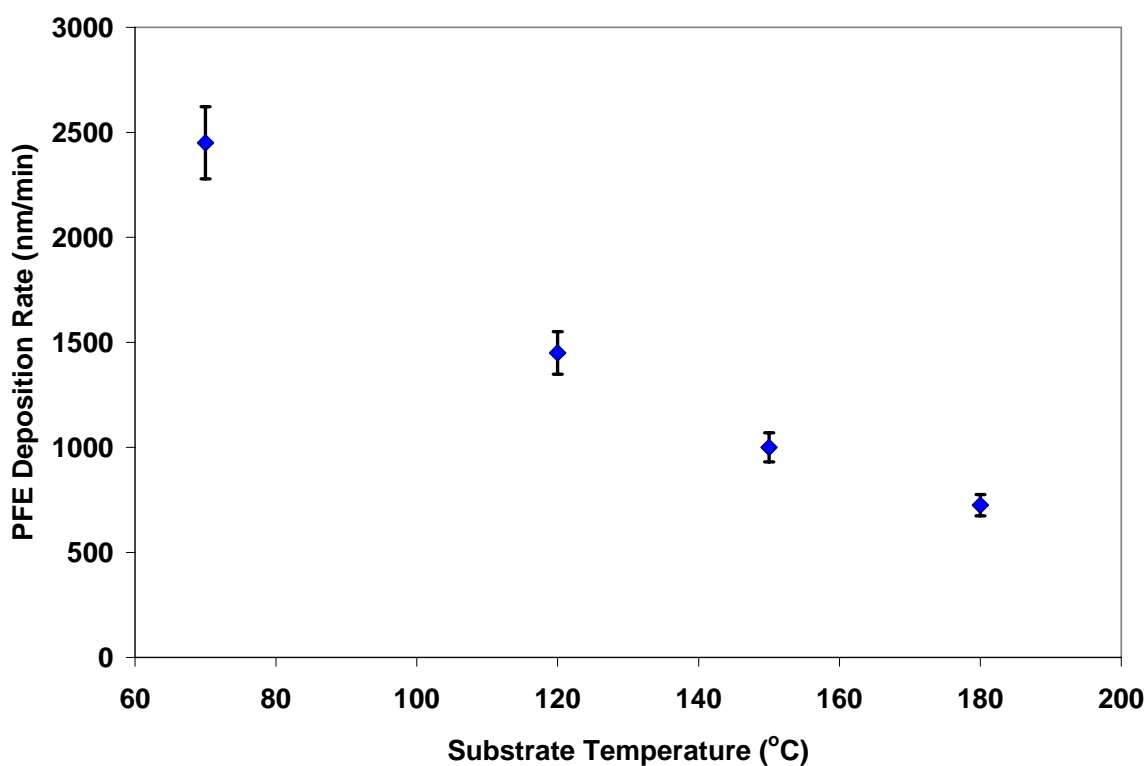


Figure 4.8 Deposition rate of PFE (nm/min) with varying substrate temperature (°C) [Other deposition conditions constant: P = 1 Torr; RF = 100 W; Ar flowrate = 75 sccm; PFE flowrate = 20 sccm].

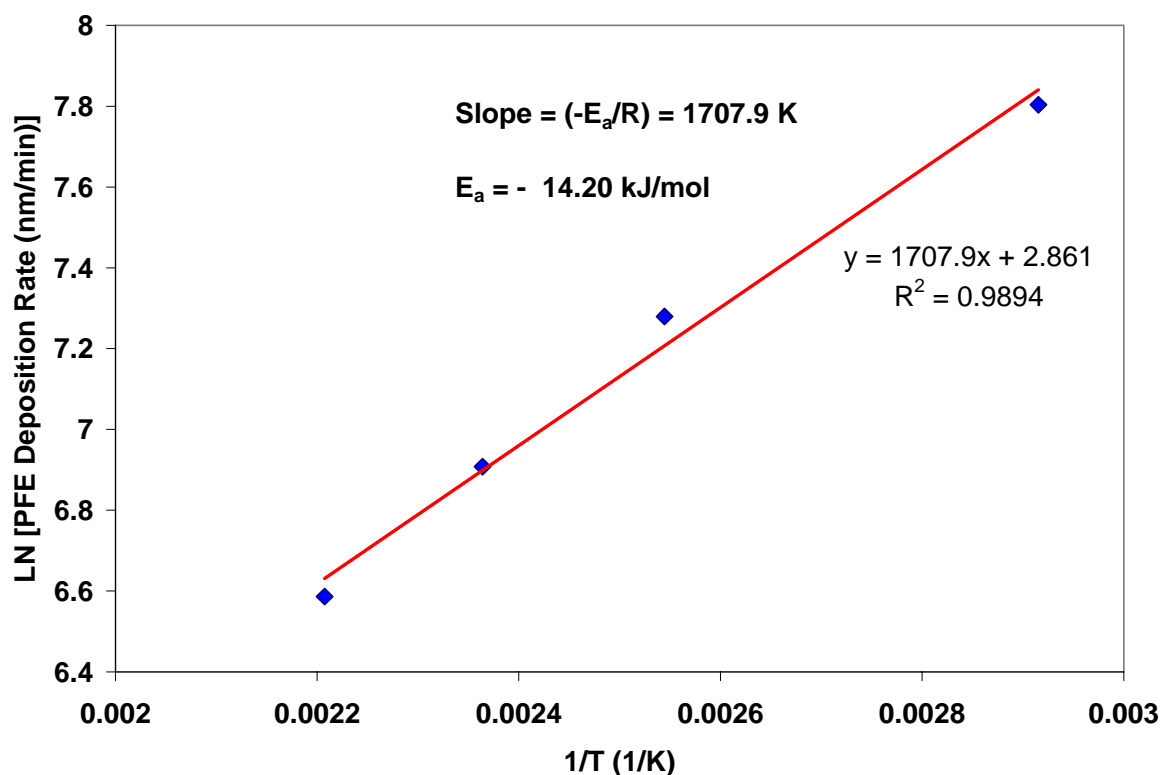


Figure 4.9 Arrhenius plot for PFE film deposition [P = 1 Torr; RF = 30 W; Ar flowrate = 75 sccm; PFE flowrate = 20 sccm; 6-inch electrode size]

4.1.2 XPS studies on Fluorocarbon Films

XPS studies were performed on fluorocarbon films deposited on both cellulose and Si wafers. Survey scans (Figure 4.10) of cellulose indicated the presence of C and O peaks, which is consistent with cellulose composition $[(C_6H_{10}O_5)_n]$.

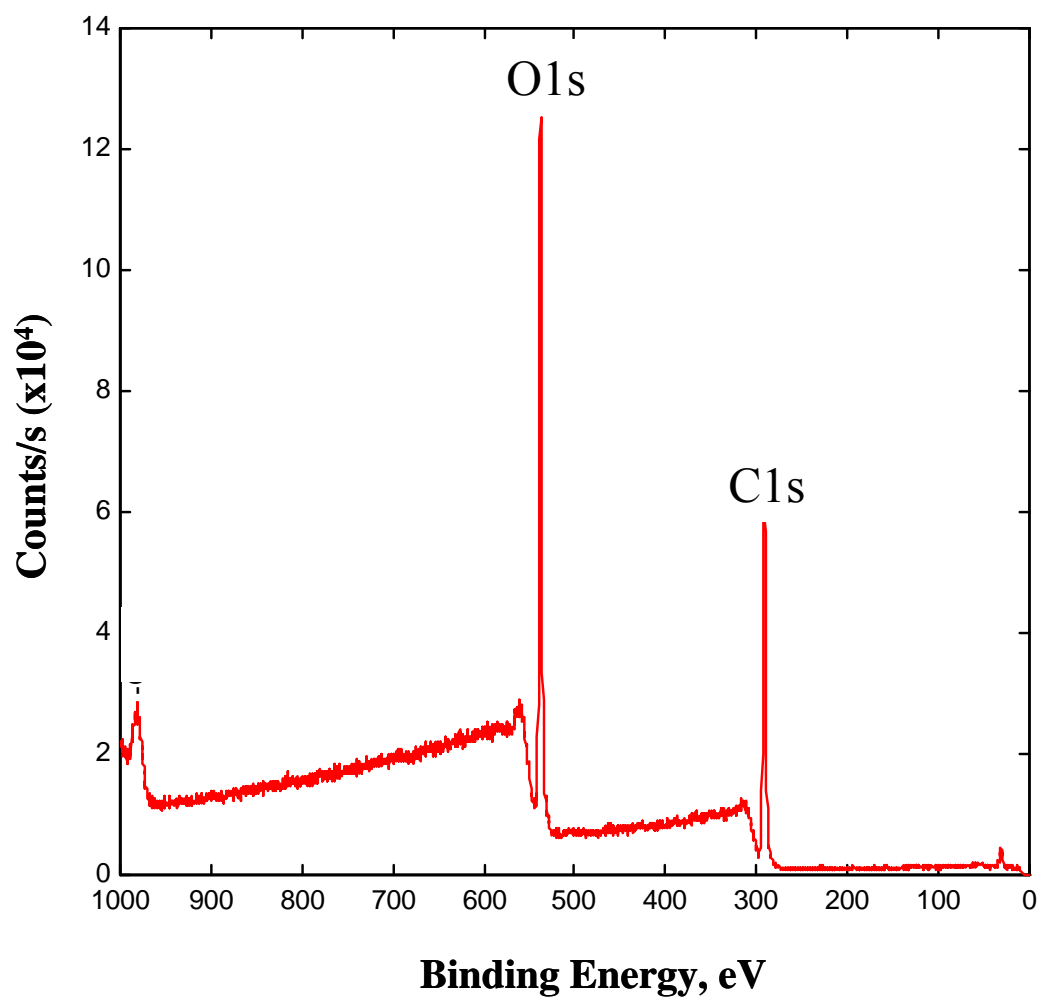


Figure 4.10 XPS survey scan of cellulose showing carbon and oxygen peaks

Cellulose is a linear polysaccharide polymer with many glucose monosaccharide units as shown in Figure 4.11 [106].

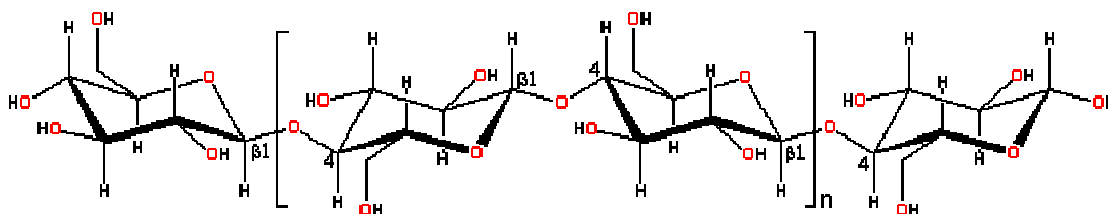


Figure 4.11 Structure of cellulose consists of long polymer chains of glucose units connected by a *beta-acetal* linkage [106].

A high resolution C1s scan was also collected to determine the bonding structures present on the cellulose surface. Figure 4.12 presents the C1s spectrum deconvoluted into four Gaussian peaks corresponding to C-C or C-H (285 eV), C-O (287 eV), C=O (288.5 eV), and C≡O (289.5 eV) with FWHM of 1.8 eV. The order of these peaks in terms of increasing binding energy matches that observed by other authors, who propose four different types of bonds on cellulose surfaces [107-109].

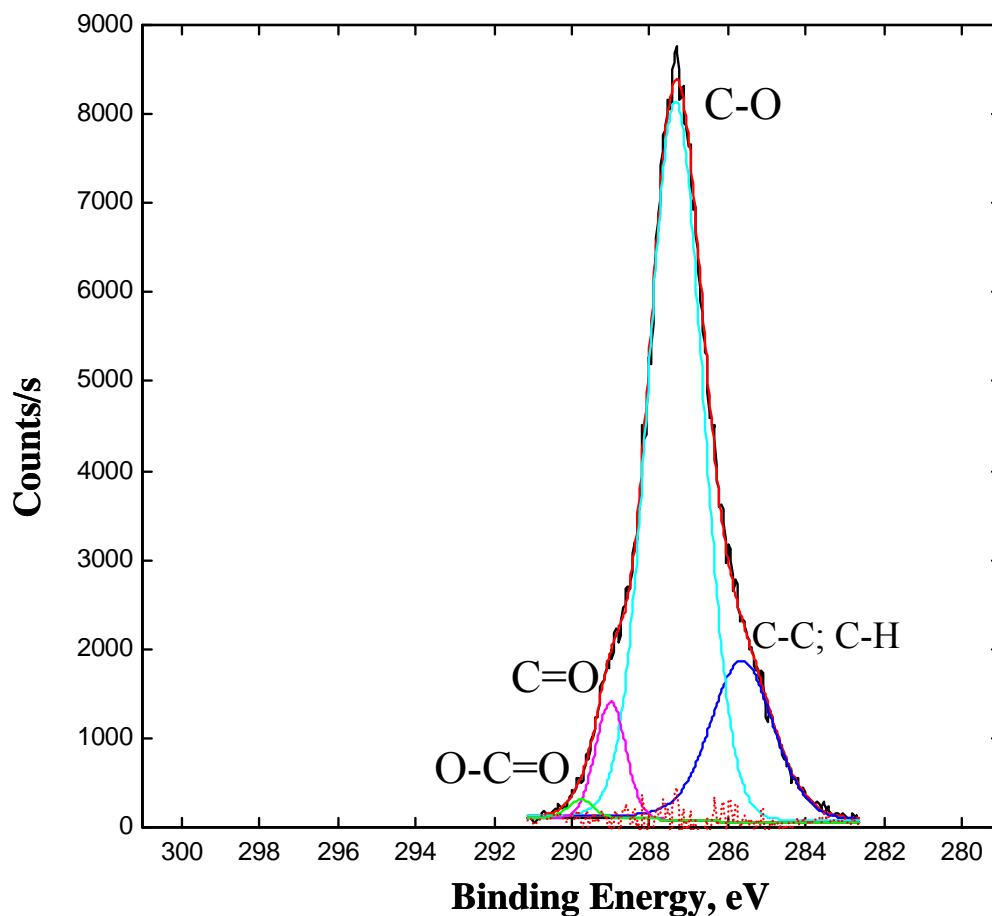


Figure 4.12 Cellulose C1s peak deconvoluted into four Gaussian peaks corresponding to C-C or C-H, C-O, C=O, O-C=O.

After fluorocarbon film deposition using PFE as a precursor, XPS data was collected to study the surface composition and bonding information. A survey scan of a fluorocarbon coated cellulose sample indicated the presence of carbon, fluorine and a small amount of oxygen, as indicated in Figure 4.13.

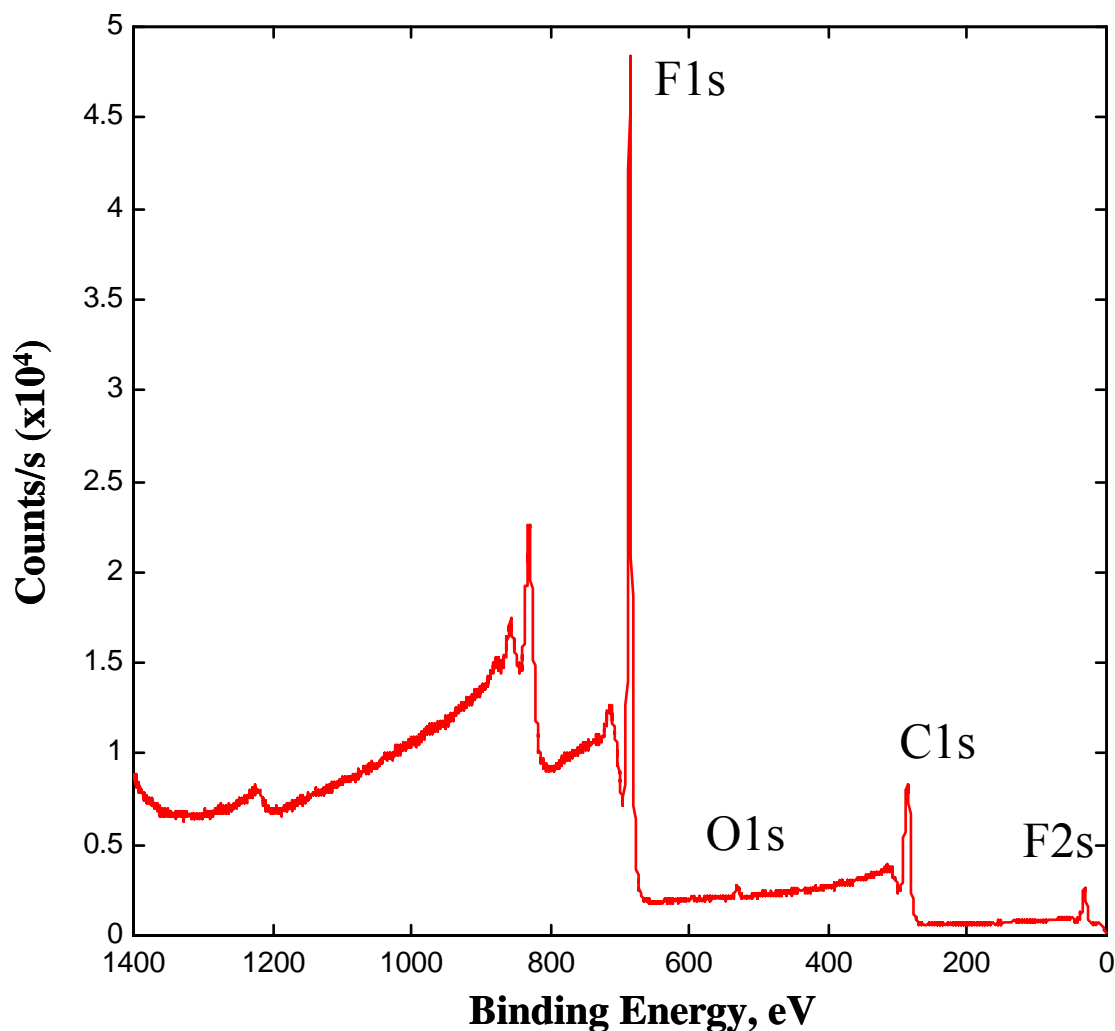


Figure 4.13 Survey scan of fluorocarbon film deposited from PFE showing C1s, F1s, and O1s peaks.

A high resolution scan was conducted to gather bonding information. Since the oxygen content in fluorocarbon films was low, the C1s spectrum was deconvoluted into five Gaussian peaks corresponding to CF₃ (293 eV), CF₂ (290.9 eV), CF (288.5 eV), C-CF_x (286.5 eV), and C-C or C-H (284.9 eV) with a constant FWHM of 1.6 eV. These assigned binding energies are within the range of published literature values as shown in Table 4.1.

Table 4.1 Published literature values of absolute binding energies [19, 110-115].

Peak/Group	Binding Energy range, eV
CF ₃	292.6 – 295
CF ₂	290.3 – 293
CF	288 – 290
C-CF _x	285.5 – 287.2
C-C; C-H	283.5 – 286

Figure 4.14 presents the C1s peak deconvolution for fluorocarbon films deposited from PFE [Deposition conditions: 30W, 120 °C; 1 Torr]. A pass energy of 11.75 eV was used for all high resolution spectra collected in this study. The contribution of each chemical moiety can be determined by calculating the area under each Gaussian peak. It should be noted that the film composition with respect to surface groups (CF₃, CF₂, etc.) did not change significantly with changes in RF power level or substrate temperature. Table 4.2 presents the relative concentrations of the chemical moieties present in fluorocarbon films deposited from PFE and C₄F₈. The largest concentration (area under the curve) corresponds to that of C-CF_x structures, indicating a highly crosslinked film [19, 116].

Table 4.2 Relative Concentrations of chemical moieties in fluorocarbon films deposited from PFE and C₄F₈ precursors.

Group	PFE (%)	C ₄ F ₈ (%)
CF ₃	14 – 18	14 – 19
CF ₂	22 – 24	24 – 28
CF	22 – 24	23 – 26
C-CF _x	32 – 36	26 – 30
C-C or C-H	2 – 4	2 – 6

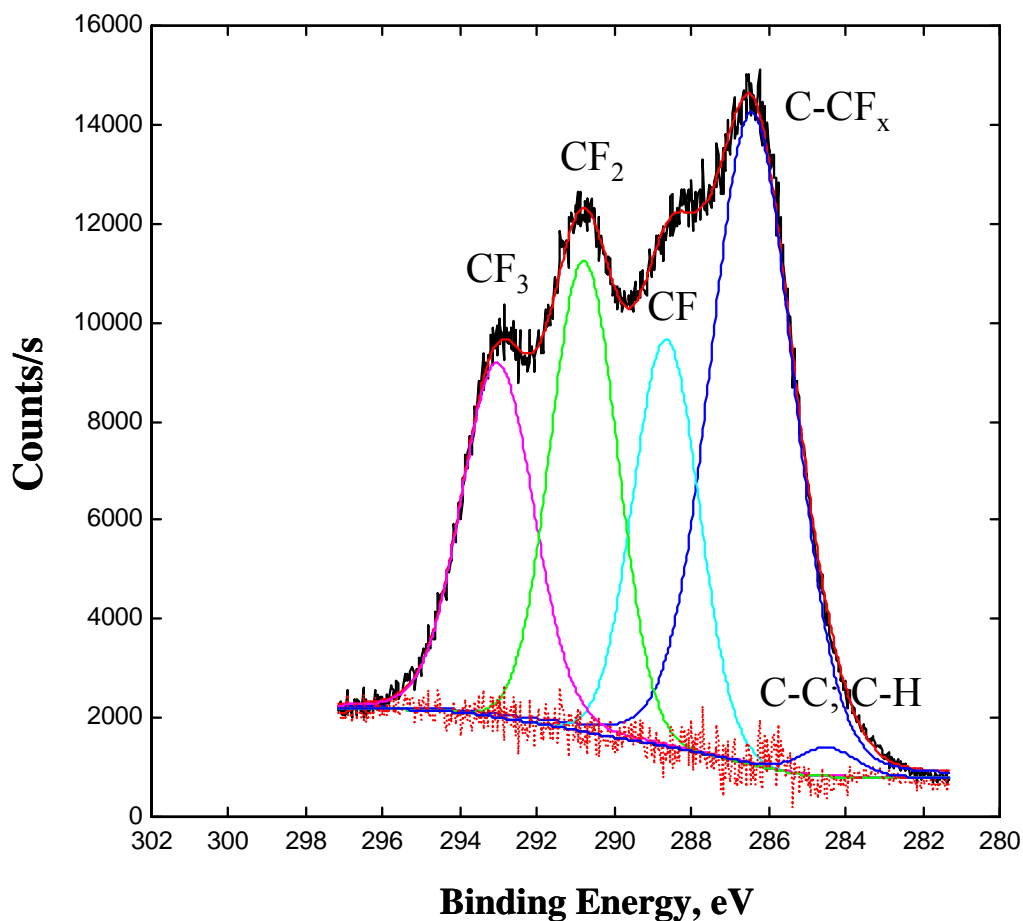


Figure 4.14 High resolution C1s spectrum of fluorocarbon film deposited on cellulose surface [Deposition conditions: RF = 30 W; P = 1 Torr, T = 120 °C; PFE flowrate = 20 sccm, Ar flowrate = 75 sccm]

High-resolution spectral analyses of C-1s, F-1s and O-1s indicate a F/C ratio between 1.02 and 1.12 and an O/C ratio less than 0.04 for the fluorocarbon films deposited using PFE as a precursor. The low F/C ratio indicates that the deposited films are highly crosslinked [117].

Pulsing experiments were carried out in the 6-inch parallel plate system using PFE as a precursor. The continuous wave (CW) power was initially fixed at 100 W and depositions were carried out using standard deposition conditions: P = 1 Torr, T = 120 °C, RF power = 100 W, Ar flowrate = 75 sccm, PFE flowrate = 20 sccm. In pulsing, RF power was applied for a specific “on” time, followed by an “off” period during which no RF excitation was used. During the “on” time, both ions and reactive neutrals are produced. Since the ions have shorter lifetimes than the neutrals, the ratio of neutrals to ions increases during the “off” cycle. Thus, film deposition occurs mainly due to reactive neutrals. An “on” time of 10 ms was selected and was held constant during all pulsing experiments while the “off” time was varied. The “off” times selected were 20ms, 50 ms, 100 ms, and 200 ms. The equivalent power is given by:

$$Equivalent\ Power(W) = \left(\frac{t_{on}}{t_{on} + t_{off}} \right) P_{on} \quad (4.1)$$

where P_{on} is the power applied during the “on” time or CW power.

Plasma pulsing alters the chemical composition of the fluorocarbon films as demonstrated by high resolution XPS spectra. Analogous to previous results, the C1s

peak was deconvoluted into five Gaussian peaks (CF_3 ; CF_2 ; CF ; C-CF_x ; C-C or C-H). The contribution of each group was determined by calculating the area under each Gaussian peak. Table 4.3 presents the concentration (% contribution in C1s peak) of various groups with varying “off” times for an RF “on” power (P_{on}) of 100 W. It is clear from the table that as pulsing “off” time increases (keeping the “on” time constant), the relative concentrations of CF_3 and CF_2 groups increases in the fluorocarbon film. The increase in CF_3 and CF_2 content in the film may be important for various film properties, especially with respect to hydrophobic behavior because a higher percentage of ($\text{CF}_3 + \text{CF}_2$) leads to lower surface energies and therefore to increased hydrophobic character (higher water contact angles) [25, 34]. Thus, pulsed plasma films are expected to show greater hydrophobicity due to increased ($\text{CF}_3 + \text{CF}_2$) concentrations compared to films deposited using CW plasmas under similar conditions.

Table 4.3 Relative Concentrations of chemical moieties in fluorocarbon films deposited from PFE with varying plasma duty cycle (varying t_{off} time in pulsing).

Pulsing Time, $t_{\text{on}}/t_{\text{off}}$	% CF_3	% CF_2	% CF	% C-CF_x	% C-C, C-H
CW	14 – 18	22 – 24	22 – 24	32 – 36	2 – 4
10ms/20ms	15 – 19	22 – 25	21 – 23	31 – 34	2 – 3
10ms/50ms	16 – 21	24 – 27	19 – 20	30 – 31	2 – 3
10ms/100ms	19 – 23	26 – 29	17 – 18	29 – 30	1 – 2
10ms/200ms	20 – 24	28 – 30	12 – 16	29 – 30	1 – 2

4.1.3 Fourier Transform Infrared Spectroscopy of Fluorocarbon Films

To investigate the chemical bonding groups present in the films, FTIR studies were performed. Figure 4.15 presents an infrared spectrum of a fluorocarbon film deposited from PFE. The broad peak between 980 and 1450 cm^{-1} indicates the presence of CF_x (CF , CF_2 , CF_3) species in the film and is commonly found in plasma polymerized fluorocarbon films due to CF_x stretching [19, 36, 116, 118, 119]. The prominent peak centered at 1250 cm^{-1} contains symmetric and asymmetric stretches [118]. The peak at 740 cm^{-1} can be attributed to the CF_2 symmetric stretch and indicates crosslinking in the film [120]. The broad peak between 1600 and 1850 cm^{-1} can be attributed to various unsaturated fluorocarbon bonds [111]. For instance, the absorption band at 1633 cm^{-1} corresponds to $\text{C}=\text{C}$ stretching; $\text{C}=\text{CF}_2$ groups appear between 1735 and 1755 cm^{-1} , and $-\text{CF}=\text{CF}_2$ stretching occurs between 1780 and 1800 cm^{-1} [54, 121]. The peak at 1833 cm^{-1} can be attributed to $-\text{CF}=\text{O}$ and might be due to post-deposition oxidation of dangling bonds [122]. It should be noted that no peaks occur at 2954 cm^{-1} (olefinic sp^2 $-\text{CH}_2$ stretch and sp^3 $-\text{CH}_3$ stretch), 2925 cm^{-1} (sp^3 $-\text{CH}_2$), and 2870 cm^{-1} (sp^3 $-\text{CH}_2$ or $-\text{CH}_3$), indicating little hydrogen incorporation in the films [123].

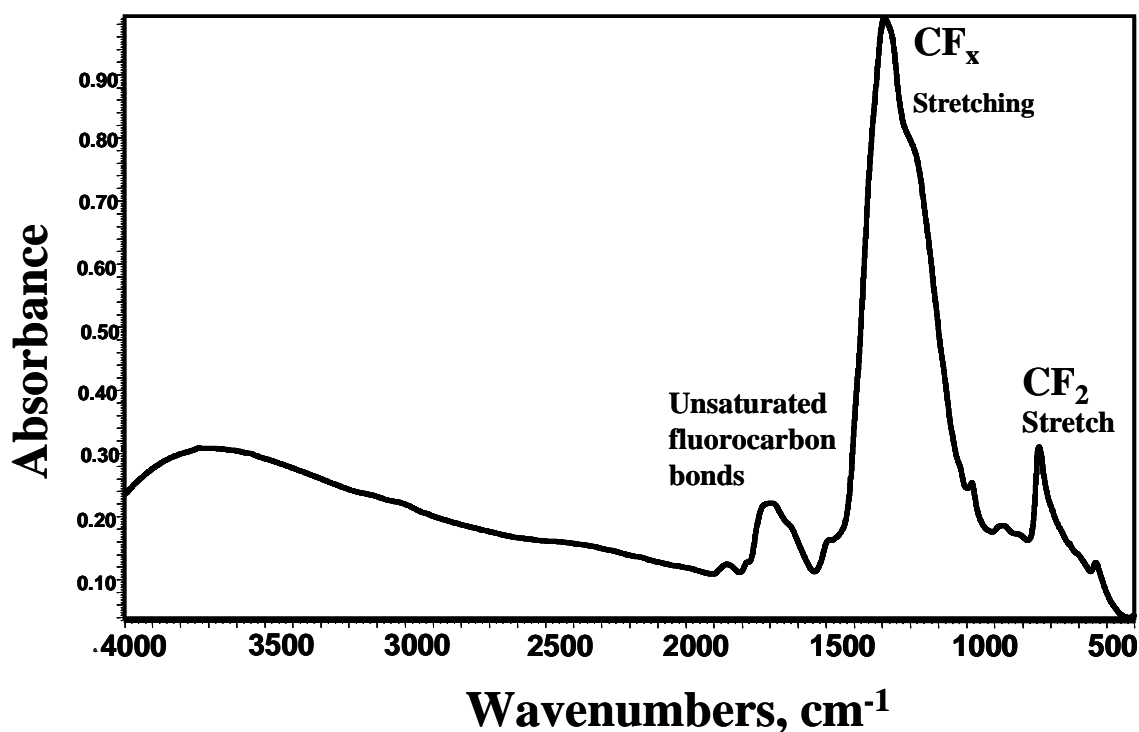


Figure 4.15 FTIR absorption spectra of fluorocarbon film deposited from PFE [P = 1 Torr, RF = 30 W, T = 120 °C; Ar flowrate = 75 sccm; PFE flowrate = 20 sccm]

4.1.4 Scanning Electron Microscopy

Scanning electron microscopy (SEM) studies were conducted on fluorocarbon films deposited on silicon and paper substrates to investigate the film morphology. A one-micron thick fluorocarbon film using PFE as a precursor was deposited onto regular copy paper and a silicon wafer. In general, most plasma polymerized films show a globular, cauliflower-type morphology, which arises from gas-phase dominated plasma polymerization [124]. Rapid polymerization may occur in the gas phase and produce solid nano- and microparticles, which then aggregate on the surface of the substrate [124-

126]. Further polymerization on the substrate and surface nucleation and growth fills in the areas between globules.

Figure 4.16 presents an SEM micrograph of a PFE film on a silicon substrate deposited under standard conditions [P = 1 Torr; T = 120 °C; RF = 100 W on 6" platen). Globular morphology is evident on the silicon wafer, consistent with that of plasma polymerized films reported previously [124, 126].

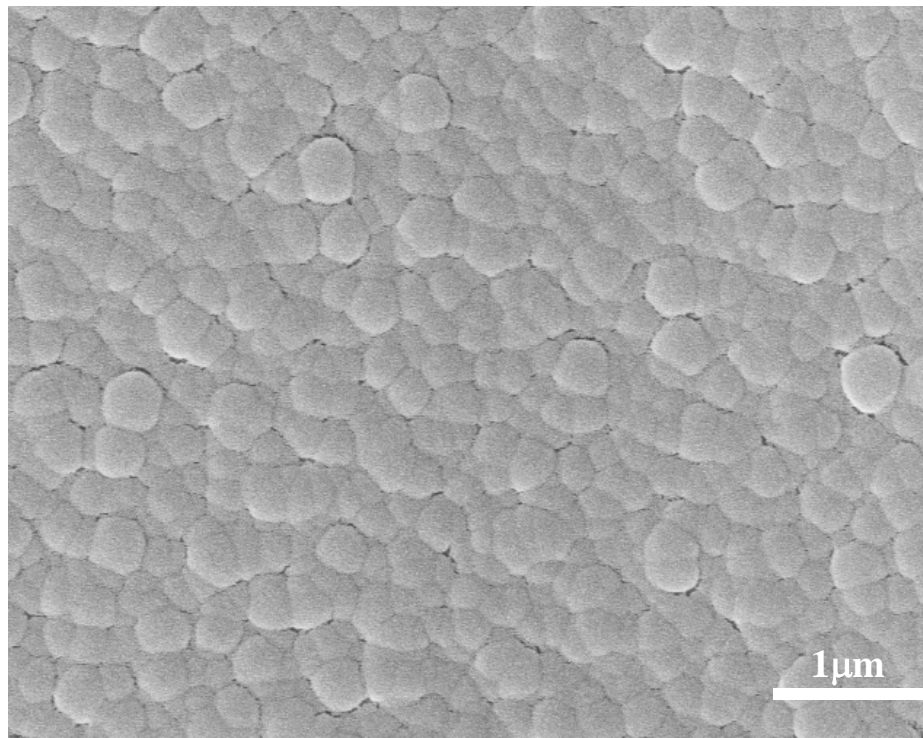
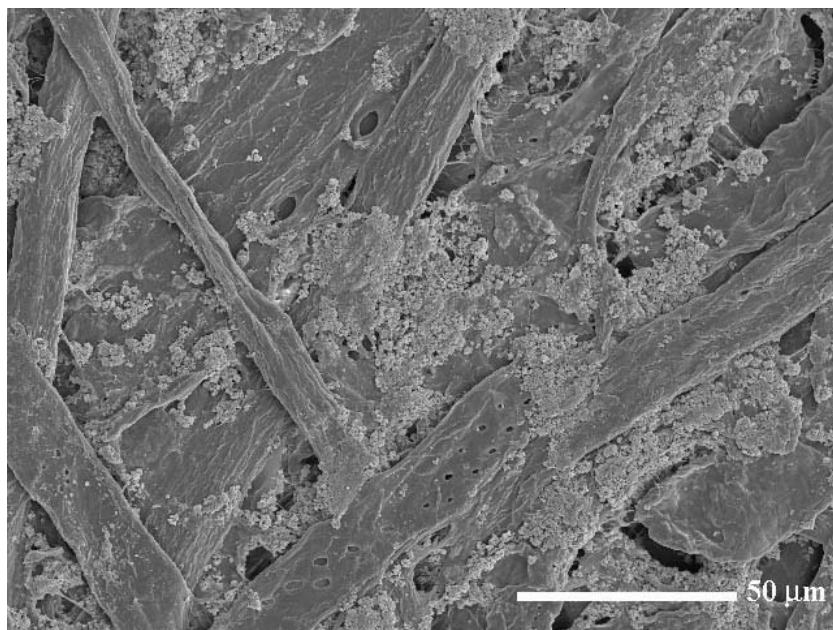


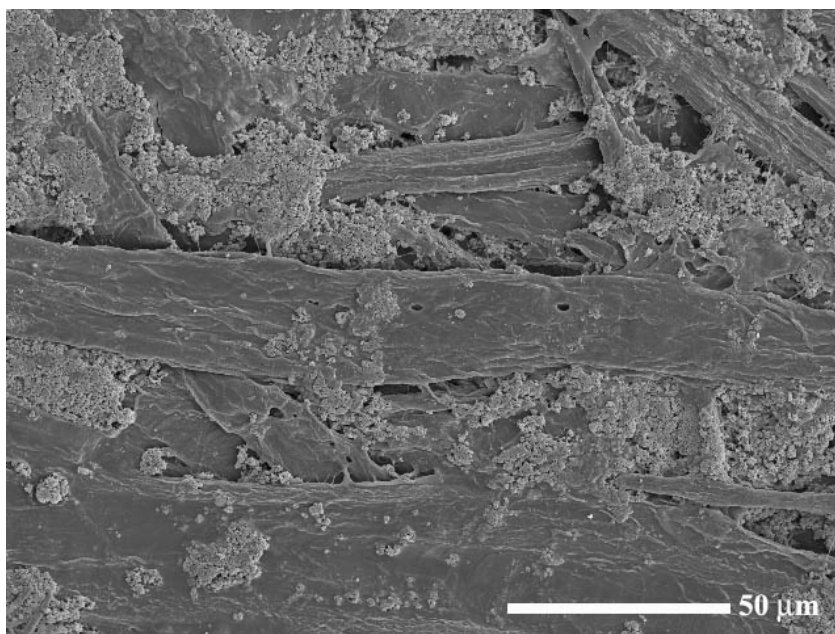
Figure 4.16 SEM micrograph of PFE film deposited on silicon wafer [P = 1 Torr, T = 120 °C; RF = 100 W on 6" platen; Film thickness = 1 μm]

SEM studies were also conducted on uncoated and PFE coated paper samples. Figure 4.17 presents SEM micrographs of the surface of: (a) an uncoated paper sample, and (b) a coated paper (260 μm thick PFE film) sample. To the extent discernable by SEM, there is no change in the surface morphology as a result of PFE deposition, indicating that the individual fibers are coated during deposition. Therefore, the coating changes the surface properties but should have little, if any, effect on bulk paper properties.

Figure 4.18 presents SEM micrographs of the cross-section of: (a) an uncoated paper sample, and (b) a coated paper (260 μm thick PFE film) sample. Again, no apparent difference between the SEM micrographs of coated and uncoated paper is detectable, suggesting no change in paper morphology as a result of PFE film deposition.

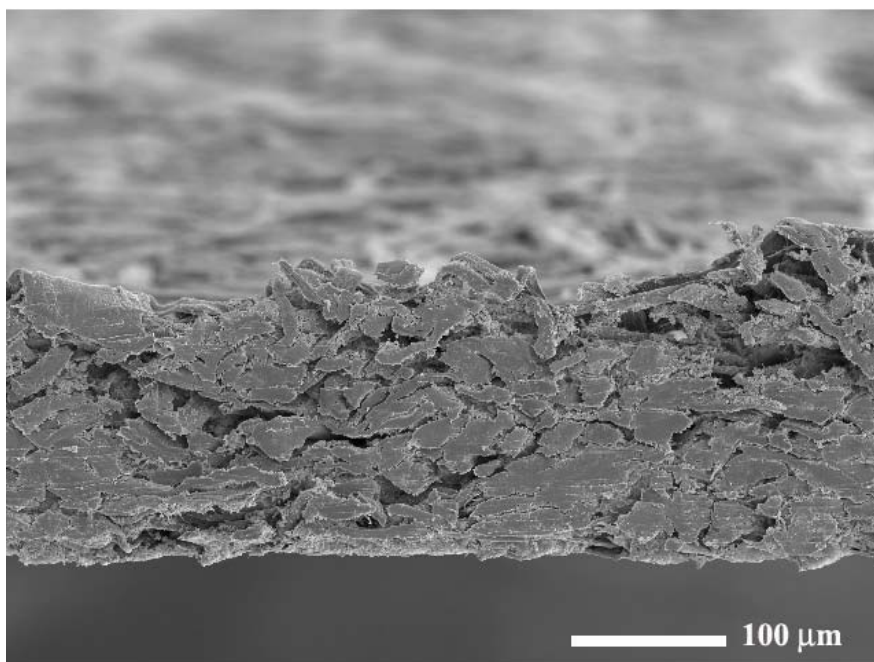


(a)

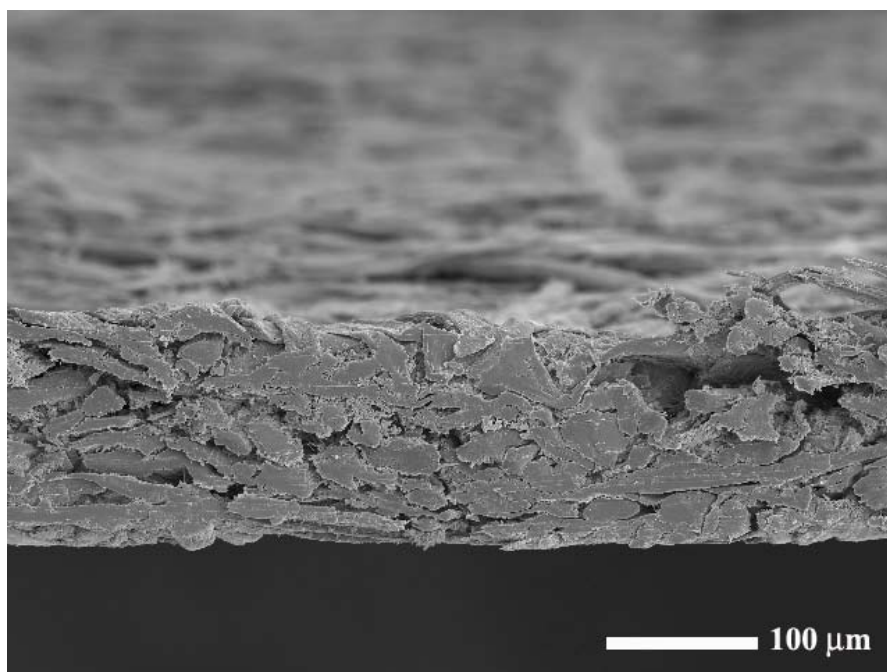


(b)

Figure 4.17 SEM micrograph of the surface of: (a) an uncoated paper sample, and (b) a PFE coated paper sample. Solid aggregates between the fibers are inorganic filler material in the paper.



(a)



(b)

Figure 4.18 SEM micrograph of the cross-section of: (a) an uncoated paper sample, and (b) a PFE coated paper sample.

To investigate the effect of PFE film thickness on the surface morphology of coated paper, a thick PFE film ($\sim 5\ \mu\text{m}$) was deposited on the surface of copy paper; the SEM micrograph is shown in Figure 4.19. The paper surface appears to be smoothed by the thick PFE film, i.e. the surface roughness has decreased. The film appears to have over-coated the paper surface in addition to the fibers, filling most of the pores or spaces between the fibers. Such a coating will exhibit increased barrier properties as the surface is uniformly covered by a coating blocking the pores in addition to establishing a low surface energy due to CF_2 , and CF_3 groups on the film surface.

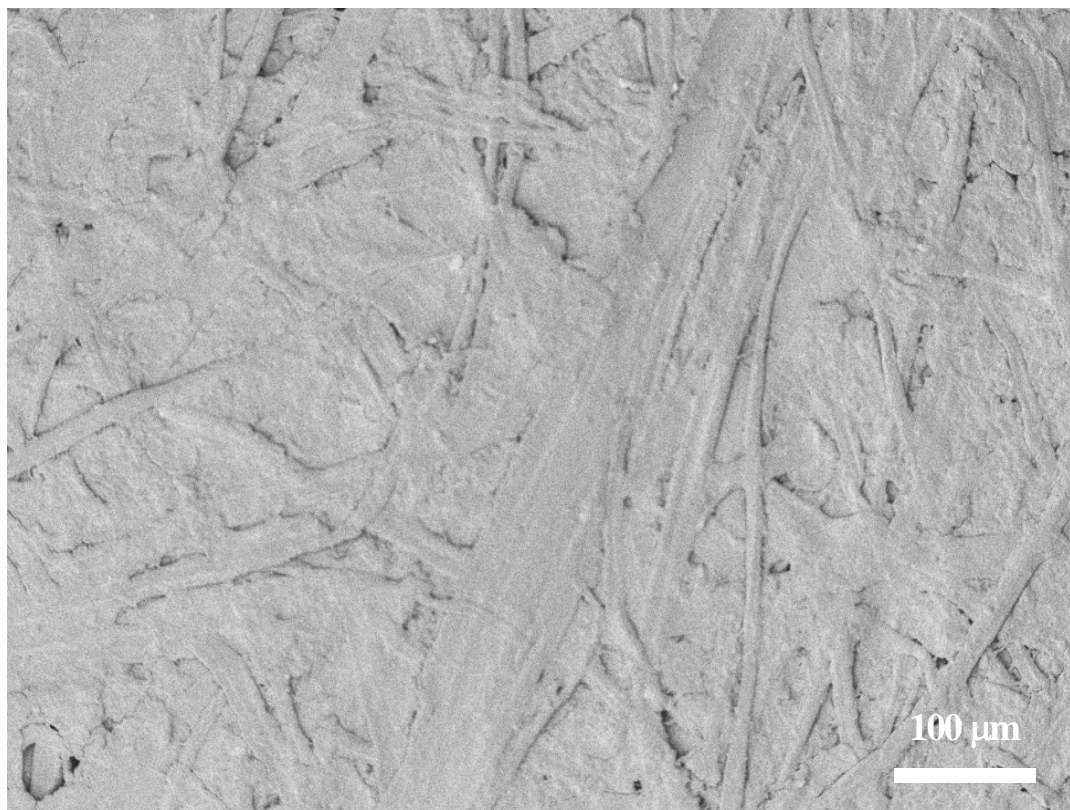
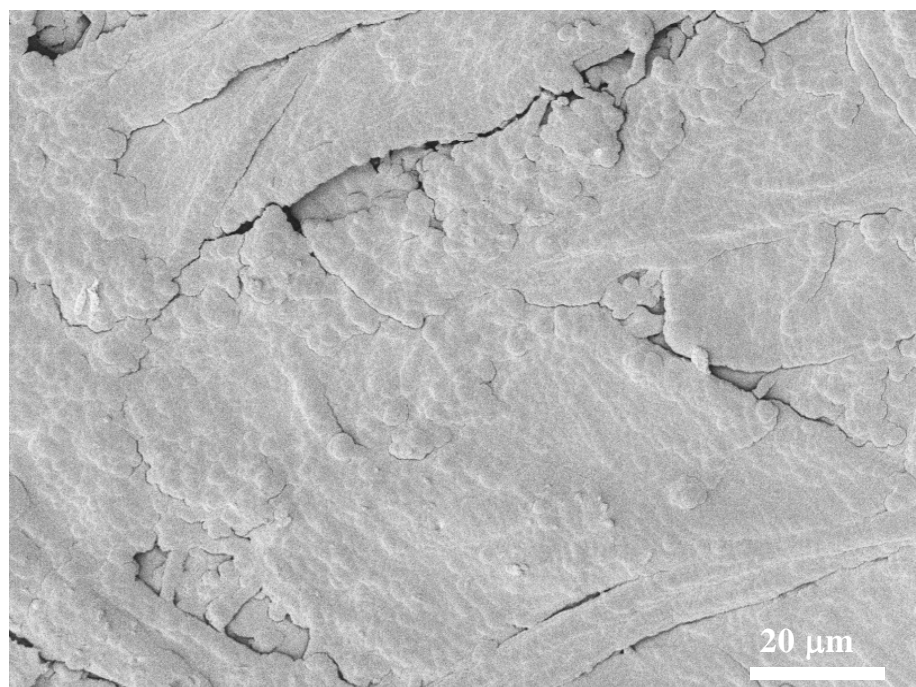
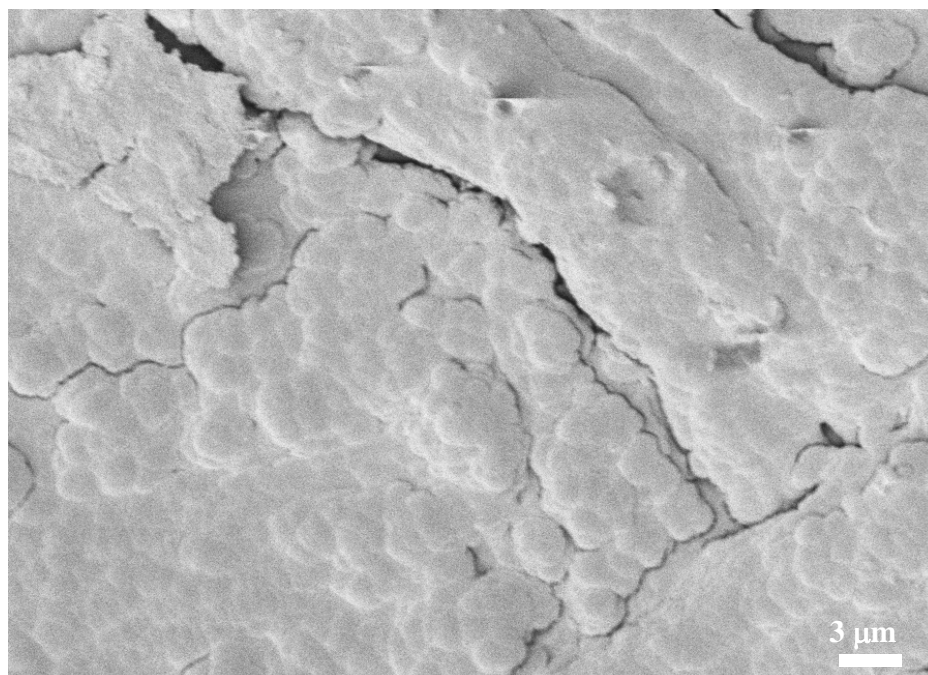


Figure 4.19 SEM micrograph of a copy paper coated with 5 μm PFE film [P = 120 °C, T = 120 °C; RF = 100 W on 6" platen]

Figure 4.20 presents higher magnification SEM micrographs of copy paper coated with a 5 μm PFE film. The surface of the fiber is coated with a globular coating, confirming the presence of a PFE film covering the fibers and penetrating into the paper substrate. Thus, during PFE film deposition, polymerization on the substrate and growing film fills in the area between the globules.



(a)



(b)

Figure 4.20 High magnification SEM micrographs of copy paper coated with 5 μm PFE film. Globule-like morphology of plasma polymerized PFE is evident.

5. HYDROPHOBIC PROPERTIES OF FLUOROCARBON FILMS ON PAPER/CELLULOSE AND MOISTURE ABSORPTION STUDIES USING A QUARTZ CRYSTAL MICROBALANCE

In this chapter, hydrophobic properties of paper and cellulose coated with fluorocarbon films are presented as measured by contact angle goniometry. This chapter also presents the effect of fluorocarbon film thickness and chemical composition on hydrophobic properties of coated paper. The fluorocarbon films are hydrophobic and are not “wetted” when liquid water contacts these layers; however, the films allow water vapor diffusion. Although water vapor uptake of the fluorocarbon films is low, moisture diffusivity through the films is high; that is, moisture penetrates the films but is not chemically bonded. Quartz crystal microbalance (QCM) studies were conducted on fluorocarbon films to evaluate the absorption of water vapor. Transient moisture absorption studies were also conducted using the QCM to evaluate the rate of moisture uptake and diffusivity.

5.1 Hydrophobic Properties of Fluorocarbon Films

Paper and cellulose surfaces are porous hydrophilic materials. The untreated cellulose membrane absorbs water droplets quickly due to the combination of a hydrophilic surface and capillary effects. The surface contact angle is essentially zero and thus cannot be

accurately measured. Fluorocarbon films were deposited on the surface of cellulose and paper using PFE as a precursor. Copy paper [International Paper Company's *Copy Plus*; Brightness: 84; Weight Basis (500 sheets): 20 lb or 75 g/m²; Thickness: 0.1 mm] and cellulose [Spectra/Por4 Flat Sheet Membranes, supplied by Spectrum Chemical, CA] were used as substrate materials for the experiments.

5.1.1 Hydrophobic Properties with Varying Fluorocarbon Film Thickness.

Contact angle measurements were performed on cellulose membranes onto which plasma deposited fluorocarbon layers were formed. The studies were conducted in a controlled humidity environment (95% - 99% RH) to prevent evaporation of the dispensed water droplet. Varying thicknesses of fluorocarbon films using PFE as the precursor were deposited onto the surface of cellulose. Deposition conditions were constant during the experiments (30 W RF power, substrate temperature = 120 °C, pressure = 1 Torr) while the deposition time was varied. Under these conditions, the deposition rate of PFE films was approximately 50 nm/min. Contact angle measurements were performed on fresh cellulose, a control cellulose substrate, and cellulose with fluorocarbon films of thickness 27 nm, 50 nm, 70 nm, and 90 nm. Contact angles were measured at three different points on a each sample; the reported contact angle is an average of these three values. Since a Si wafer was placed next to the cellulose sample during deposition in all experiments to enable film thickness measurement, contact angles of fluorocarbon films on Si wafers were also measured. Figure 5.1 shows the screen shot of a contact angle measurement (video contact angle) on a 90 nm fluorocarbon film on cellulose.

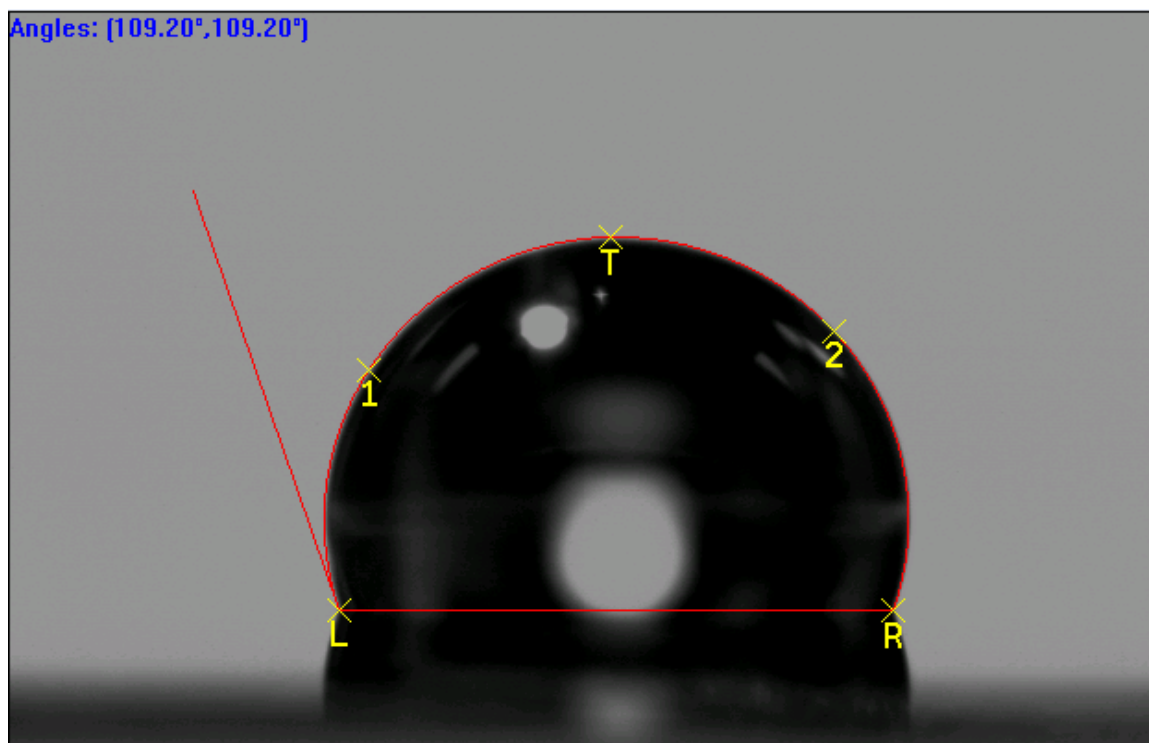


Figure 5.1 Video contact angle of water droplet on surface of 90 nm fluorocarbon coated cellulose. High contact angle indicates hydrophobic behavior. [1, t, 2, L, and R points on the water droplet above indicate curve fitting points]

In these studies, a control cellulose sample was one in which the cellulose sample was placed in the plasma reactor, and was subjected to the same temperature, pressure, and time conditions as the ones that received plasma deposition, but no film was deposited. The contact angle for a 27 nm fluorocarbon film was unstable as the contact angle decreased from 105° to 0° within 15 minutes suggesting that the surface was not completely covered with fluoropolymer. This is consistent with studies on sized paper where the initial contact angle is used as a measure of the paper's ability to resist wetting.

The sample with a 50 nm fluorocarbon film also shows an unstable contact angle that decreases from 105° to 54° in 45 minutes. Cellulose films with fluorocarbon coatings of 70 nm and 90 nm thicknesses reached a stable contact angle ($\sim 104^{\circ}$) indicating hydrophobic surfaces. The experimental error in these measurements was between 1° and 2° . The contact angle in both films was high ($\sim 104^{\circ}$) even after 1 hr. These results suggest that surface modification of cellulose where the film thickness is < 70 nm may result in non-uniform fiber coating. Thus, determination of the extent of surface modification or treatment is critical in controlling the surface properties (e.g. hydrophobicity) of cellulose. Figure 5.2 shows the dependence of the contact angle on time for films of different thicknesses. It is evident that both 70 nm and 90 nm thick films exhibit a high contact angle even after long water droplet exposure times, which suggests the establishment of a stable hydrophobic surface.

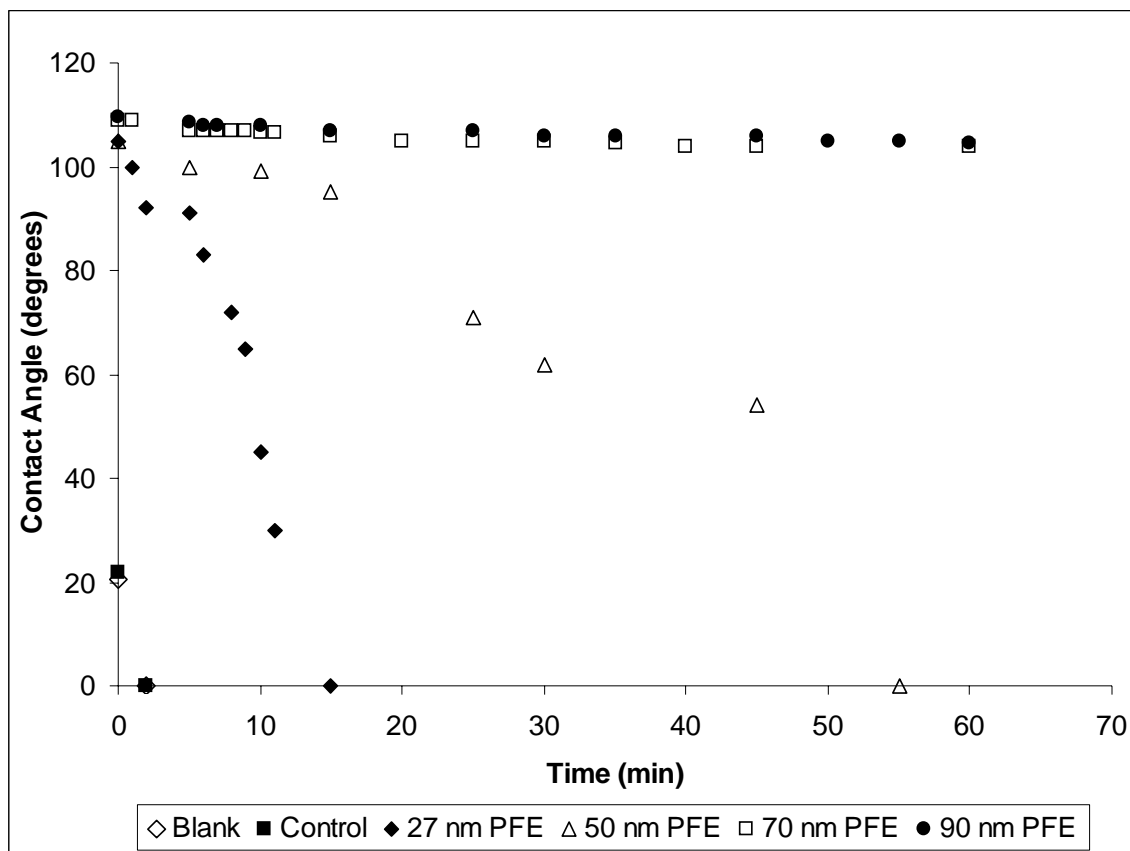


Figure 5.2 Variation of water contact angle with time for PFE films of different thicknesses deposited on cellulose. Films with > 70 nm of PFE thickness provide stable contact angles over an extended period of time.

Contact angles measured on Si wafers were in the $103^{\circ} - 106^{\circ}$ range for film thicknesses ranging from 25 nm to 90 nm and did not change with time. It should be noted that contact angles on cellulose were higher than on silicon because surface roughness can cause an increase in the apparent contact angle and hence an apparent surface energy that is lower than the true surface energy [71, 127]. Since copy paper has a rougher surface (RMS roughness $\sim 5 \mu\text{m}$) than a cellulose membrane, the contact angle measured on copy paper coated with a 90 nm fluorocarbon film was 120° .

Paper and cellulose coated with fluorocarbons are hydrophobic because the fluorocarbon film lowers their surface energy. On a macroscopic scale, a surface that is not wetted by a particular liquid has a lower critical surface tension than the surface tension of that liquid. In the case of flat substrates, it is the chemical nature of the functional group packing which governs surface wettability [128, 129]. Fluorocarbon coating covalently bonds to the surface of paper and cellulose fibers, creating an abundance of highly fluorinated groups such as CF_3 , CF_2 , CF and highly crosslinked group such as C-CF_x on the surface. The tightly bound, nonbonding electron pairs surrounding each fluorine atom core shell in F-C bonds are not easily polarized, and therefore hinder hydrogen bonding and dispersion interactions with polar and nonpolar liquids, respectively [130, 131]. This type of non-attractive behavior increases with the degree of fluorine substitution at each carbon center (i.e. $\text{CF}_3 > \text{CF}_2 > \text{CF}$). High resolution C1s XPS spectra of cellulose (Figure 4.12, Chapter 4) show the presence of hydrophilic groups which can easily attach to water through hydrogen bonds. When coated with a fluorocarbon film, the cellulose surface is covered by fluorocarbon moieties (CF_3 , CF_2 , CF , etc.) as indicated by the high resolution C1s spectra in figure 4.14 (Chapter 4). The surface concentration of fluorinated moieties ($\%\text{CF}_3 + \%\text{CF}_2 + \%\text{CF}$) is as high as 60% as shown in Table 4.2 (Chapter 4), leading to hydrophobic behavior. It is the CF_3 and CF_2 moieties that primarily contribute to the hydrophobicity of fluorocarbon films [25, 30, 46, 72, 111, 132, 133].

Fluorocarbon film thickness on cellulose or paper surfaces plays an important role in the extent of hydrophobic behavior displayed by coated substrates. At low film thickness,

fibers on the cellulose or paper surface are not covered adequately, leaving uncoated surface areas which are wetted by polar and nonpolar liquids. As the fluorocarbon film thickness increases, almost complete coverage of surface and near-surface fibers on cellulose is achieved. Thus, the extent of hydrophobic behavior desired can be controlled by varying the fluorocarbon film thickness on cellulose based substrates such as paper. It is not very clear if it is the incomplete coverage of the fibers or the shallow coating depth into the paper/cellulose at short deposition times that yields unstable contact angles.

5.1.2 Hydrophobic Properties with Varying Fluorocarbon Film Composition

As discussed in previous chapters (Chapter 2 and Chapter 4), pulsing the plasma in the millisecond regime is a very simple and effective method to control the film chemistry, and thus the film composition. Pulsed plasma experiments (as described in Chapter 4) were conducted to deposit fluorocarbon films on the surface of paper. Pulsing experiments were conducted in the 6-inch parallel plate system using PFE as a precursor. While pulse “on” time was constant at 10 ms, pulse “off” time was varied as 20 ms, 50 ms, 100 ms, and 200 ms. Other deposition conditions were constant during pulsing experiments ($P = 1$ Torr; $T = 120$ °C; RF power = 100 W; Argon flowrate = 75 sccm; and PFE flowrate = 20 sccm). A film thickness of ~100 nm was selected for experiments under various pulsing conditions. Consequently, the film deposition times increased at low duty cycles (higher pulse “off” times) due to a decrease in equivalent RF power.

Figure 5.3 presents contact angles as a function of time for fluorocarbon films with varying pulse “off” times and hence varying plasma duty cycle. It is evident that all films exhibit a high contact angle even after long water droplet exposure times, which suggests the establishment of a stable hydrophobic surface. It is also evident that as pulse “off” time increases (or plasma duty cycle decreases), the contact angle increases. This increase can be attributed to an increase in concentration of CF₃ and CF₂ moieties on the surface of coated paper. Table 5.1 presents the various pulse “off” times used in the study and their effect on the concentrations of various CF_x (x = 1, 2, 3) as obtained from high resolution C1s XPS peak deconvolution using Gaussian peak fitting. Fluorine to carbon ratio (F:C) was obtained using the following expression [118]:

$$F:C = \frac{(3 \times \% CF_3) + (2 \times \% CF_2) + (\% CF)}{100} \quad (5.1)$$

As plasma duty cycle decreases, the concentration of CF₃ and CF₂ moieties in the fluorocarbon films increases. This is consistent with the results obtained by other researchers [34]. With increasing CF₃ and CF₂ concentration, F:C ratio in the films also increases leading to increased hydrophobic behavior.

Table 5.1 Effect of varying plasma duty cycle on composition of fluorocarbon films deposited on paper.

t_{on} , ms	t_{off} , ms	Duty Cycle (%)	% CF_3	% CF_2	%CF	(% CF_3 + % CF_2)	F:C
10	0	100.0%	16	23	23	39	1.17
10	20	33.3%	17	23.5	22	40.5	1.20
10	50	16.7%	18.5	25.5	19.5	44	1.26
10	100	9.1%	21	27.5	17.5	48.5	1.36
10	200	4.8%	22	29	14	51	1.38

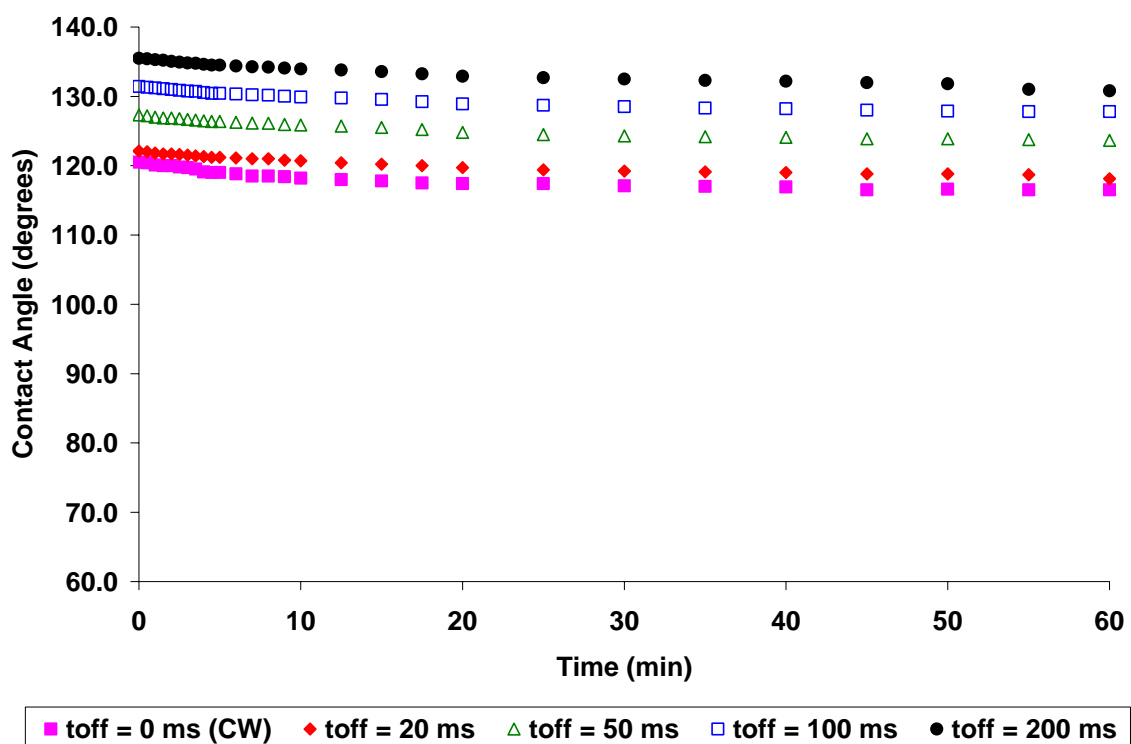


Figure 5.3 Contact angle data with time for ~100 nm fluorocarbon films deposited on paper with varying pulse “off” times [RF power = 100 W; t_{on} = 10 ms; P = 1 Torr; T = 120 °C for all the samples]

The initial water contact angle ($t = 0$ min) on fluorocarbon films deposited on paper is plotted as a function of the sum of CF_3 and CF_2 concentrations in Figure 5.4. Clearly, higher concentrations of CF_3 and CF_2 moieties leads to higher contact angles indicating increased hydrophobic behavior. Again, this behavior is consistent with that observed by other researchers [34].

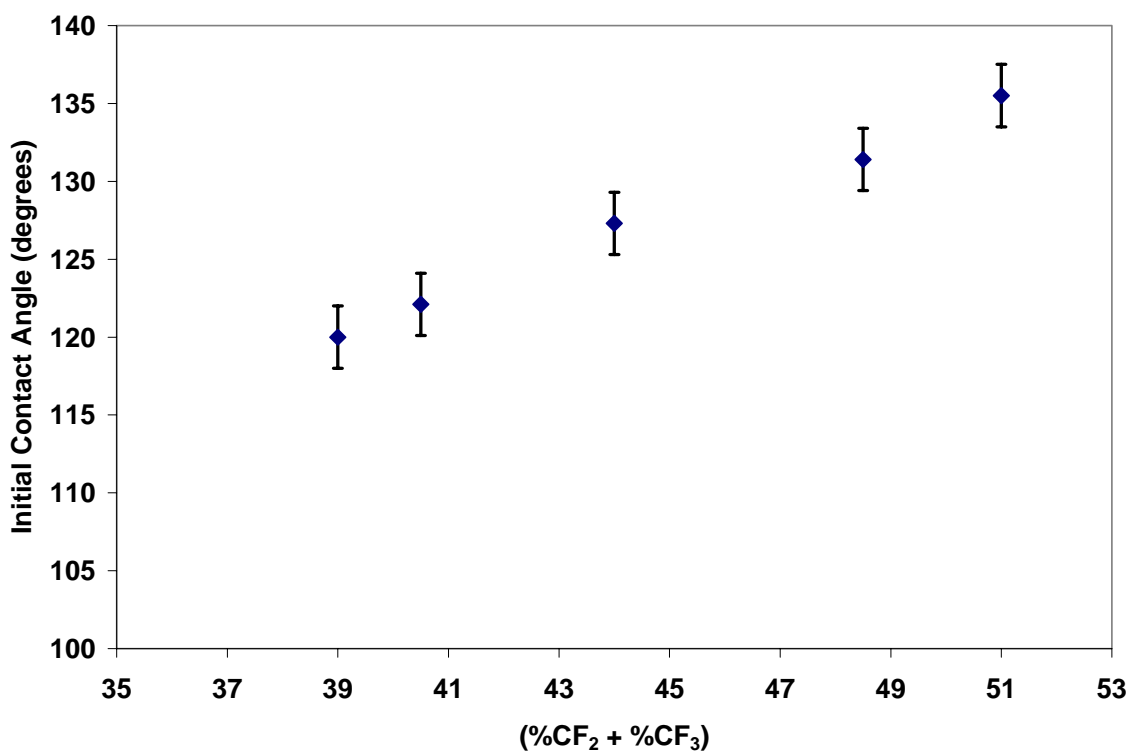


Figure 5.4 Sessile drop initial water contact angle ($t = 0$ min) measured on coated paper substrate as a function of ($\%\text{CF}_3 + \%\text{CF}_2$) incorporation in fluorocarbon film.

An increase in CF_3 and CF_2 concentration results from an increase in t_{off} times as the plasma duty cycle decreases, as shown in Figure 5.5. Figure 5.6 presents the effect of varying “off” time on the F:C ratio of the fluorocarbon films deposited using pulsing.

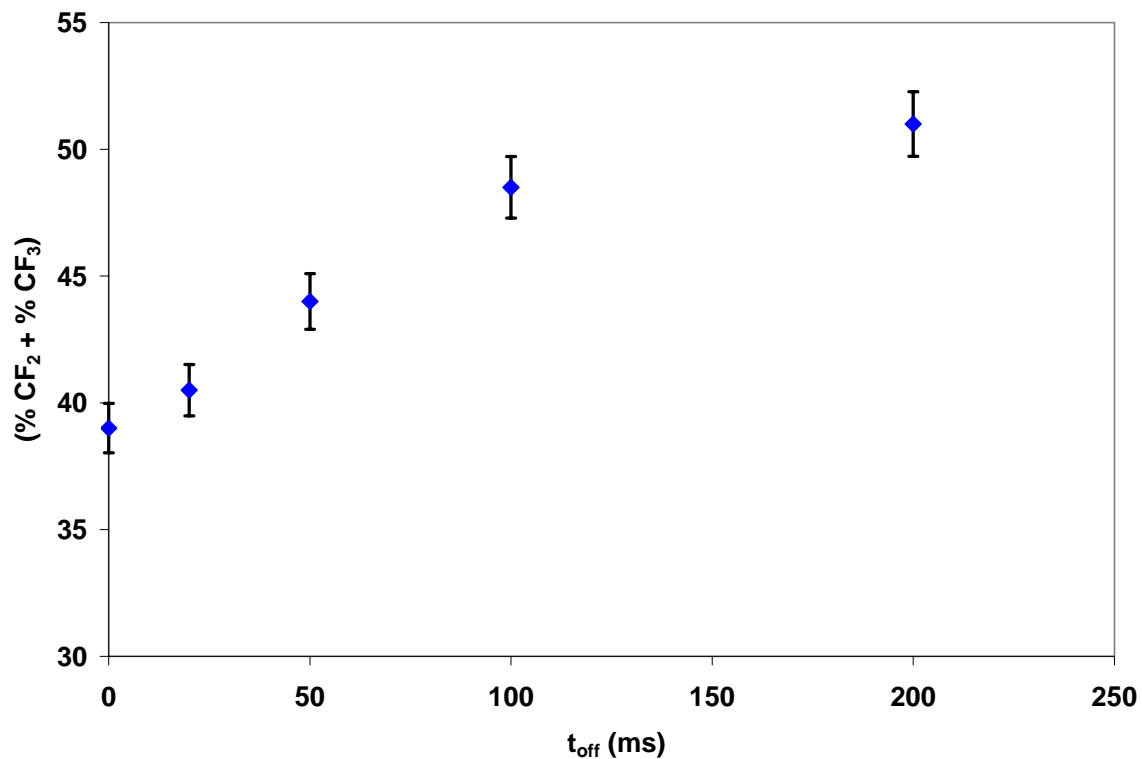


Figure 5.5 Percentage (CF_3 + CF_2) incorporation in fluorocarbon film with varying “off” times in plasma pulsing.

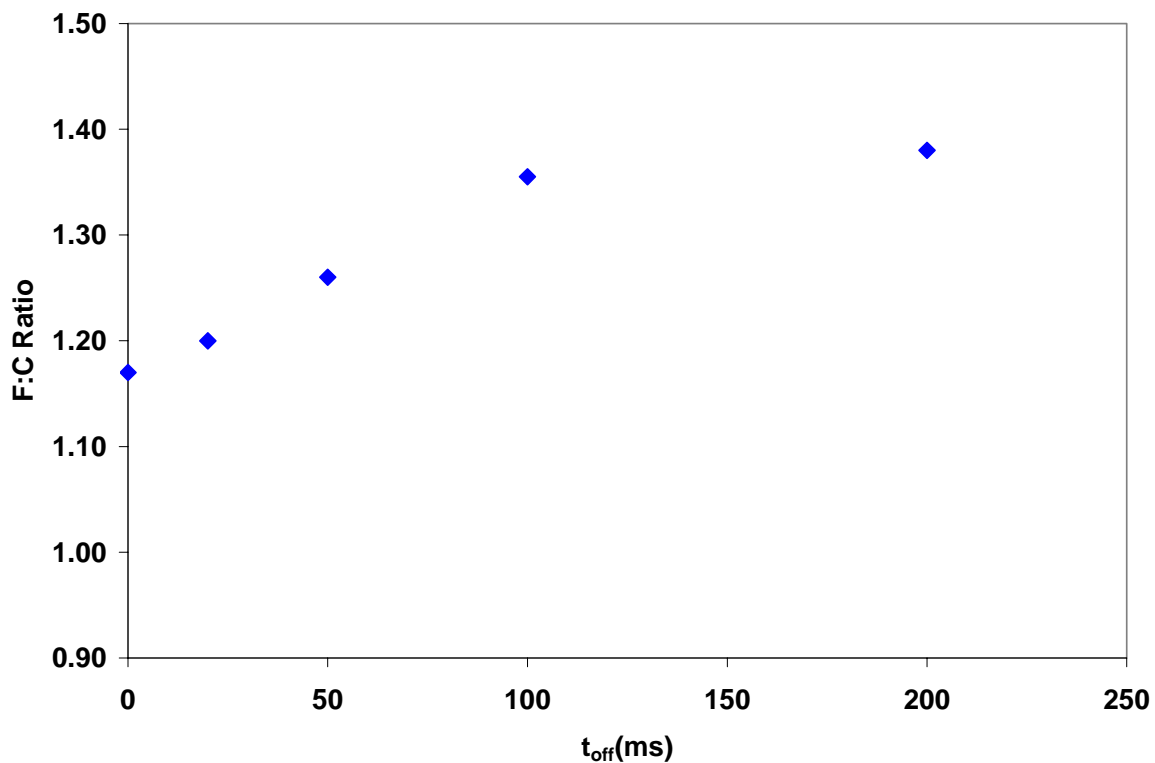


Figure 5.6 Effect of varying pulse “off” times on F:C ratio of fluorocarbon films.

The contact angle is a function of both surface roughness and surface composition [134].

The surface roughness of paper is higher than that of Si and therefore, contributes to the observed higher initial contact angle when compared to initial contact angles on a Si wafer (Figure 5.7).

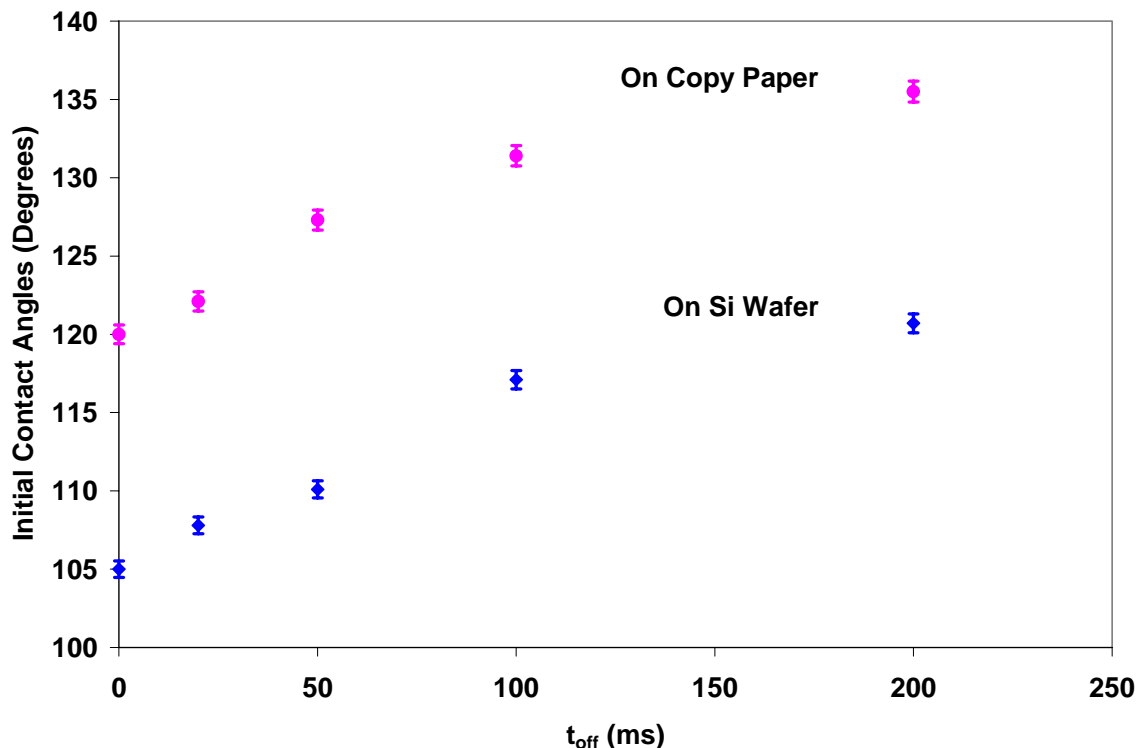


Figure 5.7 Comparison of initial water contact angle ($t = 0$ ms) on fluorocarbon coated copy paper and on a Si wafer with varying pulse “off” times. Higher surface roughness of paper contributes to its higher contact angle. Both surfaces follow essentially the same trend with varying pulse “off” times.

It is possible that some of the variation in water contact angle on coated paper is due to sample to sample variation in paper surface roughness. However, the samples used in the experiments were cut from same paper sheet in an attempt to eliminate sample to sample substrate variation. Thus, the change in contact angle with varying pulse “off” times is primarily attributed to a change in the surface composition of fluorocarbon films.

The reasons for the increase in hydrophobicity with increased CF_3 and CF_2 concentration (and therefore increased F:C ratio) has been well documented [30, 34, 72, 76, 118, 135-

138]. As discussed previously, an increase in the number of fluorine atoms attached to a carbon center increases the hydrophobic nature of the chemical group. Increasing the hydrophobicity of the groups making up the surface will increase the contact angle; therefore a film with higher CF₂ and CF₃ concentrations should display a higher contact angle than one with higher concentrations of CF and quaternary carbon groups. Alternatively, it can be stated that with an increase in F:C ratio, surface fluorination increases which leads to increased hydrophobicity.

The above results demonstrate that fiber coverage sufficient to coat the hydrophilic groups on paper or cellulose is necessary to impart stable hydrophobic properties via plasma surface modification. Fluorocarbon coating depth into paper/cellulose is another important factor that may control the extent or stability of hydrophobic properties. Also, variation in surface composition in a pulsed plasma environment leads to a variation in the degree of hydrophobic character imparted.

5.2 Moisture Absorption Studies using QCM Measurements

The extent of moisture absorption on coated paper or cellulose has implications for hydrophobic properties as well as on the retention of bulk physical properties for paper or cellulosic materials. It is, therefore, important to determine if the coating applied on the surface of paper or cellulose allows moisture permeation and if it does, to what extent. A film that does not allow moisture to permeate (i.e. is not breathable) and reach the

underlying cellulosic substrate may lead to bulk property degradation since moisture is important to retain the physical properties and, therefore, the mechanical strength of paper [139].

Quartz crystal microbalance (QCM) studies were conducted to demonstrate that the absorption of water vapor is a bulk phenomenon in which the moisture penetrates into and through the film. Equilibrium moisture uptake of the fluorocarbon films deposited from PFE and OFCB precursors was also evaluated, and finally, transient moisture absorption studies were conducted using the QCM to evaluate the rate of moisture uptake and diffusivity.

Two films of different thicknesses were deposited onto quartz crystals (10 MHz) using each fluorocarbon precursor. Thicknesses and refractive indices of the fluorocarbon films deposited on silicon wafers are given in Table 5.2 as measured ellipsometrically at a wavelength of 600 nm. The ratio of thicknesses of the two films, (t_2/t_1), in set 1 is 2.76, while the same ratio in set 2 (t_4/t_3) is 3. Films deposited using C_4F_8 have lower refractive indices (1.38 compared to 1.41) than the films in which PFE was used as the precursor. The refractive indices of the films are in agreement with those reported previously [140]. The F/C ratio of the films deposited from C_4F_8 ($F/C = 1.1-1.3$) was slightly higher than that of PFE-based films ($F/C = 1-1.2$). The lower refractive index of films deposited from C_4F_8 /argon plasmas is consistent with their high F/C ratio. XPS data demonstrates that the two films differ slightly in their structure and bonding, consistent with results reported previously [140].

Table 5.2 Thickness and Refractive Index of Fluorocarbon Films Deposited on Silicon

Set 1 (Precursor: Pentafluoroethane (20 sccm); Carrier Gas: Ar (75 sccm); RF Power = 30W; Pressure = 1 Torr; Substrate Temperature = 120 °C)			
<u>S.N.</u>	<u>Deposition Time</u>	<u>Film Thickness</u>	<u>Refractive Index @ 600 nm</u>
1.	15 min.	$t_1 = 681 \pm 9.2 \text{ nm}$	1.41
2.	45 min.	$t_2 = 1880 \pm 11.4 \text{ nm}$	1.41
Set 2 (Precursor: Octafluorocyclobutane (15 sccm); Carrier Gas: Ar (75 sccm); RF Power = 30W; Pressure = 1 Torr; Substrate Temperature = 120 °C)			
<u>S.N.</u>	<u>Deposition Time</u>	<u>Film Thickness</u>	<u>Refractive Index @ 600 nm</u>
1.	5 min.	$t_3 = 770 \pm 2.4 \text{ nm}$	1.38
2.	15 min.	$t_4 = 2322 \pm 13 \text{ nm}$	1.38

5.2.1 Steady State Moisture Uptake

Figure 5.8 presents the moisture uptake of films deposited on 10 MHz quartz crystals using PFE as a precursor. Clearly, the ratio of moisture absorbed by the thicker film to that absorbed by the thinner film is approximately equal to the ratio of film thicknesses ($t_2/t_1 = 2.76$) at each humidity point. This result demonstrates that the moisture uptake is a bulk film as opposed to a surface phenomenon, where the moisture penetrates into the bulk of the film rather than simply adsorbing on the film surface. Figure 5.9 presents the same data for films deposited using C_4F_8 as the precursor. Again, the ratio of moisture absorbed by the two films of different thickness is approximately equal to the ratio of film thicknesses.

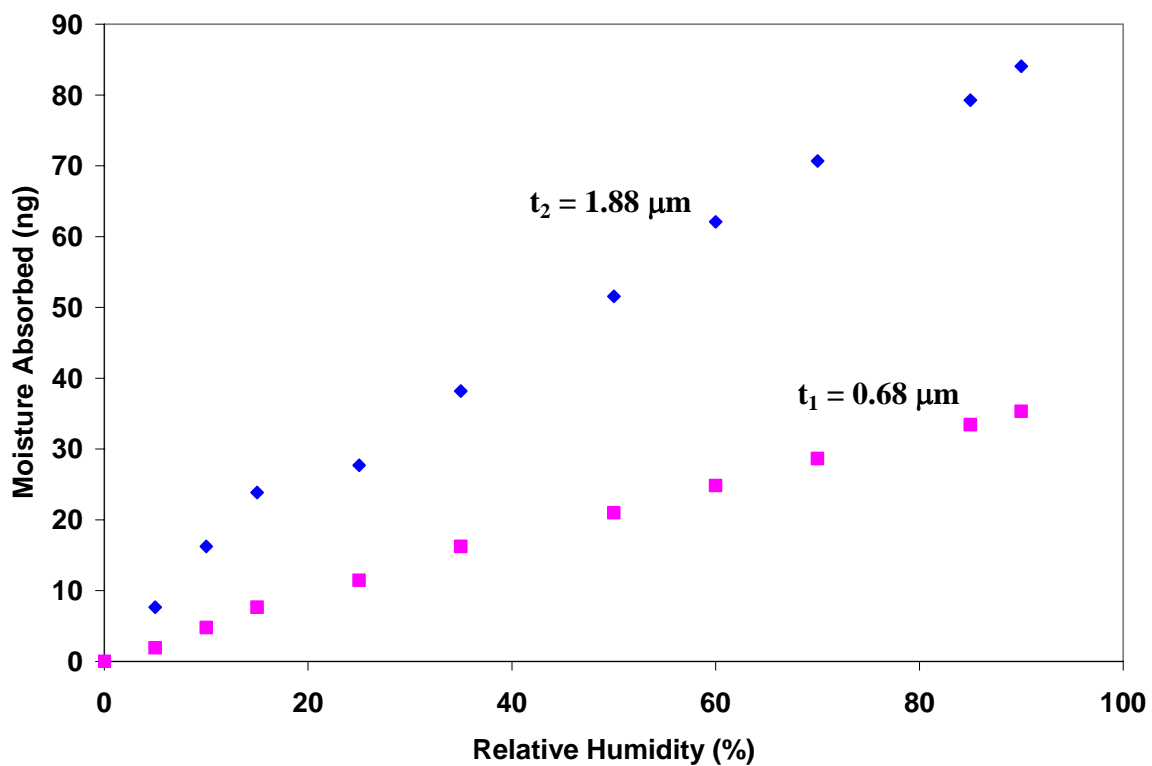


Figure 5.8 Steady-state moisture uptake (ng) as a function of relative humidity (%) for films of two different thicknesses ($t_1 = 0.68 \mu\text{m}$ and $t_2 = 1.88 \mu\text{m}$) deposited from PFE. Deposition conditions: 30W, 120 °C, 1 Torr. The data points were reproducible with less than 3% variation.

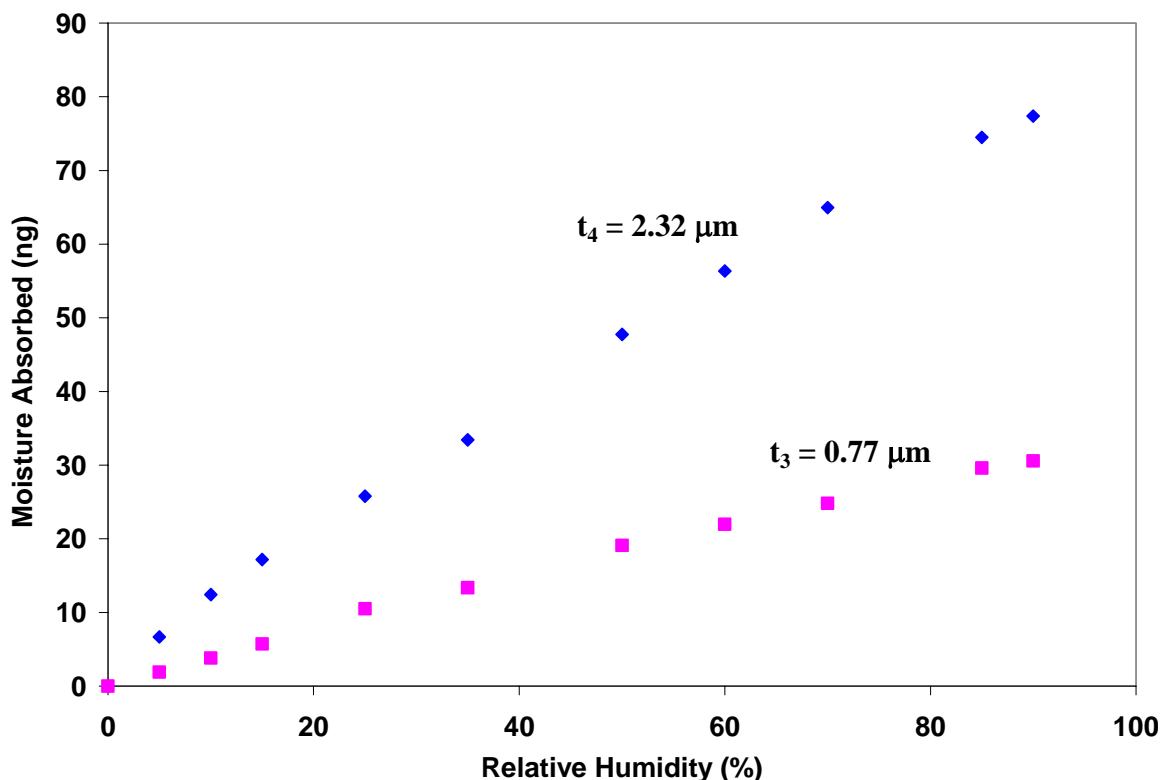


Figure 5.9 Steady-state moisture uptake (ng) as a function of relative humidity (%) for films of two different thicknesses ($t_3 = 0.77 \mu\text{m}$ and $t_4 = 2.32 \mu\text{m}$) deposited from C_4F_8 . Deposition conditions: 30W, 120 °C, 1 Torr. The data points were reproducible with less than 3% variation.

The equilibrium moisture content of the films deposited from PFE and C_4F_8 monomers is plotted as a function of relative humidity (% RH) in Figure 5.10. Fluorocarbon films deposited from C_4F_8 have slightly lower moisture uptake than films deposited from PFE, which may be due to the higher F/C ratio and therefore a lower number of binding sites in these films [141]. However, the equilibrium moisture content for all films deposited from either monomer did not exceed 0.14 wt%. This indicates that the deposited fluorocarbon films are hydrophobic. It should be noted that when the humidity was subsequently reduced to zero, the moisture completely desorbed from these films (at least to the level

detectable by QCM: ~ 0.5 ng) indicating that moisture is not chemically bonded into the film structure. The mass of the fluorocarbon films in this study, depending on the thickness, was in the μg range. These observations are consistent with results reported previously [141]. Such film properties are crucial to certain applications of plasma-deposited fluorocarbon layers in the modification of paper surfaces. For instance, water vapor permeation into paper or cellulose is needed to prevent drying of these substrates, which causes physical property degradation.

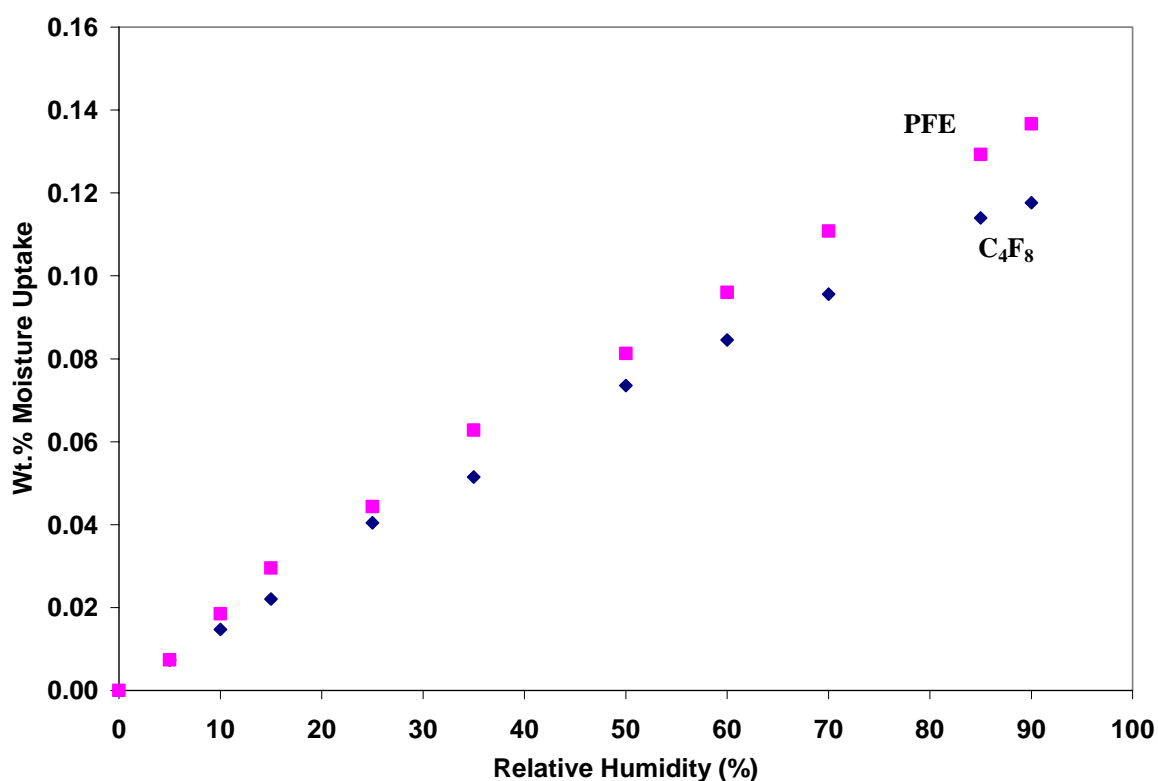


Figure 5.10 Steady-state moisture uptake (wt %) as a function of relative humidity (%) for films deposited from PFE and C₄F₈ (PFE = 0.68 μm ; C₄F₈ = 0.77 μm). Deposition conditions: 30W, 120 °C, 1 Torr. The data points were reproducible with less than 3% variation.

5.2.2 Transient Moisture Absorption Studies

Transient moisture absorption studies were conducted to determine the rate of moisture uptake and diffusivity through the fluorocarbon films. QCM studies were performed at a relative humidity of 85% ($T = 25\text{ }^{\circ}\text{C}$) on a plasma deposited PFE film ($680 \pm 9\text{ nm}$) and a plasma deposited C_4F_8 film ($770 \pm 2\text{ nm}$). Mass uptake initially increases rapidly with time and gradually reaches a steady state value for both films. Figure 5.11 shows a plot of normalized water vapor mass uptake for PFE film as a function of square root of time (\sqrt{t}) divided by film thickness (L). Water vapor uptake is initially linear up to a fractional mass uptake of 0.8. This initial linear behavior is attributed to Fickian type I diffusion [142, 143]. The deviation from Fickian behavior for fractional mass uptake of approximately 0.8 is characteristic of dual-mode sorption, commonly observed in a variety of polymer systems [144-148].

The Fickian diffusion model developed by Crank and Park was used to quantify moisture diffusion in both films (Equation 5.2) [143, 149],

$$\frac{M(t)}{M(\infty)} = 1 - \frac{8}{\pi^2} \sum_{n=0}^{\infty} \frac{1}{(2n+1)^2} \exp\left[-\frac{\pi^2 (2n+1)^2}{L^2} D t\right] \quad (5.2)$$

where $M(t)$ is the moisture uptake at time 't', $M(\infty)$ is the moisture uptake at $t = \infty$, L is the film thickness, and D is the water vapor diffusivity. Equation 5.2 can be modified for short times and rearranged to yield Equation 5.3,

$$D = \frac{\pi}{16} \left(\frac{M_1/M_\infty}{\sqrt{t}/L} \right)^2 \quad (5.3)$$

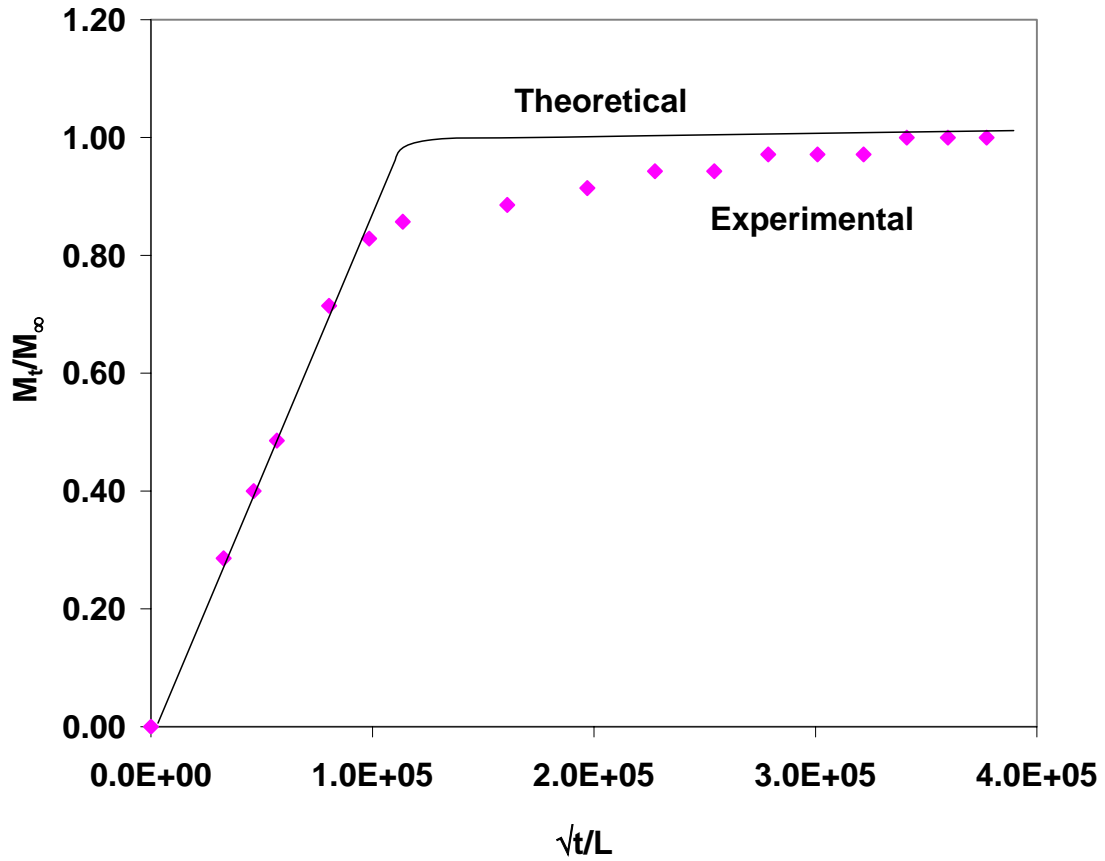


Figure 5.11 Normalized water vapor mass uptake by PFE film (at RH = 85%) as a function of square root of time (\sqrt{t}) divided by film thickness (L) [Deposition conditions: 30W, 120 °C, 1 Torr]. Theoretical plot refers to purely Fickian Type I Diffusion.

Figure 5.12 presents a plot of normalized water vapor mass uptake for OFCB film as a function of square root of time (\sqrt{t}) divided by film thickness (L). Water vapor uptake is

initially linear up to a fractional mass uptake of 0.84. The sorption behavior exhibited by film deposited from OFCB is similar to that of PFE.

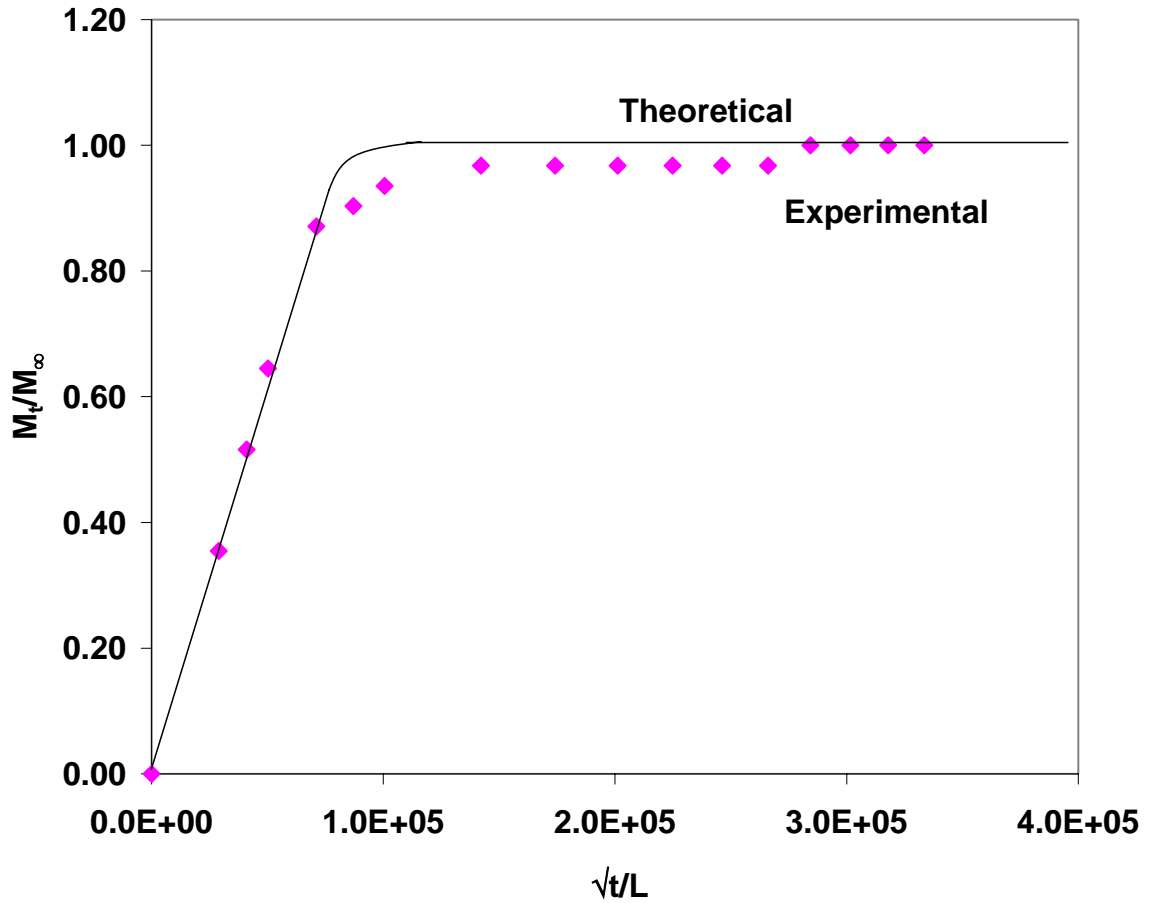


Figure 5.12 Normalized water vapor mass uptake by OFCB film (at RH = 85%) as a function of square root of time (\sqrt{t}) divided by film thickness (L) [Deposition conditions: 30W, 120 °C, 1 Torr]. Theoretical plot refers to purely Fickian Type I Diffusion.

From the initial slopes in Figure 5.11 and Figure 5.12, water vapor diffusivities were calculated in PFE and OFCB films using Equation 2. Table 5.3 presents film density and diffusivity data for PFE and C₄F₈ films at 85% relative humidity.

Table 5.3 Diffusivity data for PFE and C₄F₈ films at 85% relative humidity [Deposition Conditions: 30W, 120°C, and 1 Torr]

Precursor	Thickness (nm)	Density (g/cm ³)	Diffusivity (cm ² /sec)
PFE	680	1.93	1.01 x 10 ⁻¹¹
C ₄ F ₈	770	1.72	4.72 x 10 ⁻¹¹

Water vapor diffusivity for the C₄F₈ film is higher than that of the PFE film since the higher deposition rate of C₄F₈ relative to PFE leads to a lower density for C₄F₈ films (Table 5.3). It should be noted that there was a finite delay (~ 5 sec while switching from dry to humid environment) during which the cell reached equilibrium at the desired relative humidity. Hence, the values of diffusivity calculated (based on the assumption of a step change in relative humidity) from these data represent a lower estimate of the diffusivity. Film densities obtained in this study are higher than those reported previously [141]. One of the main reasons for this could be the use of higher RF power density in this study (three times) as compared to the previous study. Diffusivities obtained in this study were also an order of magnitude lower than those reported previously [141]. This can also be attributed to higher film densities (and therefore more extensive crosslinking)

as compared to the previous study. Water vapor diffusivity values for conventional (non-plasma polymerized) polymers such as polyimide (Kapton), polystyrene, polyethyl methacrylate, and ethyl cellulose are in the range of $10^{-7} - 10^{-9} \text{ cm}^2/\text{s}$ [150-152]. The two to three order of magnitude lower moisture diffusivity of plasma polymerized fluorocarbon films can be attributed to enhanced crosslinking in the highly reactive plasma environment.

In summary, fluorocarbon films deposited from PFE and OFCB were hydrophobic and the equilibrium moisture content for all films deposited from either monomer did not exceed 0.14 wt%. The moisture uptake in fluorocarbon films was found to be a bulk film as opposed to a surface phenomenon, where the moisture penetrates into the bulk of the film rather than simply adsorbing on the film surface. Furthermore, when the humid environment is removed (i.e. RH is brought down to zero or to the “dry” environment level), the moisture is completely desorbed from these films indicating that moisture is not chemically bonded into the film structure. This trend is similar to the trend observed by Tanikella et al. for fluorocarbon films deposited from PFE and C_4F_8 [141]

6. LIPOPHOBIC PROPERTIES OF FLUOROCARBON FILMS ON PAPER AND QUANTIFICATION OF GREASE BARRIER PROPERTIES

This chapter describes lipophobic (grease or oil barrier) properties of fluorocarbon films deposited on the surface of paper using PFE as a precursor. Fluorocarbon coated paper was analyzed for grease barrier properties using oleic acid penetration test and TAPPI test methods. Since none of these methods provides quantitative information on the grease barrier properties of coated paper, one of the main goals in this chapter is to develop methods for the quantification of grease barrier properties. Organic vapor quartz crystal microbalance (QCM) and magnetic resonance imaging (MRI) techniques were employed for the quantification of grease barrier properties where hexadecane was chosen as a grease surrogate. This chapter also describes the use of photoacoustic spectroscopy (PAS) to evaluate the fluorocarbon coating depth in plasma coated paper; these studies offer some indication of the depth to which the paper substrate has been modified.

6.1 Grease Barrier Materials and Properties

Grease barrier or oil repellence properties of materials is gaining wider attention in areas such as food packaging as the demand for food items such as fast food, pet food, and

bakery products increases. A number of coating systems are used to impart paper and paperboard with grease barrier properties both for packaging and non-packaging applications. Growth in the demand for barrier-coated products include fundamental changes in the packaging industry, new packaging applications related to changes in lifestyle such as microwave use and consumption of pre-prepared meals, the increased need for recycling cardboard cartons thus necessitating the replacement of wax and extrusion coatings, and the demand for better quality graphics.

Grease barrier properties can be primarily achieved in two ways: (1) mechanical action on pulp fibers, and (2) chemical addition to the fiber surface. Mechanical action applied to the fibers can be performed by either beating or refining the pulp to produce a hydrated pulp in which cellulose molecules and water link together to create a grease barrier, or by calendering or pressing paper between rolls, which densifies the sheet. In both cases of mechanical action, the grease barrier properties are achieved by enhanced fiber bonding and greater compaction to reduce the pore size and sheet porosity. It should be noted that mechanical action is an energy intensive operation and may not be preferred if energy costs are high.

Chemicals can be added to the paper either internally (wet end application) or as a surface treatment. When added to the paper at the wet end, the chemicals adhere to each individual fiber and a grease barrier is created as the bulk paper sheet is formed. Chemicals can be applied as a coating at the dry end creating a surface that repels oil or grease. Since paper has a porous structure, it is difficult to obtain complete coverage of

the paper surface unless a thick overcoat layer is applied. Thus it is not surprising that the porosity of paper has a direct effect on the degree to which the surface coating can provide grease barrier properties.

Some of the coating systems/methods used to provide oil barrier coatings are [5]:

- 1) Extrusion coating/lamination with various polyolefins.
- 2) Coating with fluorochemicals.
- 3) Hot-wax-based treatments.
- 4) Coating/lamination with aluminum.

In addition, coatings that come in contact with food must meet regulatory limits as mandated by U.S. Food and Drug Administration (U.S. FDA).

Paper and cellulose materials treated with fluorochemicals offer some advantages over polymer coated paper or laminates. For example, paper treated with fluorochemicals provides the flexibility of varying the amount of fluorochemical to control the degree of oil repellency required for a particular application. Also, paper treated with fluorochemicals can be easily recycled whereas polymer extrusion coatings and waxes must be separated from the paper during the recycling process.

Fluorochemical sizes can be applied during the paper manufacturing process and are generally applied in concentrations less than 0.1% fluorine by weight of paper. The

fluorochemicals can be applied internally (wet end) and externally (size press) [5]. There are four fluorochemical sizings available to the paper industry; the commercial names and manufacturers are [5]:

- 1) LODYNE (Ciba)
- 2) Zonyl (DuPont)
- 3) Scotchban (3M)
- 4) AsashiGuard (Asashi).
- 5) Maltase (ICI).

All of these paper fluorochemical sizings contain bisperfluoroalkyl functional groups which provide paper with grease repellency. The chemical groups also provide thermal stability to fibers which allows them to be exposed to temperatures greater than 250 °C. All of the above paper sizes also contain carboxylate or phosphate groups that ensure that fluorochemical paper sizes dissolve in water in order to help in dry or wet application.

Another method to coat paper and paper based materials is to use plasma enhanced chemical vapor deposition. In this technique, a fluorine-containing precursor is dissociated in a plasma environment and the fragments subsequently react at the paper/fiber surface to form a film. Coulson et al. (2000) have used perfluorocarbons such as 1H, 1H, 2H-perfluoro-1-dodecane in a pulsed inductively coupled, RF reactor to deposit low surface energy films [34]. The deposited films show both hydrophobic and oleophobic behavior due to the low surface tension surface created as a result of

perfluorocarbon deposition. Hydrophobicity and oleophobicity were measured using contact angle studies with water (for hydrophobic behavior) or organic liquids such as decane, hexadecane, heptane, pentane, etc. (for oleophobic behavior).

Recently, the oleophobicity of plasma polymerized fluorocarbon films has been investigated. Plasma polymerized fluorocarbon films rich in CF_2 species were deposited onto polyethylene (PE) using 1H,1H,2H-perfluoro-1-dodecene as the monomer [30]. The high concentration of CF_2 species in the resulting fluorocarbon films led to oil-repellent films with surface energies as low as 2.7 mJ/m^2 . One possible reason for the oleophobicity cited in this work was that the films might have CF_2 chain orientation normal to the substrate terminated by CF_3 groups. However, no information on the permeation of oleophobic molecules through these fluorocarbon films was presented.

There are a number of methods that are used to evaluate grease barrier properties of fluorochemically treated paper and paperboard materials.

1) Oil Kit Test (TAPPI Test T559)

A standard TAPPI test for grease resistance of paper employs mixtures of castor oil, toluene, and n-heptane [153]. This test was used to assess the grease resistance of the films for technical purposes in paper product applications. TAPPI test T559 for grease resistance is conducted by using a kit of 12 different mixtures of castor oil, toluene and n-heptane in order of decreasing surface energies, starting with pure castor oil and the 12th

test solution being a 45:55 mixture of toluene and n-heptane, respectively. In this manner, values between 1 and 12 are assigned to describe the grease resistance of the material. The paper is thus given a rating corresponding to the number of the mixture with the lowest surface tension that does not penetrate the paper (a higher number translates to better grease resistance).

2) Hot Mazola Oil Test

One milliliter of corn oil at 110 °C is added to paper to test the resistance of fluorochemically treated paper. Penetration of oil is observed over a 20 minute period, after which the oil is wiped off the paper using 5 plies of tissue paper having a basis weight of 25 g/m². The amount of oil uptake is recorded and converted to a percentage of the original oil drop mass that was absorbed.

3) Turpentine Resistance Test (TAPPI T454 om-00)

This is one of the most widely used test for grease resistance [154]. Turpentine is used as grease surrogate. The rate at which turpentine penetrates the treated paper (results expressed in seconds) is referred to as the measure of grease resistance. However, it is often difficult to tell at exactly what point the grease or oil actually penetrates the paper. Surface staining is easily detectable, but complete penetration is difficult to discern.

6.2 Grease Barrier Properties of PFE Coated Copy Paper

Fluorocarbon films using PFE as a precursor were deposited on regular copy paper for grease barrier experiments. Two methods (Oleic acid penetration test and TAPPI T559) were employed initially to assess the grease barrier properties of the coated paper.

6.2.1 Oleic Acid Penetration Studies

To evaluate the barrier properties of fluorocarbon-coated paper towards lipophilic materials, the penetration of oleic acid through fluorocarbon layers was studied. Fluoropolymer films with two different thicknesses (0.25 μm and 1 μm) were deposited onto the surface of regular copy paper (International Paper Company's *Copy Plus*; Brightness: 84; Weight Basis (500 sheets): 20 lb or 75 g/m^2 ; Thickness: 0.1 mm) using PFE as the precursor. Deposition conditions were: P = 1 Torr, T = 120 $^{\circ}\text{C}$, RF = 30 W on 4-cm platen, PFE flowrate = 20 sccm, and Argon flowrate = 75 sccm.

A clean sheet of paper was placed below the sheet to be tested. For the control (untreated) paper sample, the oleic acid drop was absorbed immediately ($< 1\text{s}$), likely due to capillary action. Oleic acid migrated through the paper within one minute and was absorbed into the clean paper sheet beneath. In the case of the 0.25 μm thick PFE film on paper sample, the oleic acid drop initially rested on the surface and penetrated slowly into the thin-film coated paper. After about 30 minutes, migration of oleic acid through the sample sheet to the underlying paper was observed. The area of the clean sheet below the

test sheet that was stained was approximately one order of magnitude smaller than in the case of the control sample. Even after several days, oleic acid residue was visible on the upper sample surface. In the case of the 1 μm thick film coated sample, the oleic acid drop was sessile on the sample surface and its presence was observed after several days. The oleic acid-stained area of the clean sheet placed underneath was even smaller than in case of the 0.25 μm film. Although the paper with a 1 μm fluorocarbon film thickness showed the least penetration of oleic acid, a small amount penetrated the sample within one minute. SEM studies indicate no change in surface morphology (i.e. no significant change in pore size) after fluorocarbon film deposition, indicating that individual fibers are coated during the deposition process; thus, the sheet is porous and partially permeable to lipophilic material. Overall, the fluorocarbon plasma coated surface results in increased grease barrier properties of paper, although additional studies are needed in order to tailor the film properties to yield a surface that displays negligible grease penetration.

6.2.2 TAPPI T559 Grease Barrier Test

TAPPI test T559 for grease resistance was also conducted to test the grease resistance of PFE coated paper samples. As mentioned earlier, the TAPPI test T559 (also known as “kit test”) was conducted using 12 test kits that use probe oils containing varying ratios of castor oil, toluene, and n-heptane. Table 6.1 presents the composition of probe liquid in a particular test kit.

Table 6.1 Test Kit Reagents (TAPPI T559 Test) [153]

Kit Number	<i>On % Volume Basis</i>		
	Castor Oil	Toluene	Heptane
1	100	0	0
2	90	5	5
3	80	10	10
4	70	15	15
5	60	20	20
6	50	25	25
7	40	30	30
8	30	35	35
9	20	40	40
10	10	45	45
11	0	50	50
12	0	45	55

Grease resistance (T559) ratings were assigned to the fluorocarbon coated paper. Table 6.2 presents the results of grease resistance testing. The data indicates that as the thickness of PFE coating increases, the grease rating number also increases indicating higher grease resistance. This qualitative trend may be due to incomplete coating of fibers at lower PFE film thickness; as the coating thickness increases, fiber coating improves, and the grease resistance increases.

Table 6.2 Grease Resistance Testing Results for PFE coated copy paper (TAPPI T559).

	Blank	Treatment Time (min.)				
		1	3	7	10	20
PFE Film thickness (nm)	0	54.8 ± 0.7	138.5 ± 1.5	313.6 ± 4.6	497.1 ± 4.4	1138.2 ± 16.9
Grease Resistance Rating	0	3	4	4	4	5

From the grease barrier test results presented using both Oleic acid studies and the TAPPI T559 test, it is clear that these tests only provide qualitative information about whether or not a particular sample is grease resistant. These tests do not provide any quantitative information about the degree of grease resistance. Since grease barrier properties are an important aspect of packaging materials, it is of interest to quantify the level of grease resistance provided to paper by a particular coating or formulation. The remainder of this chapter utilizes two techniques to quantify the grease barrier properties of fluorocarbon films. One technique, quartz crystal microbalance, uses hexadecane vapors as a grease surrogate to study its sorption/desorption characteristics on a fluorocarbon film deposited onto a quartz crystal. If the fluorocarbon film is a grease barrier, it should show a low affinity for hexadecane vapors. Magnetic resonance imaging (MRI), studies the permeation of hexadecane through thick paper samples coated with fluorocarbon film.

6.3 Hexadecane Vapor Studies Using a Quartz Crystal Microbalance

Hexadecane vapor was used as a grease surrogate in the quartz crystal microbalance studies. The experimental system consisted of a 6-way cross equipped with quartz crystal sensorhead, pressure gauge, nitrogen purge, vacuum pump, view port and a syringe port to dispense a known volume (and therefore known mass) of hexadecane; the detailed experimental configuration is presented in Chapter 3.

Fluorocarbon films were plasma-deposited onto quartz crystals using PFE as a precursor. Three different film thicknesses were deposited onto the crystals: 500 nm, 750 nm, and 1

μm . The deposition conditions for all three films were held constant: $P = 1$ Torr, $T = 120$ $^{\circ}\text{C}$, $\text{RF} = 100$ W (on 6" platen), PFE flowrate = 20 sccm, and Ar flowrate = 75 sccm. All QCM sorption and desorption experiments were conducted at 35 $^{\circ}\text{C}$ to prevent the condensation of hexadecane in the system.

Hexadecane sorption experiments conducted on a blank quartz crystal (no fluorocarbon film) showed no apparent change in mass as measured by the frequency counter. This eliminates the possibility that the quartz crystal absorbs hexadecane vapor. In experiments where fluorocarbon films were deposited onto quartz crystals, varying amounts of hexadecane were injected (10 μl – 100 μl ; Step size = 10 μl) into the system at time $t = 0$ during the sorption experiment. The frequency versus time data was acquired by a LabView program during sorption and desorption cycles. When the crystal frequency no longer changed with time, the fluorocarbon coated crystal appeared to have reached equilibrium with hexadecane vapor. During the desorption cycle, the throttle valve to the vacuum pump was opened and the system was purged with nitrogen. The acquisition of frequency versus time data was terminated when hexadecane had completely desorbed from the fluorocarbon coated quartz crystal, as evidenced by recovery of the original mass (frequency) on the QCM.

6.3.1 Hexadecane Uptake by Fluorocarbon Films

Figure 6.1 resents the mass uptake of hexadecane with varying hexadecane vapor concentration by fluorocarbon films of different thicknesses. It should be noted that while

the hexadecane mass uptake increases with film thickness at all hexadecane concentrations, the ratio of mass uptake for two different thickness films is lower than the ratio of film thicknesses. For example, the ratio of mass uptake by the 750 nm film to that by 500 nm film is about 1.45 (Thickness ratio of 750 nm and 500nm = 1.5) whereas the ratio of mass uptake by 1000 nm film to that by 500 nm film is about 1.8 (Thickness ratio of 1000 nm and 500 nm = 2). This may indicate that while the thicker film absorbs more hexadecane, the hexadecane vapor may not permeate the entire mass of the film.

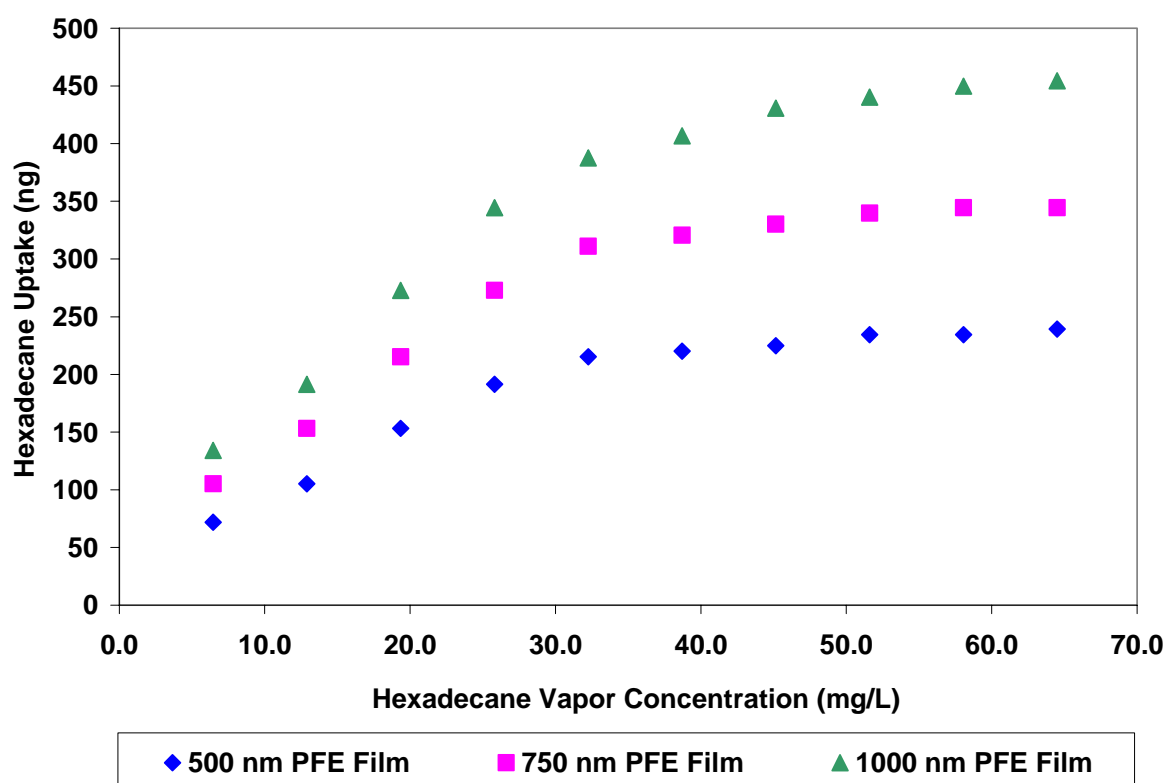


Figure 6.1 Hexadecane uptakes with varying hexadecane vapor concentration by fluorocarbon films of different thicknesses. The errors in measurements were less than 3%.

Figure 6.2 resents the weight percent hexadecane uptake with varying hexadecane vapor concentration by fluorocarbon films of different thicknesses. The weight percent of hexadecane was defined as (Equation 6.1):

$$Wt\% \text{ Hexadecane Uptake} = \frac{\text{Hexadecane uptake by the film (ng)}}{\text{Mass of the film (ng)}} \times 100 \quad (6.1)$$

It is clear from Figure 6.2 hat fluorocarbon films of different thickness show similar hexadecane absorption on a weight percent basis. It should be noted that at the highest hexadecane concentration (65 mg/L) the weight percent of hexadecane absorbed was ~0.6%, indicating low hexadecane sorption. Also, increasing the hexadecane concentration beyond 65 mg/L does not increase the hexadecane absorption in any of the films suggesting that the films are saturated at this concentration (Figure 6.1 and 6.2). It should be noted that a low percentage of hexadecane incorporation indicates that fluorocarbon films have low affinity for hexadecane, which translates into a low solubility of hexadecane in fluorocarbon films.

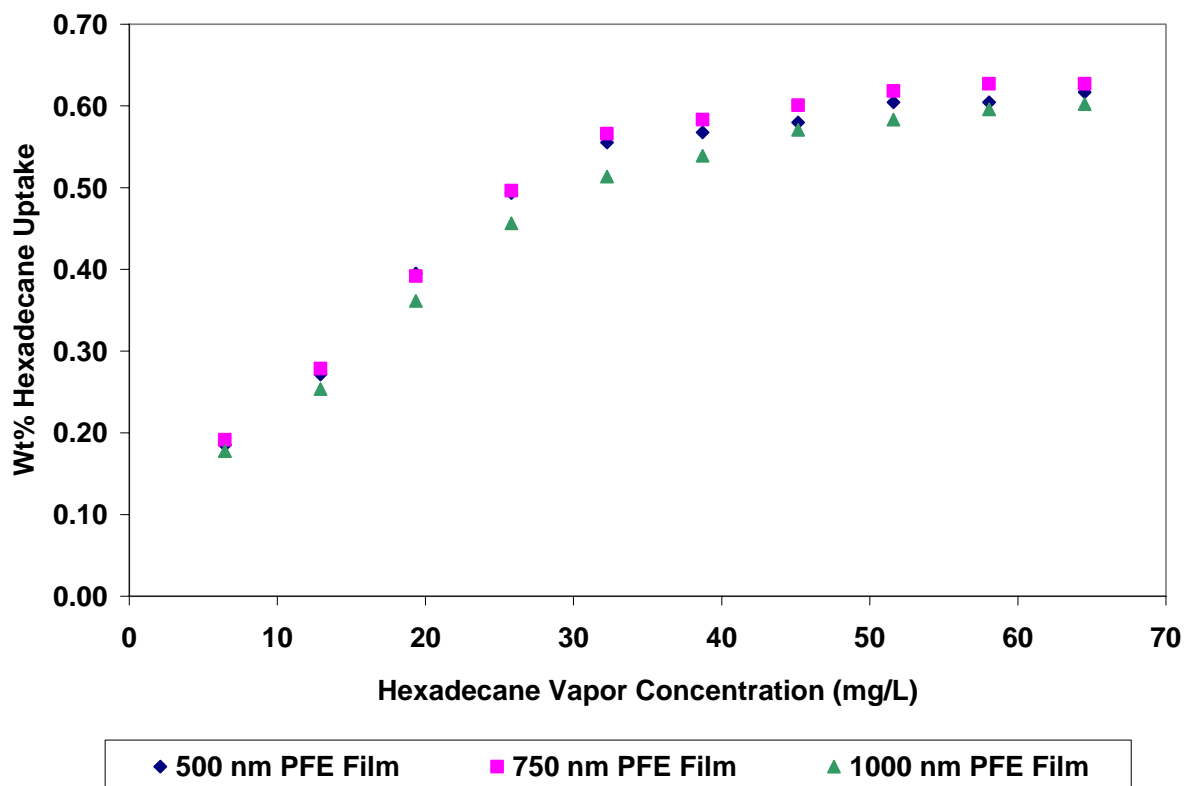


Figure 6.2 Wt% hexadecane uptakes with varying hexadecane vapor concentration by fluorocarbon films of different thicknesses. The errors in measurements were less than 3%.

6.3.2 Hexadecane Sorption and Desorption Kinetics

Absorption and desorption of hexadecane were studied as a function of time in the QCM system. Thus, transient absorption and desorption studies were conducted with varying concentrations of hexadecane. The mass of the fluorocarbon film deposited on the quartz crystal as well as the hexadecane uptake can be calculated using the Sauerbrey equation described in Chapter 3. Figure 6.3 shows a typical plot of frequency as a function of time on a quartz crystal coated with a PFE film of 500 nm with a hexadecane concentration of 6.5 mg/L. This data was obtained for PFE films of different thicknesses at various

hexadecane concentrations. The change in frequency with respect to initial frequency corresponds to the mass change of the film due to hexadecane sorption or desorption.

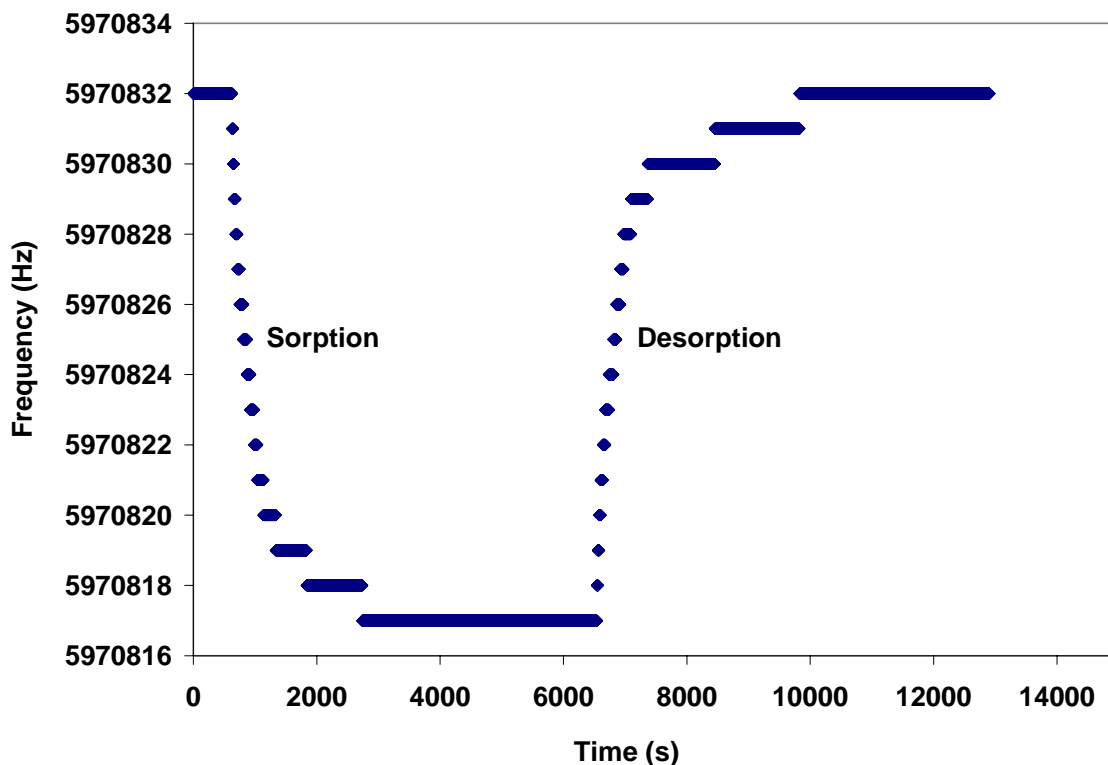


Figure 6.3 Typical frequency versus time data for hexadecane absorption and desorption on PFE film thickness of 500 nm and a hexadecane concentration of 6.5 mg/L.

Figure 6.4 shows a plot of normalized mass absorption of hexadecane versus the square root of time at a hexadecane concentration of 6.5 mg/L (lowest concentration studied) on a PFE film of thickness 500 nm, respectively. Figure 6.5 shows the same plot for the desorption cycle on 500 nm film. It should be noted that the low concentration

experiment (6.5 mg/L hexadecane concentration) was the first experiment performed on all PFE films of different thicknesses. It is clear from Figure 6.4 that after a small initial delay in hexadecane uptake, the normalized mass uptake increases linearly with the square root of time up to a mass fraction of 0.8 and then gradually plateaus to a steady state (equilibrium) value. Theoretical line represents purely Fickian Type I diffusion.

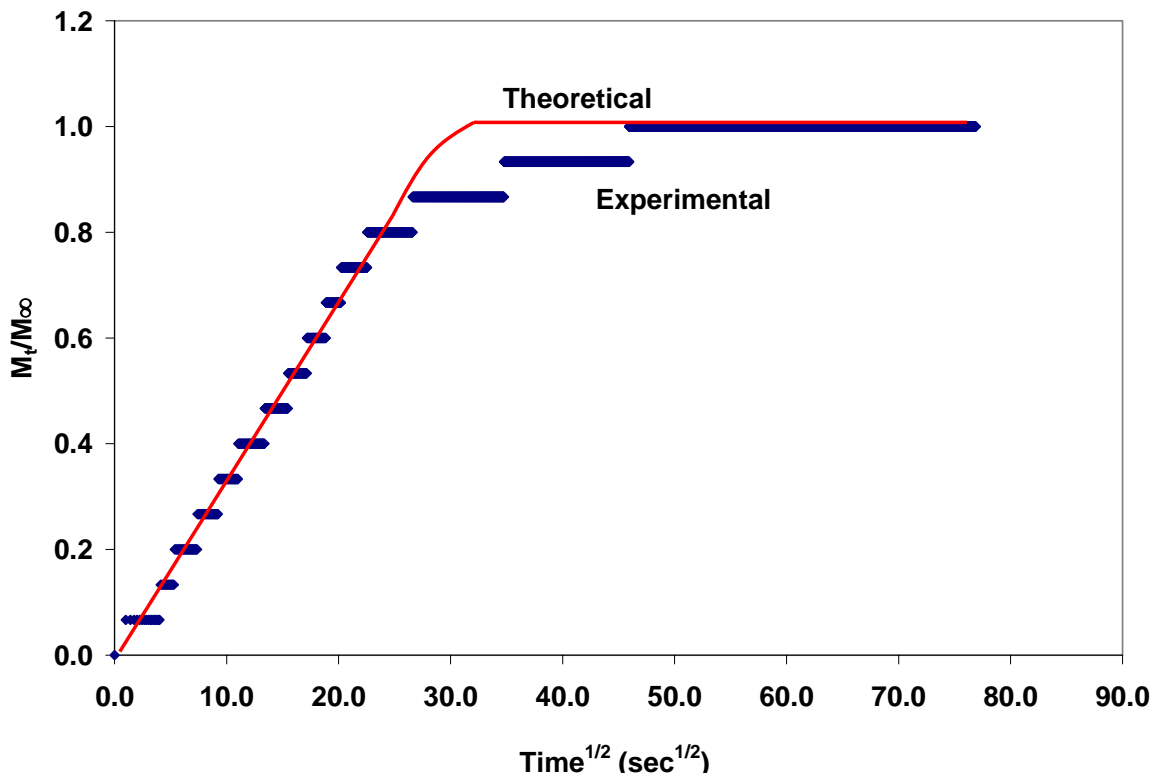


Figure 6.4 Normalized mass uptake of hexadecane vapor by a 500 nm fluorocarbon film at a hexadecane concentration of 6.5 mg/L as a function of square root of time.

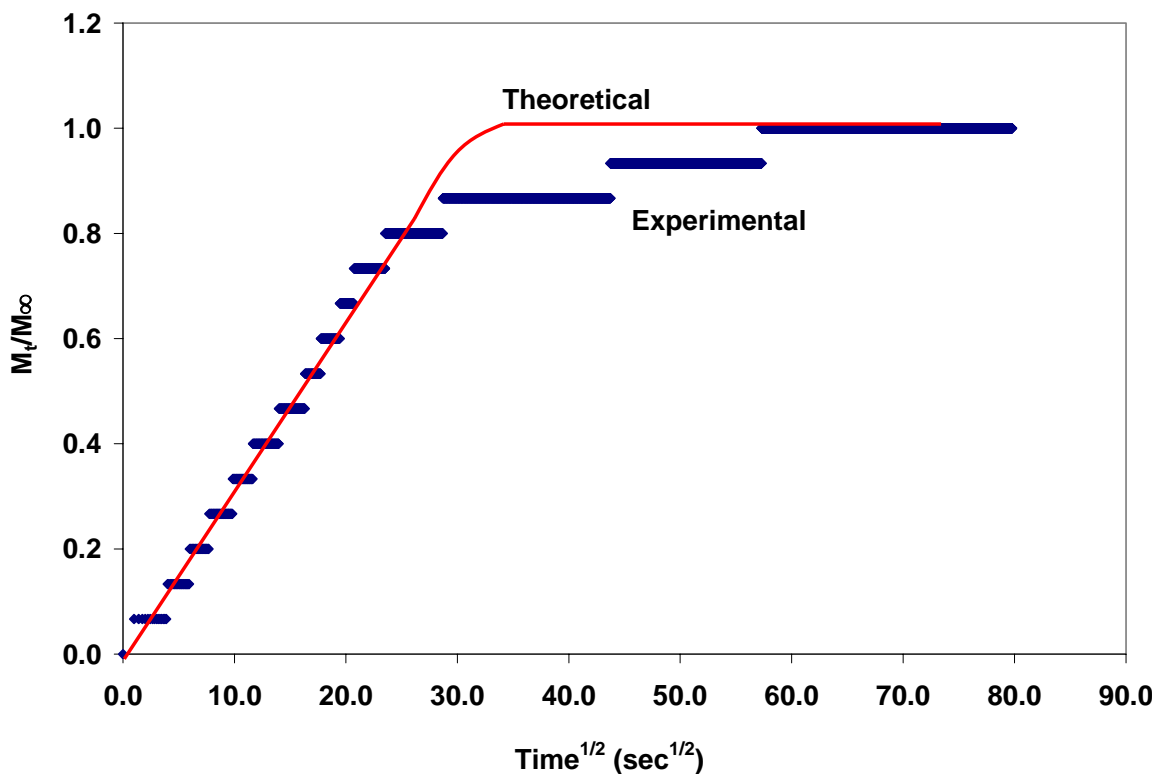


Figure 6.5 Normalized mass loss (desorption) of hexadecane by 500 nm fluorocarbon film at a hexadecane concentration of 6.5 mg/L as a function of square root of time.

Figure 6.6 and Figure 6.7 present the hexadecane sorption and desorption kinetics at a hexadecane concentration of 6.5 mg/L for PFE film thicknesses of 750 nm, respectively. Figure 6.8 and Figure 6.9 present the same kinetics plots for 1 μ m PFE film. A small initial delay is observed in both films analogous to the 500 nm PFE film. For both cases, the fractional mass uptake (M_t/M_∞) increases with the square root of time up to the fractional mass of 0.8 followed by a slower approach to equilibrium.

In all studies, the initial delay in hexadecane absorption is believed to be due to the large size of the hexadecane molecule trying to absorb in a heavily crosslinked plasma polymerized fluorocarbon film. The delay also relates to the relaxation of crosslinked plasma polymer as rapid segmental motions are likely absent. Fractional mass uptake M_t/M_∞ increases linearly with $t^{1/2}$ in all situations indicating that the sorption kinetics are controlled by Fickian diffusion. At longer times, however, the fractional mass uptake exhibits a protracted, asymptotic approach towards equilibrium. This behavior may be ascribed to mass uptake kinetics limited by polymer swelling and structural rearrangement to accommodate the penetrant rather than to Fickian diffusion. Such two stage kinetics have been observed for organic vapor sorption in glassy polymers such as linear alkanes in PET [155], acetone in PET [156], and ethyl benzene in polystyrene [157]. Since fluorocarbon films are expected to be rigid and glassy due to extensive crosslinking in the plasma environment, it is expected that they will follow a dual-mode sorption model [158, 159].

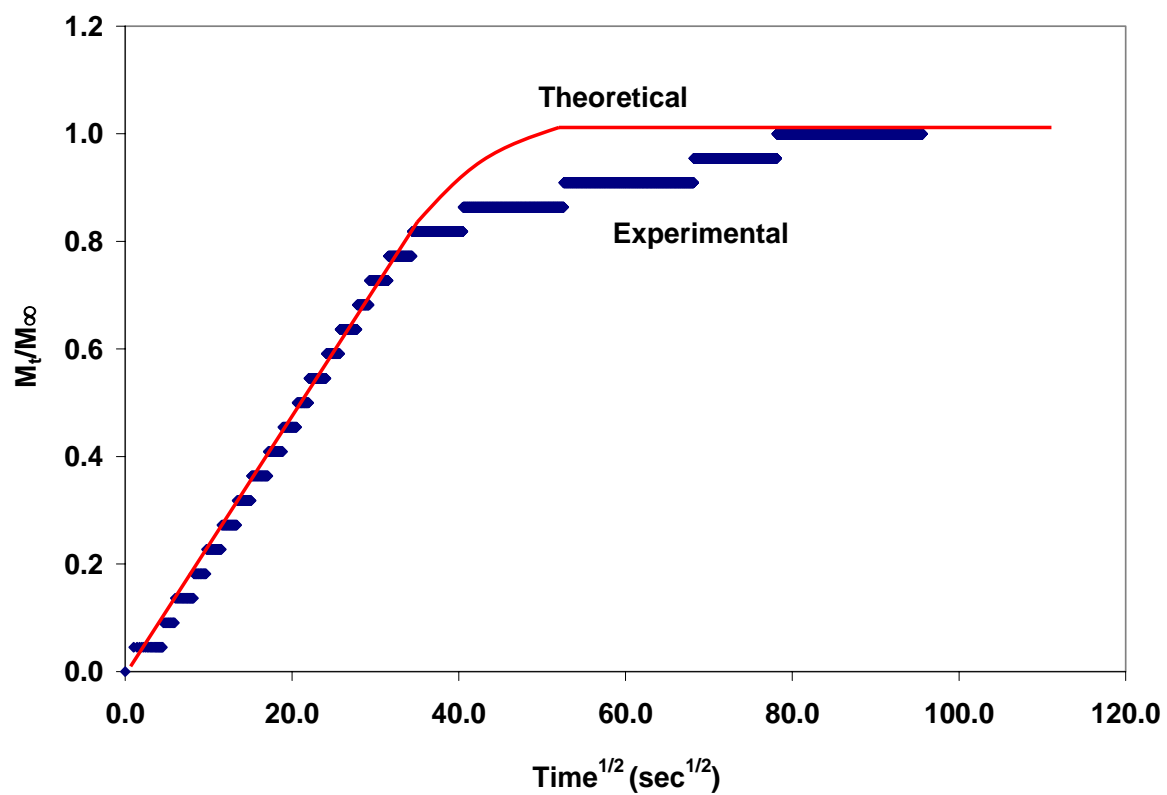


Figure 6.6 Normalized mass uptake of hexadecane vapor by 750 nm fluorocarbon film at a hexadecane concentration of 6.5 mg/L as a function of square root of time.

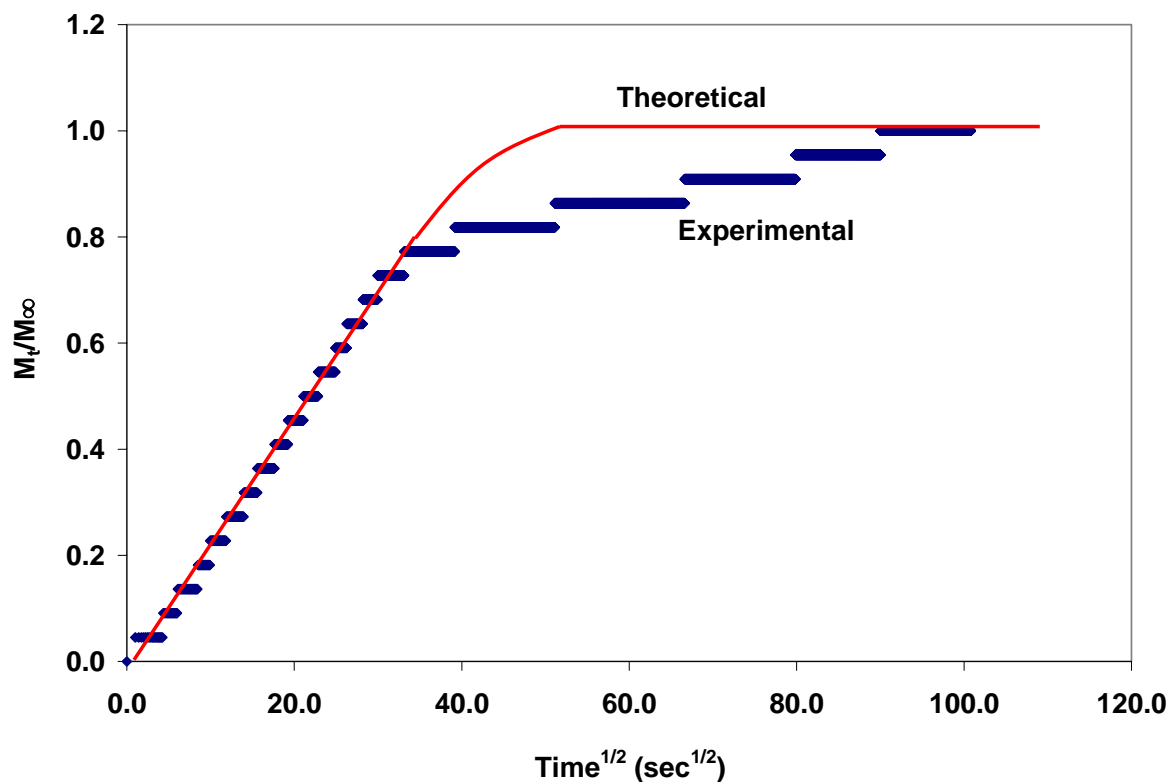


Figure 6.7 Normalized mass loss (desorption) of hexadecane by 750 nm fluorocarbon film at a hexadecane concentration of 6.5 mg/L as a function of square root of time.

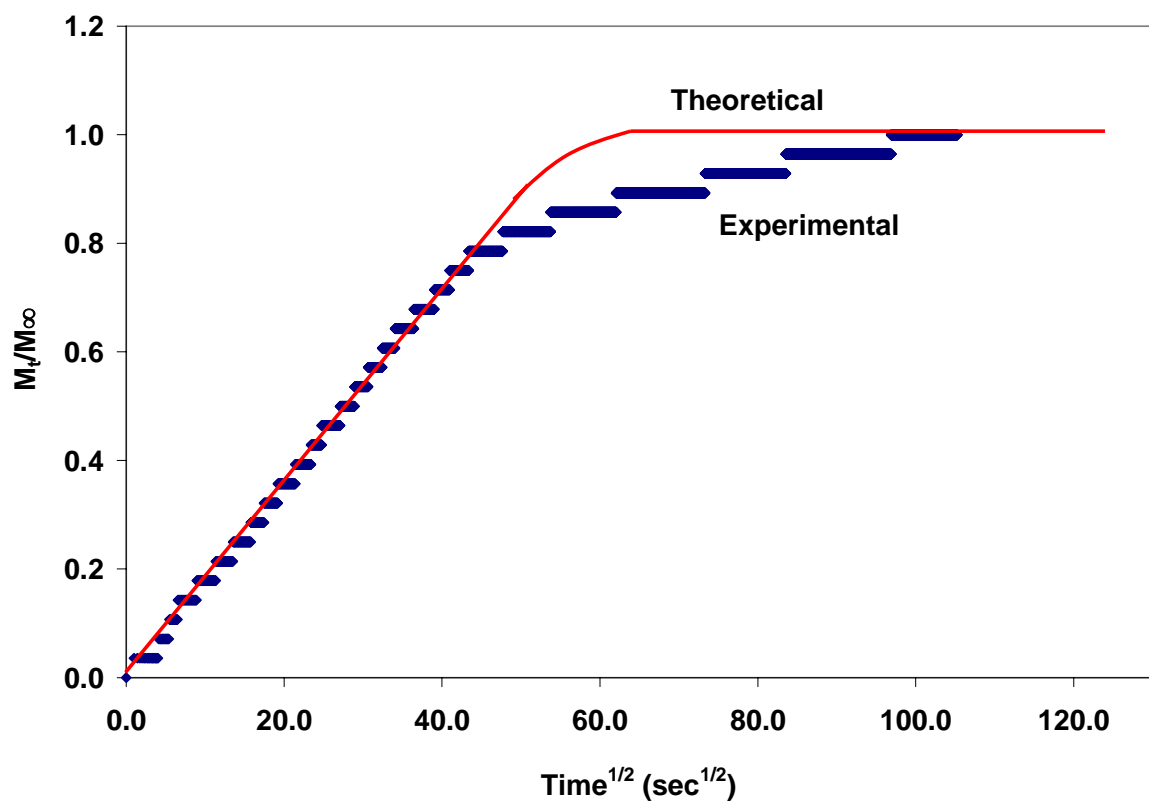


Figure 6.8 Normalized mass uptake of hexadecane vapor by 1 μm fluorocarbon film at a hexadecane concentration of 6.5 mg/L as a function of square root of time.

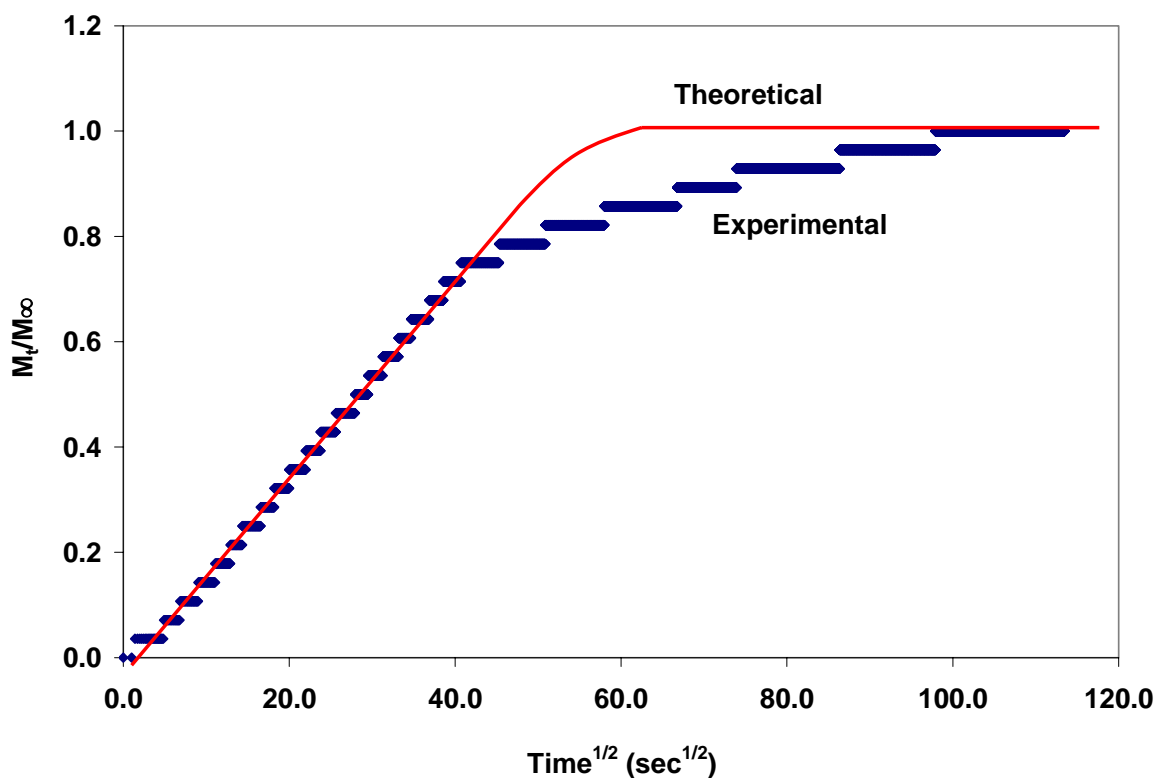


Figure 6.9 Normalized mass loss (desorption) of hexadecane by 1 μm fluorocarbon film at a hexadecane concentration of 6.5 mg/L as a function of square root of time.

After the first sorption and desorption experiment on quartz crystals coated with PFE films of different thicknesses, subsequent experiments with varying hexadecane concentrations were conducted on same PFE coated crystal after flushing with dry nitrogen to ensure complete hexadecane removal from the previous experiment. This was also confirmed by return of chamber pressure to the base pressure after each desorption experiment and dry nitrogen flush.

Figure 6.10 and Figure 6.11 present the sorption and desorption kinetics at a hexadecane concentration of 19.5 mg/L for PFE film thicknesses of 500 nm, respectively. Similarly,

Figure 6.12 and Figure 6.13 present the sorption and desorption kinetics data for 750 nm film, respectively, while Figure 6.14 and Figure 6.15 present the same data for and 1 μm PFE film. In all cases, it is clear that the initial delay, which was present in the case of the very first experiment with a hexadecane concentration of 6.5 mg/L, is not present. This can be explained if it is assumed that the fluorocarbon film structure is expanded slightly as compared to the film which has not been exposed to hexadecane, implying that the fluorocarbon film is altered for subsequent hexadecane sorption/desorption experiments. Similar kinetic data plots were obtained for varying hexadecane concentrations invoked. In case of all the PFE films, the uptake of hexadecane is initially linear up to fractional mass uptakes of 0.8. This linear behavior for fractional mass uptake up to 0.8 was observed for all the fluorocarbon films and hexadecane concentration studied. Deviation from Fickian behavior for fractional mass uptakes above 0.8 is typical of dual-mode sorption commonly observed in variety of polymer systems as explained previously [147, 155, 158, 159].

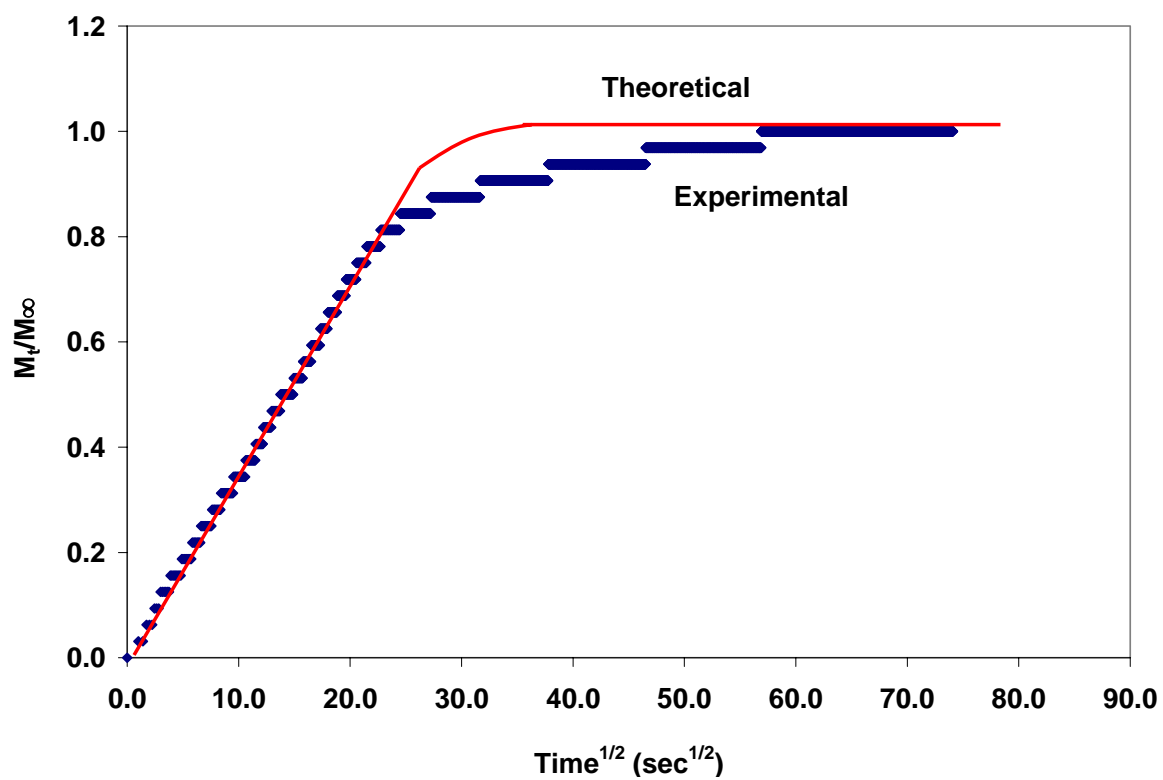


Figure 6.10 Normalized mass uptake of hexadecane vapor by 500 nm fluorocarbon film at a hexadecane concentration of 19.5 mg/L as a function of square root of time.

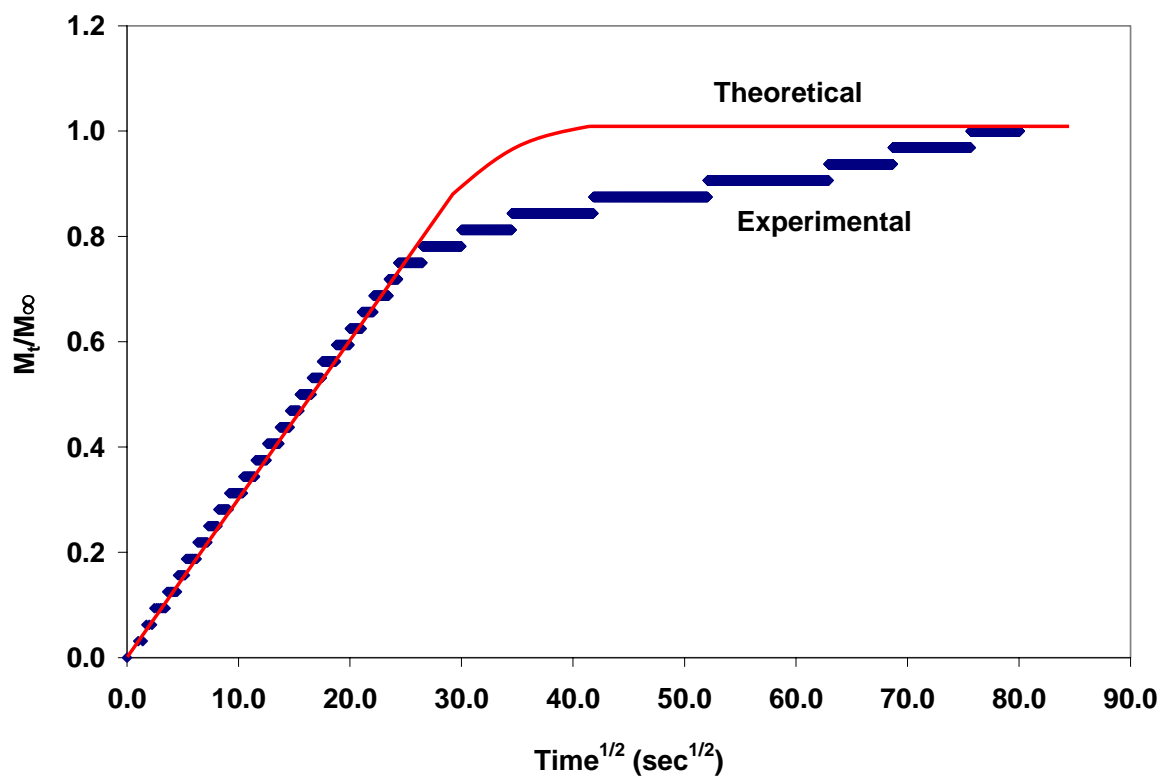


Figure 6.11 Normalized mass loss (desorption) of hexadecane by 500 nm fluorocarbon film at a hexadecane concentration of 19.5 mg/L as a function of square root of time.

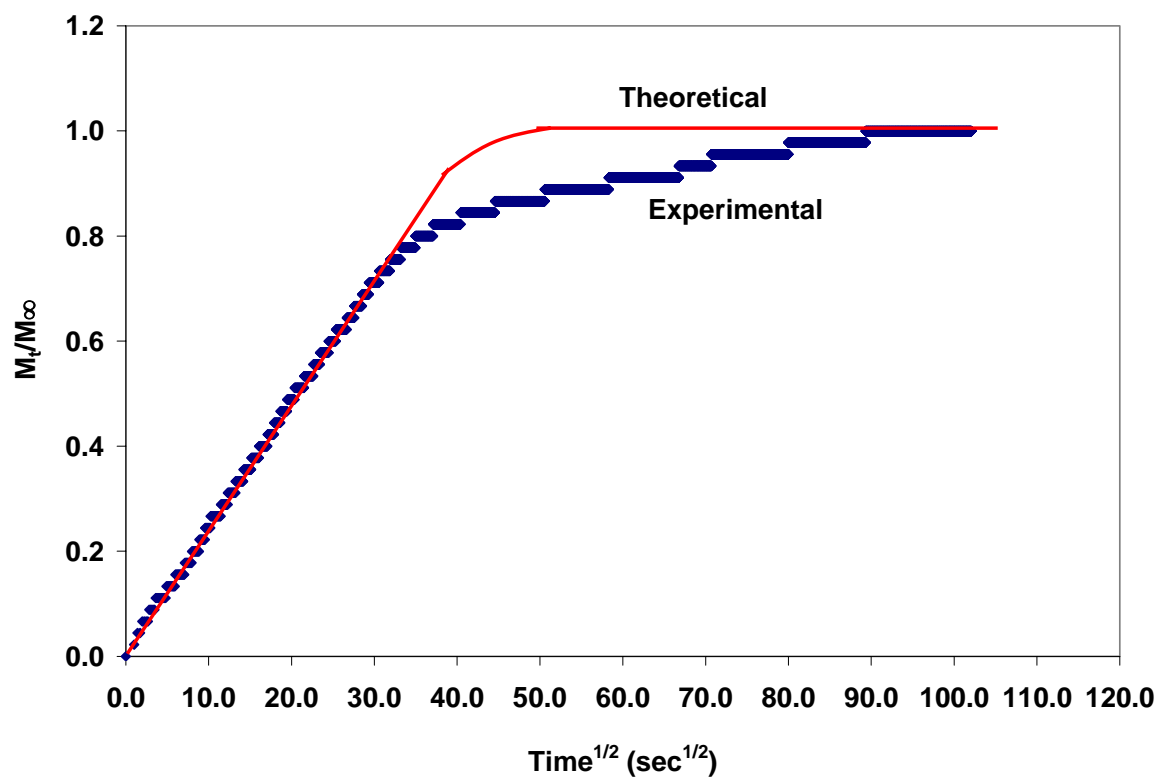


Figure 6.12 Normalized mass uptake of hexadecane vapor by 750 nm fluorocarbon film at a hexadecane concentration of 19.5 mg/L as a function of square root of time.

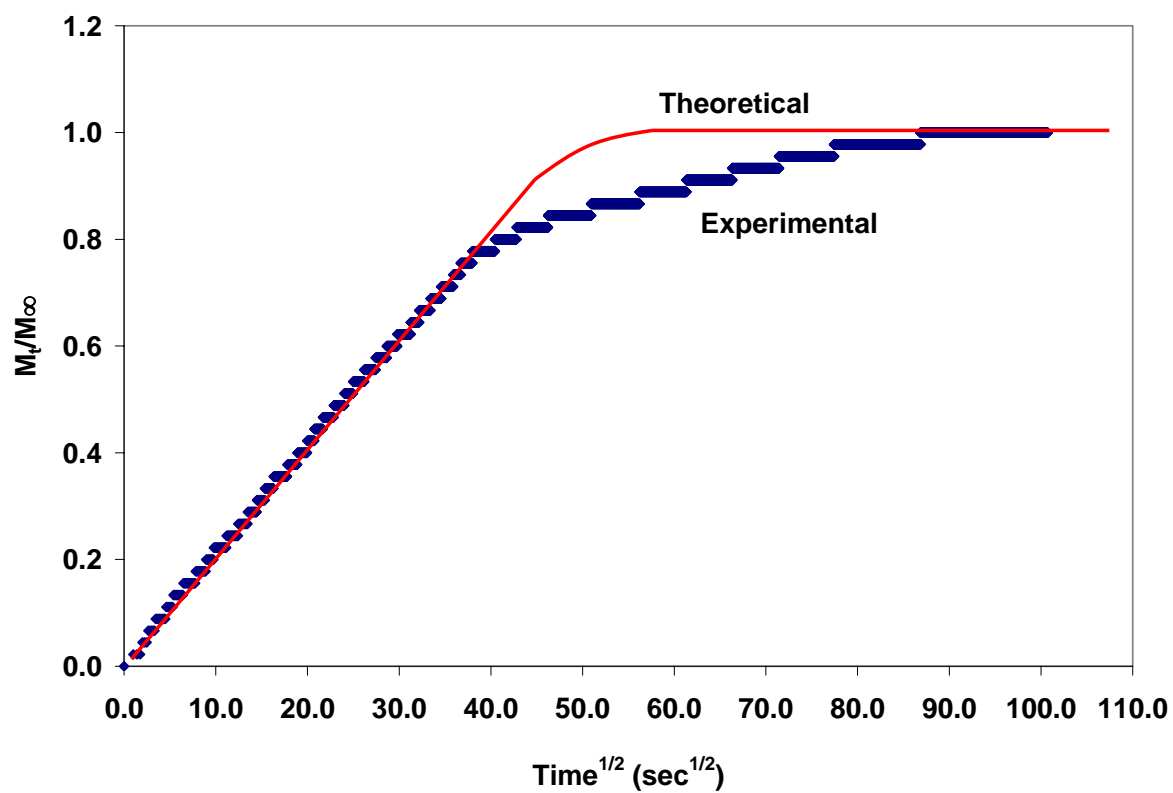


Figure 6.13 Normalized mass loss (desorption) of hexadecane by 750 nm fluorocarbon film at a hexadecane concentration of 19.5 mg/L as a function of square root of time.

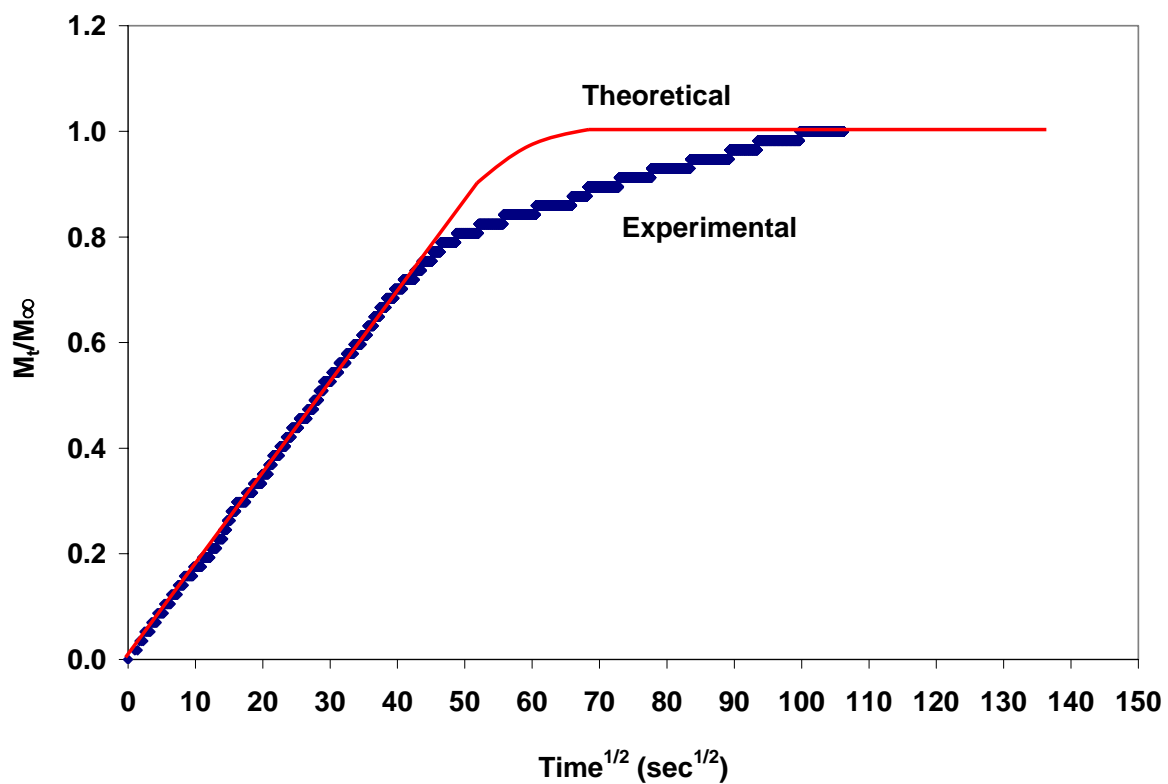


Figure 6.14 Normalized mass uptake of hexadecane vapor by 1 μm fluorocarbon film at a hexadecane concentration of 19.5 mg/L as a function of square root of time.

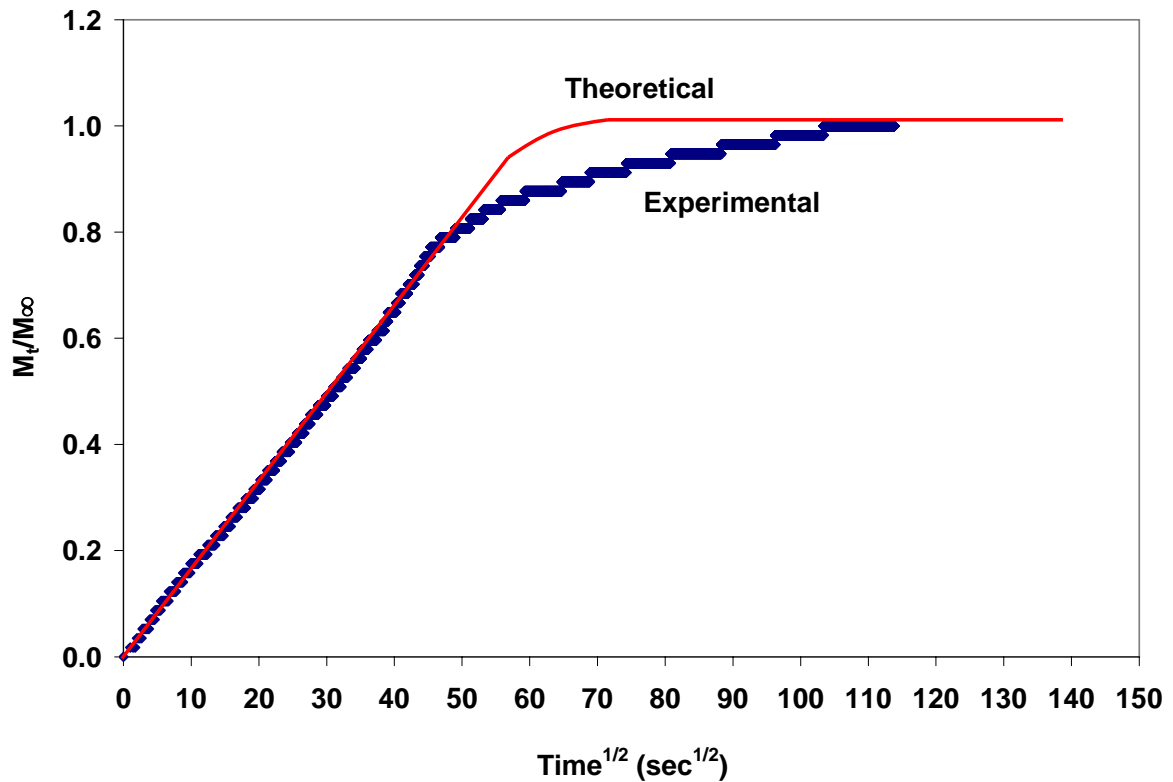


Figure 6.15 Normalized mass loss (desorption) of hexadecane by 1 μm fluorocarbon film at a hexadecane concentration of 19.5 mg/L as a function of square root of time.

6.3.3 Hexadecane Diffusion Mechanism in Fluorocarbon Films

Usually, mass transfer in a thin polymer film in a closed volume is assumed to obey one-dimensional transient Fickian diffusion. Typically, additional assumptions used to simplify the analysis are: (1) the internal mass diffusion and convection are faster than diffusion through the thin film, (2) the diffusion coefficient through the thin film is concentration-independent, (3) the source concentration of the diffused mass is constant, and (4) the diffusion process is carried out at constant temperature. Under such conditions, the following equation governs the diffusion process (Equation 6.2):

$$\frac{\partial C}{\partial t} = \frac{\partial}{\partial x} \left(D \frac{\partial C}{\partial x} \right) \quad (6.2)$$

where C is the diffusant concentration, t is time elapsed, x is the direction in which diffusion is dominant, and D is the diffusivity. This behavior is known as Fick's law of diffusion, where the flux of the diffusing species varies as the concentration gradient normal to the area [143]. In Fickian diffusion behavior, the mass increase in a polymer film due to penetrant uptake is initially proportional to the square-root of time. This is also known as Case I transport. Another requirement of Fickian diffusion behavior is that the absorption curves for films of different thicknesses should be superimposable onto a single curve if each curve is replotted in the form of a reduced curve, i.e. M_t/M_∞ is plotted against $t^{1/2}/L$. This also applies to the corresponding desorption curves obtained for different film thicknesses [143].

Fickian diffusion is commonly described by the diffusion model developed by Crank and Park, where the time-dependent mass increase for a thin polymer film can be written as (Equation 6.3)[143, 149]:

$$\frac{M(t)}{M(\infty)} = 1 - \frac{8}{\pi^2} \sum_{n=0}^{\infty} \frac{1}{(2n+1)^2} \exp \left[- \frac{\pi^2 (2n+1)^2 D}{L^2} t \right] \quad (6.3)$$

where $M(t)$ is the penetrant uptake at time 't', $M(\infty)$ is the penetrant uptake at $t = \infty$ (equilibrium), L is the film thickness, and D is the penetrant diffusivity. At short times, this expression can be simplified to Equation 6.4:

$$\frac{M_t}{M_\infty} = \frac{2}{L} \sqrt{\frac{D t}{\pi}} \quad (6.4)$$

The above expression can be rearranged to obtain a simplified expression to calculate diffusivity (Equation 6.5):

$$D = \frac{\pi L^2}{16} \left(\frac{M_t/M_\infty}{\sqrt{t}} \right)^2 \quad (6.5)$$

The quantity in the parenthesis represents the initial slope of the plot of M_t/M_∞ versus square root of 't'. Thus, the diffusion coefficient can be determined from the initial slope of the absorption curve plotted as M_t/M_∞ versus \sqrt{t} .

For the hexadecane vapor-fluorocarbon film system, it is clear that the fraction of hexadecane uptake (M_t/M_∞) increases linearly with the square root of time in all the cases, indicating Fickian behavior. Thus, the slope of each sorption and desorption kinetic plot was used to calculate the diffusivity of hexadecane in fluorocarbon films of different thicknesses. Since the sorption and desorption behavior of hexadecane (plot of M_t/M_∞ versus \sqrt{t}) scales with the inverse of film thickness, it is obvious that the reduced

diffusion plots will superimpose each other, further indicating that Fickian Type I diffusion is a valid model. Table 6.3 presents the calculated diffusivities of hexadecane vapor in PFE films of different thicknesses. The error range in the diffusivities (\pm values) represents the 95% confidence interval.

Table 6.3 Hexadecane Diffusivity in Fluorocarbon Films of Different Thicknesses (Error values represent 95% confidence interval over the mean).

Hexadecane Concentration (mg/L)	PFE Film Thickness	D (cm ² /s) (Sorption)	D (cm ² /s) x 10 ¹³ (Desorption)
6.5	500 nm	$5.42 \times 10^{-13} \pm 7.71 \times 10^{-14}$	$4.82 \times 10^{-13} \pm 1.43 \times 10^{-13}$
	750 nm	$6.06 \times 10^{-13} \pm 8.41 \times 10^{-14}$	$5.82 \times 10^{-13} \pm 1.60 \times 10^{-13}$
	1 μ m	$6.14 \times 10^{-13} \pm 6.82 \times 10^{-14}$	$6.08 \times 10^{-13} \pm 1.17 \times 10^{-13}$
19.5	500 nm	$6.09 \times 10^{-13} \pm 1.53 \times 10^{-13}$	$4.32 \times 10^{-13} \pm 2.28 \times 10^{-13}$
	750 nm	$5.96 \times 10^{-13} \pm 8.45 \times 10^{-14}$	$5.62 \times 10^{-13} \pm 1.45 \times 10^{-13}$
	1 μ m	$5.93 \times 10^{-13} \pm 1.06 \times 10^{-13}$	$5.84 \times 10^{-13} \pm 9.34 \times 10^{-14}$

From the diffusivities calculated above, there is no clear trend in hexadecane diffusivity with changing PFE film thickness. Also, the desorption diffusivities are of the same order of magnitude (10^{-13} cm²/s) as the sorption diffusivities (within the 95% confidence interval). Since the diffusion is Fickian in nature, sorption and desorption diffusivities are expected to be similar. Diffusivities were also calculated at other hexadecane concentrations with different film thicknesses and no general trends were observed. In all cases, hexadecane sorption and desorption diffusivities were on the order of 10^{-13} cm²/s.

After a fractional mass uptake of 0.8, the hexadecane uptake is slower as equilibrium is approached. This indicates that there is two-stage absorption process; the first stage is Fickian in nature, followed by an anomalous stage which is not diffusion controlled [143]. Many explanations have been put forward for the anomalous behavior including time dependent solubility [160], variable surface concentration [161], polymeric relaxation [162], and free volume [163]. Also, the diffusion coefficient could be thickness dependent near the interface. In general, the initial fast stage in for hexadecane was found to be Fickian and the initial slope can be used to calculate the diffusion coefficient for hexadecane [143]. The anomalous behavior in hexadecane absorption is probably related to polymer matrix expansion/relaxation from small swelling stresses that allow an increased amount of hexadecane incorporation into the film [164, 165].

The weight percent sorption of hexadecane vapor in fluorocarbon films is $\sim 0.6\%$ for films of different thicknesses indicating low affinity of fluorocarbon films towards hexadecane. Thus, these results present quantitative information on the amount of hexadecane incorporation into fluorocarbon films deposited from PFE. The diffusivity of hexadecane in fluorocarbon films is on the order of $10^{-13} \text{ cm}^2/\text{s}$. It should be noted that the diffusivity of hexadecane in PFE films is two to three orders of magnitude lower than that of water vapor [141, 166]. This can be attributed to the larger size of the hexadecane molecule compared to that of water.

6.4 Magnetic Resonance Imaging of Hexadecane Permeation

Magnetic resonance imaging (MRI) was used to quantify the grease barrier properties of fluorocarbon coated paper. Liquid hexadecane was used as a grease surrogate since it is a long chain hydrocarbon liquid. While regular copy paper with an average thickness of 100 μm was used as a substrate for fluorocarbon deposition in most of the experiments, this thickness was not sufficient to track the permeation of hexadecane through paper. The magnetic resonance imaging system used to image materials has a resolution of about 25 μm i.e. it generates one pixel of the image for a film depth of 25 μm . Thus, a very few (only four) data points would be obtained if regular copy paper was used. Thick hand sheets (1.4 – 1.8 mm) of varying freeness were prepared using Soft Wood Bleached Kraft (SWBK) pulp. The valley beater method was used to generate pulps of different freeness using the TAPPI T200 method [99].

6.4.1 MRI Sample Preparation

Six different freeness papers were prepared for the MRI experiments by refining SWBK pulp in a valley beater. The term freeness is used to define how quickly water is drained from the pulp. The opposite of freeness is slowness. Freeness or slowness is a function of beating or refining. Freeness and slowness reported in ml CSF (Canadian Standard Freeness) and degree SR respectively are also a measure of the degree of refining or beating. Refining refers to the mechanical treatment of the fibers in water to increase surface area, flexibility and promote bonding when dried. With increased refining time in

a valley beater, the surface area of fibers is increased as they become finer, thereby improving the fiber bonding. Thus, a more refined pulp will make a more compact paper with lower porosity as compared to unrefined or less refined pulp. Freeness, porosity, and average pore size of the paper pulp, therefore, decrease with increased refining due to increase compaction. Various parameters of six different handsheets prepared for this study are presented in Table 6.4.

Table 6.4 Parameters of handsheets fabricated from SWBK with varying refining time.

Refining Time (min)	Freeness (ml) CSF	Average Thickness (mm)	Porosity (s) (100 cm ³ of air)	Surface Roughness (μm)
0	785	1.8	10	11.6
5	730	1.6	32	10.1
15	628	1.6	BDL [*]	15.2
25	480	1.6	BDL [*]	13.1
35	330	1.5	BDL [*]	13.2
45	140	1.4	BDL [*]	15.1

* BDL refers to “below detectability limit” of the instrument (Gurley Densometer)

It is clear from the above table that increased refining time leads to lower freeness and lower porosity. Handsheets with the above parameters were coated with fluorocarbon films deposited using PFE as a precursor using typical deposition conditions [P = 1 Torr, T = 120 °C, RF = 100 W on 6” platen, PFE flowrate = 20 sccm, and Ar flowrate = 75 sccm]. The fluorocarbon film deposition was conducted for a period of time sufficient to deposit an average PFE film thickness of 5.5 μm on all handsheets. The main reason for using thicker films was to provide enhanced surface coverage to the paper and to improve

the fluorination of the paper matrix. This should improve the grease barrier properties of PFE coated handsheets.

6.4.2 MRI Experiment Methodology

During the MRI experiments, a known volume of hexadecane (10 μ l) was dispensed onto the surface of uncoated and PFE coated samples of different handsheets. Approximately 40 seconds were required to load the sample into the MRI instrument and begin data collection (images). For each sample on which 10 μ l of hexadecane was dispensed, 64 frames (images) were collected with a collection time of 34 seconds per frame (image). The data was acquired using the Spin Echo (SE) technique described in chapter 3. A 10 mm RF coil was used in the experiment with a 90° hard pulse length equal to 200 μ s and 180° Gaussian-shaped pulse length equal to 1000 μ s. The field of view for the sample was 0.3 cm in the z-direction (direction perpendicular to paper surface, through plane) and 2 cm in x-direction (direction parallel to paper surface, in-plane). For the SE method, TE was set equal to 2.46 ms, and TR was set equal to 500 ms in all the experiments. Each image collected in the experiments mapped the SE signal intensity due to hexadecane permeation at various points in the sample. Contrast images indicated the presence (or absence) of hexadecane at various layers of the paper sample. By comparing contrast images obtained from all 64 frames, time dependent SE signal intensity at each point in the sample can be obtained. It should be noted that the data was acquired in terms of SE signal intensity in arbitrary units. To quantify the signal intensity information and to

convert it into a meaningful format, a calibration curve to convert signal intensity into mass units was required.

6.4.3 MRI Calibration Curve for Quantifying MRI SE Signal Data

To quantitatively obtain hexadecane distributions in paper samples as a function of position and time, it is important to convert the hexadecane SE signal intensity distribution versus distance and time into mass or weight percent units. To achieve this objective, a calibration curve was created by imaging series of paper samples soaked and equilibrated with varying amounts (mg) of hexadecane. The weight of each dry paper sample (cut to the size of a 9 mm circle for MRI analysis) was first noted using a sensitive microbalance. Varying amounts of hexadecane were then dispensed onto different paper samples and the samples stored in a dessicator for 24 hrs to equilibrate and allow uniform hexadecane distribution. Before MRI imaging, the sample was weighed again using a microbalance and the change in weight with respect to the dry sample was recorded to determine the weight percent of hexadecane in the paper sample (Equation 6.6):

$$Wt\% \text{ Hexadecane} = \left(\frac{Wt. \text{ of } paper \text{ \& } hexadecane - Wt. \text{ of } dry \text{ paper}}{Wt. \text{ of } dry \text{ paper}} \right) \times 100 \quad (6.6)$$

After weight determination, the sample was imaged immediately using the standard SE technique to obtain a MRI spin echo image. The SE signal intensity was noted at the

center point on the sample. To eliminate the effect of background signal intensity, the dry paper sample (no hexadecane) was also imaged. The signal intensity of the blank paper sample was subtracted from the signal intensity of the samples with hexadecane to remove background effects. After subtracting the background signal intensity, the resulting signal intensity was correlated with the wt% of hexadecane on that particular sample. Repeating this procedure for samples with varying hexadecane concentrations, the calibration curve with SE signal intensity as a function of wt% of hexadecane was obtained. Figure 6.16 presents the MRI calibration curve for hexadecane in paper samples. A fourth-order polynomial was fitted to data (least squares method) to obtain an analytical expression to calculate the wt% hexadecane with a known signal intensity. It should be noted that deviation from linearity (at lower concentrations) in the calibration curve can be ascribed to the compact manner in which hexadecane is distributed in paper at low concentrations.

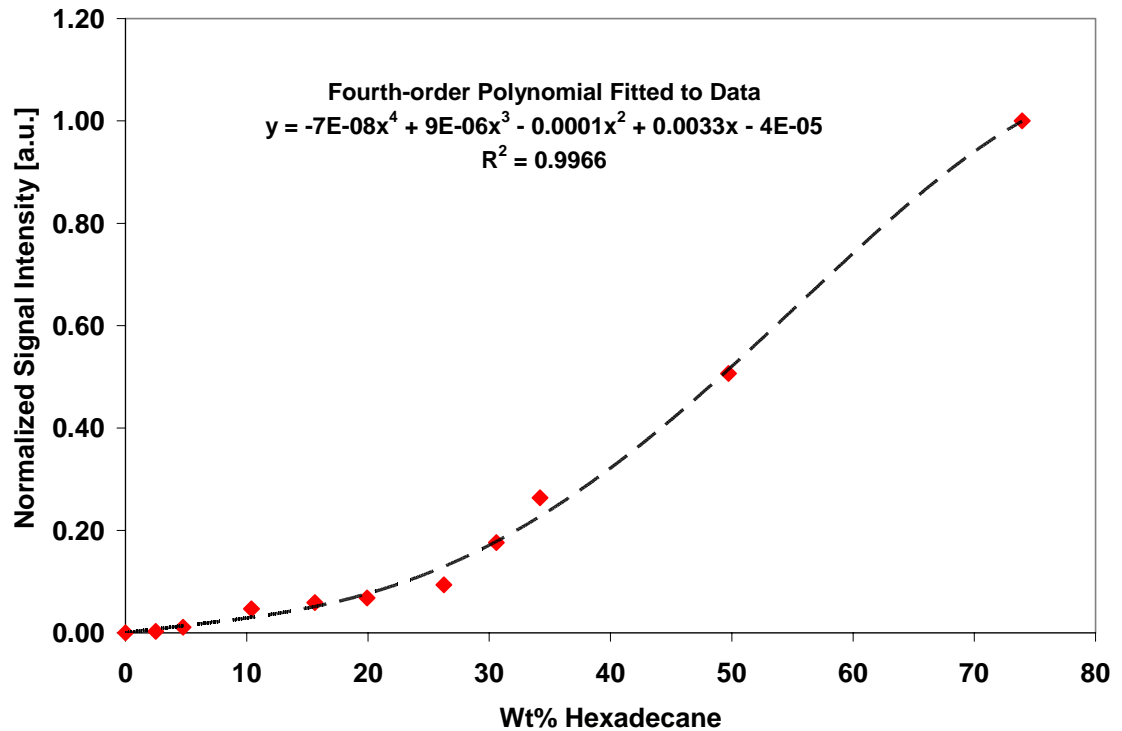


Figure 6.16 MRI Calibration Curve for relating MRI Signal Intensity to Wt% of Hexadecane in Paper Sample.

6.4.4 MRI Image and Data Processing

After the image data set was acquired, the image could be converted to signal intensity data using a MATLAB program. Another MATLAB program was used to convert the SE signal intensities to wt% hexadecane concentration by employing the calibration equation. A third MATLAB program was developed to plot both the signal intensity and hexadecane concentration with time for each sample slice (through-plane, z-direction). A step size (1 to 64) could be chosen to display the concentration profile for a specified number of frames. The ‘number’ of the frame corresponds to the time domain since each

frame took about 30 seconds to collect. In this manner, hexadecane concentration profiles were mapped inside the paper sample as a function of time and position.

Figure 6.17 presents the MRI image obtained for uncoated paper samples that had undergone 5 minutes of refining (intermediate porosity and freeness). The image shows that hexadecane is well distributed throughout an uncoated paper sample from the first frame (beginning of the experiment). As mentioned previously, it takes about 40 seconds to load the sample into the MRI instrument and 30 seconds to acquire one image. Therefore, it should be noted that first frame corresponds to a delay of 70 seconds, during which hexadecane permeates and distributes into the paper sample. Subsequent frames (Frame 16, 32, and 64 (final frame) are shown in Figure 6.17) do not show much change since hexadecane permeation into the uncoated paper sample is rapid. It should be noted that hexadecane presence is indicated by white contrast in the image. The whiter the image at a given location, the higher the concentration of hexadecane at that position. Figure 6.18 presents the signal intensity data as a function of time and position for uncoated paper that had undergone 5 minutes of refining. Figure 6.19 quantifies the signal intensity data in Figure 6.19 and presents the wt% hexadecane distribution as a function of time and position.

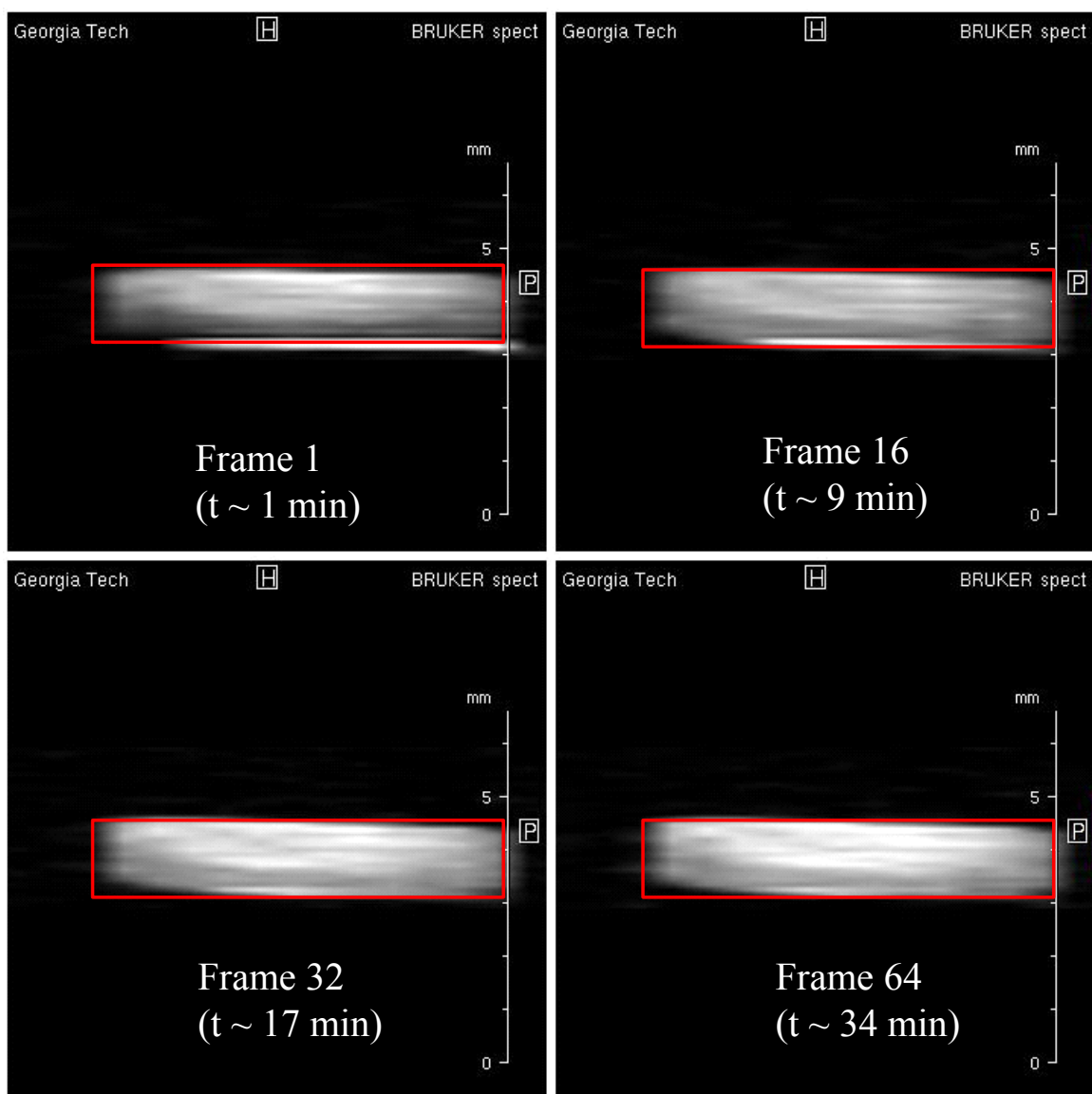


Figure 6.17 MRI images of paper samples with 10 μl of hexadecane dispensed as a function of time. The red box represents the paper sample and white contrast represents the hexadecane distribution (Higher the concentration of hexadecane, higher the image contrast).

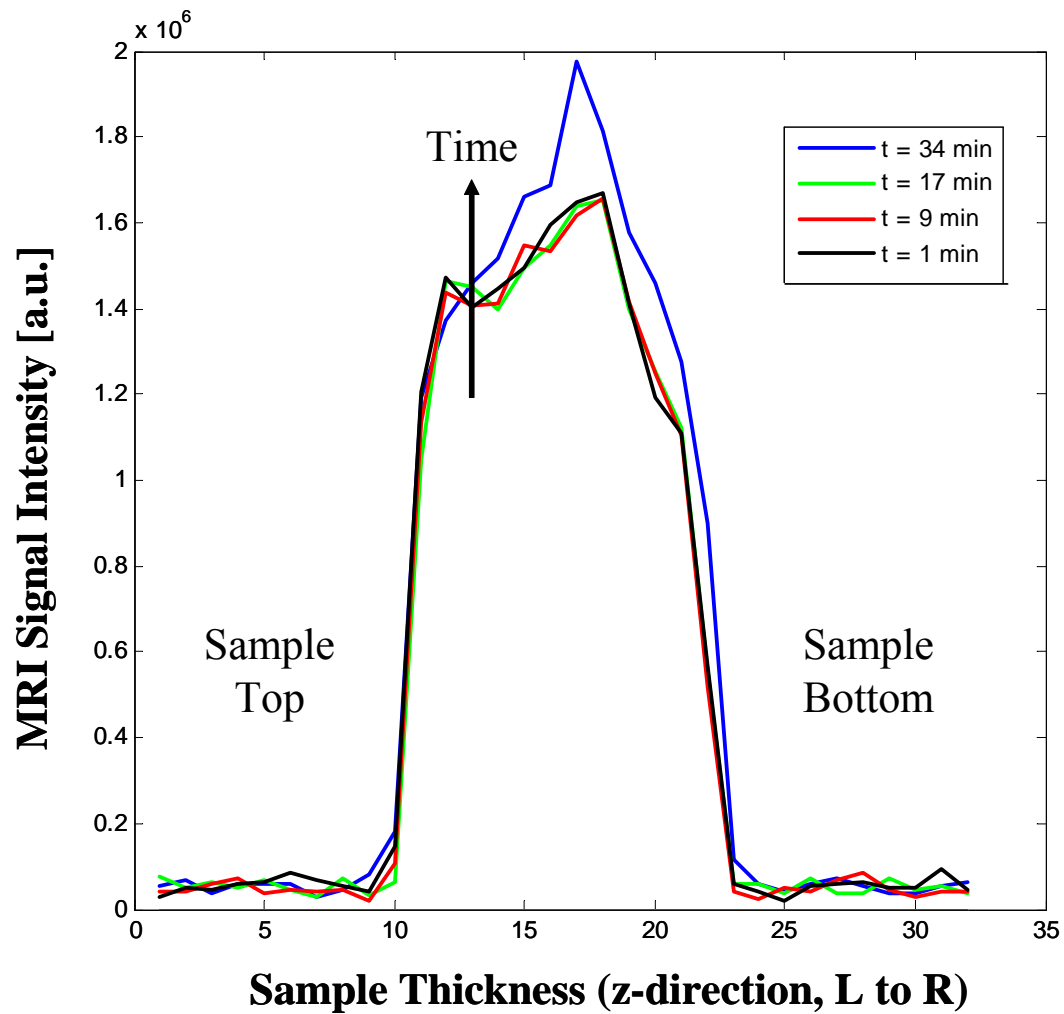


Figure 6.18 MRI signal intensity as a function of time and position for an uncoated paper sample that had undergone 5 minutes of refining.

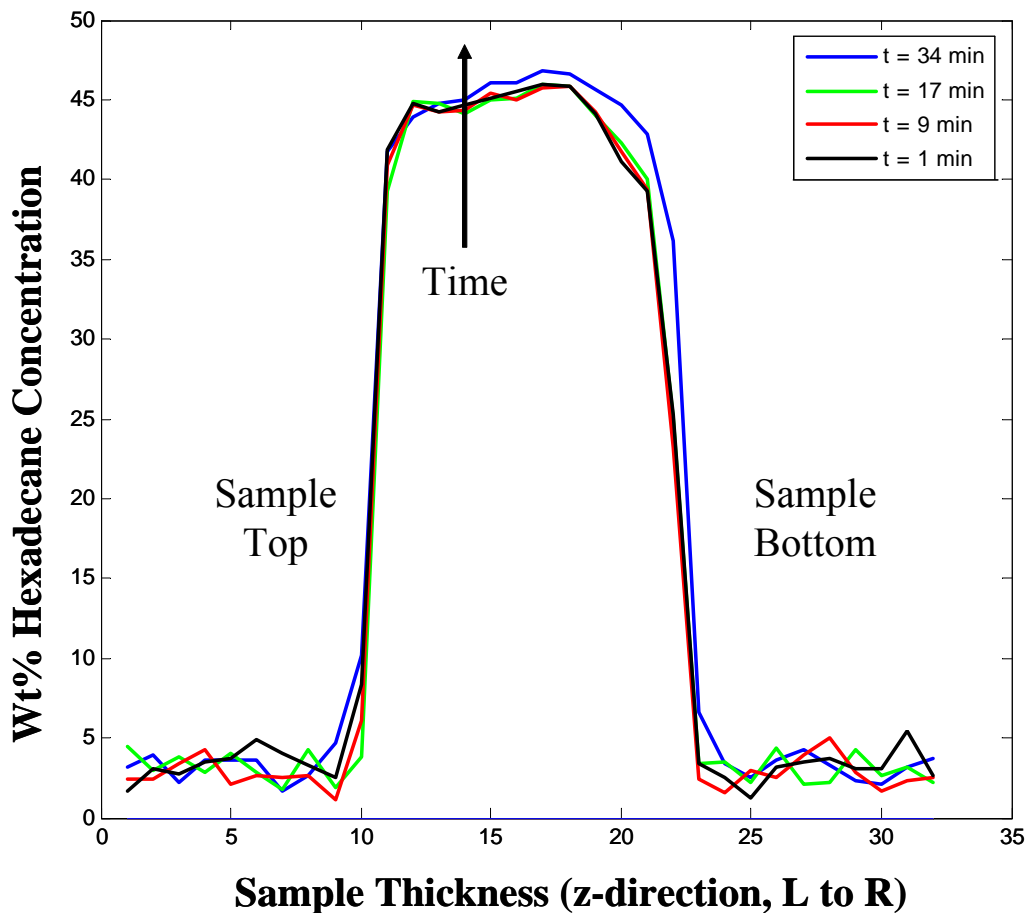


Figure 6.19 Wt% hexadecane as a function of time and position for an uncoated paper sample that had undergone 5 minutes of refining.

From Figure 6.19 it is clear that little change in MRI signal intensity and therefore wt% hexadecane concentration as a function of time and position is observed; thus, hexadecane penetrates the uncoated paper sample during the first 70 seconds.

The same amount of hexadecane (10 μ l) was dispensed on a PFE coated paper sample (PFE film thickness = 5.5 μ m). Figure 6.20 presents the MRI image obtained for the PFE coated paper sample that had 5 minutes refining (intermediate porosity and freeness). The

image shows that hexadecane is confined to the top layers of the paper and does not permeate throughout the PFE coated paper. The image shows some initial hexadecane absorption beginning from the first frame (beginning of the experiment). As mentioned previously, it takes about 40 seconds to load the sample in MRI instrument and 30 seconds to acquire one image. Therefore, it should be noted that the first frame corresponds to a delay of 70 seconds, during which some of the hexadecane permeates and distributes into the top layers of coated paper sample. Subsequent frames (Frame 16, 32, and 64 (final frame) are shown in figure 6.20) do not show much change relative to the first frame of the hexadecane permeation into the coated paper sample. This observation indicates that while some hexadecane permeates the top layers of PFE coated paper and extends to nearly 40% of the paper thickness, the PFE coated paper sample is a barrier to hexadecane transport. Even after 20 hrs, hexadecane was confined to the top 40% of the thickness of the PFE coated paper sample indicating substantially improved grease resistance. Figure 6.21 presents the signal intensity data as a function of time and position on a PFE coated paper sample that had undergone 5 minutes of refining; Figure 6.22 quantifies the signal intensity data and presents the wt% hexadecane distribution as a function of time and position.

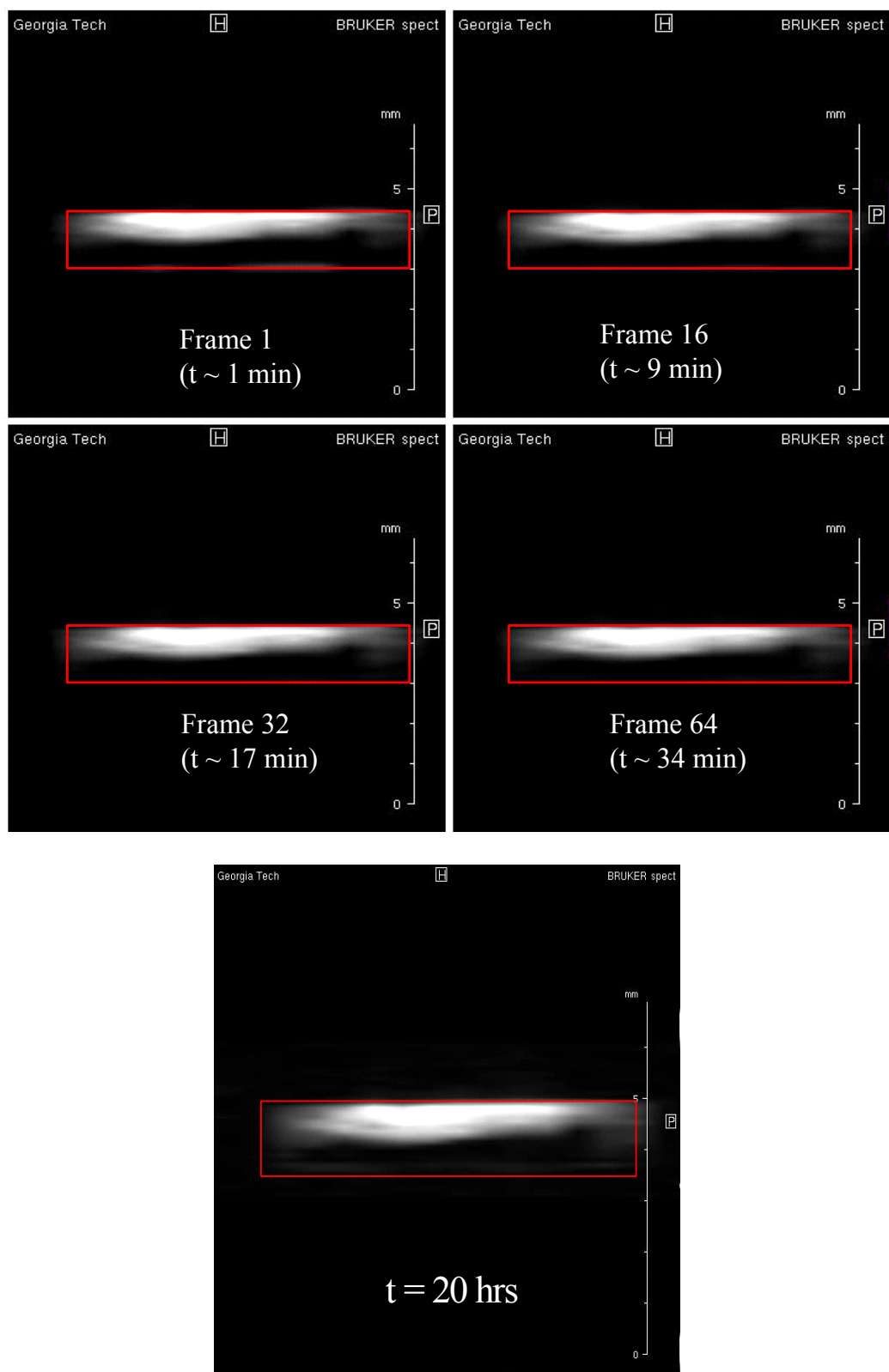


Figure 6.20 Figure 6.13 MRI images of PFE coated paper sample with 10 μ l of hexadecane dispensed as a function of time. Red box represents the paper sample.

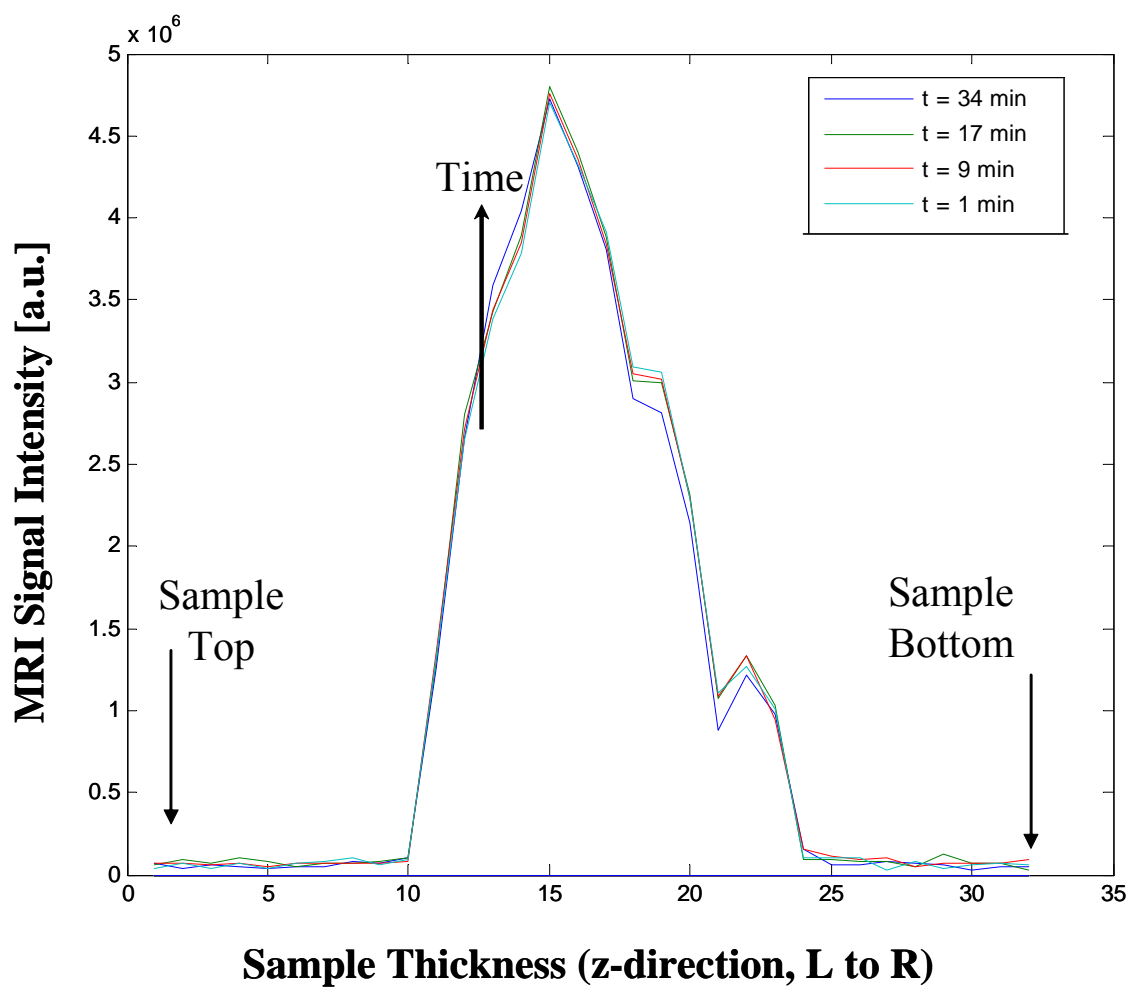


Figure 6.21 MRI signal intensity as a function of time and position on PFE coated paper sample that had undergone 5 minutes of refining [PFE film thickness = $5.5 \mu\text{m}$].

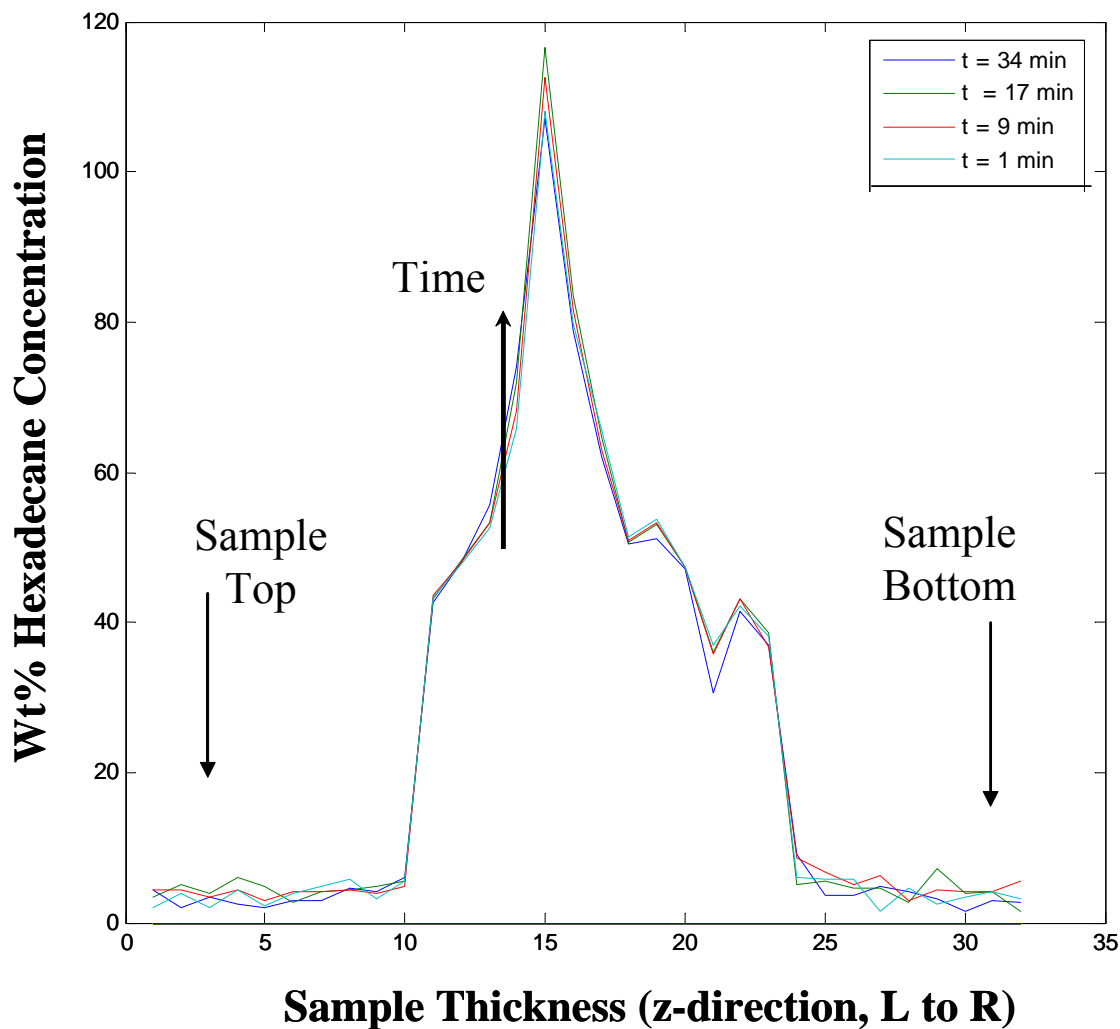


Figure 6.22 Wt% hexadecane as a function of time and position on PFE coated paper sample that had undergone 5 minutes of refining [PFE film thickness = 5.5 μm].

From figures 6.21 and 6.22, it is clear that the maximum concentration of hexadecane occurs at the 45% (= 15 slices/32 slices) depth of the PFE coated paper. At deeper layers, the hexadecane concentration is quite low, thereby demonstrating the grease barrier properties of PFE coated paper. Again, since there is no discernible difference between the hexadecane concentration profile as a function of time primarily because some

hexadecane permeates the PFE paper coated in first 70 seconds and is confined mainly in the top 45% of coated paper even at long times (~ 20 hrs).

Similarly, MRI analyses were conducted on paper samples with varying refining levels (freeness) for both uncoated and PFE coated cases. For the unrefined case, uncoated paper quickly absorbed hexadecane throughout the mass of the paper. With a 5.5 μm PFE coating, unrefined paper showed similar behavior to that of coated paper refined for 5 minutes. Hexadecane was confined to the top 50% of the PFE coated paper. For PFE coated paper with increasing refining levels (decreasing freeness), the hexadecane resistance increased. For PFE coated paper with 15, 25, 35, and 45 minute refining, hexadecane did not penetrate through the coated paper samples but flowed to the edges and was absorbed. This phenomenon occurred because the edges of the paper were not protected by a PFE film and therefore did not offer a barrier to hexadecane permeation. Attempts to prevent the flow of hexadecane to the sides of the paper such as sealing the edges with the various kinds of glue and Teflon tape largely failed. One glue (GOOP), however, sealed the edges of the PFE coated paper very well and prevented the permeation of hexadecane at the edges. Although hexadecane did not flow through the paper (z-direction), some of it flowed towards the edges and was incorporated into the glue while some of it remained on top of the PFE coated paper. Uncoated paper samples at all refining levels did not offer resistance to hexadecane permeation. That is, hexadecane was completely and uniformly absorbed in uncoated paper samples at all refining levels.

The MRI results on uncoated and PFE coated paper demonstrate that PFE coated paper substantially improves the barrier to hexadecane permeation, and therefore, shows promise as a barrier to lipophilic materials. At increased refining levels, PFE coated paper offered an increased barrier to hexadecane primarily because of a reduction in average pore size and porosity with increased refining. While the grease barrier properties of PFE coated paper were quantified using MRI data in conjunction with a calibration curve, it was not possible to deduce the mechanism of hexadecane transport. The main reason for this was the initial delay of 70 seconds during which the majority of hexadecane permeation took place. One of the potential factors that could be involved in rapid hexadecane permeation in case of PFE coated paper that had undergone 5 minutes of refining is the wicking of hexadecane into capillaries inside paper surface. Five minute refined paper has larger average pore size and substrate porosity as compared to the ones that had undergone refining for longer time. Larger pore size and higher porosity may lead to rapid absorption of hexadecane into the relatively unrefined paper substrate even though it is coated with PFE. At higher refining levels, hexadecane does not permeate into coated paper but rather flows to the sides.

6.5 Flow Through Porous Media

Paper is a porous matrix of cellulose fibers. Paper substrates can therefore allow in-plane and through-plane fluid flow. The pores in paper have different sizes and are interconnected in a three-dimensional arrangement such that fluid flowing through it

follows a tortuous path unlike straight flow through a capillary tube. Pore size, pore structure, and fiber arrangement have a significant impact on the fluid flow process.

The fluid flow in porous media is important in a number of processes such as oil recovery, packed bed absorption columns and filtration, soil physics, paper treatment, printing and barrier coatings. In the paper industry, during paper coating and sizing, fluid penetration into paper influences the process speed as well as the treatment effects. In the printing industry, a better understanding of the mechanism of fluid permeation into paper or other porous media will be helpful in printing adjustment, print quality control including print clarity and print gloss, and preparation of substrates to be printed.

It is important to define various parameters such as pore size, porosity, and absorption capacity associated with the porous media. Pores are the open spaces or voids between the fibers and are distributed throughout the volume of porous substrates. Porosity (ϕ) is defined as the ratio of the void space in a porous medium to the total bulk volume of the medium (Equation 6.7). Porosity is a dimensionless quantity.

$$\phi = \frac{V_{Void}}{V_{Total}} \quad (6.7)$$

where V_{Void} is void volume in porous medium and V_{Total} is volume of the medium (including voids). Equation 6.7 can also be written in terms of density instead of volume as equation 6.8:

$$\phi = 1 - \frac{\rho_{bulk}}{\rho} \quad (6.8)$$

where ρ_{bulk} is the bulk density of the porous medium and ρ is the density of the material making up the medium. For a porous medium with regular geometry such as regularly packed spheres, porosity is easily determined from geometrical considerations. For randomly packed fibers, porosity may be quite difficult to determine geometrically.

To study macroscopic flow through porous media, various models have been used depending on the complexity of the porous medium. One of the most common models used to describe the flow through porous substance is Darcy's law [167-170]. Darcy's law is an empirical relationship valid in many situations of flow through porous media and is considered valid for linear and slow steady state flow. It states that the rate of fluid flow through a porous medium is proportional to the potential energy gradient within that fluid (Equation 6.9).

$$q = -K \frac{\Delta P}{L} \quad (6.9)$$

where q is the volumetric flow rate per unit cross-sectional area of flow, ΔP is the net pressure head that is responsible for flow, and L is length in direction of flow. The constant of proportionality (K) is the hydraulic conductivity of the porous medium; the hydraulic conductivity is a property of both the porous medium and the fluid moving through the porous medium. Hydraulic conductivity is also defined as the ratio of the

permeability of the medium (k) to fluid viscosity (η). While fluid viscosity can be easily determined, the permeability of a medium is difficult to evaluate because it depends on structural and geometrical factors such as porosity, tortuosity, and specific surface area. Since it is not always possible to determine permeability (k) experimentally, theoretical models and empirical correlations are invoked [171]. It should be noted that Darcy's law is valid only for slow laminar flows. Other approaches to the study of liquid flow through porous media include the Kozeny-Carman approach, the drag theory approach, the network model approach, and other empirical variations of these methods [170-173].

The Kozeny-Carman approach treats the flow of fluid through porous media as flow through a conduit and uses the concept of "hydraulic radius" in place of non-circular cross-sections of conduits [170, 172, 173]. The channel diameter D_H is defined as four times the cross-sectional area divided by the wetted perimeter and can be expressed as (Equation 6.10).

$$D_H = \frac{4\phi}{S_o(1-\phi)} \quad (6.10)$$

where S_o is the surface area of the channel per unit volume of the solid material in porous medium and ϕ is the porosity. The Kozeny-Carman approach is applicable for beds of uniform spherical particles.

In the drag theory model, the pore walls are regarded as obstacles to the flow of fluid [172]. The drag from each element that comprises the pore wall is calculated using the

Navier-Stokes equation; the sum of the drag from all elements is equated to the flow resistance of the porous medium. This approach has been used by various researchers to study high porosity media [174, 175].

Network models represent the most important and widely used class of geometric models for porous media. Network models approximate the porous structure by networks of randomly distributed bands and nodes through which fluid flow occurs [170, 176-178]. As a result, these models require detailed information on the pore structure of the absorbent material. Network models have not been very successful in calculating permeabilities of beds with non-uniform particles [171].

Fluid penetration into a porous media is a process of capillary-driven flow. When capillary forces are present to draw liquid into the porous substrate, the Lucas-Washburn equation is often used to predict the depth of penetration (L):

$$L = \sqrt{\frac{\gamma R \cos(\theta) t}{2 \mu}} \quad (6.11)$$

where γ is the fluid surface tension, R is the capillary radius, θ is the contact angle between the fluid and the solid phase, μ is the coefficient of viscosity, and t is the time. The Lucas-Washburn relationship has been used for both long capillaries and porous materials [170].

For a simple case of penetration absorbency, porous media can be idealized as a bundle of many vertical parallel cylindrical (capillary) pores randomly distributed in the medium [171, 173]. Figure 6.23 shows a schematic of liquid penetration through a pore where gravitational forces, external pressure and surface tension are acting on the drop of liquid.

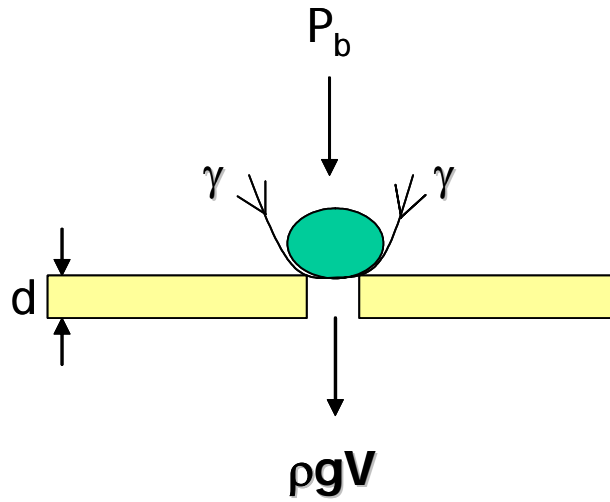


Figure 6.23 Schematic showing liquid penetration through a pore.

The total pressure acting downwards is (Equation 6.12):

$$\Delta P = P_b + P_w + P_s \quad (6.12)$$

where ΔP is the net driving pressure, P_b is the external pressure, P_w is the pressure generated by the weight of the liquid drop and P_s is the capillary pressure. These pressures can be expressed by:

$$P_w = \frac{\rho g V}{\pi r_c^2} \quad (6.13)$$

and

$$P_s = \frac{2 \gamma \cos(\theta)}{r_c} \quad (6.14)$$

where r_c is the capillary radius, γ is the surface tension of fluid, ρ is the fluid density, and θ is the contact angle.

Flow in the capillary can be defined by the Hagen-Poiseulle equation [179, 180]:

$$q = \frac{r_c^2 \Delta P}{8 \mu L} \quad (6.15)$$

where q is the volume flow rate per unit cross-sectional area, L is the wetted length, and μ is the coefficient of viscosity. Substituting ΔP from equation 6.12, rearranging, and integrating equation 6.15 over the sample thickness (d), we get equation 6.16:

$$\int_0^d L dL = \int_0^{t_p} \frac{r_c^2}{8\mu} \left(P_b + \frac{\rho g V}{\pi r_c^2} + \frac{2\gamma \cos(\theta)}{r_c} \right) dt \quad (6.16)$$

Equation 6.16, therefore, represents the relationship between the penetration time and the pore dimensions including depth and radius for a given set of fluid and interfacial properties [171, 173]. Equation 6.16 can be used to study the effect of various parameters (pore size, contact angle, surface tension, and coefficient of viscosity) on the penetration time [171]. Figures 6.24 to 6.27 present the results of parameter variation on the penetration time of liquids in porous media (Figures have been reproduced from Reference [171]).

As pore size increases, the penetration time decreases. Also, for a fixed pore size, penetration time decreases as the external pressure (which tends to force the fluid inside the pore) increases (Figure 6.24).

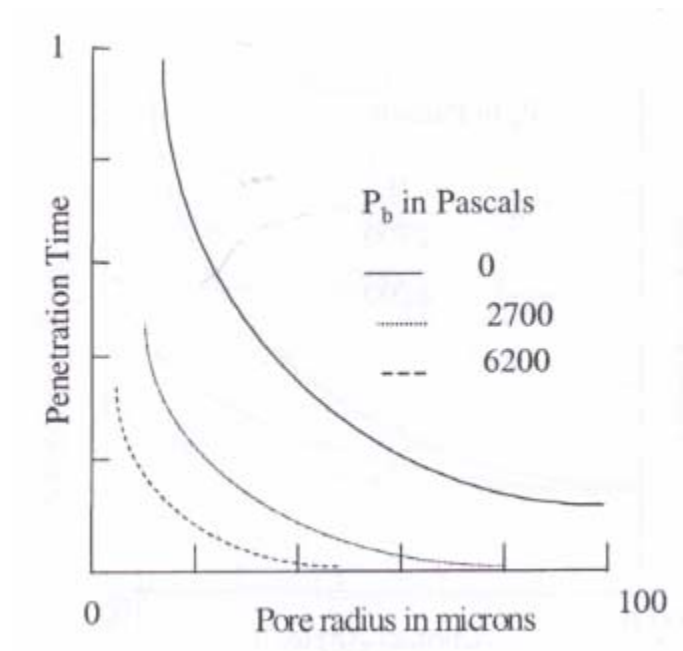


Figure 6.24 Influence of pore size (r_c) on the penetration time of fluid in porous media [171]

As the liquid contact angle increases, the penetration time also increases (Figure 6.25). With increased contact angle the drop is expected to bead up on the surface and show a decreased tendency to penetrate the substrate leading to an increase in penetration time. Again, as pressure increases, penetration time decreases.

Capillary forces are higher for liquids with higher surface tension indicating that high surface tension liquids should absorb faster, i.e. have lower penetration time as compared to low surface tension liquids. This trend is depicted in Figure 6.26.

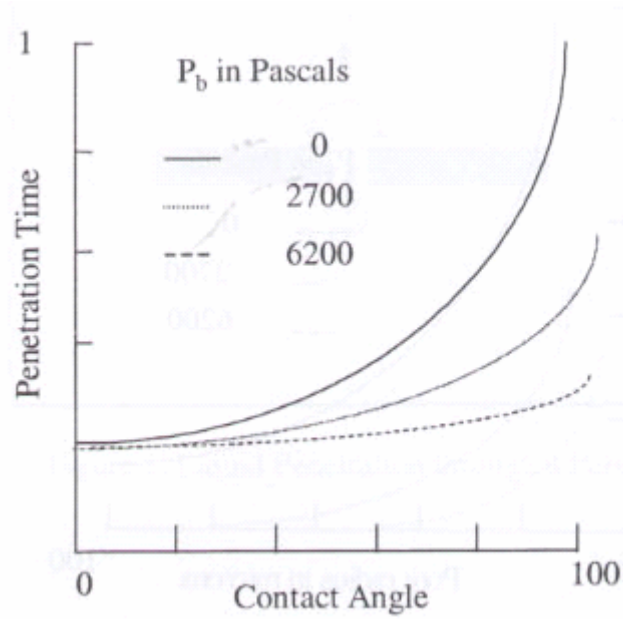


Figure 6.25 Influence of contact angle (θ) on the penetration time of fluid in porous media [171].

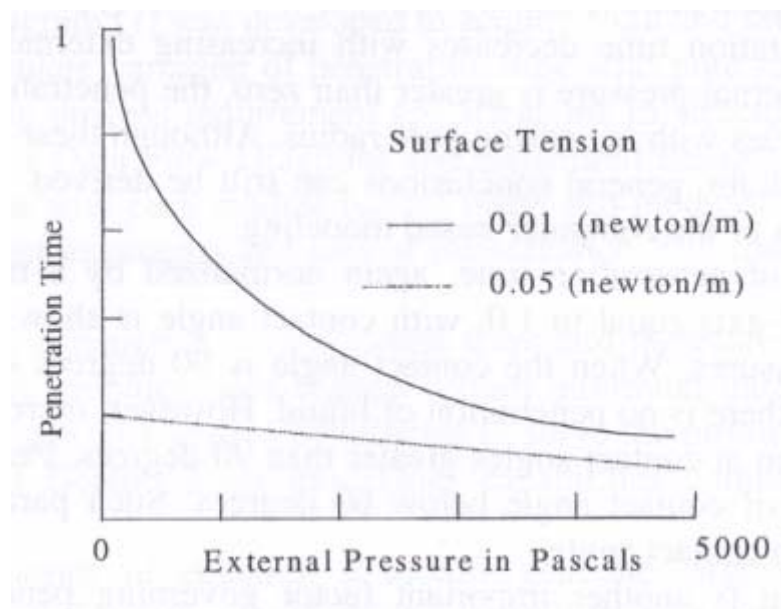


Figure 6.26 Influence of surface tension (γ) on the penetration time of fluid in porous media [171].

The viscosity of the fluid also affects the penetration rate. As the viscosity of a fluid increases, the penetration time also increases primarily because the fluid flow through porous media is slower due to increased fluid viscosity. Figure 6.27 presents the variation of penetration time with the coefficient of viscosity.

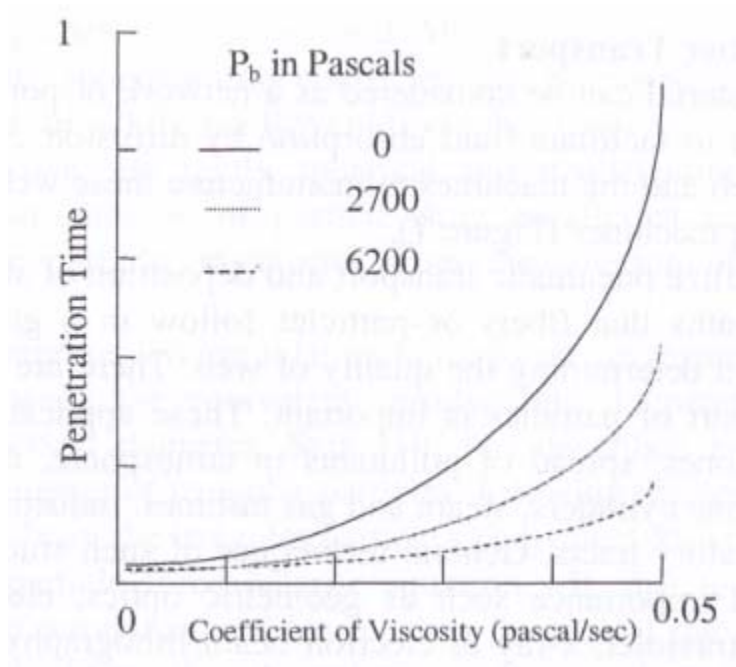


Figure 6.27 Influence of coefficient of viscosity (μ) on the penetration time of fluid in porous media [171].

MRI studies on hexadecane permeation in a 5 min refined PFE coated sample show that hexadecane stagnates at approximately half depth in the sample. This result is rather

surprising since the PFE coating exists at the top layers of the paper sample and after the hexadecane has penetrated the top layers, it should penetrate the remaining depth quite quickly unless the pores have been narrowed or blocked. While a good explanation for this phenomenon is lacking at this point, one of the possible explanations is the creation of capillary “stop valves” at half sample depth. Microfluidic capillary-driven valves have recently received a lot of attention [181-183]. A sudden expansion (or contraction) channel, called capillary stop valve is usually used to stop the fluid by changing the channel geometry. Consider a capillary cross-section which suddenly expands from a diameter h_n to h_c as shown in Figure 6.28.

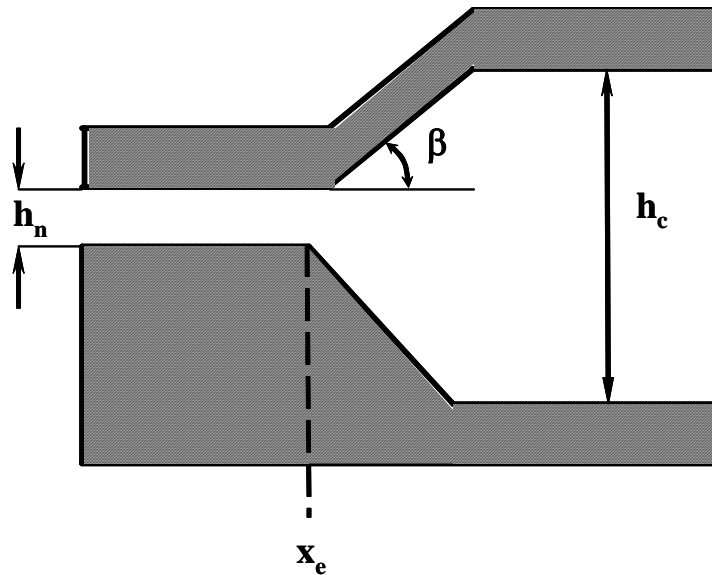


Figure 6.28 Cross-section of a capillary suddenly expanding from narrow neck to a wider neck.

When the liquid is first introduced into this capillary geometry, it wicks in the necked region and abruptly stops at the neck outer edge (x_e) preventing further flow. This behavior has been explained in terms of energy changes in the liquid-solid-gas interface system [183]. The total interfacial energy of the above system is (Equation 6.17):

$$U_T = A_{sl} \gamma_{sl} + A_{sa} \gamma_{sa} + A_{la} \gamma_{la} \quad (6.17)$$

where A_{sl} , A_{sa} , and A_{la} are solid-liquid, solid-air, and liquid-air interface areas, and γ_{sl} , γ_{sa} , and γ_{la} are corresponding surface energies per unit area. Young's equation can be used to correlate surface energies to the contact angle (θ_c) as:

$$\gamma_{sa} = \gamma_{sl} + \gamma_{la} \cos \theta_c \quad (6.18)$$

Combining equations 6.17 and 6.18, we get equation 6.19 [183]:

$$U_T = (A_{sl} + A_{sa}) \gamma_{sa} - A_{sl} \gamma_{la} \cos \theta_c + A_{la} \gamma_{la} = U_o - A_{sl} \gamma_{la} \cos \theta_c + A_{la} \gamma_{la} \quad (6.19)$$

where U_o is constant because the sum ($A_{sl} + A_{sa}$) remains invariant.

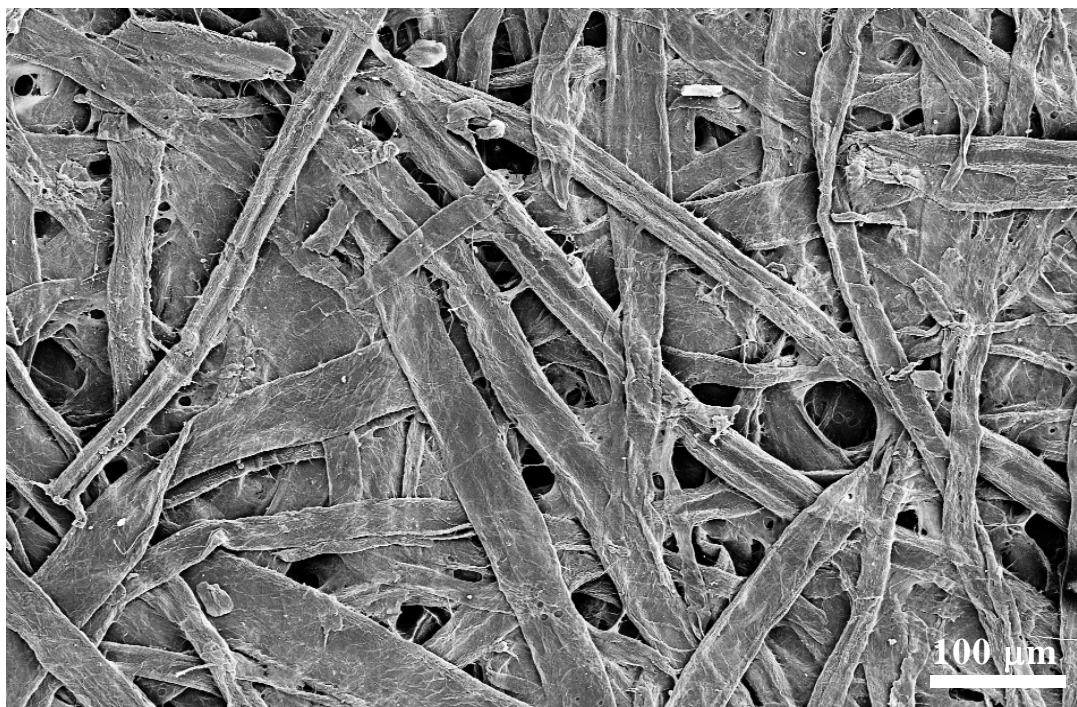
The total energy depends on the injected volume V_1 because wetted area changes if V_1 changes. The pressure in the liquid can be obtained by differentiating the total energy (U_T) with respect to V_1 (Equation 6.20) [183]:

$$P = - \frac{dU_T}{dV_l} = \gamma_{la} \left(\cos \theta_c \frac{dA_{sl}}{dV_l} - \frac{dA_{la}}{dV_l} \right) \quad (6.20)$$

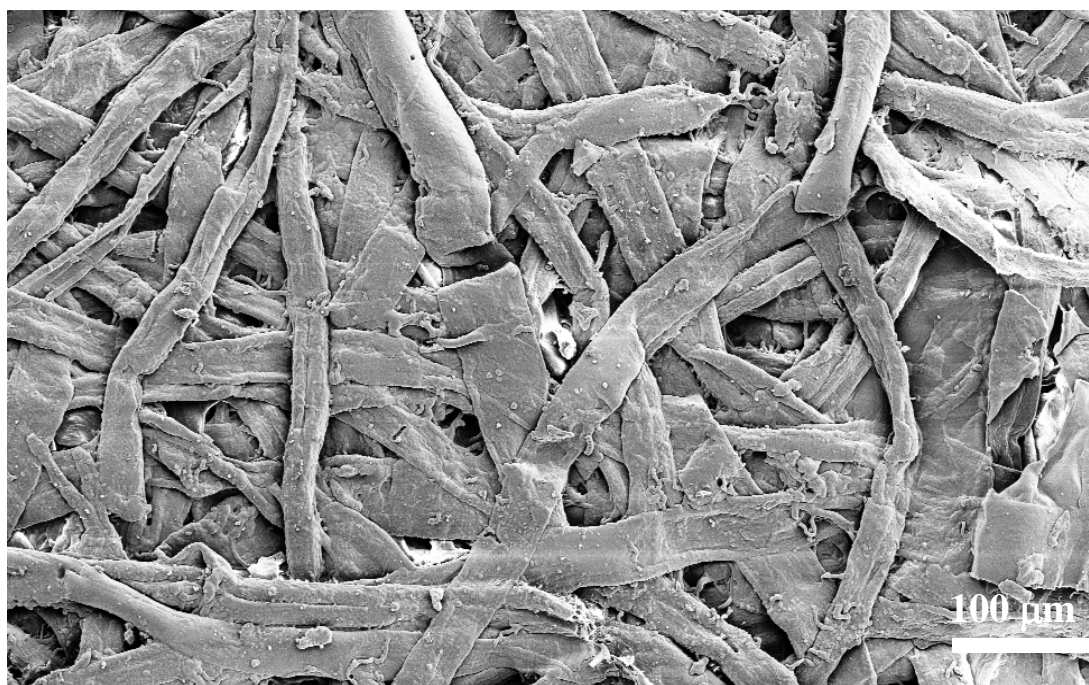
In uniform channels (i.e. no change in the channel geometry) with $\theta_c \leq 90^\circ$, $\gamma_{sa} > \gamma_{sl}$, A_{sa} is fixed, and A_{sl} increases linearly with penetration distance. Thus, liquid wicks in and wets the entire channel surface with a constant and positive pressure (P) driving the flow. In capillary stop valves, the channel geometry causes the P to become negative. This is achieved for $\theta_c \leq 90^\circ$ by an abrupt enlargement in the channel cross-section. Due to channel enlargement, A_{la} increases more than A_{sl} for the given volume change resulting in a negative opposing pressure which stops the flow. A detailed mathematical treatment for capillary stop valves can be found in Reference [183] from which the above equations were obtained.

For the case of hexadecane stagnation at half depth in the PFE coated paper (5 minute refined) sample, it is possible that the capillaries up to half depth have been narrowed due to the fluorocarbon coating penetration such that the remaining depth comprises capillaries with bigger pore sizes. In such a situation, hexadecane liquid in narrow pores sees an abrupt pore enlargement (analogous to capillary stop valves) and is, therefore, stopped at half depth. Figure 6.29 shows SEM micrographs of 5 minute refined uncoated and PFE coated (5.5 μm) paper samples. The uncoated paper sample shows a porous surface through which hexadecane can readily permeate. While PFE coating reduces the pore size considerably, coated paper is still porous and allows the hexadecane to penetrate initially. Figure 6.30 shows the SEM micrograph of 25 minute refined uncoated

and PFE coated (5.5 μm) paper samples. A 25 minute refined uncoated paper sample is less porous compared to a 5 minute refined uncoated paper sample as expected (also evident by lower freeness). The SEM micrograph of a 25 minute refined PFE coated paper shows essentially complete surface coverage with nearly all the pores blocked by the fluorocarbon coating. MRI studies indicate negligible permeation of hexadecane in a PFE coated paper sample which was refined for 25 minutes, thereby confirming the complete surface coverage.

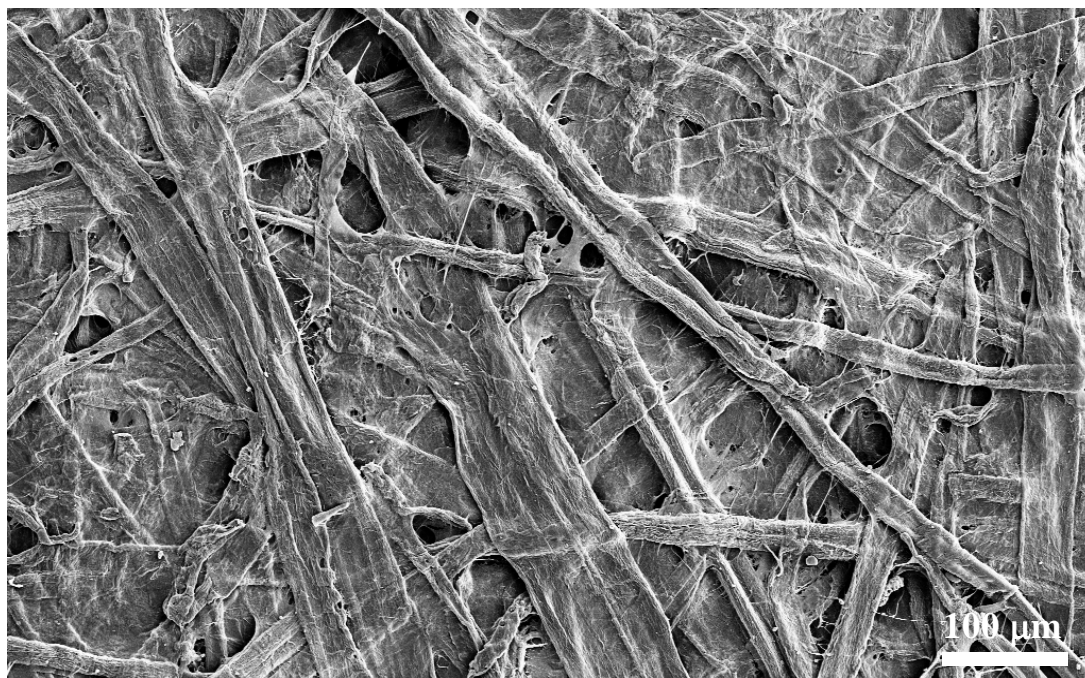


(a)

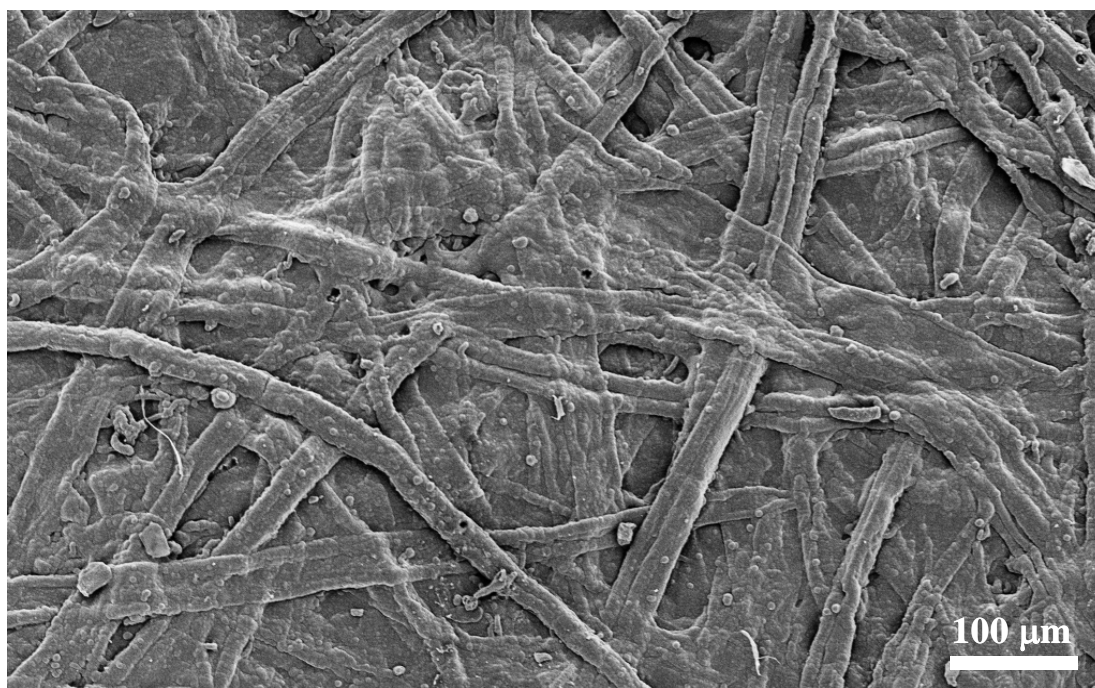


(b)

Figure 6.29 SEM micrograph of 5 minute refined (a) an uncoated paper sample, (b) a 5.5 μm PFE coated paper sample.



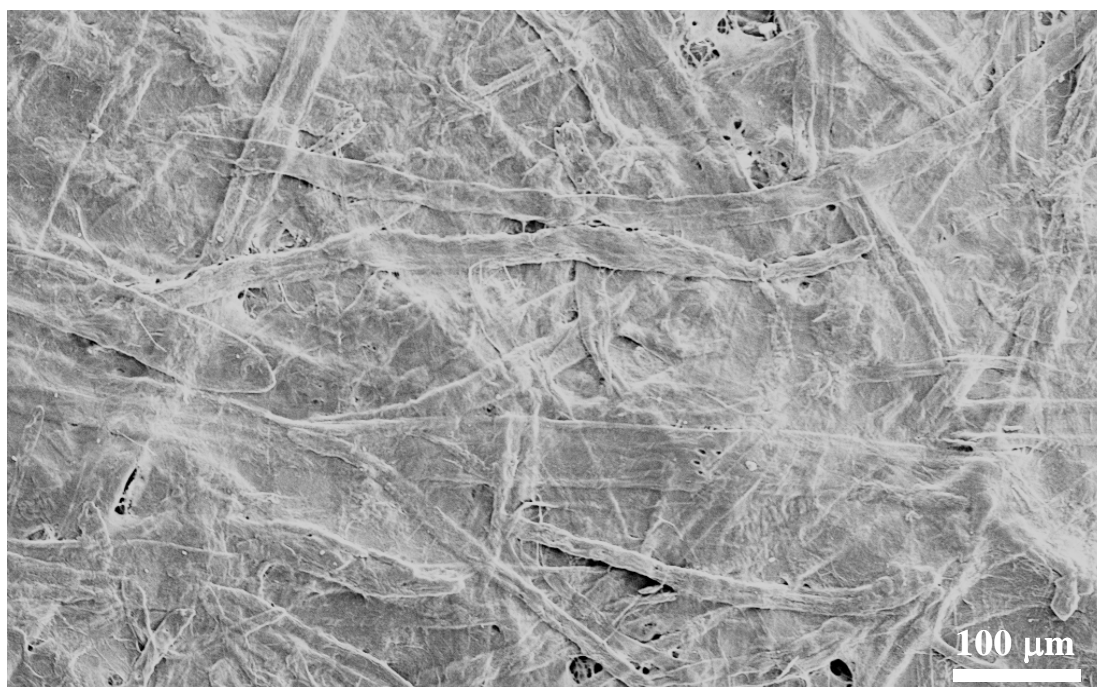
(a)



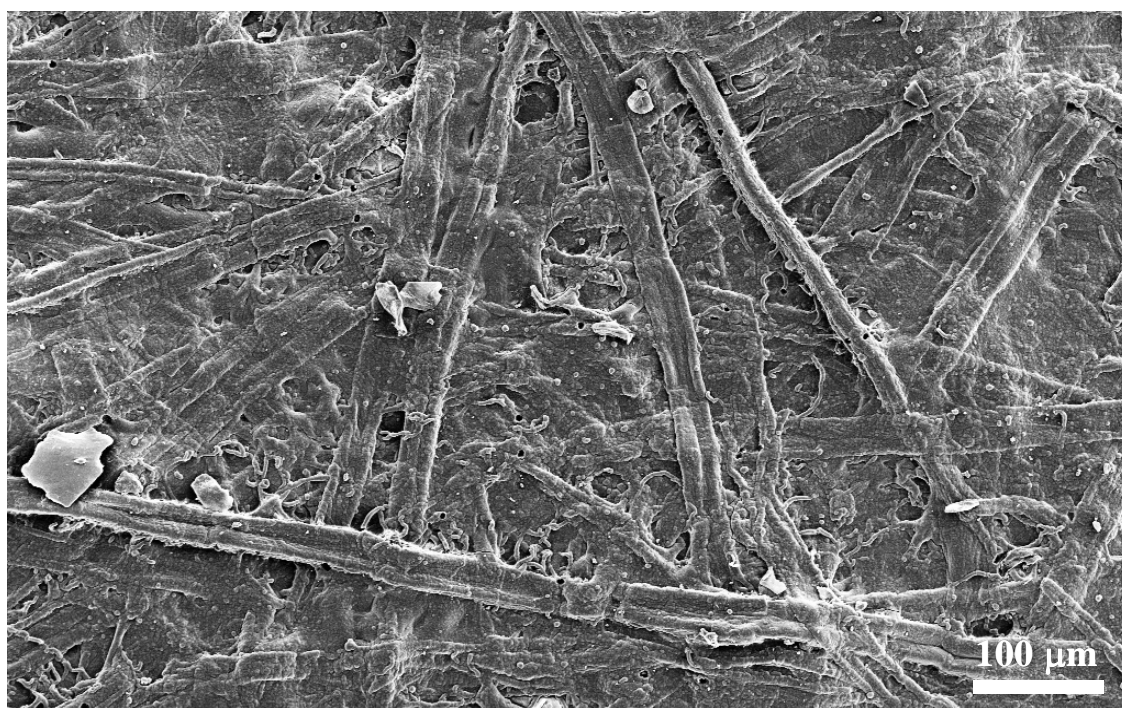
(b)

Figure 6.30 SEM micrograph of 25 minute refined (a) an uncoated paper sample, (b) a 5.5 μm PFE coated paper sample.

Figure 6.31 shows the SEM micrograph of 45 minute refined uncoated and PFE coated (5.5 μm) paper samples. A 45 minute refined uncoated paper sample is still less porous as compared to 25 minute refined uncoated paper sample as expected (also evident by lower freeness). The SEM micrograph of a 45 minute refined PFE coated paper shows complete surface coverage with all the pores blocked by the fluorocarbon coating. Again, MRI studies indicate negligible permeation of hexadecane in a PFE coated paper sample which was refined for 45 minutes confirming the complete surface coverage. Figure 6.32 shows the high resolution SEM micrograph of a both 25 minute and 45 minute refined paper sample coated with a 5.5 μm PFE film. The micrographs show cauliflower-like globular surface morphology covering the pores in both cases. The coating globules are visible beneath the top surface fibers indicating fluorocarbon penetration into the paper substrate. Gas phase polymerization is responsible for the globular morphology as explained in Chapter 4. While the thickness of the fluorocarbon film is 5.5 μm , the globules created as a result of gas phase polymerization cause bridging of the gaps and spaces between the fibers resulting in virtually complete surface coverage.

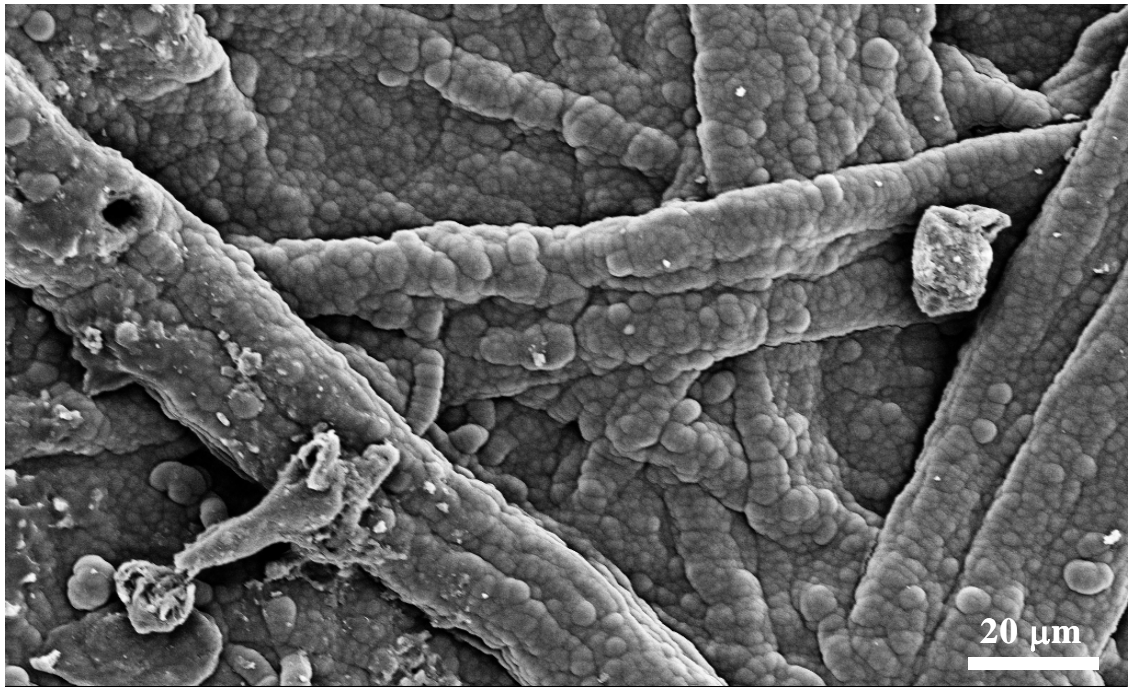


(a)

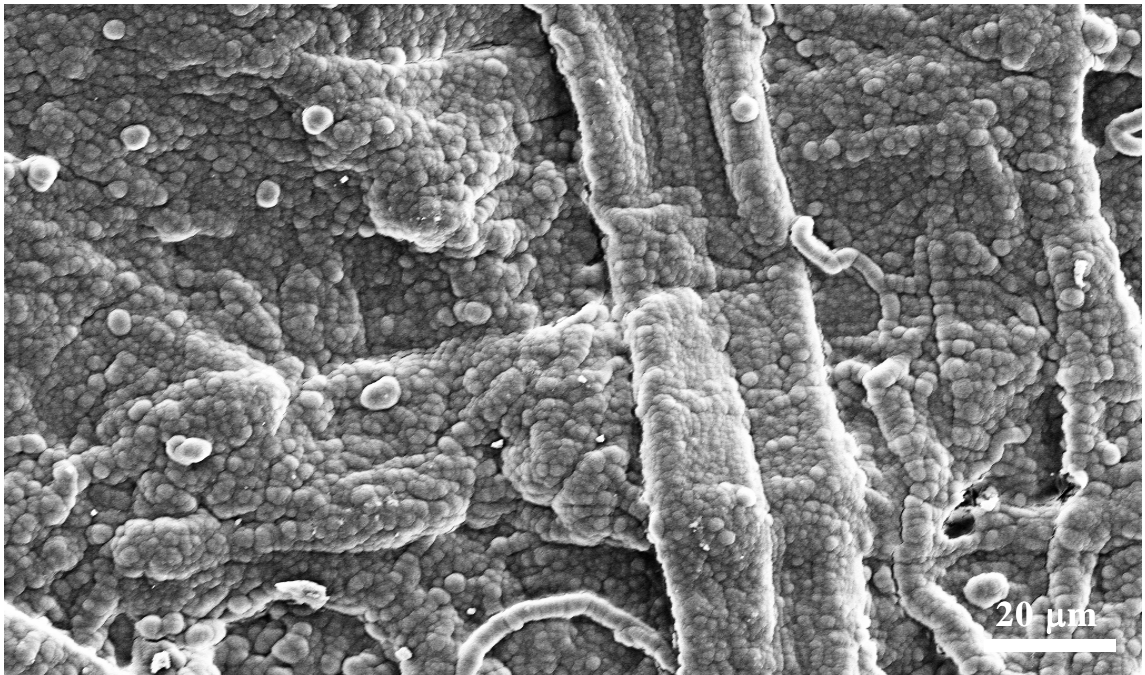


(b)

Figure 6.31 SEM micrograph of 45 minute refined (a) an uncoated paper sample, (b) a 5.5 μm PFE coated paper sample.



(a)



(b)

Figure 6.32 High resolution SEM micrograph of (a) 25 minute refined (b) a 45 refined paper sample both coated with a 5.5 μm PFE film.

6.6 Fluorocarbon Penetration Depth in PFE Coated Paper

In order to understand the extent of barrier properties provided by fluorocarbon films on paper or cellulosic substrates, it is important to quantify the depth of fluorocarbon coating into porous paper substrates. While the fluorocarbon film thickness was typically measured on Si wafers using spectroscopic ellipsometry, the fluorocarbon film thickness on paper fibers was not known but was assumed to be same as that on Si wafers. However, during plasma polymerization of fluorocarbon films, the free radicals and ions generated in the plasma may penetrate the porous structure of paper and incorporate fluorocarbon moieties such as CF₃, CF₂, and CF deeper into the bulk of the paper matrix. This may lead to fluorination perpendicular to the paper substrate surface and result in a coating which penetrates into the paper, unlike the situation on an impervious Si wafer. To evaluate the fluorocarbon coating depth into paper, photoacoustic spectroscopy was employed. The details of the technique have been presented in Chapter 3.

To evaluate the fluorocarbon coating depth into paper, photoacoustic IR spectra of uncoated paper was first collected at various modulation frequencies. The depth (μ_s) over which the thermal signal is generated is directly related to the modulation frequency (f):

$$\mu_s = \left(\frac{\alpha}{\pi f} \right)^{1/2} \quad (6.21)$$

where α is the thermal diffusivity (m^2/s) of the material (in these experiments, paper). The thermal diffusivity of paper as evaluated by Morikawa et al. was used ($\alpha = 0.7 \times 10^{-7} \text{ m}^2/\text{s}$) [184]. Using the depth profiling equation described above, the sampling depth into paper can be determined by varying the modulation frequency. Figure 6.33 presents the photoacoustic spectra of an uncoated paper at a modulation frequency of 209 Hz. The spectrum can be resolved into various Gaussian and Lorentzian curve shapes to fit the absorption bands associated with the overall spectrum. This is also known as peak deconvolution by nonlinear least squares method [104]. Similarly, Figure 6.34 presents the photoacoustic spectra of a fluorocarbon coated paper [Paper thickness = 1.7 mm, PFE thickness measured on Si wafer = $5.5 \text{ }\mu\text{m}$] at a modulation frequency of 209 Hz.

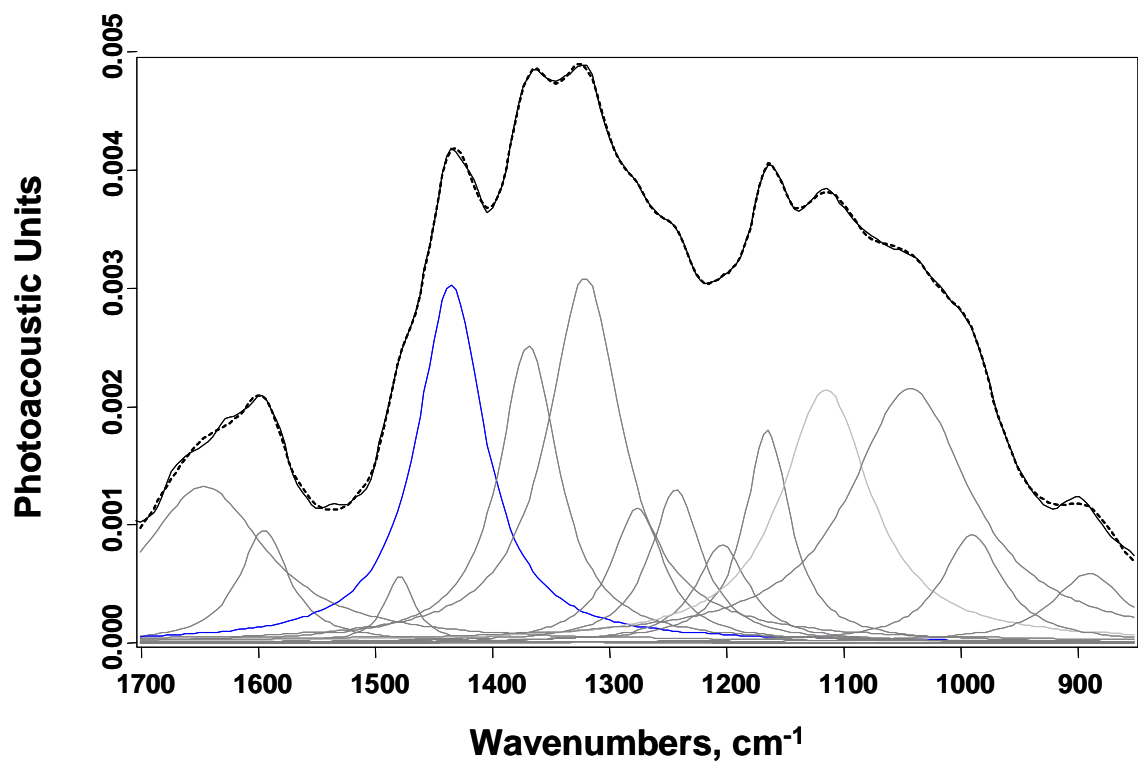


Figure 6.33 Photoacoustic Spectra of Uncoated Paper Sample at a Modulation Frequency of 209 Hz.

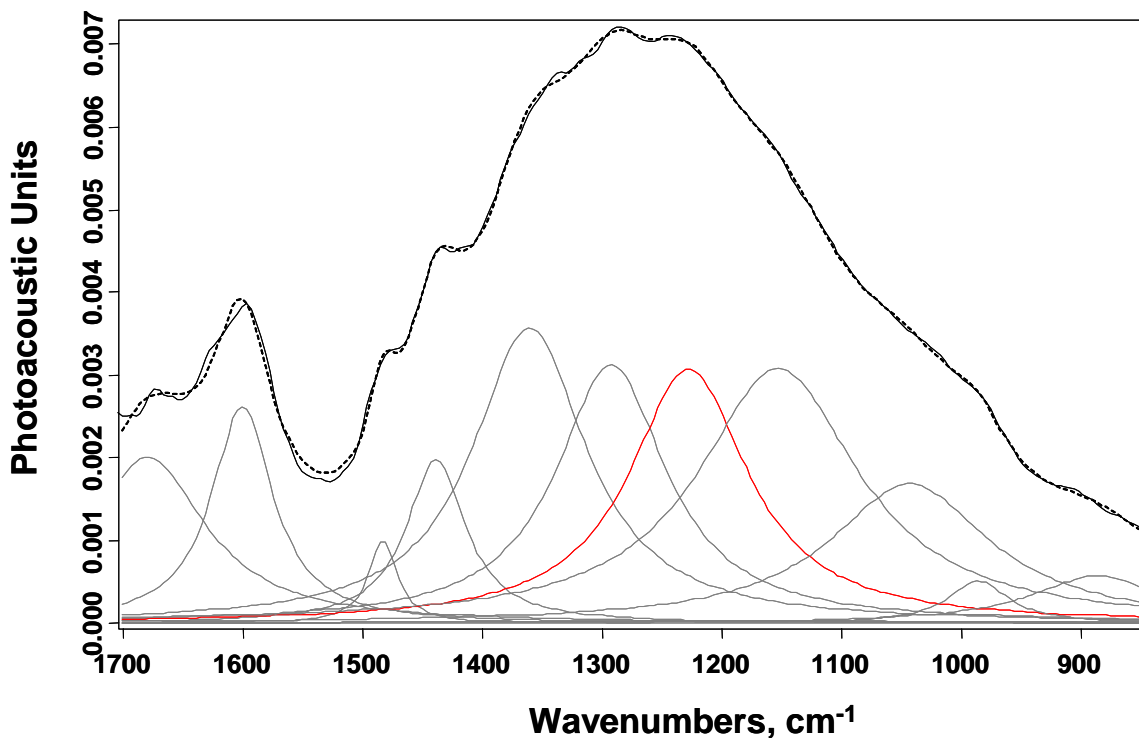


Figure 6.34 Photoacoustic Spectra of PFE coated Paper Sample at a Modulation Frequency of 209 Hz [PFE film thickness measured on Si wafer = 5.5 μm].

Spectral peaks representative of fluorocarbon films are well-known.. The broad peak between 980 and 1450 cm^{-1} indicates the presence of CF_x (CF , CF_2 , CF_3) species present in the film and is commonly found in plasma polymerized fluorocarbon films due to CF_x stretching [19, 36, 116, 118]. The prominent peak centered at 1250 cm^{-1} contains very strong symmetric and asymmetric stretches [118]. This peak was used as a representative of fluorocarbon film in the PFE coated paper sample. For the paper substrate, a strong peak at 1438 cm^{-1} corresponding to CH_2 and CH_3 deformations was chosen to be representative of the paper substrate. Figure 6.35 presents the photoacoustic spectra of PFE coated paper resolved into characteristic fluorocarbon and paper substrate peaks at a modulation frequency of 209 Hz.

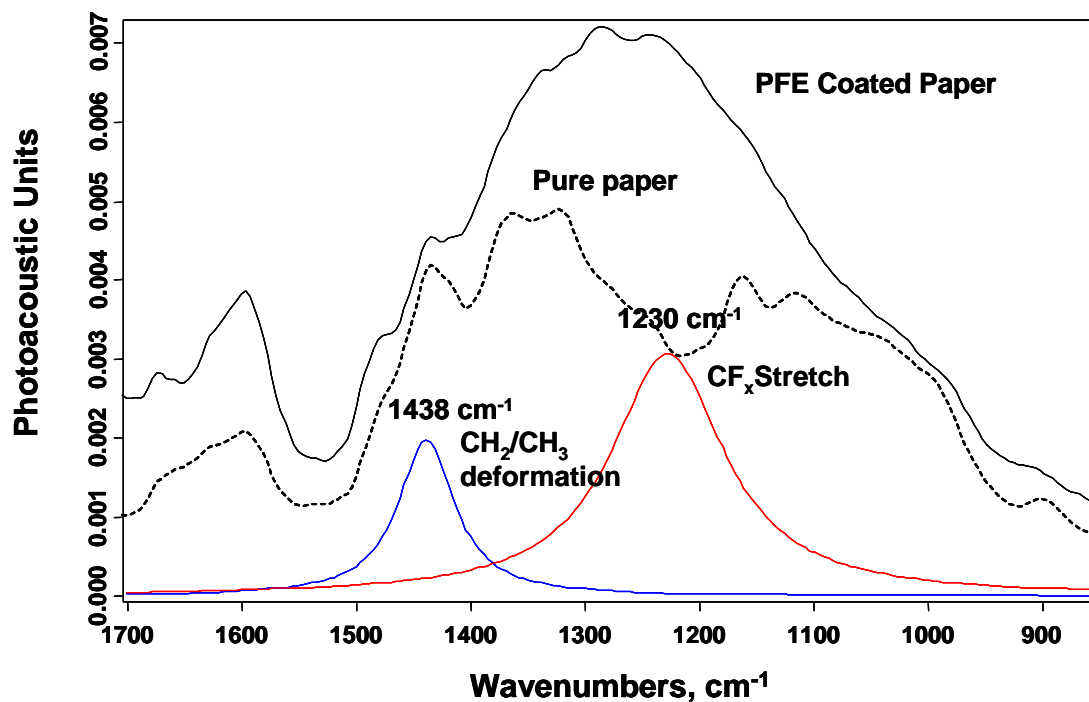


Figure 6.35 Characteristic Peak Identification in Photoacoustic Spectra.

Photoacoustic spectra of PFE coated paper was obtained for the modulation frequencies 54, 101, 154, 209, 292, 418, 585, and 732 Hz. At all modulation frequencies, the ratio of the integral area under a characteristic fluorocarbon peak (1230 cm^{-1}) to that of the characteristic paper peak (1438 cm^{-1}) was calculated after peak deconvolution. As mentioned previously, the penetration depth of the thermal signal is dependent upon modulation frequency. Thus, after relating penetration depth to modulation frequency, the ratio of peak areas (Fluorocarbon/Paper) was plotted with penetration depth for each PFE coated paper sample. A sudden change in the ratio of peaks indicates the interface of a

pure fluorocarbon film with the pure paper substrate. The penetration depth at which this change occurs represents the interface of pure PFE with the pure paper substrate, thereby indicating the penetration depth of PFE into paper [104]. Figure 6.36 presents the penetration depth of the PFE film into paper with varying refining levels or varying freeness levels.

It should be noted that the fluorocarbon film thickness on paper (or penetration depth of PFE in paper) as obtained by this method is accurate within $\pm 1\mu\text{m}$. Also, photoacoustic spectroscopy can only distinguish between a pure PFE film and a pure paper substrate and cannot identify an interface with fluorocarbon composition gradients in a paper matrix. Thus, the calculated PFE film thickness of approximately $6.2\mu\text{m}$ represents the interface of a pure fluorocarbon film (minimal contribution from paper due to the high concentration of CF_x species) with paper. The paper matrix below this penetration depth obviously has some concentration of fluorine moieties but it is small compared to bulk paper and, therefore, does not produce a strong photoacoustic signal.

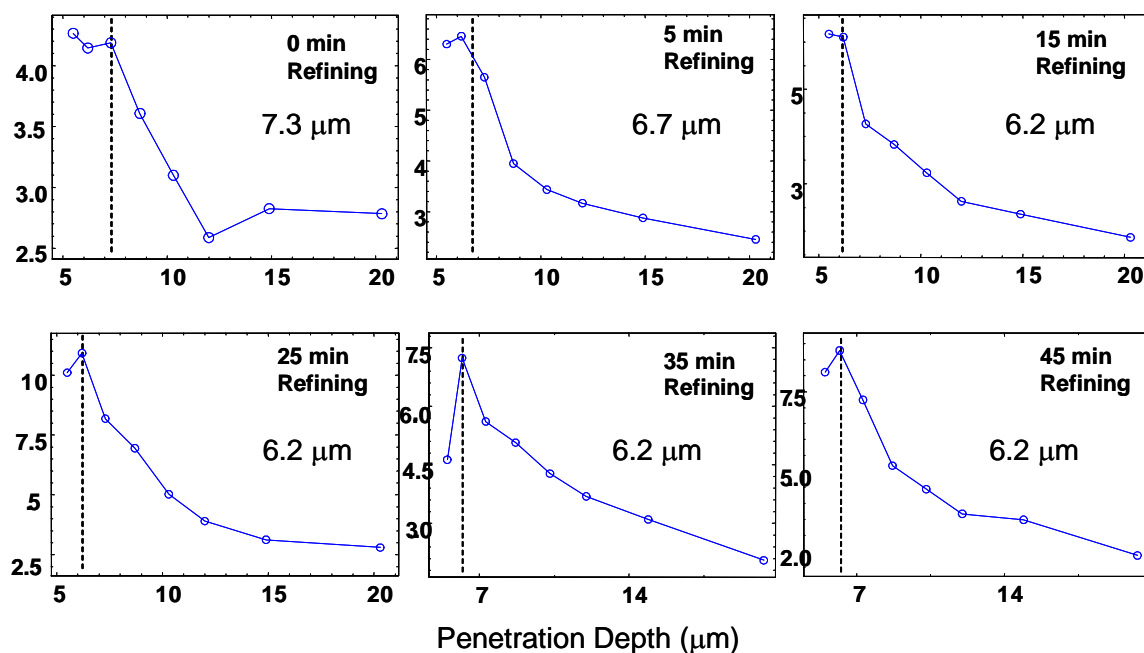


Figure 6.36 Ratio of Integrated Fluorocarbon Peak to that of Paper Peak with Varying Penetration Depth of Thermal Signal for different Paper Samples.

Therefore, photoacoustic spectroscopy can only determine the interface of a pure fluorocarbon film (highly concentrated) with a paper substrate. Any variation in fluorocarbon species concentration cannot be detected by this technique because no clear interface is formed if the concentration of fluorocarbon moieties changes gradually with sample depth. Thus, within experimental error of the photoacoustic technique, the fluorocarbon film depth into paper or the fluorocarbon film penetration into paper substrates ($7.3 \mu\text{m}$ for unrefined and $6.2 \mu\text{m}$ for refined paper substrate) was approximately equal to the fluorocarbon film thickness obtained on a Si wafer ($5.5 \mu\text{m}$). The reverse side of the coated paper surface exhibited hydrophobic behavior (contact angle $\sim 120^\circ$), indicating the presence of fluorocarbon moieties. However, the

concentration of these species was too small to be detected by photoacoustic spectroscopy.

6.7 Conclusions of Grease Barrier Experiments

To study whether a paper is grease resistant or not, qualitative techniques such as turpentine penetration test and TAPPI “oil kit” test are commonly used. While these tests are valuable indicators of resistance to lipophilic materials, they provide no quantification of lipophobic behavior. In this work, two techniques were investigated in this work to quantify the grease barrier properties of fluorocarbon coated paper. Quartz crystal microbalance studies on fluorocarbon films suggested that PFE films have low affinity for hexadecane, which was used as a grease surrogate. Even at higher concentrations of hexadecane present in the system, only up to 0.6 wt% of hexadecane was absorbed by the films. Furthermore, the calculated diffusivity of hexadecane was two to three orders of magnitude lower than that of water. Magnetic resonance imaging results showed that while the fluorocarbon coated paper at low refining level were grease barriers, some amount of grease penetrated up to 45-50% depth in paper in less than 70 seconds. For a 5 minute refined PFE coated paper sample, hexadecane stagnated at half the sample depth. One of the possible explanations for this phenomenon is the creation of capillary stop valves at half sample depth due to fluorocarbon penetration which prevents hexadecane from further penetration. Although the MRI helped quantify the hexadecane penetration into paper, it was difficult to interpret the permeation mechanism because majority of penetration took place during first 70 s (delay in acquiring the first image). Fluorocarbon

penetration depth in paper calculated using photoacoustic spectroscopy, within margin of error, indicated similar thickness as obtained on silicon wafer. This was primarily due to photoacoustic spectroscopy's limitation to only locate interface between pure fluorocarbon film and paper.

7. DUAL LAYER FILMS OF FLUOROCARBON AND HYDROGEL

This chapter delves into deposition of dual layer films on silicon. The main objective of this study was to demonstrate that dual layer films using the precursors pentafluoroethane (PFE) and n-isopropylacrylamide (NIPAAM) can be deposited on silicon wafers using plasma enhanced chemical vapor deposition (PECVD). The deposited films were characterized using ellipsometry, XPS, and contact angle goniometry.

7.1 Multilayer Structures for Packaging

Fluorocarbon films deposited on paper and cellulose have shown excellent barrier properties towards water (hydrophobicity) and exhibit good grease barrier properties (oleophobicity) as well. In addition, the fluorocarbon films developed in this work allow moisture permeation which maintains the physical properties of the underlying paper substrate. However, due to the increased demand of flexible packaging materials and newer applications for these materials, there may be a need to provide additional functionalities. The development of an ever-increasing range of sophisticated barrier films in the form of laminations, coextrusions and coatings, including metallization and silica depositions, has been pivotal to the success of flexible packaging, especially in the food, medical and pharmaceutical sectors [185]. Progress in this arena has been rapid in recent years. Research in the area includes the development of films with barrier

properties tailored to meet the needs of specific foods, and the development of ‘smart’ films which can modify their barrier properties in response to changes in temperature and humidity.

Multilayer structures are important because of the desire to combine the best properties of a number of different materials into a structure when no single material can provide the needed performance. As an example, polyethylene (PE) is inexpensive material and is a good moisture barrier but a poor oxygen barrier. On the other hand, polyethylene terephthalate (PET) is a good oxygen barrier, is expensive, and does not seal well [186]. If both these materials are combined either by lamination or coextrusion, the requisite properties can be obtained from the dual film layer. Three methods are commonly invoked to achieve multiple layers for packaging applications [186, 187]:

- 1) *Adhesive Lamination*: Adhesive lamination is the process of bonding two component or "substrate" parts by sandwiching them together with an intervening layer of adhesive material. The majority of adhesive laminates are manufactured using a dry bonding process. A liquid adhesive is applied on one substrate and is dried using hot air. This dried surface is then brought into contact with a second substrate while applying heat and pressure. In the case of wet bonding, the adhesive is applied between two substrates and both are joined and dried together in an oven [187].
- 2) *Extrusion Lamination*: In extrusion coating and lamination, a resin is melted and formed into a thin hot film, which is coated onto a moving, flat substrate such as

paper, paperboard, metal foil, or plastic film. The coated substrate then passes between a set of counter-rotating rolls, which press the coating onto the substrate to ensure complete contact and adhesion. Substrates that can be coated with polyolefins include paper, paperboard, biaxially oriented polypropylene (BOPP), biaxially-oriented nylon (BON), polyester and other plastic films, metal foil, fabrics, and glass fiber mat.

- 3) *Coextrusion*: Coextrusion is a process of extruding two or more materials through a single die with two or more orifices arranged so that the extrudates merge and weld together into a laminar structure before chilling. The advantage of coextrusion is that each ply of the laminate imparts a desired characteristic property, such as stiffness, heat-sealability, impermeability or resistance to various environments; such properties would be impossible to attain with any single material [187].

Surface modification is a useful way of applying coatings to a surface. There are three main approaches to surface modification: (1) traditional coating; (2) vacuum metallization and silica deposition; and (3) surface treatment. Traditional coatings are applied by rollers (lacquers, varnishes, and wax), extrusion (polyethylene and polypropylene), and dipping (hot wax impregnation) [185, 187]. In vacuum deposition, a metal (e.g. aluminum), silicon dioxide (glass) or silicon nitride can be vacuum deposited onto the surface of PET, cellophane, polypropylene, and nylon [185]. Surface treatment includes such processes as chemical priming, etching, thin plasma coating, and surface cleaning. While the first two methods pose significant recycling problems and

environmental burdens, the surface treatment methods are not usually limited by such issues. Thus, applying multiple layers onto a substrate using surface treatments (e.g., plasma deposition of thin films) may be an attractive alternative to traditional coating methods.

In this work, dual layer film deposition using plasma techniques was explored assess the use of plasma deposited multilayer coatings for various barrier applications. Either a thin layer of fluorocarbon (PFE film) was deposited onto a thin layer of hydrogel (n-isopropylacrylamide film) or the reverse sequence was employed, both a silicon wafer as the substrate. The primary goal was to demonstrate that dual layer films can be generated using plasma techniques. The deposited films were characterized using contact angle goniometry, ellipsometry and XPS.

7.2 Dual layer films (Fluorocarbon film and hydrogel film)

Fluorocarbon films have been demonstrated to have excellent hydrophobicity and good resistance to lipophilic material. However, it may not be possible to print effectively onto the fluorocarbon coated surface with water based ink due to the water repellence properties of fluorocarbon films. If a hydrogel coating, which is hydrophilic in nature, is applied on top of a fluorocarbon coating, printing may be facilitated while retaining the barrier properties provided by fluorocarbon films. This is one potential application where dual layer coatings can be used in paper and paper board industries for packaging applications, where barrier properties and printability are both important. Another

application where dual layer films of fluorocarbon and hydrogel might be used is to create an effective barrier against water and lipophilic material (or grease). Fluorocarbon films repel water (and to some extent grease) while hydrophilic coatings (hydrogel) should repel non polar compounds such as oil and grease. Thus, it is appropriate to investigate dual layer films of fluorocarbon (PFE film) and hydrogel (p-NIPAAM film).

7.3 Dual Layer Film Deposition Using Plasma Enhanced CVD

A PFE film was first deposited onto a silicon wafer. This PFE coated sample was then exposed to a NIPAAM plasma to deposit a p-NIPAAM film on top of the fluorocarbon film. In the reverse sequence, a NIPAAM film was first deposited onto the silicon wafer followed by PFE film deposition.

7.3.1 Experimental Conditions

PFE films were deposited in a 6" parallel plate plasma reactor under the following conditions: $P = 1$ Torr, $T = 120$ °C, RF = 95 W on 6" dia. platen (Power Density ~ 0.5 W/cm²); argon was used as the carrier gas in all experiments.

P-NIPAAM films were deposited in 4 cm parallel plate plasma reactor under following conditions: $P = 700$ mTorr, $T = 150$ °C, RF = 30 W on 4 cm dia platen (Power Density ~ 2.38 W/cm²); argon was used as the carrier gas in all experiments

The following depositions were performed using PECVD:

Thin PFE film (10 nm) on top of NIPAAM layer (275 nm)

Thick PFE film (286 nm) on top of NIPAAM layer (275 nm)

Thin NIPAAM film (4.5 nm) on top of PFE layer (280 nm)

Thick NIPAAM film (257 nm) on top of PFE layer (280 nm)

In all cases, the substrate was silicon and a 15 sec O₂ plasma pretreatment was performed between film depositions to promote adhesion.

7.3.2 Dual Layer Film Characterization

Spectroscopic ellipsometry was used to measure the thickness and refractive index of the plasma deposited films. XPS was used to determine the chemical composition and bonding structure of the films. Angle resolved XPS was also used to study the variation in film composition with depth and to probe the dual layer interface. A contact angle goniometer was used for contact angle studies; all measurements were performed at room temperature (25 °C) under ambient conditions. A drop size of 5 µl was dispensed onto the surface of the sample and contact angle data was collected. Error in the contact angle data was between 1.5° – 2°.

7.3.3 Results and Discussion

A schematic for the situation where a PFE film was the top layer (p-NIPAAM film beneath) is shown in Figure 7.1.

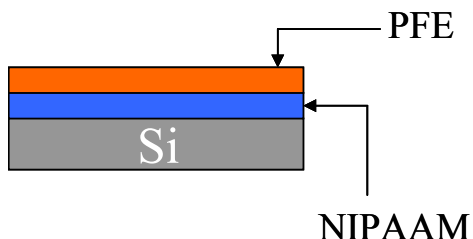


Figure 7.1 Schematic arrangement of dual layer films on Si substrate (PFE film at top)

The thickness of the p-NIPAAM film deposited was 275 nm (Refractive Index = 1.52 at 600 nm) as measured using spectroscopic ellipsometry. PFE films of two different thicknesses (10 nm and 286 nm, Refractive Index = 1.41 at 600 nm) were deposited on top of the 275 nm p-NIPAAM film. Contact angle data on the dual layer films where the PFE layer is the top layer is presented in Figure 7.2. PFE films deposited on a Si wafer under similar conditions are also shown for comparison.

Both PFE films (10 nm and 286 nm) on Si wafers show stable water contact angles $\sim 107^\circ$. Both the PFE films on top of the NIPAAM film show higher initial contact angles as compared to that on Si possibly because of the surface roughness of the underlying NIPAAM layer. A thin PFE layer (10 nm) on NIPAAM shows a decrease in contact

angle with time since the 10 nm PFE film may not provide sufficient coverage for hydrophobicity, leaving some hydrophilic groups exposed.

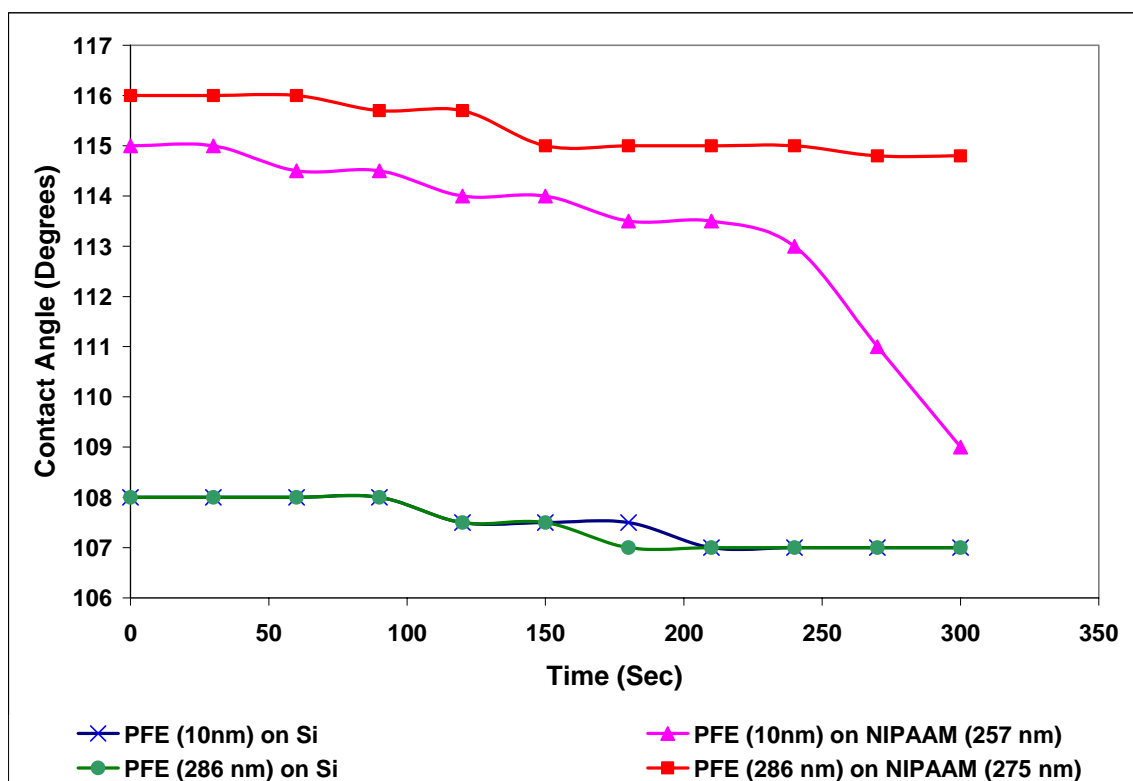


Figure 7.2 Contact angle data for dual layer films where 10 nm and 286 nm PFE films are the top layers (p-NIPAAM layer below). Contact angle data for PFE films deposited on Si under similar conditions are also shown for comparison.

A schematic for the situation where a p-NIPAAM film was the top layer (PFE film beneath) is shown in Figure 7.3.

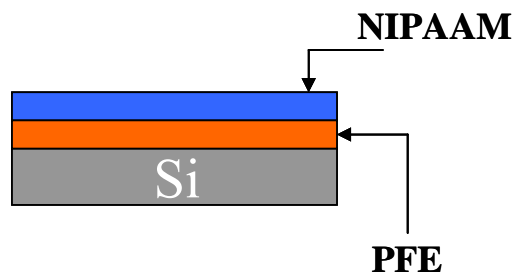


Figure 7.3 Schematic arrangement of dual layer films on Si substrate (p-NIPAAM film at top)

The thickness of the PFE film deposited was 280 nm (Refractive Index = 1.41 at 600 nm) as measured using spectroscopic ellipsometry. P-NIPAAM films of two different thicknesses (4.5 nm and 275 nm, Refractive Index = 1.51 at 600 nm) were deposited on top of the 280 nm PFE films. Contact angle data on the dual layer films where p-NIPAAM layer is the top layer is presented in Figure 7.4. P-NIPAAM films deposited on Si wafers under similar conditions are also shown for comparison.

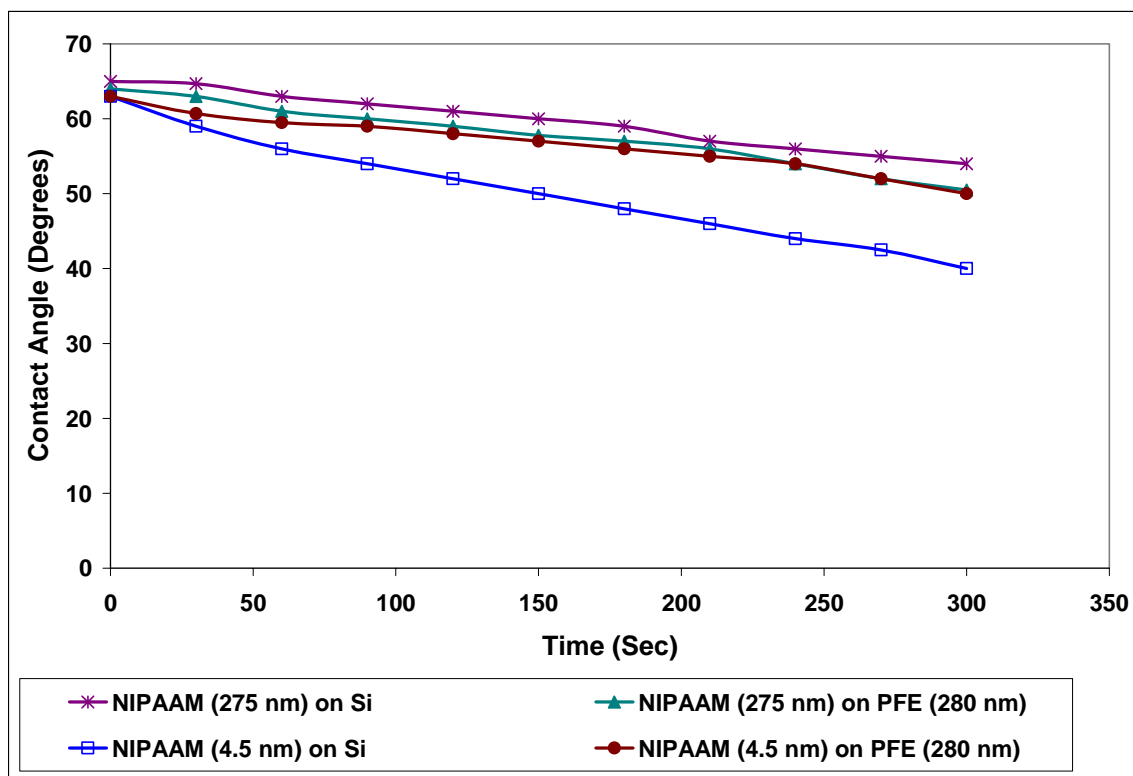


Figure 7.4 Contact angle data for dual layer films where 4.5 nm and 275 nm p-NIPAAM films are the top layers (PFE layer below). Contact angle data for p-NIPAAM films deposited on Si under similar conditions are also shown for comparison.

The contact angle decreases with time in all cases where the NIPAAM layer (hydrogel) is the top layer since it continually absorbs water. The contact angle for a thin NIPAAM layer (4.5 nm) on Si decreases faster than that for the thicker layer, possibly due to partial dissolution of the film in water because of limited cross-linking present in the thin film. The thin NIPAAM film (4.5 nm) on PFE exhibits hydrophilicity even though it is on top of a hydrophobic layer indicating that hydrophilic groups are present at the surface of the PFE film.

XPS studies were performed on the dual layer films to study the surface composition and interfacial bonding. In the cases where thick films (PFE or p-NIPAAM) were the upper layers, the XPS scan shows the film composition of that particular material (PFE or p-NIPAAM) since the sampling depth of XPS is in the range of 6–8 nm [81]. Figure 7.5 shows a survey scan of a 275 nm p-NIPAAM film on top of a PFE film.

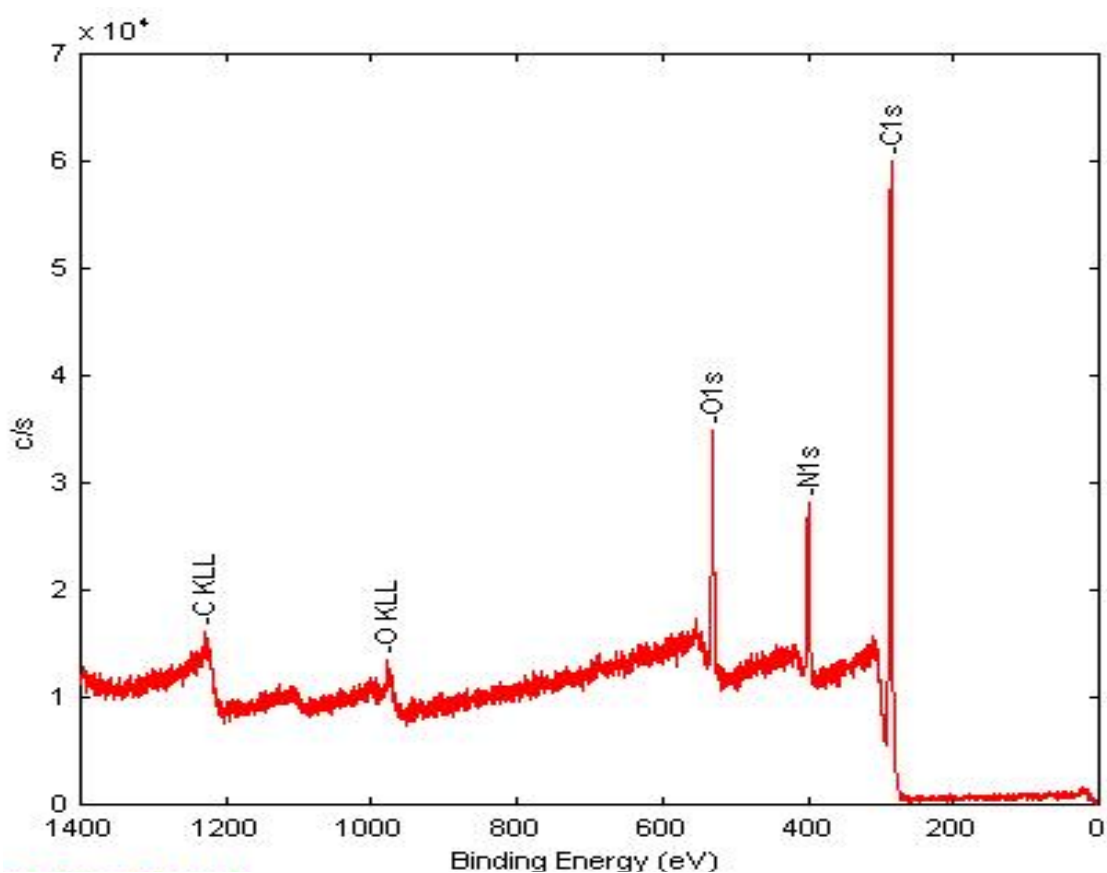


Figure 7.5 XPS survey scan of 275 nm p-NIPAAM film on top of PFE film. This scan is characteristic of p-NIPAAM film on Si wafer [188].

Figure 7.6 presents the XPS survey scan of 280 nm PFE film on top of p-NIPAAM film. Clearly, the film consists mainly of C and F. A small amount of oxygen (<0.1%) is present due to post deposition oxidation of dangling bonds.

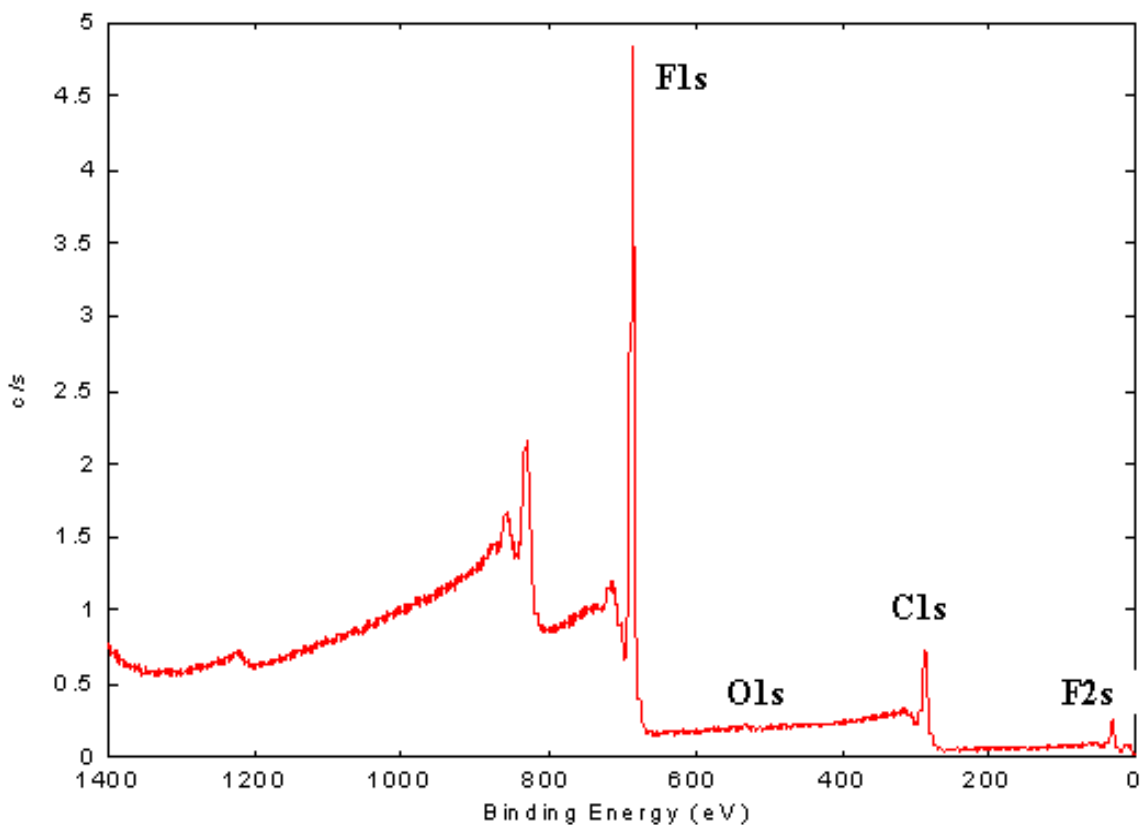


Figure 7.6 XPS survey scan of 280 nm PFE film on top of p-NIPAAM film.

The effective sampling depth in XPS can be varied (for flat samples) by changing the angle of the sample with respect to the detector. The effect of sample orientation with respect to the analyzer can be determined by considering the schematic in Figure 7.7.

About 95% of the signal arises from an electron path length of 3λ in the solid, where λ is the inelastic mean free path of the photoelectron. The actual depth sampled, d , is given by equation 7.1:

$$d = 3 \lambda \sin \theta \quad (7.1)$$

where θ is the angle between the sample surface and the analyzer acceptance plane (also known as the “take off” angle). Thus, at $\theta = 90^\circ$, the sample surface is perpendicular to the line of acceptance of the analyzer, and d is equal to the maximum sampling depth of 3λ .

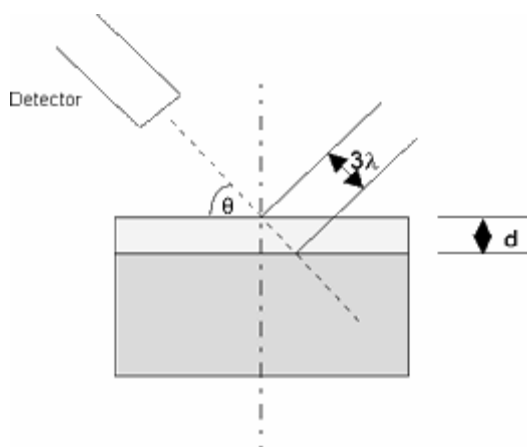


Figure 7.7 Schematic for determining the XPS sampling depth for a given take-off angle.

As θ tends to 0° , the outermost surface species account for a larger proportion of the signal detected. As an example, the sampling depths for various angles are given in the Table 7.1 for an element where $\lambda = 2\text{nm}$:

Table 7.1 XPS sampling depths at various take-off angles for an element with $\lambda = 2\text{nm}$.

θ	90°	50°	30°	15°	7.5°
d (nm)	6.0	4.6	3.0	2.6	0.78

Since λ varies from element to element, the sampling depth is generally quoted as a range; e.g. at $\theta = 90^\circ$, the analysis depth is quoted as 5 - 10nm.

Angle resolved XPS was performed on a thin p-NIPAAM film (4.5 nm) on top of a PFE film (280 nm). Table 7.2 shows the elemental composition of the dual layer films at different take-off angles with respect to the detector.

Table 7.2 Elemental Composition of thin p-NIPAAM film (4.5 nm) on top of PFE film at various take-off angles with respect to the detector

Angle	%C	%O	%F	%N
15°	63.25	16.91	10.24	9.60
30°	62.94	16.80	12.26	8.00
45°	61.13	16.37	14.89	7.61
60°	61.15	14.46	17.33	7.06
70°	60.76	13.56	19.28	6.40
75°	60.67	13.11	19.99	6.20
80°	61.49	12.90	20.49	5.12

At shallow angles, the percentage of oxygen and nitrogen is higher compared to that at deep angles indicating that the top layers have more of a hydrogel like composition (p-NIPAAm) and are therefore expected to be hydrophilic. This is consistent with the contact angle data. At higher angles, the percentage of fluorine is about twice that at shallow angles indicating that the film at the deeper levels (~6 to 10 nm) has more hydrophobic character compared to that at a shallower level.

The C1s peak was deconvoluted to identify the contributions from different chemical groups at various takeoff angles. . Figure 7.8 shows the C1s peak deconvolution of a 4.5 nm p-NIPAAm film on top of a PFE film. Table 7.3 shows the percentage composition of various chemical groups at different take-off angles with respect to the detector.

Table 7.3. High Resolution C1s spectra peak deconvolution of dual layer film (4.5 nm p-NIPAAm on top of PFE film).

Angle	C-C, C-H	C-CF _x	CF	CF ₂	CF ₃	C-N	C=O
15°	61.03%	-	-	2.42%	-	17.25%	19.30
30°	59.36%			3.99%	3.93%	15.64%	21.01%
45°	61.23%				3.91%	11.40%	23.46%
60°	59.46%	27.97%		7.97%	4.62%		
70°	58.97%	28.08%		9.31%	3.64%		
75°	63.53%	20.59%		11.55%	4.33%		
80°	63.98%	17.37%	-	14.84%	3.82%	-	-

At shallow angles, the bonding configuration is typical of p-NIPAAm (C-C/C-H; C-N, and C=O) [188], indicating that the top layers are hydrophilic in nature. There is small

amount of CF_2 and CF_3 present in top layers because of PFE film beneath, indicating that there may be covalent bonding between hydrogel layer and the PFE layer. At larger angles, a higher concentration of C-CF_x , CF_2 , and CF_3 indicate that the deeper levels ($\sim 6 - 8$ nm) are hydrophobic in nature because of the underlying PFE film. Also, at deeper levels, the contributions from C-N and C=O are expected to be too small to detect and thus account for in peak deconvolution.

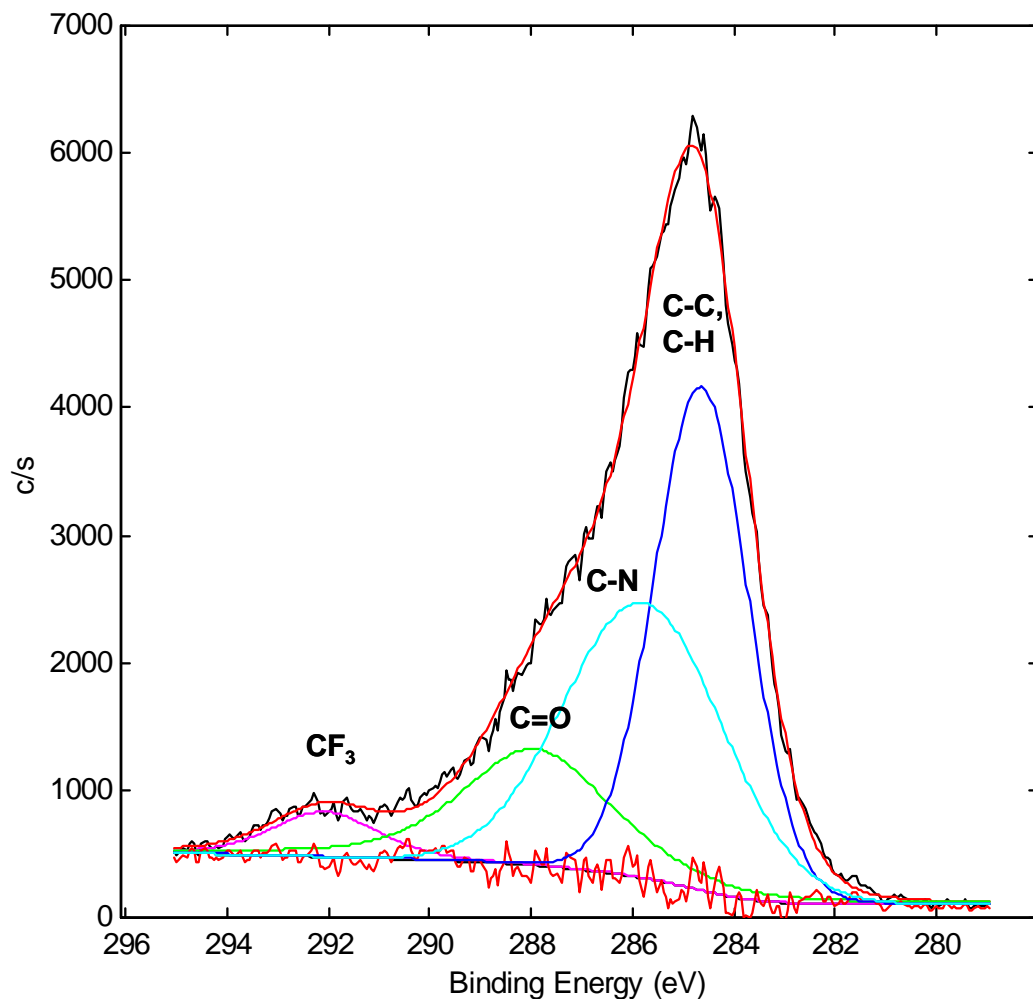


Figure 7.8 C1s Peak Deconvolution of thin p-NIPAAAM (4.5 nm) film on top of PFE film (at 45° takeoff angle)

Angle resolved XPS was also performed on a thin PFE film (10 nm) on top of a p-NIPAAAM film (275 nm). Table 7.4 shows the elemental composition of the dual layer films at different take-off angles with respect to the detector.

Table 7.4 Elemental Composition of thin PFE film (10 nm) on top of p-NIPAAM film at various take-off angles with respect to the detector

Angle	%C	%O	%F	%N
45°	45.16	2.29	52.55	-
60°	44.53	2.49	51.34	1.59
75°	44.44	2.88	50.19	2.41
80°	43.31	2.91	50.46	3.32

Since the sampling depth of XPS is in the range of 5 nm to 10 nm, the dual layer film composition primarily depicts the composition of PFE film in this case. The F/C ratio in the films is roughly 1.15 which explains the hydrophobicity of the films. At larger angles, the concentration of carbon and fluorine decreases slightly; however, the F/C ratio is still high (~1.15). Also, at larger angles, the concentration of oxygen and nitrogen increases indicating the presence of the p-NIPAAM layer beneath. The presence of oxygen and nitrogen in the films at all angles suggests the presence of covalent bonds between the PFE and p-NIPAAM films.

The C1s peak was deconvoluted to identify the contributions from different chemical groups at various takeoff angles. Figure 7.9 shows the C1s peak deconvolution of a 10 nm PFE film on top of a p-NIPAAM film. Table 7.5 shows the percentage composition of various chemical groups (after peak deconvolution) at different take-off angles with respect to the detector.

Table 7.5 High Resolution C1s spectra peak deconvolution of dual layer film (10 nm of PFE on top of p-NIPAAM film).

Angle	C-C, C-H	C-CF _x	CF	CF ₂	CF ₃	C-N	C=O
45°	7.95	28.12	28.65	20.28	15.00		
60°	4.05	37.90	23.60	18.09	16.36		
75°	3.42	40.22	21.86	19.67	14.83		
80°	3.10	40.83	22.23	19.14	14.70	-	-

At larger angles (i.e. deeper layers probed), the contributions from C-N and C=O are expected to be too small to show up in peak deconvolution. However, the higher concentration of CF, CF₂ and CF₃ groups confirms the fact that the films are hydrophobic in nature. These results are consistent with the contact angle data. However, the presence of oxygen in the films may indicate insufficient coverage of the underlying p-NIPAAM film resulting in a decrease in contact angle with time. It is also possible that that p-NIPAAM film can give up oxygen as a result of reaction with fluorine or ion bombardment so that oxygen is incorporated into the fluorocarbon film. A high concentration of C-CF_x groups indicates extensive cross-linking due to the plasma environment. Because the PFE layer is thicker than the XPS sampling depth, higher detector angles yield limited bonding and compositional variation information.

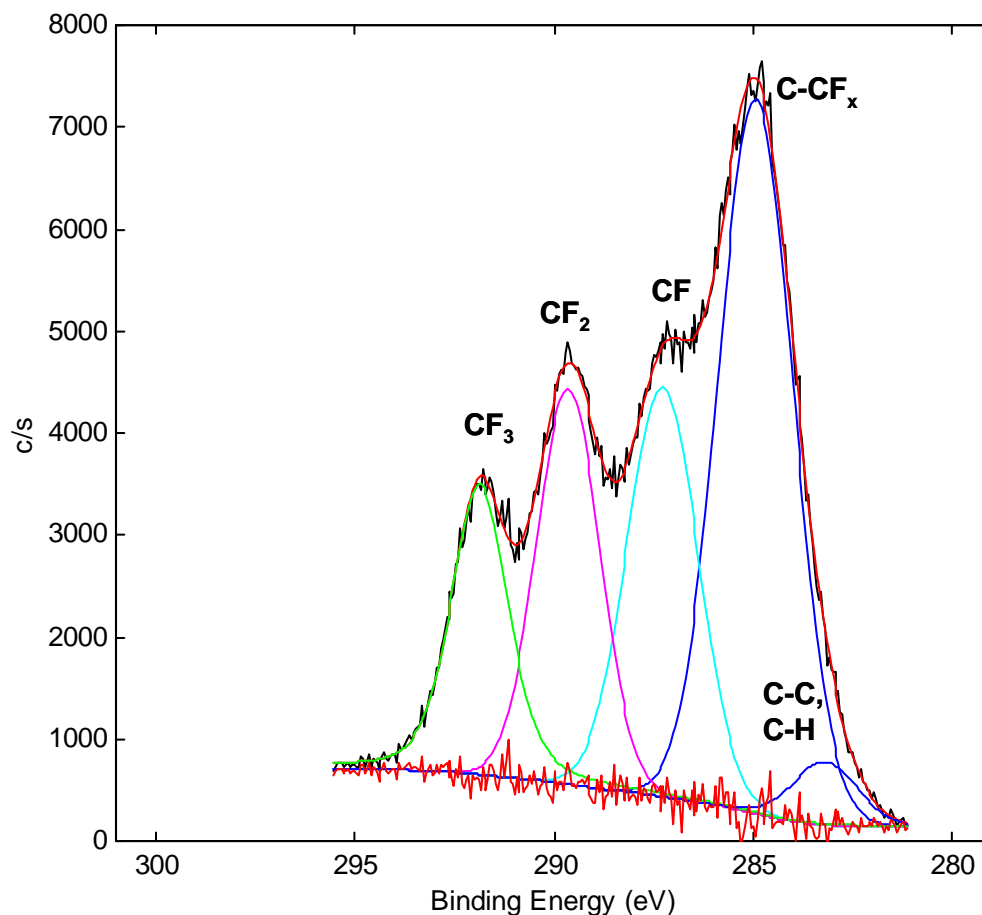


Figure 7.9 C1s Peak Deconvolution of a thin PFE (10 nm) film on top of a p-NIPAAM film (at 45° takeoff angle)

7.3.4 Conclusions

Dual layer films of PFE and p-NIPAAM can be deposited on a Si wafer using plasma enhanced CVD. Contact angle data suggests that thin p-NIPAAM film of (4.5 nm) on PFE is hydrophilic, indicating surface modification of the hydrophobic PFE film. Also, a thin PFE film (10 nm) on a p-NIPAAM film shows hydrophobic character. Angle-resolved XPS analysis of the dual layer films shows the compositional and bonding variation with sampling depth. The XPS data also suggests that the p-NIPAAM film may

be covalently bonded to the PFE film. The studies conducted will be useful in evaluating the performance of dual layer films on different substrates. Dual layer films can be deposited on paper and cellulose in a similar manner to that on Si.

8. SUMMARY AND FUTURE DIRECTIONS

8.1 Summary

Global demand for flexible packaging is growing at a rapid pace due to changing lifestyles of people, newer applications to which the flexible materials are being applied, and environmental regulations. Most of the packaging materials encountered in day to day life are either paper or plastic based - the raw materials being wood or fossil fuels. Plastic is manufactured from fossil fuels (oil and coal), a non-renewable natural resource, whereas paper is derived from wood, a renewable natural resource. Due to low cost, biodegradability, light weight, flexibility and ease of recycle, paper-based materials are important candidates for flexible packaging applications provided that suitable barrier properties are imparted.

In this work, a surface film deposition and thus surface modification technique was employed to impart barrier properties to paper and cellulosic materials for potential applications in packaging. Plasma enhanced chemical vapor deposition was employed to deposit thin fluorocarbon films on the surface of paper and cellulose to achieve hydrophobic and lipophobic properties. Pentafluoroethane (PFE) and octafluorocyclobutane (OFCB) were invoked as precursors to deposit fluorocarbon films on paper in a parallel plate RF plasma system operating at low pressure (1 Torr). Fluorocarbon coated paper/cellulose exhibits hydrophobicity (water repellence), while

allowing water vapor permeation to maintain the physical properties of the underlying (bulk paper) substrate. Additionally, the fluorocarbon coated paper showed good resistance to grease and lipophilic materials. Both hydrophobic and lipophobic properties were characterized by various experimental techniques. Dual layer films of fluorocarbon coating (hydrophobic) and hydrogel coating (hydrophilic) were deposited using PECVD and characterized using the same analytical techniques.

Fluorocarbon film depositions were performed in parallel plate plasma reactor systems with either 4-cm or 6-inch diameter electrodes. As expected, the fluorocarbon film deposition rate for both PFE and OFCB increased with an increase in applied RF power in both reactor systems. The film deposition rate decreased with an increase in substrate temperature indicating that the deposition process was adsorption limited. The OFCB film deposition rate was higher (~ 4 times) than the deposition rate of the PFE films. This observation can be explained on the basis of the difference between their plasma dissociation chemistries, where OFCB produces more polymerizing fragments when compared to the PFE precursor. Film thicknesses were measured using spectroscopic ellipsometry. Refractive indices for PFE and OFCB films were 1.41 and 1.38 at 600 nm, respectively. XPS analysis was performed to determine the surface composition and bonding structure of the fluorocarbon films. XPS data suggested that films deposited from OFCB had a higher F:C ratio of 1.15-1.3 compared to those deposited from PFE (F:C = 1.0-1.2) indicating that OFCB films probably have a lower degree of crosslinking than films deposited from PFE. There was some oxygen present in the fluorocarbon films, which was attributed to post deposition dangling bond oxidation of the

fluorocarbon films. However, the low O:C ratio indicated that the films had low concentrations of dangling bonds. C1s peak deconvolution indicated the presence of five different moieties (CF_3 , CF_2 , CF , C-CF_x , and C-H/C-C) present on the surface of the fluorocarbon film deposited from both precursors. Scanning electron microscopy of the surface of the PFE film deposited on a Si wafer indicated a cauliflower-like globular morphology, attributed to gas-phase dominated plasma polymerization.

Paper and cellulose surfaces coated with thin fluorocarbon films deposited from PFE displayed hydrophobic character as evidenced by contact angle measurements with water. The fluorocarbon film thickness was varied on the cellulose substrate to study the effect of film thickness on the water contact angle. It was observed that PFE films with greater than 70 nm thickness provided a stable hydrophobic character to the cellulose substrate. Hydrophobic character was attributed to fluorinated moieties (CF_x : CF_3 and CF_2) since the fluorination of carbon prevents hydrogen bonding with water. Furthermore, the effect of fluorocarbon film composition on water contact angle and, therefore, hydrophobicity was studied by pulsed plasma experiments. Water contact angles increased with increasing concentration of CF_3 and CF_2 moieties in the fluorocarbon films. SEM studies on paper coated with a thin fluorocarbon film (1 μm) did not show any change in surface morphology indicating that surface and near surface fibers are coated during fluorocarbon deposition without overcoating the paper surface.

Moisture absorption studies conducted on fluorocarbon films deposited from PFE and OFCB using a quartz crystal microbalance (QCM) show that the wt% of moisture

absorbed did not exceed 0.14 wt% for either of the films, again indicating the hydrophobic behavior of the films. Although water vapor uptake of the fluorocarbon films is low, moisture diffusivity through the films is high; that is, moisture penetrates the films but is not chemically bonded. QCM studies also demonstrate that the absorption of water vapor is a bulk phenomenon in which the moisture penetrates into the film. Transient moisture absorption studies were conducted using the QCM to evaluate the rate of moisture uptake and diffusivity. Water vapor diffusivities were evaluated to be of the order of 10^{-11} m²/s for both the films.

Fluorocarbon coated paper exhibits improved grease barrier properties in addition to being hydrophobic. Oleic acid penetration tests conducted on uncoated and fluorocarbon coated paper samples indicate that 1 μ m PFE coated paper displays good resistance to oleic acid penetration. The presence of an oleic acid droplet was observed on the surface of coated paper even after several days whereas on uncoated paper, the droplet was absorbed within one minute. The TAAPI “oil kit” test was also conducted to study the oleophobic properties of fluorocarbon coated paper. For a paper sample coated with a 1 μ m PFE film, an “oil kit” rating of 5 was assigned indicating good grease barrier properties. Both oleic acid penetration test and TAPPI “oil kit” test were qualitative in nature. While these tests demonstrate that the PFE coated paper displays improved grease barrier properties, they did not provide any quantitative information on the oleophobic properties of coated paper. QCM studies using hexadecane vapor (grease surrogate) were conducted to quantify the grease barrier properties of fluorocarbon films. Fluorocarbon films deposited from PFE showed very low affinity for hexadecane and only 0.6wt% of

hexadecane was absorbed into fluorocarbon films of varying thicknesses (500 nm, 750 nm, and 1 μm). The diffusivity of hexadecane vapor in fluorocarbon films ($\sim 10^{-13} \text{ cm}^2/\text{s}$) was also two to three orders of magnitude lower than that of water vapor, indicating slow transport within the films.

Magnetic resonance imaging (MRI) was another method employed to quantify the grease barrier properties of PFE coated paper. Thick paper samples were produced using a TAPPI method and hexadecane permeation through the PFE coated and uncoated paper samples was studied. The spin echo technique in MRI allowed the presence of hexadecane to be imaged (contrast image) in terms of spin echo signal intensity. The signal intensity was directly proportional to the concentration of hexadecane present in the paper sample. Using a calibration curve, the signal intensity data was converted into hexadecane concentration data at various depths inside the paper sample as a function of time. Since there was a finite delay in acquiring the first image ($\sim 70 \text{ s}$), hexadecane completely penetrates the uncoated paper sample and $\sim 45\%$ of the PFE coated paper sample. Subsequent images (increasing time) showed little difference between hexadecane concentrations at various depths with time. While the hexadecane penetration into the paper samples could be quantified, it was difficult to study quantitatively the diffusion behavior of hexadecane in coated and uncoated paper samples.

Photoacoustic spectroscopy was employed to determine the fluorocarbon coating depth of fibers within the paper samples. This technique could only determine the location of the interface between a pure fluorocarbon (highest concentration) layer and the paper

substrate. Based on the pure polymer interface data, the fluorocarbon film penetration depth in paper was similar to the film thickness measured on a Si wafer. Photoacoustic spectroscopy cannot detect the interface if there is a gradual change in the concentration of fluorocarbon moieties with depth, i.e., if no well defined interface exists.

Dual layer films of PFE and plasma-deposited n-isopropylacrylamide (p-NIPAAM) were deposited on silicon wafers using PECVD. The main goal in this case was to demonstrate the feasibility of dual layer formation using plasma techniques. The dual layer films were characterized using contact angle studies and XPS analysis. XPS analysis was performed to study the surface composition while angle resolved XPS (ARXPS) was employed to gather the interfacial bonding information.

8.2 Recommendations for Future Work

The fluorocarbon films described in this research provide excellent water repellence properties to cellulose and paper in addition to acting as a reasonable grease barrier. However, applications such as food packaging may require a material that is both an excellent water and grease barrier. Dual layer films of the kind described in thesis may hold promise for providing adequate water and grease barrier properties for packaging applications. Hydrophilic films such p-NIPAAM and polyethylene glycol (PEG) are expected to repel grease or oil molecules whereas hydrophobic films like PFE or OFCB will repel water. Thus, both grease and water barrier properties might be achieved with a dual layer film structure deposited on the surface of paper. Although this thesis

demonstrates that dual layer films of PFE and p-NIPAAM can be deposited using PECVD, additional work is needed in terms of depositing the films on the surface of paper and characterizing the resulting structures. It is also important to know how the film structure changes on the surface of paper when exposed to water or grease.

Another potential application of dual layer films worth investigating is in printing. Since fluorocarbon films have excellent water repellence properties, it may not be possible to print effectively onto the fluorocarbon coated surface with water based ink. If a hydrophilic coating (such as p-NIPAAM or PEG) is applied on top of a fluorocarbon coating, printing may be facilitated while retaining the barrier properties provided by fluorocarbon films. This can be used in paper and paper board industries for packaging applications, where barrier properties and printability are both important

While photoacoustic spectroscopy provided some information on the paper coating depth of fluorocarbon films, it could not detect the fluorocarbon moieties below the pure fluorocarbon and paper interface. This may lead to understated fluorocarbon coating depth and therefore understated measurement to which paper structure has been modified. Methods to investigate the coating depth of fluorocarbon film in paper need to be explored in detail. One of the techniques that can be used to characterize the fluorocarbon coating depth is staining using osmium tetroxide (OsO_4) followed by SEM imaging. Osmium tetroxide is primarily used as a staining agent for biological samples in the process known as “fixing.” Fixing allows very small structures to be seen under an electron microscope.

OsO₄ forms cross-linked complexes with C=C double bonds. As evident from the FTIR spectra of fluorocarbon films, the broad peak between 1600 to 1850 cm⁻¹ corresponds to unsaturated fluorocarbon bonds (C=C; C=CF₂, and -CF=CF₂). Such unsaturated bonds present in PFE films can easily form complexes with OsO₄. Thus, an improved visualization of the pore structure and fluorocarbon film penetration depth may be obtained by staining the fluorocarbon films on paper with OsO₄. The stained fluorocarbon films will appear brighter and may be clearly discerned from the paper matrix in which the coating penetrates. This will not only improve visualization of the fluorocarbon penetration but may also indicate details of the pore structure and morphology, allowing quantification of change in substrate morphology. Image analysis of micrographs of OsO₄-stained paper sample cross-sections may thus offer an interesting way of assessing the structure of coating layers. However, due to its toxicity, proper precautions must be taken during staining.

While it is important to determine the fluorocarbon film depth in paper substrates, it may not provide details on the amount of fluorocarbon penetration into the individual fibers. This information is important for evaluating the extent and stability of surface modification of paper fibers. The depth of fluorocarbon penetration in individual fibers is another important aspect that needs investigation. Staining techniques such as OsO₄ can also be applied to study the coating penetration depth in fibers.

Another area where further investigation is needed is the quantification of grease barrier properties as studied by MRI. It should be noted that due to limitations in speed with which the sample is loaded into the MRI machine for analysis, it is difficult to observe incorporation of grease (or surrogates) on the PFE coated paper surface during first few seconds after hexadecane is dispensed. A slight but expensive modification in MRI hardware can address this issue. A plastic microsyringe actuated by an electrostatic switch positioned above the coated paper sample can be used to dispense a known volume of hexadecane at time $t = 0$. The images can be collected using low spatial resolution but high temporal resolution i.e. sampling time for each image can be reduced to a few seconds at the cost of image resolution. A high sensitivity MRI machine can be employed to address the low image resolution issue. The modification in MRI hardware will not only help in better quantification of hexadecane permeation into the coated and uncoated paper but will also provide valuable insight into the mechanism of permeation.

MRI studies on hexadecane permeation in a 5 min refined PFE coated sample showed that hexadecane stagnates at approximately half depth in the sample. A possible explanation offered for this phenomenon was the creation of capillary “stop valves” at half sample depth due to fluorocarbon coating penetration such that the remaining depth comprises capillaries with larger pore sizes. To evaluate this possibility, MRI studies can be performed by dispensing hexadecane on the reverse side of the coated sample and monitoring hexadecane permeation as a function of time. When dispensed on the reverse side, hexadecane will not be exposed to a sudden expansion in the pore size and is expected to permeate completely through the sample. Another way to verify pore

narrowing or blockage is to perform cross-sectional SEM on the sample. If SEM micrographs of the PFE coated sample show pore expansion midway through the sample, the occurrence of capillary “stop valves” will be demonstrated, lending credibility to this mechanism. The globular morphology of the PFE film can be used as an indicator to verify that pores are narrowed or blocked as a result of PFE coating at half depth in the sample.

Finally, the fluorocarbon films developed in this study can be applied to a variety of other applications in addition to coating paper and cellulose for flexible packaging applications. Application of fluorocarbon films can be investigated in permselective membranes for separation, in fuel cells to reduce methanol permeation, and in biological science for protein retention and formation of thromboresistant coatings.

REFERENCES

- [1] R. Beswick and D. J. Dunn, "Plastics in Packaging - Western Europe and North America (Market Report, 2002)," 2002.
- [2] The_Freedonia_Group_Inc, "US flex-pack demand: \$14 billion in 2008.," in *Converting Magazine*, vol. 22, 2004, pp. 8.
- [3] Kline&Co, "Aim barrier films at today's snack market for top flex-pack sales tomorrow," in *Converting Magazine*, vol. 17, 1999, pp. 10.
- [4] T. Koltzenburg, "High-Barrier Packaging: Yesterday, Today, and Tomorrow," in *Paper, Film & Foil CONVERTER (PFFC)*: PRIMEDIA Business Magazines & Media Inc., 2000.
- [5] E. Deisenroth, C. Jho, M. Haniff, and J. Jennings, "The designing of a new grease repellent fluorochemical for the paper industry," *Surface Coatings International*, vol. 81, pp. 440, 1998.
- [6] N. Inagaki, *Plasma Surface Modification and Plasma Polymerization*: Technomic Publishing Co., Inc., PA, 1996.
- [7] F. Denes, "Synthesis and Surface Modification by Macromolecular Plasma Chemistry," *Trends in Polymer Science*, vol. 5, pp. 23, 1997.
- [8] B. Lindberg, "Interaction Phenomena and Barrier Properties of Plastic Packaging Material in Relation to Foodstuff," presented at International Symposium on Interactions: Food - Food Packaging Materials, Lund, Sweden, 1994.
- [9] FDA, "Title21 (Food and Drugs)," vol. 21 CFR - Code of Federal Regulations Register, D. o. H. a. H. Services, Ed.: Food and Drug Administration, 2003.
- [10] M. A. Lieberman and A. J. Lichtenberg, *Principles of Plasma Discharges and Materials Processing*: Wiley Interscience, 1994.

- [11] G. S. Oehrlein, M. F. Doemling, B. E. E. Kastenmeier, P. J. Matsuo, N. R. Rueger, M. Schaepkens, and T. E. F. M. Standaert, "Surface science issues in plasma etching," *IBM Journal of Research and Development (Plasma processing)*, vol. 43, 1999.
- [12] N. Inagaki, S. Tasaka, K. Narushima, and K. Teranishi, "Surface modification of poly(tetrafluoroethylene) with pulsed hydrogen plasma," *Journal of Applied Polymer Science*, vol. 83, pp. 340, 2002.
- [13] J. W. Coburn and H. F. Winters, "Plasma etching - a discussion of mechanisms," *Journal of Vacuum Science and Technology*, vol. 16, pp. 391-403, 1979.
- [14] D. L. Flamm, "Introduction to Plasma Chemistry," in *Plasma Etching - An Introduction*, D. M. Manos and D. L. Flamm, Eds. San Diego, CA: Academic Press, Inc., 1989.
- [15] K. Endo and T. Tatsumi, "Preparation and properties of fluorinated amorphous carbon thin films by plasma enhanced chemical vapor deposition," in *Materials Research Society Symposium - Proceedings, v 381, Low-Dielectric Thin Films for Microelectronics Applications*, vol. 381, A.-. Proceedings of the 1995 Spring Meeting of MRS, Ed. San Francisco, CA, USA: Materials Research Society, 1995, pp. 249.
- [16] K. Endo and T. Tatsumi, "Fluorinated amorphous carbon thin films grown by plasma enhanced chemical vapor deposition for low dielectric constant interlayer dielectrics," *Journal of Applied Physics*, vol. 78, pp. 1370, 1995.
- [17] D. R. Cote, S. V. Nguyen, A. K. Stamper, D. S. Armbrust, D. Tobben, R. A. Conti, and G. Y. Lee, "Plasma-assisted chemical vapor deposition of dielectric thin films for ULSI semiconductor circuits," *IBM Journal of Research and Development*, vol. 43, pp. 5, 1999.
- [18] K. Endo and T. Tatsumi, "Fluorinated amorphous carbon thin films grown by helicon plasma enhanced chemical vapor deposition for low dielectric constant interlayer dielectrics," *Applied Physics Letters*, vol. 68, pp. 2864, 1996.
- [19] C. B. Labelle and K. K. Gleason, "Pulsed plasma-enhanced chemical vapor deposition from CH₂F₂, C₂H₂F₄, and CHClF₂," *Journal of Vacuum Science & Technology, A: Vacuum, Surfaces, and Films*, vol. 17, pp. 445-452, 1999.

- [20] W. Mountsier and J. A. Samuels, "Precursor selection for plasma deposited fluorinated amorphous carbon films," *Thin Solid Films*, vol. 332, pp. 362, 1998.
- [21] R. D. Chambers, *Fluorine in Organic Chemistry*. New York: John Wiley & Sons, 1973.
- [22] L. E. Cruz-Barba, S. Manolache, and F. Denes, "Generation of Teflon-like layers on cellophane surfaces under atmospheric pressure non-equilibrium SF₆-plasma environments," *POLYMER BULLETIN*, vol. 50, pp. 381, 2003.
- [23] H. T. Sahin, S. Manolache, R. A. Young, and F. Denes, "Surface fluorination of paper in CF₄-RF plasma environments," *Cellulose (Dordrecht, Netherlands)*, vol. 9, pp. 171-181, 2002.
- [24] F. Navarro, F. Davalos, F. Denes, L. E. Cruz, R. A. Young, and J. Ramos, "Highly hydrophobic sisal chemithermomechanical pulp (CTMP) paper by fluorotrimethylsilane plasma treatment," *CELLULOSE*, vol. 10, pp. 411, 2003.
- [25] S. R. Coulson, I. S. Woodward, J. P. S. Badyal, S. A. Brewer, and C. Willis, "Ultralow Surface Energy Plasma Polymer Films," *Chemistry of Materials*, vol. 12, pp. 2031-2038, 2000.
- [26] P. Favia, G. Cicala, A. Milella, F. Palumbo, P. Rossini, and R. d'Agostino, "Deposition of super-hydrophobic fluorocarbon coatings in modulated RF glow discharges," *Surface and Coatings Technology*, vol. 169-170, pp. 609-612, 2003.
- [27] T. Hiyama, *Organofluorine Compounds: Chemistry and Applications*. Berlin, Germany: Springer-Verlag, 2000.
- [28] R. d'Agostino, *Plasma Polymerization, Treatment, and Etching of Polymers*. San Diego, CA: Academic Press, 1990.
- [29] U. Vohrer, M. Muller, and C. Oehr, "Glow-discharge treatment for the modification of textiles," *SURFACE & COATINGS TECHNOLOGY*, vol. 98, pp. 1128, 1998.
- [30] J. E. Chase and F. J. Boerio, "Deposition of plasma polymerized perfluoro methylene-dominated films showing oil-repellency," *Journal of Vacuum Science & Technology, A: Vacuum, Surfaces, and Films*, vol. 21, pp. 607-615, 2003.

- [31] A. G. Pittman, in *Fluoropolymers*, vol. 25, L. A. Wall, Ed. New York: Wiley, 1972.
- [32] Y. Momose, T. Takada, and S. Okazaki, "CF₄ AND C₂F₆ PLASMA FLUORINATION OF HYDROCARBON AND FLUOROCARBON POLYMERS," presented at Proceedings of the ACS Division of Polymeric Materials, Polymeric Materials Science and Engineering, CO, 1987.
- [33] T. A. Blanchet, in *Handbook of Thermoplastics*, O. Olabisi, Ed. New York: Marcel Dekker, Inc., 1997.
- [34] S. R. Coulson, I. S. Woodward, J. P. S. Badyal, S. A. Brewer, and C. Willis, "Plasmachemical Functionalization of Solid Surfaces with Low Surface Energy Perfluorocarbon Chains," *Langmuir*, vol. 16, pp. 6287-6293, 2000.
- [35] R. J. Young and P. A. Lovell, *Introduction to Polymers*, 2nd ed. London, UK: Chapman and Hall, 1991.
- [36] S. J. Limb, K. K. Gleason, D. J. Edell, and E. F. Gleason, "Flexible fluorocarbon wire coatings by pulsed plasma enhanced chemical vapor deposition," *JOURNAL OF VACUUM SCIENCE & TECHNOLOGY A-VACUUM SURFACES AND FILMS*, vol. 15, pp. 1814, 1997.
- [37] P. Favia and R. d'Agostino, "Plasma treatments and plasma deposition of polymers for biomedical applications," *SURFACE & COATINGS TECHNOLOGY*, vol. 98, pp. 1102, 1998.
- [38] E. Kinder, *Biofouling*, vol. 6, pp. 193-200, 1992.
- [39] R. E. Banks, B. E. Smart, and J. C. Tatlow, *Organofluorine Chemistry: Principles and Commercial Applications*. New York: Plenum Press, 1994.
- [40] R. R. Thomas, *Fluoropolymers 2: Properties*. New York: Plenum Press, 1999.
- [41] D. W. Grainger and C. W. Stewart, "Fluorinated Coatings and Films: Motivation and Significance," in *Fluorinated Surfaces, Coatings, and Films (ACS Symposium Series 787, 2001)*, D. G. Castner and D. W. Grainger, Eds.: The American Chemical Society, 2001.

- [42] D. Kiaei and A. S. Hoffman, "Exvivo and Invitro Platelet-Adhesion on RFGD Deposited Polymer," *JOURNAL OF BIOMEDICAL MATERIALS RESEARCH*, vol. 26, pp. 357, 1992.
- [43] K. K. S. Lau, J. A. Caulfield, and K. K. Gleason, "Variable angle spectroscopic ellipsometry of fluorocarbon films from hot filament chemical vapor deposition," *JOURNAL OF VACUUM SCIENCE & TECHNOLOGY A-VACUUM SURFACES AND FILMS*, vol. 18, pp. 2404, 2000.
- [44] P. Groning, A. Schneuwly, L. Schlapbach, and M. T. Gale, ""Self-thickness-limited" plasma polymerization of an ultrathin antiadhesive film," *JOURNAL OF VACUUM SCIENCE & TECHNOLOGY A-VACUUM SURFACES AND FILMS*, vol. 14, pp. 3043, 1996.
- [45] L. M. Han, R. B. Timmons, and W. W. Lee, "Pulsed plasma polymerization of an aromatic perfluorocarbon monomer: formation of low dielectric constant, high thermal stability films," *Journal of Vacuum Science & Technology, B: Microelectronics and Nanometer Structures*, vol. 18, pp. 799-804, 2000.
- [46] S. R. Coulson, I. Woodward, J. P. S. Badyal, S. A. Brewer, and C. Willis, "Super-Repellent Composite Fluoropolymer Surfaces," *Journal of Physical Chemistry B*, vol. 104, pp. 8836-8840, 2000.
- [47] S. Samukawa and S. Furuoya, "Time-modulated electron cyclotron resonance plasma discharge for controlling the generation of reactive species," *Applied Physics Letters*, vol. 63, pp. 2044-6, 1993.
- [48] C. R. Savage, R. B. Timmons, and J. W. Lin, "Molecular Control of Surface-Film Compositions via Pulsed Radiofrequency Plasma Deposition of Perfluoropropylene Oxide," *CHEMISTRY OF MATERIALS*, vol. 3, pp. 575, 1991.
- [49] C. Courteille, J. L. Drier, C. Hollenstein, L. Sansonnens, and A. A. Howling, "Partial-depth modulation study of anions and neutrals in low-pressure silane plasmas," *Plasma Sources Science & Technology*, vol. 5, pp. 210-215, 1996.
- [50] C. Charles, R. W. Boswell, and H. Kuwahara, "SiO₂ deposition from oxygen/silane pulsed helicon diffusion plasmas," *Applied Physics Letters*, vol. 67, pp. 40-2, 1995.

- [51] H. Yasuda and T. Hsu, "Some Aspects of Plasma Polymerization Investigated by Pulsed RF Discharge," *Journal of Polymer Science Part A - Polymer Chemistry*, vol. 15, pp. 81, 1977.
- [52] C. L. Rinsch, X. Chen, V. Panchalingam, R. C. Eberhart, J.-H. Wang, and R. B. Timmons, "Pulsed Radio Frequency Plasma Polymerization of Allyl Alcohol: Controlled Deposition of Surface Hydroxyl Groups," *Langmuir*, vol. 12, pp. 2995-3002, 1996.
- [53] C. R. Savage, R. B. Timmons, and J. W. Lin, "Spectroscopic characterization of films obtained in pulsed radio-frequency plasma discharges of fluorocarbon monomers," *Advances in Chemistry Series*, vol. 236, pp. 745-68, 1993.
- [54] N. M. Mackie, D. G. Castner, and E. R. Fisher, "Characterization of pulsed-plasma-polymerized aromatic films," *Langmuir*, vol. 14, pp. 1227-1235, 1998.
- [55] V. Panchalingam, X. Chen, C. R. Savage, R. B. Timmons, and R. C. Eberhart, "Molecular tailoring of surfaces via pulsed RF plasma depositions," *Journal of Applied Polymer Science: Applied Polymer Symposium*, vol. 54, pp. 123-41, 1994.
- [56] H. Yasuda, *Plasma Polymerization*. Orlando, FL: Academic Press, 1985.
- [57] J. d. A. Clark, *Pulp Technology and Treatment for Paper (2nd Ed.)*. San Francisco: Miller Freeman Publications, Inc., 1985.
- [58] P. Stenius and H. Pakarinen, "Forest Products Chemistry," in *Papermaking Science and Technology*, vol. Book 3, J. Gullichsen and H. Paulapuro, Eds. Helsinki: Published in cooperation with the Finnish Paper Engineers' Association and TAPPI, 1998.
- [59] K. W. Britt, "Handbook of Pulp and Paper Technology (2nd Ed.)." New York: Van Nostrand Reinhold Company, 1970.
- [60] J. Sundholm, "Mechanical Pulping," in *Papermaking Science and Technology*, vol. Book 5, G. J. and H. Paulapuro, Eds. Helsinki: Published in cooperation with the Finnish Paper Engineers' Association and TAPPI, 1998.

- [61] J. Gullichsen and C.-J. Fogelholm, "Chemical Pulping," in *PaperMaking Science and Technology*, vol. Book 6, G. J. and H. Paulapuro, Eds. Helsinki: Published in cooperation with the Finnish Paper Engineers' Association and TAPPI, 1998.
- [62] J. P. Casey, "Pulp and Paper - Chemistry and Chemical Technology (Vol. 2)," 3rd ed. New York: John Wiley & Sons, 1980.
- [63] EPA, "WasteWise Update, Environmentally Preferable Purchasing," in *EPA530-N-01-002*: U.S. EPA Office of Solid Waste and Emergency Response, 2001.
- [64] Perkins_Papers_Ltd., "Certified Processed Chlorine Free," in *Chlorine Free Products Association Press Release*: <http://www.chlorinefreeproducts.org>.
- [65] EPA, "Pulp and Paper Cluster Rule, Preamble to the Final Rule," vol. <http://www.epa.gov/fedrgstr/EPA-WATER/1998/April/Day-15/w9819.htm>.: Federal Register, 1998.
- [66] H. Paulapuro, "Papermaking Part 1, Stock Preparation and Wet End," in *Papermaking Science and Technology*, vol. Book 8, J. Gullichsen and H. Paulapuro, Eds. Helsinki: Published in cooperation with the Finnish Paper Engineers' Association and TAPPI, 1998.
- [67] TAPPI, *TAPPI Standard T205 - sp2 (Forming handsheets for physical tests of pulp)*. Atlanta, GA: TAPPI Press, 2002.
- [68] A. Nakajima, K. Hashimoto, and T. Watanabe, "Recent studies on super-hydrophobic films," *MONATSHEFTE FUR CHEMIE*, vol. 132, pp. 31-41, 2001.
- [69] C. M. Chan, T. M. Ko, and H. Hiraoka, "Polymer surface modification by plasmas and photons," *SURFACE SCIENCE REPORTS*, vol. 24, pp. 3-54, 1996.
- [70] F. J. Dutoit, R. D. Sanderson, W. J. Engelbrecht, and J. B. Wagener, "The Effect of Surface Fluorination on the Wettability of High-Density Polyethylene," *JOURNAL OF FLUORINE CHEMISTRY*, vol. 74, pp. 43-48, 1995.
- [71] W. L. E. Magalhaes and M. Ferreira de Souza, "Solid softwood coated with plasma-polymer for water repellence," *Surface and Coatings Technology*, vol. 155, pp. 11-15, 2002.

- [72] S. M. Mukhopadhyay, P. Joshi, S. Datta, J. G. Zhao, and P. France, "Plasma assisted hydrophobic coatings on porous materials: influence of plasma parameters," *Journal of Physics D: Applied Physics*, vol. 35, pp. 1927-1933, 2002.
- [73] F. Denes, Z. Q. Hua, E. Barrios, and R. A. Young, "Influence of RF-cold plasma treatment on the surface properties of paper," *Journal of Macromolecular Science, Pure and Applied Chemistry*, vol. A32, pp. 1405-43, 1995.
- [74] C. M. G. Carlsson and G. Stroem, "Reduction and oxidation of cellulose surfaces by means of cold plasma," *Langmuir*, vol. 7, pp. 2492-7, 1991.
- [75] F. D. Gunstone and F. A. Norris, *Lipids in Foods: Chemistry, Biochemistry and Technology*: Pergamon Press, New York, 1983.
- [76] S. Sigurdsson and R. Shishoo, "Surface properties of polymers treated with tetrafluoromethane plasma," *Journal of Applied Polymer Science*, vol. 66, pp. 1591-1601, 1997.
- [77] Y. Ikada, M. Suzuki, and Y. Tamada, *Polymer Preprints (American Chemical Society, Division of Polymer Chemistry)*, vol. 24, pp. 19, 1989.
- [78] Y. Wu, Y. Kong, X. Lin, W. Liu, and J. Xu, "Surface-modified hydrophilic membranes in membrane distillation," *Journal of Membrane Science*, vol. 72, pp. 189-196, 1992.
- [79] P. P. Tsai, L. C. Wadsworth, and J. R. Roth, "Surface modification of fabrics using a one-atmosphere glow discharge plasma to improve fabric wettability," *TEXTILE RESEARCH JOURNAL*, vol. 67, pp. 359, 1997.
- [80] A. W. Adamson, *Physical Chemistry of Surfaces*. New York: Wiley, 1990.
- [81] D. Briggs and M. P. Seah, *Practical Surface Analysis: Auger and X-Ray Photoelectron Spectroscopy*, 2nd Edition ed: John Wiley & Sons Ltd, 1996.
- [82] R. Nix, "An Introduction to Surface Chemistry (http://www.chem.qmw.ac.uk/surfaces/scc/scat5_3.htm)," 2004.

- [83] N. L. Alpert, W. E. Keiser, and H. A. Szymanski, *IR Theory and Practice of Infrared Spectroscopy*, 2nd ed. New York: Plenum Press, 1970.
- [84] R. A. Nyquist, *Interpreting Infrared, Raman, and Nuclear Magnetic Resonance Spectra*. San Diego: Academic Press, 2001.
- [85] K. K. Kanazawa and O. R. Melrot, "The Quartz Resonator: Electrochemical Applications," *IBM Journal of Research and Development*, vol. 37, pp. 157, 1993.
- [86] C. Lu and A. W. Czanderna, *Applications of Piezoelectric Quartz Crystal Microbalances*, vol. 7. New York: Elsevier Science Publishing Company, Inc., 1984.
- [87] J. I. Goldstein, D. E. Newbury, P. Echlin, D. C. Joy, C. Lyman, E. Lifshin, L. Sawyer, and J. R. Michael, *Scanning Electron Microscopy and X-Ray Microanalysis*, 3rd ed. New York: Kluwer Academic/Plenum Publishers, 2003.
- [88] S. Chumbley, "<http://www.mse.iastate.edu/microscopy/beaminteractions.html>," 2004.
- [89] M. A. Brown and R. C. Semelka, *MRI: Basic Principles and Applications*. New York: Wiley-Liss, 1995.
- [90] W. A. Edelstein, J. M. S. Hutchinson, G. Johnson, and T. W. Redpath, "Spin Warp NMR Imaging and Applications to Human Whole-body Imaging," *Physics in Medicine and Biology*, vol. 25, pp. 751-756, 1980.
- [91] R. R. Ernst, G. Bodenhausen, and A. Wokaun, *Principles of Nuclear Magnetic Resonance in One and Two Dimensions*. New York: Oxford University Press, 1987.
- [92] A. Pines, "'Shining Light" on NMR and MRI in porous materials.," *Magnetic Resonance Imaging*, vol. 19, pp. 307-309, 2001.
- [93] V. McBrierty, "Solid polymers - a challenge for NMR," *Solid State Nuclear Magnetic Resonance*, vol. 9, pp. 21-27, 1997.

- [94] P. Callaghan, *Principles of Nuclear Magnetic Resonance Microscopy*. Oxford: Clarendon Press, 1991.
- [95] R. J. Abraham, J. Fisher, and P. Loftus, *Introduction to NMR Spectroscopy*. New York: John Wiley & Sons Ltd., 1988.
- [96] J. Leisen, B. Hojjatie, D. W. Coffin, S. A. Lavrykov, B. V. Ramarao, and H. W. Beckham, "Through-Plane Diffusion of Moisture in Paper Detected by Magnetic Resonance Imaging," *Industrial & Engineering Chemistry Research*, vol. 41, pp. 6555-6565, 2002.
- [97] A. Abragam, *The Principles of Nuclear Magnetism*. Oxford: Clarendon Press, 1961.
- [98] I. V. Koptug, S. I. Kabanikhin, K. T. Iskakov, V. B. Fenelonov, L. Y. Khitrina, R. Z. Sagdeev, and V. N. Parmon, "A quantitative NMR imaging study of mass transport in porous solids during drying," *Chemical Engineering Science*, vol. 55, pp. 1559-1571, 2000.
- [99] TAPPI, *T 200 sp-01 (Laboratory beating of pulp (Valley beater method))*. Atlanta, GA: TAPPI Press, 2002.
- [100] TAPPI, *T 227 om-99 (Freeness of pulp (Canadian standard method))*. Atlanta, GA: TAPPI Press, 2002.
- [101] J. F. McClelland, S. J. Bajic, R. W. Jones, and L. M. Seaverson, "Photoacoustic Spectroscopy (Chapter 6)," in *Modern Techniques in Applied Molecular Spectroscopy*, F. M. Mirabella, Ed. New York: Wiley, 1998, pp. pp. 221-265.
- [102] J. F. McClelland, R. W. Jones, S. Luo, and S. M. Seaverson, "A Practical Guide to FT-IR Photoacoustic Spectroscopy (Chapter 5)," in *Practical Sampling Techniques for Infrared Analysis*, P. B. Coleman, Ed. Boca Raton, FL: CRC Press, 1993, pp. pp. 107-144.
- [103] D. W. Vidrine, "Photoacoustic Fourier Transform Infrared Spectroscopy of Solids and Liquids (Chapter 4)," in *Fourier Transform Infrared Spectroscopy*, vol. Volume 3, J. R. Ferraro and L. J. Basile, Eds. New York: Academic Press, 1982, pp. pp. 125-148.

- [104] W. Oh and S. Nair, "Concentration Profiling of a Molecular Sieve Membrane by Step-Scan Photoacoustic Spectroscopy," *Journal of Physical Chemistry B*, vol. 108, pp. 8766-8769, 2004.
- [105] J. S. Francisco and M. M. Maricq, "Making Sure That Hydrofluorocarbons Are "Ozone Friendly"," *Accounts of Chemical Research*, vol. 29, pp. 391-397, 1996.
- [106] M. Chaplin, "<http://www.lsbu.ac.uk/water/hycl.html>," October, 2004.
- [107] D. G. Gray, "The surface analysis of paper and wood fibers by ESCA. III. Interpretation of carbon (1s) peak shape.," *Cellulose Chemistry and Technology*, vol. 12, pp. 735, 1978.
- [108] G. M. Dorris and D. G. Gray, "The surface analysis of paper and wood fibers by ESCA (electron spectroscopy for chemical analysis). I. Application to cellulose and lignin.," *Cellulose Chemistry and Technology*, vol. 12, pp. 9, 1978.
- [109] G. M. Dorris and D. G. Gray, "The surface analysis of paper and wood fibers by ESCA. II. Surface composition of mechanical pulps.," *Cellulose Chemistry and Technology*, vol. 12, pp. 721, 1978.
- [110] P. J. Astell-Burt, J. A. Cairns, A. K. Cheetham, and R. M. Hazel, "A study of the deposition of polymeric material onto surfaces from fluorocarbon RF plasmas.," *Plasma Chemistry and Plasma Processing*, vol. 6, pp. 417, 1986.
- [111] N. M. Mackie, N. F. Dalleska, D. G. Castner, and E. R. Fisher, "Comparison of Pulsed and Continuous-Wave Deposition of Thin Films from Saturated Fluorocarbon/H₂ Inductively Coupled rf Plasmas.," *Chemistry of Materials*, vol. 9, pp. 349, 1997.
- [112] H. Yasuda and C. R. Wang, "Plasma polymerization investigated by the substrate temperature dependence.," *Journal of Polymer Science, Polymer Chemistry Edition*, vol. 23, pp. 87, 1985.
- [113] M. J. O'Keefe and J. M. Rigsbee, "Plasma polymerization of fluorocarbon thin films on glass and metal substrates.," *Materials Research Society Symposium Proceedings*, vol. 304(Polymer/Inorganic Interfaces), pp. 179, 1993.

- [114] A. Hynes, M. Shenton, and J. P. S. Badyal, "Pulsed plasma polymerization of perfluorocyclohexane.," *Macromolecules*, vol. 29, pp. 4220, 1996.
- [115] C. B. Labelle and K. K. Gleason, "Pulsed plasma deposition from 1,1,2,2-tetrafluoroethane by electron cyclotron resonance and conventional plasma enhanced chemical vapor deposition," *Journal of Applied Polymer Science*, vol. 80, pp. 2084-2092, 2001.
- [116] C. B. Labelle, K. K. S. Lau, and K. K. Gleason, "Pulsed plasma enhanced chemical vapor deposition from CH₂F₂, C₂H₂F₄, and CHClF₂," *Materials Research Society Symposium Proceedings*, vol. 511(Low-Dielectric Constant Materials III), pp. 75, 1998.
- [117] A. J. Bariya, H. Shan, C. W. Frank, S. A. Self, and J. P. McVittie, "The etching of trifluoromethane plasma polymer in fluorine-containing discharges.," *Journal of Vacuum Science & Technology, B: Microelectronics and Nanometer Structures*, vol. 9, pp. 1, 1991.
- [118] E. J. Winder and K. K. Gleason, "Growth and characterization of fluorocarbon thin films grown from trifluoromethane (CHF₃) using pulsed-plasma enhanced CVD," *Journal of Applied Polymer Science*, vol. 78, pp. 842-849, 2000.
- [119] S. Agraharam, D. W. Hess, P. A. Kohl, and S. A. Bidstrup Allen, "Plasma chemistry in fluorocarbon film deposition from pentafluoroethane/argon mixtures," *Journal of Vacuum Science & Technology, A: Vacuum, Surfaces, and Films*, vol. 17, pp. 3265-3271, 1999.
- [120] R. d'Agostino, L. Martinu, and V. Pische, "Effect of bias and temperature on the bulk and surface properties of gold-containing plasma-polymerized fluorocarbons.," *Plasma Chemistry and Plasma Processing*, vol. 11, pp. 1, 1991.
- [121] N. B. Colthup, L. H. Daly, and S. E. Wiberly, *Introduction to Infrared and Raman Spectroscopy*, 3rd ed. New York: Academic Press, 1990.
- [122] W. K. Fisher and J. C. Corelli, "Effect of ionizing radiation on the chemical composition, crystalline content and structure, and flow properties of polytetrafluoroethylene.," *Journal of Polymer Science, Polymer Chemistry Edition*, vol. 19, pp. 2465, 1981.

- [123] B. Dischler, "Amorphous Hydrogenated Carbon Films," in *Proceedings of E-MRS*, vol. 17, P. Koidl and P. Oelhafen, Eds., 1987, pp. 189.
- [124] R. Chen, V. Gorelik, and M. S. Silverstein, "Plasma polymerization of hexafluoropropylene: film deposition and structure.," *Journal of Applied Polymer Science*, vol. 56, pp. 615, 1995.
- [125] K. Takahashi and K. Tachibana, "Solid particle production in fluorocarbon plasmas. I. Correlation with polymer film deposition.," *Journal of Vacuum Science & Technology, A: Vacuum, Surfaces, and Films*, vol. 19, pp. 2055, 2001.
- [126] K. Takahashi and K. Tachibana, "Solid particle production in fluorocarbon plasmas II: Gas phase reactions for polymerization.," *Journal of Vacuum Science & Technology, A: Vacuum, Surfaces, and Films*, vol. 20, pp. 305, 2002.
- [127] P. B. Leezenberg, T. C. Reiley, and G. W. Tyndall, "Plasma induced copolymerization of hexafluoropropylene and octafluoropropane," *JOURNAL OF VACUUM SCIENCE & TECHNOLOGY A-VACUUM SURFACES AND FILMS*, vol. 17, pp. 275, 1999.
- [128] M. K. Bennett and W. A. Zisman, "Wetting properties of tetrafluoroethylene and hexafluoropropylene copolymers.," *Journal of Physical Chemistry B*, vol. 64, pp. 1292, 1960.
- [129] M. K. Bennett, N. L. Jarvis, and W. A. Zisman, "Surface activity of fluorinated organic compounds at organic liquid-air interfaces. IV. Effect of structure and homology.," *Journal of Physical Chemistry B*, vol. 66, pp. 328, 1962.
- [130] B. E. Smart, in *Organofluorine Chemistry: Principles and Commercial Applications*, R. E. Banks, Ed. New York: Plenum Press, 1994.
- [131] B. E. Smart, "Physical and physicochemical properties [of fluorinated organic compounds]." vol. 187(Chemistry of Organic Fluorine Compounds II). ACS Monograph, 1995, pp. 979.
- [132] J. Seth and S. V. Babu, "Fluorohydrogenated amorphous carbon (a-C:H,F) films prepared by the r.f. plasma decomposition of 1,3-butadiene and carbon tetrafluoride," *Thin Solid Films*, vol. 230, pp. 90, 1993.

- [133] I. T. Martin, G. S. Malkov, C. I. Butoi, and E. R. Fisher, "Comparison of pulsed and downstream deposition of fluorocarbon materials from C_3F_8 and $c-C_4F_8$ plasmas," *JOURNAL OF VACUUM SCIENCE & TECHNOLOGY A-VACUUM SURFACES AND FILMS*, vol. 22, pp. 227, 2004.
- [134] A. W. Adamson and A. P. Gast, *Physical Chemistry of Surfaces*, 6th ed. New York: Wiley, 1997.
- [135] Y. Kong, X. Lin, Y. Wu, J. Chen, and J. Xu, "Plasma polymerization of Octafluorocyclobutane and hydrophobic microporous composite membranes for membrane distillation," *Journal of Applied Polymer Science*, vol. 46, pp. 191, 1992.
- [136] R. A. Lampitt, J. M. Crowther, and J. P. S. Badyal, "Switching Liquid Repellent Surfaces," *Journal of Physical Chemistry B*, vol. 104, pp. 10329-10331, 2000.
- [137] H. J. Qi, D. Wang, Z. L. Ma, S. Q. Sun, Q. Y. Sui, W. P. Zhang, and J. J. Lu, "Molecular structure and hydrophobicity of polymeric fluorocarbon films deposited on PET substrates," *Journal of Applied Polymer Science*, vol. 85, pp. 1843, 2002.
- [138] S.-D. Lee, S. Manolache, M. Sarmadi, and F. Denes, "Deposition of high fluorine content macromolecular thin layers under continuous-flow-system corona discharge conditions," *POLYMER BULLETIN*, vol. 43, pp. 409, 1999.
- [139] K. Niskanen, "Paper Physics," in *Papermaking Science and Technology*, vol. Book 16, J. Gullichsen and H. Paulapuro, Eds. Helsinki: Published in cooperation with the Finnish Paper Engineers' Association and TAPPI, 1998.
- [140] S. Agraharam, D. W. Hess, P. A. Kohl, and S. A. Bidstrup Allen, "Comparison of plasma chemistries and structure-property relationships of fluorocarbon films deposited from octafluorocyclobutane and pentafluoroethane monomers," *Journal of Vacuum Science & Technology, B: Microelectronics and Nanometer Structures*, vol. 19, pp. 439-446, 2001.
- [141] R. V. Tanikella, S. Agraharam, S. A. Bidstrup Allen, D. W. Hess, and P. A. Kohl, "Moisture absorption studies of fluorocarbon films deposited from pentafluoroethane and octafluorocyclobutane plasmas," *Journal of Electronic Materials*, vol. 31, pp. 1096-1103, 2002.

- [142] M. G. McMaster and D. S. Soane, "Water sorption in epoxy thin films," *IEEE Transactions on Components, Hybrids, and Manufacturing Technology*, vol. 12, pp. 373, 1989.
- [143] J. Crank and G. S. Park, *Diffusion in Polymers*: Academic Press, London, 1968.
- [144] C. Zhang, J. Wyatt, and D. H. Weinkauff, "Analogous sorption phenomena in plasma and conventionally polymerized microsensor films," *Polymer Preprints (American Chemical Society, Division of Polymer Chemistry)*, vol. 43, pp. 1009-1110, 2002.
- [145] C. Zhang, J. Wyatt, and D. H. Weinkauff, "Carbon dioxide sorption in conventional and plasma polymerized methyl methacrylate thin films.," *Polymer*, vol. 45, pp. 7665, 2004.
- [146] C. Zhang, J. Wyatt, S. P. Russell, and D. H. Weinkauff, "Methanol vapor sorption in plasma polymerized thin films.," *Polymer*, vol. 45, pp. 7655, 2004.
- [147] S. N. Dhoot, B. D. Freeman, and M. E. Stewart, "Sorption and transport of linear and branched ketones in biaxially oriented polyethylene terephthalate," *Polymer*, vol. 45, pp. 5619, 2004.
- [148] S. N. Dhoot, B. D. Freeman, and M. E. Stewart, "Sorption and Transport of Linear Esters and Branched Alkanes in Biaxially Oriented Poly(ethylene terephthalate)," *Industrial & Engineering Chemistry Research*, vol. 43, pp. 2966, 2004.
- [149] J. Crank, *The Mathematics of Diffusion*: Clarendon Press, Oxford, UK, 1975.
- [150] J. Bandrup, E. H. Immergut, and E. A. Grulke, *Polymer Handbook*, 4th. ed: John Wiley, NY, 1999.
- [151] J. Bandrup and E. H. Immergut, *Polymer Handbook*, 3rd ed: Wiley, New York, 1989.
- [152] J. Bandrup and E. H. Immergut, *Polymer Handbook*, 2nd ed: John Wiley, NY, 1974.

- [153] TAPPI, "T559 Grease Resistance Test for Paper and Paper Board," in *Tappi Test Methods*. TAPPI Press, Norcross, GA, 2002.
- [154] TAPPI, "T 454 om-00 - Turpentine test for voids in glassine and greaseproof papers," in *Tappi Test Methods*. TAPPI Press, Norcross, GA, 2000.
- [155] S. N. Dhoot, B. D. Freeman, M. E. Stewart, and A. J. Hill, "Sorption and Transport of Linear Alkane Hydrocarbons in Biaxially Oriented Polyethylene Terephthalate," *Journal of Polymer Science Part B: Polymer Physics*, vol. 39, pp. 1160, 2001.
- [156] C. C. McDowell, B. D. Freeman, and G. W. McNeely, "Acetone sorption and uptake kinetic in poly(ethylene terephthalate)," *Polymer*, vol. 40, pp. 3487-3499, 1999.
- [157] G. F. Billovits and C. J. Durning, "Two stage weight gain in the polystyrene-ethylbenzene system," *Polymer Communications*, vol. 31, pp. 358-361, 1990.
- [158] J. H. Petropoulos, "On the Dual Mode Gas Transport Model for Glassy Polymers," *Journal of Polymer Science, Part B: Polymer Physics*, vol. 26, pp. 1009-1020, 1988.
- [159] J. A. Horas and F. Nieto, "Generalization of dual mode transport theory for glassy polymers," *Journal of Polymer Science, Part B: Polymer Physics*, vol. 32, pp. 1889-1898, 1994.
- [160] J. H. Petropoulos, "Interpretation of Anomalous Sorption Kinetics in Polymer-Penetrant Systems in Terms of a Time-dependent Solubility Coefficient.," *Journal of Polymer Science, Part B - Polymer Physics*, vol. 22, pp. 1885-1900, 1984.
- [161] F. A. Long and D. Richman, *Journal of American Chemical Society*, vol. 82, pp. 513-519, 1960.
- [162] A. R. Berens and H. B. Hopfenberg, "Diffusion and Relaxation in Glass Polymer Powders EM DASH 2. Separation of Diffusion and Relaxation Parameters," *Polymer*, vol. 19, pp. 489-496, 1978.
- [163] J. S. Vrentas, J. L. Duda, and H.-C. Ling, "Antiplasticization and Volumetric Behavior in Glassy Polymers," *Macromolecules*, vol. 21, pp. 1470-1475, 1988.

- [164] P. Neogi, "ANOMALOUS DIFFUSION OF VAPORS THROUGH SOLID POLYMERS. PART II: ANOMALOUS SORPTION," *AIChE Journal*, vol. 29, pp. 833-839, 1983.
- [165] M. Sanopoulou and J. H. Petropoulos, "Systematic analysis and model interpretation of micromolecular non-Fickian sorption kinetics in polymer films," *Macromolecules*, vol. 34, pp. 1400-1410, 2001.
- [166] S. Vaswani, J. Koskinen, and D. W. Hess, "Surface modification of paper and cellulose by plasma-assisted deposition of fluorocarbon films," *Surface and Coatings Technology*, vol. In Press, 2004.
- [167] H. Darcy, "Les fontaines publiques de la ville de Dijon; Victor Dalmont, Paris," 1856.
- [168] R. A. Freeze and J. A. Cherry, *Groundwater*. Englewood Cliffs, NJ: Prentice-Hall, 1979.
- [169] J. Bear, *Dynamics of Fluids in Porous Media*. New York: Elsevier, 1972.
- [170] F. A. L. Dullien, *Porous Media - Fluid Transport and Pore Structure*. New York, N.Y.: Academic Press, 1979.
- [171] P. K. Chatterjee and B. S. Gupta, "Absorbent Technology," in *Textile Science and Technology - 13*, vol. 13. Amsterdam: Elsevier, 2002.
- [172] A. Scheidegger, *The Physics of Flow Through Porous Media*. Toronto: University of Toronto Press, 1960.
- [173] P. K. Chatterjee, "Absorbency," in *Textile Science and Technology - 7*, vol. 7. Amsterdam: Elsevier, 1985.
- [174] A. S. Iberall, "Permeability of glass wool and other highly porous media," *J. Research Natl. Bur. Standards*, vol. 45, pp. 398-406, 1950.
- [175] H. C. Brinkman, "A calculation of the viscous force exerted by a flowing fluid on a dense swarm of particles," *Applied Sci. Research*, vol. A1, pp. 27-34, 1947.

- [176] I. Fatt, "The network model of porous media III. dynamic properties of network with tube radius distribution," *AIME Petroleum Transactions*, vol. 207, pp. 164, 1956.
- [177] I. Fatt, "The network model of porous media II. dynamic properties of a single size tube network," *AIME Petroleum Transactions*, vol. 207, pp. 160, 1956.
- [178] I. Fatt, "The network model of porous media I. capillary pressure characteristics," *AIME Petroleum Transactions*, vol. 207, pp. 144, 1956.
- [179] D. Hillel, *Soil and water: Physical principles and processes*. New York: Academic Press, 1971.
- [180] G. K. Batchelor, *An introduction to fluid dynamics*. Cambridge, UK: Cambridge Univ. Press, 1967.
- [181] T.-S. Leu and P.-Y. Chang, " Pressure barrier of capillary stop valves in micro sample separators," *Sensors and Actuators, A: Physical*, vol. A115, pp. 508-515, 2004.
- [182] S.-J. Kim, Y. B. Shin, D.-S. Lee, H. Yang, K. Kim, S. H. Park, and Y. T. Kim, "Capillary-Driven Passive Retarding Microvalve Based on an Aspect Ratio Concept," presented at 7th International Conference on Miniaturized Chemical and Biochemical Analysis Systems, October 5-9, 2003, Squaw Valley, California, 2003.
- [183] P. F. Man, C. H. Mastrangelo, M. A. Burns, and D. T. Burke, "Microfabricated capillarity-driven stop valve and sample injector," presented at Proceedings - IEEE Annual International Workshop on Micro Electro Mechanical Systems: An Investigation of Micro Structures, Sensors, Actuators, Machines and Systems, 11th, Heidelberg, Jan. 25-29, 1998, 1998.
- [184] J. Morikawa and T. Hashimoto, "Thermal Diffusivity Measurement of Papers by an AC Joule Heating Method," *Polymer International*, vol. 45, pp. 207-210, 1998.
- [185] D. Twede and R. Goddard, *Packaging Materials*, 2nd. ed. Surrey, UK: Pira International, 1998.

- [186] F. A. Paine, "The Packaging User's Handbook." London: Blackie and Son Ltd., 1991.
- [187] J. F. Hanlon, R. J. Kelsey, and H. E. Forcinio, *Handbook of Package Engineering*. Lancaster, PA: Technomic Publishing, 1998.
- [188] Y. V. Pan, R. A. Wesley, R. Luginbuhl, D. D. Denton, and B. D. Ratner, "Plasma Polymerized N-Isopropylacrylamide: Synthesis and Characterization of a Smart Thermally Responsive Coating," *Biomacromolecules*, vol. 2, pp. 32, 2001.

VITA

Sudeep Vaswani was born on August 31, 1975, in Mumbai (Bombay), India, to Goverdhan Das and Kaushalya Vaswani. After schooling in St. Paul's Academy (Ghaziabad) and Delhi Public School (Ghaziabad), he attended Indian Institute of Technology, Roorkee, where he obtained his Bachelor of Engineering degree in Chemical Engineering in the year 1998. Soon after, he came to the US to pursue a M.S. degree in Environmental Engineering at North Carolina State University, Raleigh (NC). After finishing his master's degree, he joined School of Chemical and Biomolecular Engineering at Georgia Tech to pursue a Ph.D. specializing in plasma processing of thin films under the supervision of Dr. Dennis Hess. To realize his entrepreneurial dreams and to hone his business acumen, he concurrently pursued an M.B.A. (awarded December 2004) specializing in Entrepreneurship and Strategic Management at Georgia Tech Business School. He is currently employed with Intel Corp. (Santa Clara) as a Senior Process Engineer.